TRANSPORT AND DISORDER-INDUCED LOCALIZATION OF ULTRACOLD FERMI GASES

BY

WILLIAM RUSSELL MCGEHEE

DISSERTATION

Submitted in partial fulfillment of the requirements
for the degree of Doctor of Philosophy in Physics
in the Graduate College of the
University of Illinois at Urbana-Champaign, 2015

Urbana, Illinois

Doctoral Committee:

Associate Professor Nadya Mason, Chair
Professor Brian DeMarco, Director of Research
Assistant Professor Bryce Gadway
Assistant Professor Bryan Clark

Abstract

We experimentally study localization and dynamics of ultracold fermions in speckle and optical lattice potentials to explore Anderson localization, many-body localization, and relaxation dynamics in strongly correlated systems. Anderson localization is probed by releasing non-interacting, spin-polarized gases into three dimensional, anisotropic disordered potentials produced from optical speckle. A fraction of the atoms are localized by the disorder, and a mobility edge is found separating localized from extended states. The length scale of the speckle is varied, and the localized state is found to scale linearly with the geometric mean of the speckle autocorrelation length. We realize the Fermi Hubbard model by loading atoms in a cubic optical lattice. Non-equilibrium momentum distributions are created via Raman transitions, and the excitation relaxation rate is measured in the lattice. Transport experiments were performed in a disordered optical lattice to explore the disordered Hubbard model. These experiments reveal localization in the presence of strong interactions and an interaction driven metal–to–insulator transition. The localized state is found to be insensitive to a doubling in the temperature of the gas and is consistent with predictions of many-body localization.

To my family, for their many years of support and encouragement.

Acknowledgments

I want to thank my friends, labmates, and mentors for their time, encouragement, and enthusiasm—graduate school has been a great adventures that would not have been possible without you. Foremost, I thank Brian DeMarco for creating a space in which his students have the freedom to develop and explore individually, within a cohesive and supportive lab. Brian has the uncanny knack for providing the necessary encouragement and direction when it is most needed, and he has taught me how to ask the right questions without getting too lost in the details. I also owe a great deal to Josh Zirbel, who joined the ^{40}K experiment as a post-doc when the most of the apparatus was built but very little was working. Josh propelled the experiment forward and set a very positive example for us in lab. He devoted a significant portion of his time to the undergraduates and members of the Rb team, and I greatly respect how freely he offered his time to others. I also want to thank the other members of the DeMarco lab including Matt White, Matt Pasienski, David McKay, David Chen, Stan Kondov, Carrie Meldgin, Wenchao Xu, Paul Koehring, Phillip Russ, Will Morong, Pei-Wen Tsai, and Laura Wadleigh. Special thanks go to Matt White for the infrastructure he developed for the lab, and to Wenchao and Will for their camaraderie in lab and for carrying the experiment forward.

I extend many thanks to my friends in the the history cohort and Cureton gang including Nate, Lydia, Ben, Alissa, Dan, Miyuki, Alex, Marlene, Agata, Santiago, Patyrk, and Elena. Ya'll made my last three years in Urbana incredible rich, and you will be sincerely missed. Special thanks are owed to the Crutnams for their extreme generosity in housing me during my last months in Illinois. I also thank my travel partners Matthias and Adele for the many great adventures in the US and abroad. Ruth, Adele, Liz, and Ben were close friends at MIT, and their positive experiences in the CUA led me both to graduate school and to Brian's lab. I look forward to many future adventures with all of you, and my door is always open.

I thank Lauren Aycock for brightening my life and broadening my perspective. I am looking forward to starting our new life together in Maryland!

Finally, I acknowledge generous support from the University of Illinois, NSF, ONR, ARO, and DARPA.

Table of Contents

List of Tables

List of Figures

Chapter 1

Introduction

This thesis explores transport and disorder-induced localization with ultracold Fermi gases. We focus on studies of transport in speckle potentials and disordered optical lattices to probe Anderson and many-body localization. The apparatus for performing these experiments prepares an ultracold quantum gas of ^{40}K atoms and applies a variety of well controlled optical and magnetic potentials. These potentials build the physical landscape of the experiment and allow for the construction of analogs to other physical systems. Generically, we use a well controlled quantum system to simulate the behavior of another, less-understood quantum system we wish to explore—this is called quantum simulation. Quantum simulation encompasses a large number of experimental approaches, but the overarching goal of these methods is to explore a model or Hamiltonian in a regime where direct calculation is not possible either due to the scale or complexity of the system. We begin by constructing a quantum system whose underlying Hamiltonian is engineered to match or approximate the system we wish to explore, and instead of propagating the initial state forward in time using models and classical computers, we perform the experiment through the analog quantum system. In this way, one quantum system simulates the behavior of another. With ultracold gases, the simulation is "run" using atomic matter waves propagating in time through optical and magnetic potentials, and a broad spectrum of technology has been developed to provide both low entropy initialization of the simulation and precise control and calibration of the simulated Hamiltonian.

Analog quantum simulators, much like early classical computers, are purpose–built to simulate a given problem or class of problems. The apparatus discussed in this thesis was constructed to study the role of disorder and interaction in regimes relevant to materials. The available parameter space we explore is illustrated in Figure 1.1, which shows an equivalent of the Bronstein cube illustrating the boundaries of physical knowledge in the early 1920s with respect to the physical constants h, G, and 1/c. This cube is variously attributed to Bronstein as well as Gamow, Ivanenko, and Landau; and on this cube, problems with projection along multiple axes become increasingly difficult. Many are still active topics of research. Here, we are interested in the interplay of quantum states with disorder and interactions. In these systems the underlying Hamiltonian is known, but the combination of quantum degeneracy, interactions, and disorder

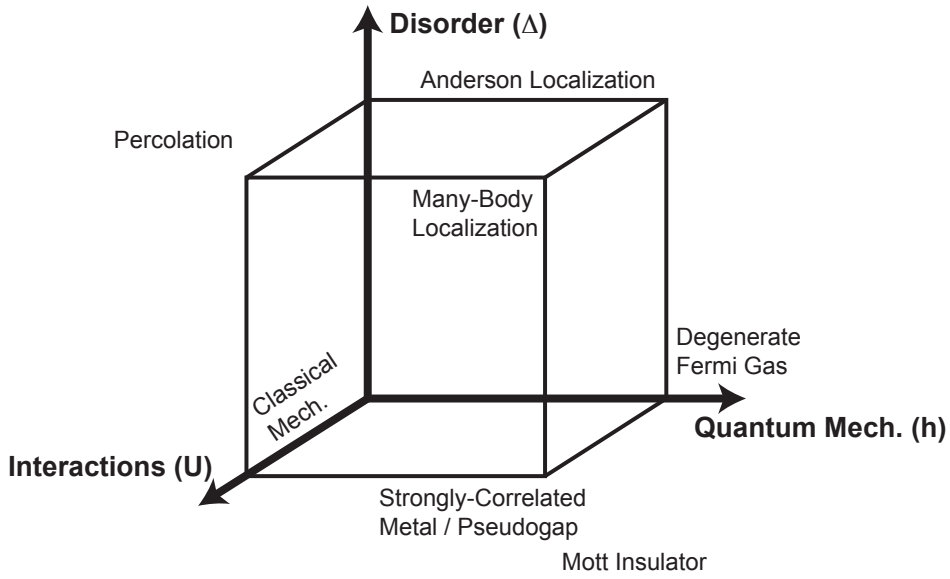

Figure 1.1: Phase space for quantum simulation of condensed matter systems. In the original Bronstein cube, axes represented the boundaries of physical knowledge set by the values of h, G, and $1/c$. Here, an equivalent cube is constructed for the quantum many-body problem with axes set by relevance of quantum mechanics, disorder, and interactions. Problems with projections along multiple axes become increasingly complex and difficult to solve numerically. In this work, we use degenerate Fermi gases to simulate behavior in the regimes of Anderson localization, strongly-correlated metals, and many-body localization.

leads to behavior that is difficult to describe with current theoretical and numerical tools. This idea is encapsulated in Phillip Anderson's famous quote describing emergent phenomena: "More is different" [7].

Experiments presented in this thesis are performed iteratively—for each initialization of our quantum simulation, parameters of the Hamiltonian are chosen and the state is evolved for a particular length of time. At the end of the experiment, an image is taken of the gas, which destroys the carefully prepared quantum state. This process is then repeated many times by first cooling a gas to the desired initial state, preparing the desired Hamiltonian, and time evolving a chosen amount. In this way, the desired phase space is explored with discrete sampling. Examples of this process are shown in Figure 1.2 where localization is explored in various disordered potentials.

This thesis presents several new measurements of transport in disordered systems relevant to longstanding problems of localization in 3D and in the presence of strong interactions. Predictions for 3D localization in correlated disorder are primarily performed in the weak scattering limit. The weak scattering approximation is likely to fail at the onset of Anderson, and the validity of the limit is largely unknown. Measurements of Anderson localization in a 3D speckle potential with variable correlation properties are presented in this thesis as a test of predictions from the weak scattering limit. Measurements are performed over a range in speckle correlation lengths to extract the scaling of thermally averaged localization lengths and the location of the

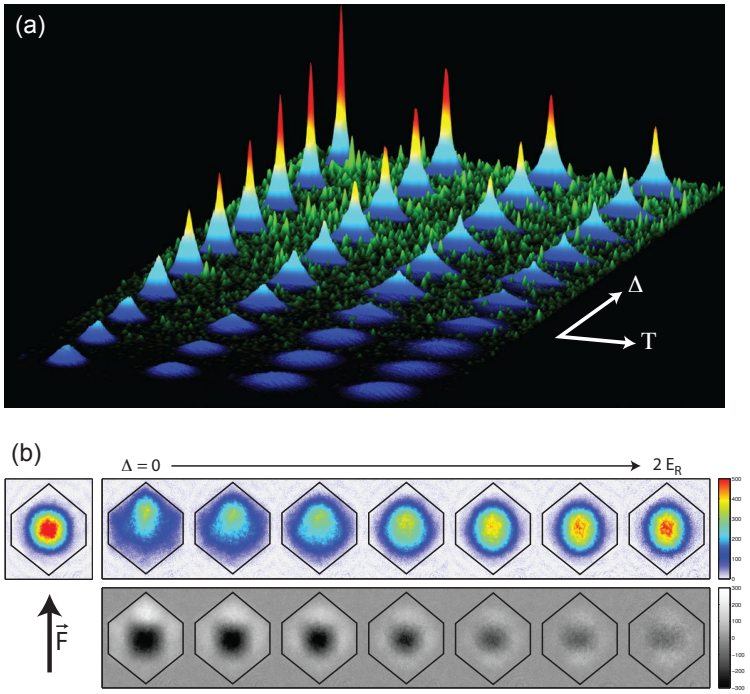

Figure 1.2: Examples of quantum simulation using ultracold quantum gases. (a) Non-interacting Fermi gases are released into a disordered potential with varying mean disorder height Δ and temperature T. The dynamics of the gas are measured as these parameters are varied to explore the desired parameter space. Data are replotted from Figure 4.3 (b) and modified from Ref. [130]. An impulse is applied to a strongly interacting gas in a 3D, disordered optical lattice. The response is observed as the disorder strength is varied. Images show the quasimomentum gas and the difference from the unperturbed state; data are replotted from Figure 6.4.

mobility edge. Comparisons to several state-of-the-art predictions are included with special emphasis given in estimating the validity of the Born approximation. Additional probes of the behavior of the localized state are performed by observing dynamics after quenching the density profile and applying a uniform force to the localized atoms. Using an interacting gas in a disordered optical lattice, we study transport and localization in the presence of strong interactions. This work connects to recent theoretical predictions of the possibility for many-body localization in isolated, interacting quantum systems. Many-body localization predicts that a system of localized particles with weak interactions and no connection to an external bath can remain insulating at finite temperature. This is surprising and raises important questions about thermalization in isolated quantum systems. We realize an analogous system of localized atoms in a disordered optical lattice and probe the stability of the localized state across a doubling of the temperature in the lattice.

1.1 Outline of Manuscript

- **Chapter 2:** This chapter details the experimental apparatus and production of ultracold, degenerate Fermi gases with ^{40}K atoms. The relevant properties of ^{40}K and its response to applied magnetic and optical potentials are presented. Significant focus is given to the technical details of the magnetic and optical potentials including the subtleties of the early stages of magnetic trap loading, residual curvature from the anti-gravity field, and active position servoing of the optical trap. Other aspects of the experiment, such as Raman optics and fringe removal in absorption imaging, are introduced.

- **Chapter 3:** The properties of optical speckle, including its intensity autocorrelation and power spectrum, are discussed in detail. Speckle is used in this work to create three-dimensional disordered potentials for studying Anderson localization in 3D and disorder-induced localization in optical lattices. To perform these measurements, the statistical properties of the disorder must be well known and accurately calibrated. The optics used to create the speckle potential are discussed and ex situ scans of 3D speckle potentials are performed with a duplicate of the experimental optics. The intensity autocorrelation of the measured speckle distributions are compared with analytic predictions and are used to build a model of speckle in the experiment.

- **Chapter 4:** We observe disorder-induced localization in 3D speckle potentials consistent with the scenario of Anderson localization. A spin-polarized, non-interacting Fermi gas is loaded into a speckle potential and is observed to break into two components: one which expands ballistically and the other which adopts a localized, anisotropic density profile whose shape is fixed in time. This thesis focuses on the scaling of the localized state as a function of the disorder correlation length. Scaling with temperature and the mean disorder potential are also discussed. Further studies probing the nature of this state involve quenching the localized density profile and measuring the stability against an external force. Detailed comparison to theoretical predictions of Anderson localization in speckle potentials within the Born approximation are made, and the validity of this approximation for our data is discussed.

- **Chapter 5:** Chapter 5 details the properties of degenerate Fermi gases in optical lattices. The Hubbard model and band structure in the lattice are introduced, and details of the alignment and calibration of the lattice potential are presented. A large problem in lattice gas experiments is accurate thermometry in the lattice, and we discuss in detail how we infer thermodynamic properties assuming isentropic transfer from the harmonic trap in which the gas is prepared to the lattice. A number of thermodynamic limits are discussed, and number occupation and quasimomentum distribution are shown for relevant

entropies and particle numbers. The relevance of single-particle localized states in the lattice is also discussed.

- **Chapter 6:** We report transport experiments in strongly correlated lattice systems. We load a spin-mixed gas into a disordered optical lattice; thereby, realizing the disordered Hubbard model. We probe the conductivity of the many-body state in the lattice by applying an external force. We observe the atom to become localized by the disorder in the presence of strong interactions and identify an interaction-induced metal-to-insulator transition. To make connection with recent work on many-body localization, we measure the response of a marginally localized gas as the temperature of the gas is increased and measure no response over a doubling in the temperature. Recent numerical work is discussed which replicates the high temperature transport data in the experiment with no free parameters and finds the data consistent with Anderson localization of Hubbard-band quasiparticles. We conclude by introducing an experimental technique for probing quasimomentum relaxation dynamics in optical lattice systems.

Chapter 2

Experimental Apparatus

2.1 Producing Degenerate Fermi Gases

We produce quantum degenerate Fermi gases of ^{40}K through standard cooling techniques. Atoms are first collected in magneto-optical trap (MOT) and then evaporatively cooled to degeneracy in magnetic and optical potentials. The apparatus presented here is based on experiments at JILA [44], borrows heavily from the rubidium experiment at Illinois [211, 156, 135], and builds on decades of laser cooling technology. The majority of the experiment was built by Stan Kondov, myself, and Josh Zirbel; and many details of the apparatus can be found Stan Kondov's thesis [100]. This chapter will briefly summarize the operation and design of the experiment with greater emphasis given to recent additions. The properties of optical speckle used in this work to create disordered potentials are described in Chapter 3.

The experiment occurs within a vacuum chamber divided into two cells: the collection cell where atoms are initially collected in a MOT [214] and the science cell where the gas is cooled to degeneracy and experiments are performed. The two cells are connected by a differential pumping tube, as shown in Fig. 2.1, that affords a pressure ratio of $\approx 10^3$ between the chambers. Experiments begin with a 3D magneto-optic trap (MOT) that collects roughly a billion atoms to $\approx 100\mu K$ [43]. A quadrupole coil is used to generate the 10 Gauss/cm gradient necessary for the MOT, and two cooling lasers at 766.7 nm address the trapping and repumping transitions. The MOT is a dark-spot design [92] where a hole is placed in the repumping beam to reduce radiation pressure in the center of the MOT. This allows for a greater total number of atoms to be captured at the expense of slower MOT loading rates and added complexity. Both glass vacuum cells are uncoated.

Atoms are loaded into the MOT from a dilute vapor of potassium in the collection cell. Four isotopically enriched potassium alkali metal dispensers (Alvatec GmbH) are attached to the collection cell in a glass arm; dispensers for rubidium are attached to the cell in a separate arm but are not used. The potassium dispensers are resistively heated using approximately 6 A to control their vapor pressure. The glass arm for holding the dispensers and the collection cell are heated using tape heaters to minimize plating of the potassium vapor

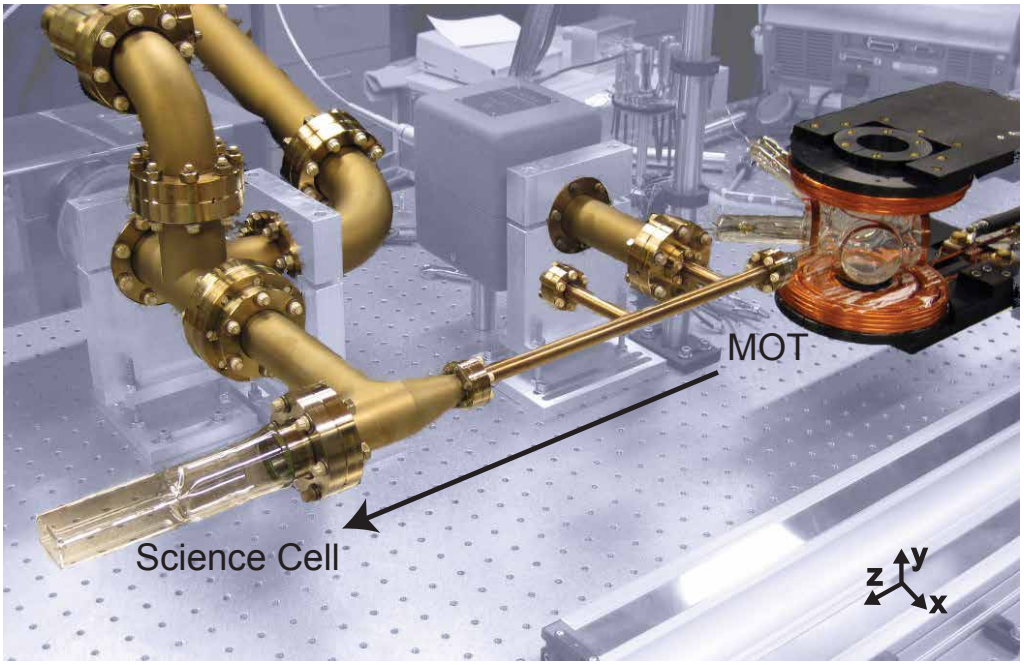

Figure 2.1: Early image of the vacuum chamber in which experiments are performed. Atoms are collected in the collection cell from a dilute potassium vapor. The MOT quadrupole coils are mounted to a linear stage and transfer the atoms through the differential pumping tube to the science cell. Evaporative cooling is performed in magnetic and optical traps (not shown) in the science cell.

on the inside of the chamber. The low vapor pressure and the dark-spot MOT configuration makes for a typical loading time of thirty seconds. This could be greatly increased with a Zeeman slower or a 2D MOT source. Recent work has explored routes to lower temperatures in potassium MOTs using a gray molasses [109, 51, 178] and narrow linewidth MOTs using the 405 nm transition [137, 48]. These improvements would not be beneficial in MOT loading in the current apparatus due to heating in the transfer and quadrupole trap loading sequence.

The background pressure in the collection cell sets the trapping lifetime in a magnetic potential to roughly one second, and the atoms are transferred to the science cell with lower pressure for further cooling. The gas is loaded into a quadrupole magnetic trap before being transferred to the science cell. Loading of the quadrupole trap is preceded by stages of compressed MOT, optical molasses, and optical pumping to the magnetically trapped states in the F = 9/2 manifold. The MOT quadrupole coils are ramped over 25 ms to a gradient of 240 Gauss/cm to tightly compress the atoms for efficient transfer through the differential pumping tube to the science cell. After optical pumping and application of the deep quadrupole field, the MOT quadrupole coils mechanically transfer the atoms 0.7 meters across the table to the science cell. The quadrupole coils are mounted on a linear stage that allows for fine control over the velocity profile of the motion to limit vibration to the table. A combination of two ion pumps maintains the differential pressure

between the two cells, and a titanium sublimation pump is also attached to the chamber for initial pumping to ultra-high vacuum. After arrival in the science cell, the atoms are transferred from the MOT quadrupole coils to a stationary QUIC trap where the $1/e$ lifetime is several hundred seconds.

Forced evaporative cooling in magnetic and optical traps is performed in the science cell to cool the gas to degeneracy [93, 37]. Initial cooling is performed in a modified QUIC trap described in Sec. 2.3.2. High energy atoms are driven to magnetically untrapped states via a microwave transition while the gas equilibrates to progressively lower temperatures. The final stages of cooling are performed in an optical dipole trap described in Sec. 2.4.1. Temperatures in this trap fall well below the p-wave barrier for single-spin evaporative cooling [42]. The spin mixture in this trap is adjusted by varying the final stages of magnetic evaporation and through spin-changing microwave and Raman transitions. Typical evaporation trajectories in the magnetic and optical trap take 40 seconds each and result in a total cycle time of approximately two minutes to reach degeneracy. The fastest BEC experiments report sub-second experimental cycle times. Fermi gas experiments in general take longer to cool to degeneracy due to the Pauli blocking that slows the collisional timescale for degenerate gases, and the fastest Fermi gas experiments can cycle every 20 seconds [196]. A common approach is to use a Feshbach resonance in the optical trap to maximize the collisional cross section and hence the speed of evaporation. Alternatives for faster cooling in magnetic traps include Doppler cooling and degenerate Raman sideband cooling [207]. These methods are relatively easy to implement and could substantially reduce the time used in the initial stages of cooling.

2.2 Properties of ^{40}K

All experiments in this thesis were performed with the fermionic isotope of potassium, ^{40}K. The natural abundance of this isotope is low (around 0.01 percent), and the sources used were enriched via neutron capture. Potassium was the first fermionic species cooled to quantum degeneracy [43]; and it remains a large player in quantum degenerate Fermi gas experiments due to its good collisional properties, a broad Feshbach resonance near 200 Gauss, and its simple atomic structure. A number of other fermionic isotopes have been successfully laser cooled and brought to quantum degeneracy including ^{6}Li and heavier, non-alkali species including ^{87}Sr [45], ^{53}Cr [22], ^{167}Er [5], ^{173}Yt [55], and both ^{161}Dy and ^{163}Dy [121]. Initially, it was thought that magneto-optical trapping of atoms such as erbium and dysprosium would be prohibitively complicated due to the large number of long-lived, metastable states that were thought to require repumping for successful formation of a MOT, but the large magnetic dipole moment of these atoms allows for recycling of the dark states due to the weak confinement from the MOT's magnetic quadrupole field [129, 217].

Cooling of all species has progressed to $T/T_F \approx 0.1$, which is the standard benchmark for modern quantum gas experiments. Work cooling to lower entropies is an area of active research and values as low $T/T_F \approx 0.05$ have been claimed [72, 73].

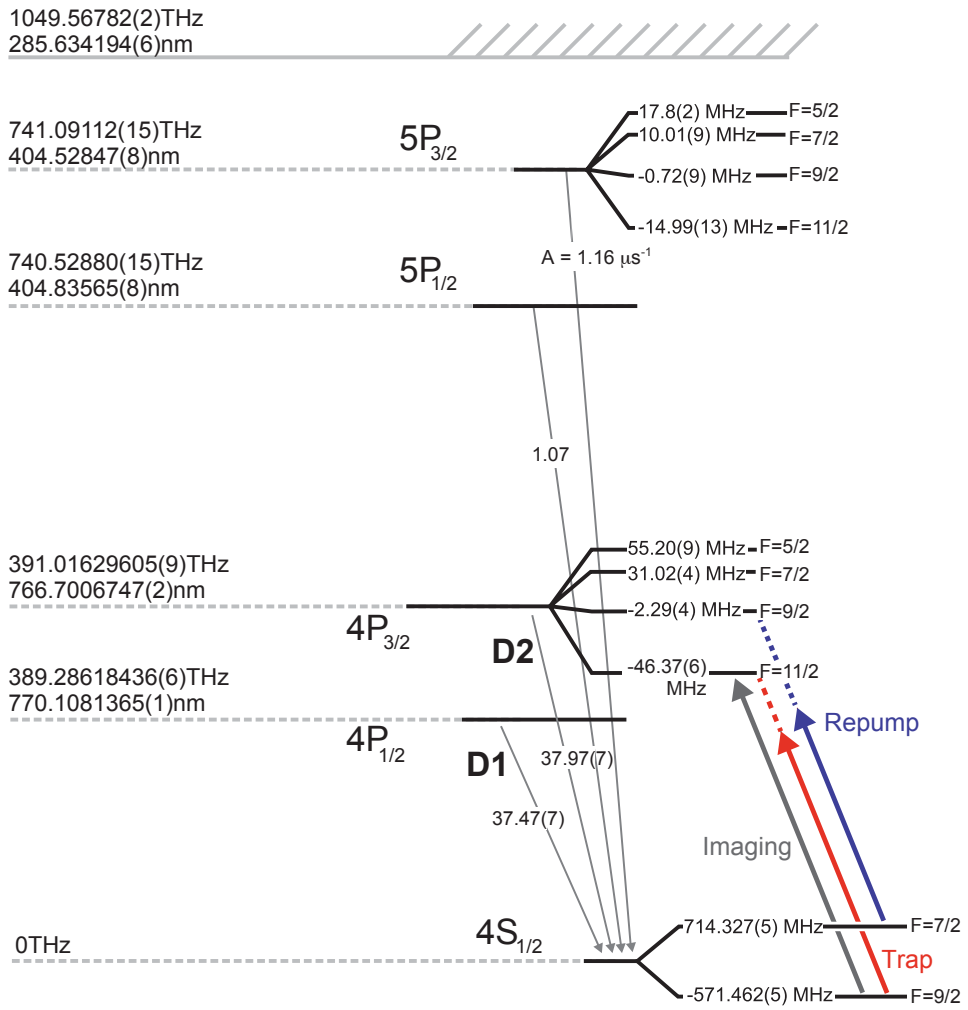

Figure 2.2: Relevant transition in ^{40}K. Primary cooling transitions are from the $4S_{1/2}$ to $4P_{3/2}$ for the MOT trap and repump beams. For all experiments in this thesis, atoms reside in the F=9/2 ground state hyperfine levels with m_F value of 9/2 and 7/2. Imaging is preformed on the cycling transition to the F = 11/2 state in $4P_{3/2}$. Figure adapted from Ref. [135].

The relevant atomic energy levels for potassium are shown in Fig. 2.2. Cooling and imaging are performed on the D2 transition from $4S_{1/2}$ to $4P_{3/2}$ using light produced by two external cavity diode lasers (EagleYard Photonics EYP-RWE-0790-04000-0750-SOT01-0000 and New Focus Vortex II) to address the two hyperfine states in the $4S_{1/2}$ electronic level. Tapered amplifiers (EagleYard Photonics EYP-TPA-0765-01500-3006-CMT03-0000) amplify the diode laser output to produce approximately 200 mW of usable light for both the

trap ($F = 9/2 \rightarrow F'$) and repump ($F = 7/2 \rightarrow F'$) transitions. Each laser is independently offset-locked to an atomic transition by performing spectroscopy on a separate potassium vapor cell. The offset in the lock is provided by an AOM and limits the tuning range of each laser to 60 MHz. Optical pumping and imaging light is produced via frequency shifting the tapered amplifier output with an AOM.

The magnetic moment of the potassium atom is used for trapping and for manipulation of the atomic internal states. ^{40}K has a nuclear spin of 4 with hyperfine levels in the electronic ground state of F=7/2 and 9/2; the hyperfine structure is inverted with the 9/2 manifold having lower energy. The nuclear spin provides a large number of Zeeman levels as shown in Fig. 2.3. At low fields, the Zeeman effect is linear and the energy of each Zeeman level scales as

$$E_{F=9/2,m_F}(B) = \frac{2}{9} m_F \mu_B \left|\vec{B}\right| \tag{2.1}$$

$$E_{F=7/2,m_F}(B) = 1285.8 \text{ MHz} - \frac{2}{9} m_F \mu_B \left|\vec{B}\right|, \tag{2.2}$$

where $\mu_B = 1.4$ MHz/Gauss and the zero in energy is defined for the F=9/2 manifold at zero field. At high fields, the coupling between the orbital and nuclear spins is no longer dominant and the magnetic moment is controlled solely by the spin of the electron. At intermediate magnetic fields, the Breit-Rabi equations can be used to calculate the energy of the magnetic levels as shown in Appendix A.4. The energy shift and magnetic moment of all states in the $F = 9/2$ and $7/2$ manifold are plotted in Fig. 2.3.

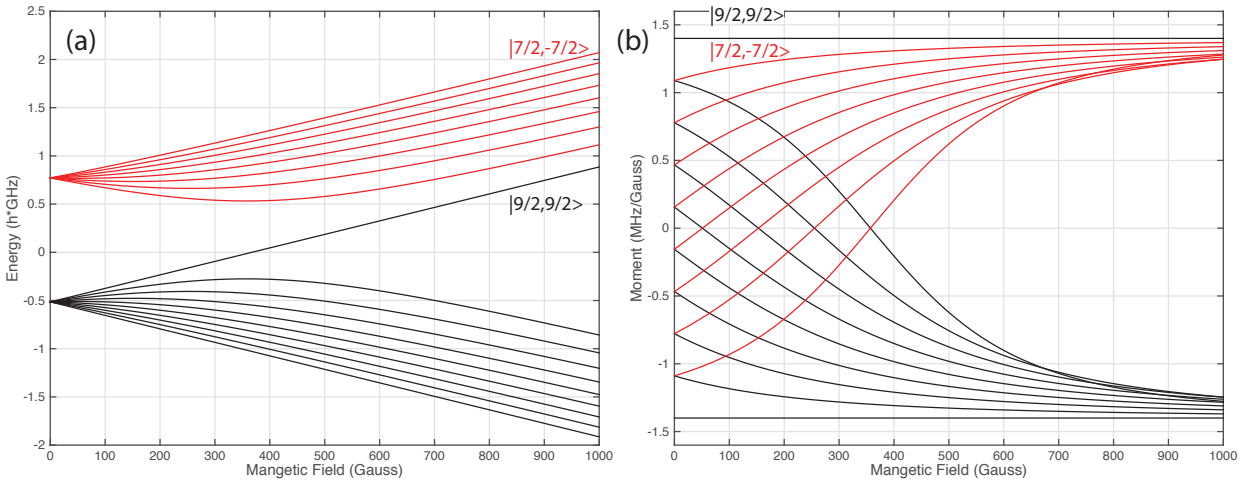

Figure 2.3: Magnetic field dependence of the $4S_{1/2}$ hyperfine states in ^{40}K. (a) Briet-Rabi diagram for the F = 9/2 and 7/2 hyperfine manifolds in the $4S_{1/2}$ state of Potassium-40. (b) Field dependence of the magnetic moment. The stretched states have $\mu \approx 1.4 MHz/G$, and the moment of the $|9/2, 7/2\rangle$ state switches sign at 357 Gauss.

2.3 Magnetic Potentials

Magnetic potentials are used to form the magneto-optical trap, to create conservative, harmonic potentials for evaporative cooling, and to provide a levitating force for experiments on Anderson localization. The potentials exploit the magnetic moment of the potassium atoms to create smoothly varying, well characterized potentials that can be accurately reproduced in the experiment. Detailed properties of these magnetic fields are discussed for each of these applications.

2.3.1 Quadrupole Ioffe-Zirbel Trap

The initial stages of evaporative cooling are performed in a modified QUIC trap [50]. Atoms are transferred from the MOT to the science cell by moving the cart coils on a linear stage as shown in Fig. 2.1. The current in the cart coils is increased to produce a quadrupole gradient of 175 G/cm along the strong direction to maximize transfer through the differential pumping tube. Evaporation in the science cell is not performed in a quadrupole trap due to Majorana spin changing transitions near the field zero that dramatically reduce the efficiency of evaporation in a quadrupole potential. Mixed-species potassium experiments have successfully employed plugged quadrupole potentials in which a repulsive optical potential is overlapped with the field zero to reduce spin-changing transitions. In this method, a bosonic species is used to sympathetically cool the potassium, and this has been accomplished for both rubidium-potassium [17] and sodium-potassium mixtures [171, 190]. Unfortunately, this method has not been successfully employed with potassium alone, and a magnetic trap without a field zero must be constructed.

Atoms are transferred from the cart quadrupole to the QUIC trap by overlapping their field minima and snapping one field off while turning the other on. The geometry of the coils is shown in Fig. 2.5 and described in detail in Ref. [100]. The QUIC trap is calculated to produce a field minimum of 0.4 Gauss / Amp at the loading current of 710 Amps. At this current the bias field is ≈ 285 Gauss and loading multiple spin states from the 9/2 hyperfine manifold is complicated by the non-linear Zeeman effect; the moment of the $|9/2, 7/2\rangle$ state vanishes at 357 Gauss. The temperature of the gas at this stage of the experiment is $\approx 600\ \mu K$. In producing a trap deep enough to efficiently capture the majority of the $|9/2, 9/2\rangle$ atoms, efficient trapping potential of the $|9/2, 7/2\rangle$ atoms is not possible. At the typical load current of 710 A, the trap for the $m_F = 7/2$ atoms is one seventh as deep as for the $m_F = 9/2$ atoms due to the modified magnetic moment and gravity as illustrated in Fig. 2.5. Slices through the 3D trapping potentials for the $m_F = 9/2$, 7/2 and 5/2 states are shown for representative currents in the QUIC trap to visualize this problem and absolute trap depths are shown for these states.

The temperature in the quadrupole trap after transfer to the science cell is measured by comparing the

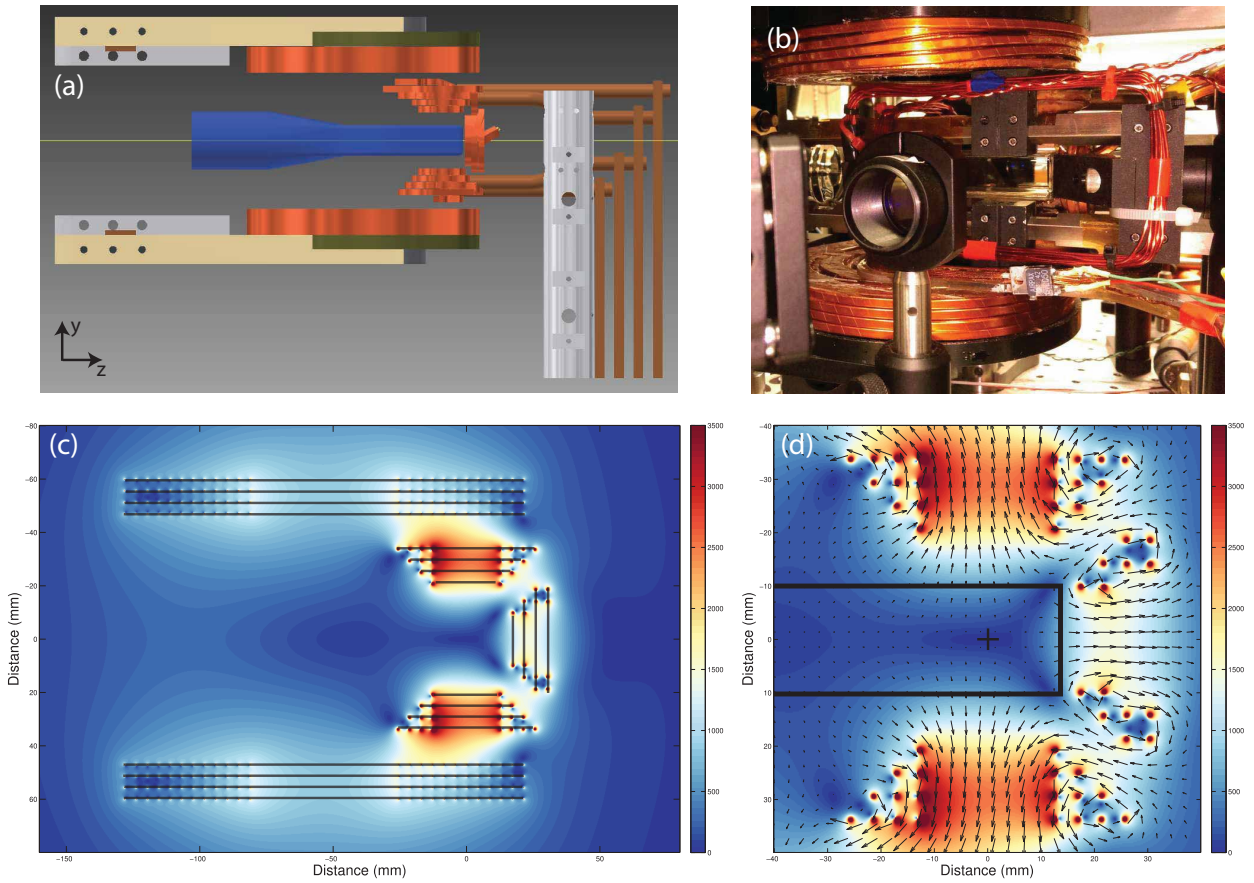

Figure 2.4: Magnetic field produced from the QUIZ trap. (a) Schematic drawing of the QUIZ trap (copper) and partial support structure around the vacuum chamber (blue). The three inner coils produce a QUIC trap and the larger coils generate the field to adjust the bias field. (b) Image of the QUIZ trap, the inner QUIC trap is largely obscured by the support structure. (c) Magnetic field generated by QUIZ trap in same orientation as (a) with 710 A in the QUIC coils and 166 A in the cart coils. Grey lines indicate the orientation of the coils. (d) Expanded view of the magnetic field near the trap minimum with vectors indicating the direction and magnitude of the field. The black square indicates the size of the vacuum chamber, and the cross shows the nominal position of the atoms.

in-trap size to thermodynamic predictions based on the known magnetic potential. The cart coil has a magnetic gradient of $\partial B/\partial\rho = 0.53$ G/cm along the weak direction, and the expected density profile can be calculated as

$$n(\vec{r}) = \exp\left(-\frac{\mu g_F m_F \frac{\partial B}{\partial \rho}\sqrt{\rho^2 + 4y^2}}{k_B T}\right). \tag{2.3}$$

Here ρ is in the x-z plane. The relationship between the gas RMS size in different directions can be calculated by integrating over the Boltzmann distribution of energies in the trap. The temperature inferred in the science cell after loading the quadrupole trap and transfer through the differential pumping tube is $600\mu K$. The in-trap size in this measurement is extrapolated from images taken in time-of-flight. The

absolute depth of the QUIC trap when loaded at 710 A is $1.85mK$ for $m_F = 9/2$, more than three times the temperature of the gas. For the $m_F = 7/2$ atoms, the depth is less than half the temperature and loading is very inefficient. No trap is formed at $710A$ for all other spin states. Loading the QUIC trap at 500 A increases the loading efficiency of the $m_F = 7/2$ atoms, but in practice, the greater total number of atoms is captured by loading at the maximum current of 710 A.

The high bias field of the QUIC trap does not produce adequate trapping frequencies for efficient evaporative cooling. To increase the trapping frequency, a uniform field is superposed with the QUIC potential to bring the field minimum close to zero and substantially increase the trap frequency along the x- and y-directions as shown in Fig. 2.6. The cart quadrupole coils are displaced by 5.3 cm from the center of the QUIC trap. This location overlaps the local maximum of the quadrupole field with the QUIC trap center and creates a a uniform field that is anti-parallel with the field produced by the QUIC trap as shown in Fig 2.4. The combination of the QUIC trap and the uniform field from the cart has been named the quadrupole-Ioffe-Zirbel (QUIZ) trap. The bias field is typically set at 2 Gauss to increase the geometric mean of the trapping frequencies from 40 to 230 Hz. A vertical slice of the field generated by the QUIZ trap is shown in Fig. 2.4. The magnetic field is calculated by assuming that each turn in the coils is an ideal ring of current, and the field from each loop can be expressed using elliptic integrals as described in Ref. [14]. The field from all the loops is summed numerically to generate the field from the assembly using the code in Appendix A. The fields can also be expressed as a series expansion as in Ref. [100], but the full solution allows for a more complete understanding of the shape and depth of the trapping volume.

2.3.2 Microwave Evaporation

Evaporation in the QUIC trap starts with a mixture of several hundred million atoms in the $|9/2, 9/2\rangle$ and $|9/2, 7/2\rangle$ states. Evaporation is performed by driving the highest energy atoms to magnetically untrapped states in the F = 7/2 manifold using microwave transitions. For the magnetically trapped states, the resonant frequency of this transition decreases with magnetic field. We evaporate the atoms by applying a series of microwave sweeps starting at 1080 MHz and ending at roughly 1270 MHz. The rate of the microwave sweep increases in time following an exponential ramp toward the trap zero found at 1280 MHz. As the sweep progresses to higher frequencies, progressively lower energy atoms are driven from the trap while the gas reëquilibrates to lower temperatures. Evaporation stops when a gas of 1-3 million atoms are cooled to $2\mu K$, with $\approx 70\%$ of the atoms in $|9/2, 9/2\rangle$. Efficeint loading of the optical dipole trap for the stretched state can be performed with near unity transfer efficiency. Under ideal evaporation conditions, evaporation would stop when even population of $|9/2, 9/2\rangle$ and $|9/2, 7/2\rangle$ were achieved in the magnetic trap. In this experiment,

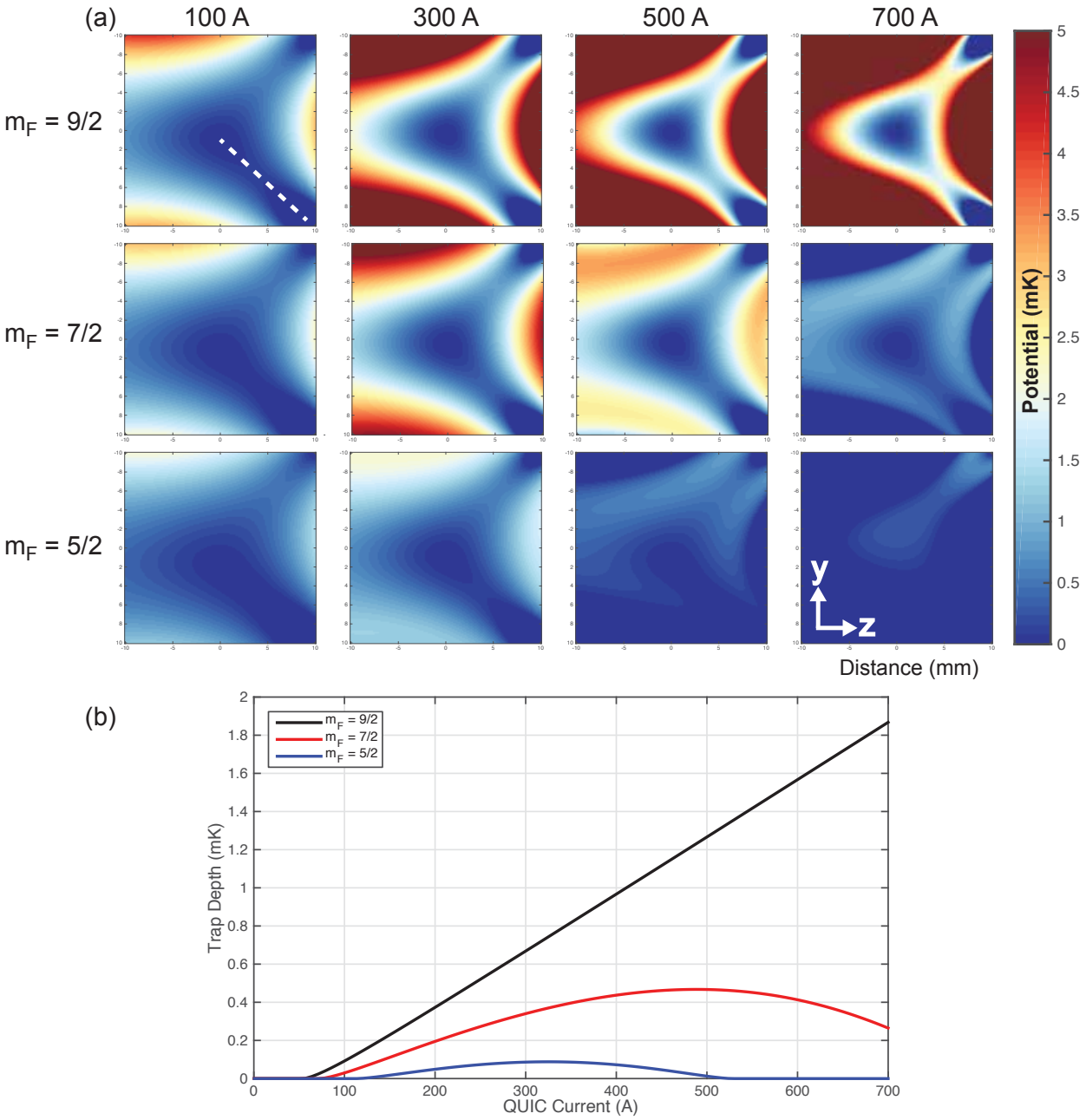

Figure 2.5: Spin-dependent potential of the QUIC trap including gravity. (a) Magnitude of QUIC trap potential for three high-field seeking Zeeman states in the F = 9/2 manifold of potassium plotted for relevant QUIC trap currents. The non-linear Zeeman effect limits the maximum trap depth trap for states other than $m_F = 9/2$. The color scale covers $5mK$ with the value in the central minimum taken as the zero in energy where possible. Slices are shown in the same plane as Fig. 2.4. The dashed line represents the "valley of death," the lowest energy path out of the trap. (b) The depth of the trapping volume is plotted versus current in the QUIC trap. This depth is set by the height of the saddle point along the dashed line. Efficient loading of $m_F = 7/2$ states at $T = 0.6mK$ is not possible as the maximum trap depth for this state is limited to less than $0.5mK$.

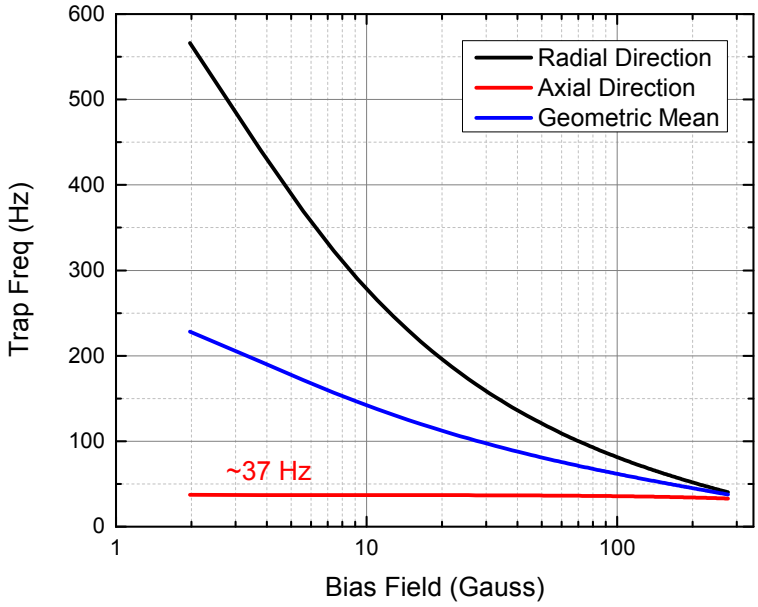

Figure 2.6: Trap frequencies for $|9/2, 9/2\rangle$ in the QUIZ trap as a function of the bias field for 710A in QUIC coils. The bias field is controlled by the current in the cart coils displace by 5.3 cm from the center of the QUIC trap. The QUIC trap is radially symmetric in the x-y plane, and 166A in the CART produces a bias field of 2 Gauss.

the two spin states load into the dipole trap unequally due to sag, and the sequence is set to maximize the transfer of $|9/2, 9/2\rangle$ into the optical trap. The spin mixture in the dipole trap is adjusted as needed with microwave or spin-changing Raman transitions at an early stage of optical trap evaporation.

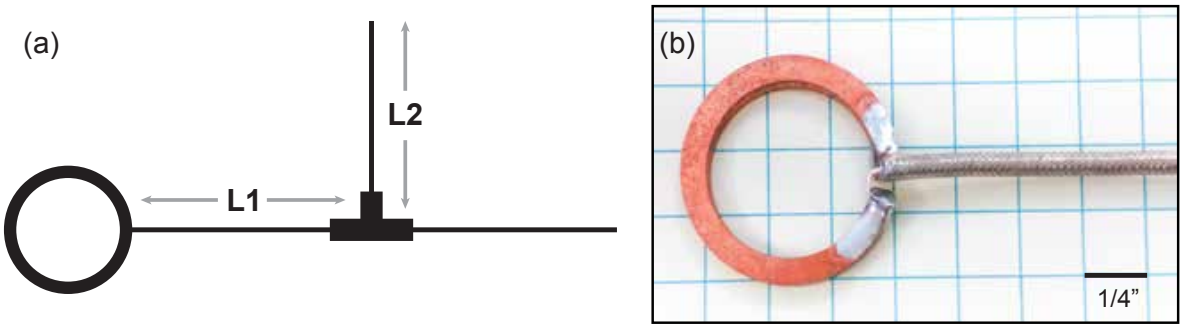

Figure 2.7: Schematic of the 1.3 GHz microwave coil used in magnetic evaporation. (a) The coil is stub tuned to better impedance match the coaxial wire by adjusting L1 and L2 to create a microwave cavity. (b) Microwave evaporation coil created from a copper vacuum gasket. The gasket is slotted and semi-rigid coax is soldered directly to the coil.

The oscillating field required to drive the hyperfine state changing transition is generated by a single-turn coil made from a 20 mm diameter copper vacuum gasket. A notch was cut in the gasket and semi-rigid coax soldered directly to the ring as shown in Figure 2.7. The resonance of the coil was adjusted by stub tuning

the coil with a single stub [170]. Tuning was optimized by measuring the reflected power from the coil with a directional coupler, and the stub length was adjusted to minimize this quantity. Designs based on high frequency laminate circuit boards were also used, but losses in the insulation caused them to perform worse than the bulk copper design. Design of the best stub tuning circuit is complicated by the small real part of the resistance of the coil, and following the ideal trajectory on the Smith chart to make the device appear as fifty ohms requires extremely fine tuning of the distance from the coil to the stub. Since the coil operates over a large frequency range, fine tuning is not required and stub tuning is coarsely optimized in the center of the frequency range.

2.3.3 Anti-Gravity Coil

A magnetic gradient is used to levitate the atoms against the force of gravity in the experiments on Anderson localization presented in Chapter 4. In these experiments, atoms in the $|9/2, 9/2\rangle$ state are released from the dipole trap and allowed to freely expand in a three-dimensional speckle potential for periods up to 1 second. A single coil is used to generate the magnetic field gradient required to levitate the atoms. The coil is roughly circular with a diameter of 4.5 inches, is composed of 50 turns, and is mounted 1.2 inches below the atoms with a field pointing in the y-direction. The center of the anti-gravity coil is not placed directly underneath the atoms as the imaging quantization coil (field in z-direction) is active while anti-gravity coil is used. The sum of the two fields is carefully adjusted to place the most-uniform region of gradient at the position of the atoms. This is accomplished by levitating the atoms while minimizing the gradients in the x- and z-directions. The resultant force on the atoms is $\vec{F} = \mu \nabla B + m\vec{g}$, and the required current necessary to levitate the atoms with moment μ is given in the following expression where R is the radius of the coil, N is the number of turns, Z is the distance above atoms to the center of the coil, and μ_0 is the permeability of free space.

$$NI = \frac{mg}{\mu\mu_0} \frac{2\left(R^2 + Z^2\right)^{5/2}}{3R^2 Z} \tag{2.4}$$

Ideally, the gradient field used for levitation would be perfectly homogeneous with no spatial variation in applied force and no residual trapping. In reality, these effects will be present due to the finite size of the coil used and the imperfections in the alignment to the atomic position. The typical method for generating a uniform magnetic field gradient is with a large, anti-Helmholtz pair of coils. Due to spatial constraints in this work, a single coil is used with geometry close the Helmholtz configuration where the coil radius equals the spacing to the atoms. A generic map of the residual curvature from a single-coil anti-gravity source is shown in Fig. 2.8(a) for a range of coil radii and axial displacements. The combined gravity plus anti-gravity

potential used in the experiment is shown along the vertical direction in Fig. 2.8(b). This combination of fields creates unwanted potential with a height of several hundred $k_B \times nK$ along the vertical direction. Crucially, the residual acceleration is limited to a few parts per thousand of gravity and the trapping period of the potential is approximately $800ms$. The effect of this potential will manifest on timescale similar to a quarter of the trap period or $200ms$. Much of the data taken exploring Anderson localization is at time scales up to this value, though some data is taken out to $1s$. The role of this potential in our measurements is discussed in Chapter 4. For the longest speckle correlation length data explored where the gas samples a greater range of the gradient non-uniformity, there is likely an effect for the anti-gravity coil residual trapping. Use of an anti-Helmholtz pair would have limited the residual acceleration to a few parts per thousand of gravity over $1.5mm$ and reduced the height of the residual potential by a factor of five over $1.5mm$.

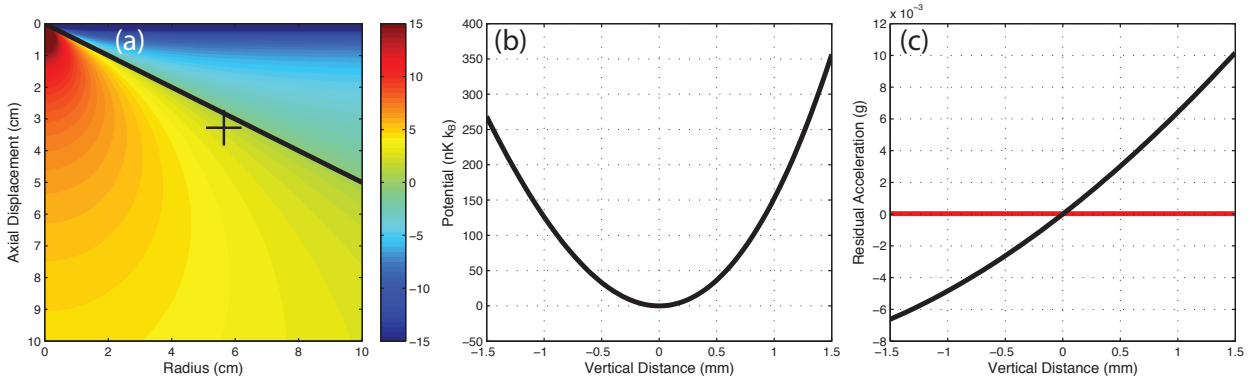

Figure 2.8: Details of anti-gravity field for levitating atoms. (a) Vertical oscillation frequency in Hz produced via a circular coil with gradient necessary to magnetically levitate against gravity. The black line indicates the zero curvature condition when the radius is half the axial displacement, as in a Helmholtz coil. The cross indicates the coil geometry used in the experiment. (b) The combined magnetic plus gravitational potential is plotted for the experimental setup. This arrangement provides a small degree of confinement along the vertical direction. (c) The residual acceleration from this potential (black line) is limited to a few parts per thousand of g over the vertical distance probed. Zero acceleration is marked in red. The role of this residual trapping potential on measurements of Anderson localization is discussed in Chapter 4.

2.4 Optical Potentials

We create a variety of well controlled optical potentials using focused, monochromatic laser beams. The potentials exploit the AC Stark effect to create attractive and repulsive potentials that we use to engineer Hamiltonians for ultracold gas experiments. In this work we use focused laser beams to create harmonic optical dipole traps, an interference pattern between three-pairs of laser beams to create a cubic optical lattice, and optical speckle to create a disordered potential with controllable properties. A wide variety

of potentials can be created using digital projection, optical holography, and time-averaged potentials as discussed in Refs. [157, 9, 62, 171], for example.

The majority of the beams employed are focused onto the position of the atoms with a Gaussian profile in space with an intensity envelope,

$$I(r,z) \;=\; \frac{2P}{\pi w(z)^2}\exp\left(-2\frac{r^2}{w(z)^2}\right) \quad \text{where} \quad w(z) = w_0\sqrt{1+(z/z_R)^2}, \tag{2.5}$$

for a beam propagating along the z-direction with radial coordinate r, power P, waist w, Rayleigh range z_R, and intensity I. The intensity is Gaussian distributed transverse to the propagation direction with a $1/e^2$ radius or waist, w, that grows hyperbolically away from the focus. The focal waist and the Rayleigh range, the distance over which the intensity drops by a factor of two from the focal intensity maximum, are intimately related and are controlled by the numerical aperture of the imaging system and the wavelength of light employed. Simple scalings of these quantities for a thin lens illuminated with a collimated Gaussian beam are given by $z_R = \pi w_0^2/\lambda$ and the $w_0 = f\lambda/\pi w_L$ where w_L is the beam waist at the lens of focal length f. Beam sizes in this thesis are written as their waist, the $1/e^2$ radii of the intensity—this is equivalent to twice the RMS radius, typically labeled as σ.

The strength of the optical potential depends on the intensity of the light, the detuning from atomic resonances, the internal state of the atom, and the polarization of the light. Ref. [69] gives a detailed treatment of this problem for the alkali atoms, with expressions for the dipole potential U_{dip} and scattering rate Γ_{sc} accounting for both the co-rotating and counter-rotating terms:

$$U_{dip}(\vec{r}) = -\frac{3\pi c^2}{2\omega_0^2}\left(\frac{\Gamma}{\omega_0-\omega}+\frac{\Gamma}{\omega_0+\omega}\right)I(\vec{r}) \tag{2.6}$$

$$\Gamma_{sc}(\vec{r}) = \frac{3\pi c^2}{2\hbar\omega_0^3}\left(\frac{\omega}{\omega_0}\right)^3\left(\frac{\Gamma}{\omega_0-\omega}+\frac{\Gamma}{\omega_0+\omega}\right)^2 I(\vec{r}). \tag{2.7}$$

Here Γ is the linewidth of the transition, ω_0 is the angular frequency of the transition, and ω in the angular frequency of the applied light. Contributions from the counter-rotating term become increasingly relevant at large detunings and should not be ignored. For example when considering the D1 or D2 transitions in potassium, the counter-rotating term is 15 to 20 percent of the co-rotating term for light at 532 and 1064 nm, respectively. The ratio of the scattering rate to the potential depth depends only on the detuning of

the light and is found by dividing the above two expressions as

$$\frac{\Gamma_{sc}}{U_{dip}} = \frac{1}{\hbar}\left(\frac{\omega}{\omega_0}\right)^3\left(\frac{\Gamma}{\omega_0-\omega}+\frac{\Gamma}{\omega_0+\omega}\right). \tag{2.8}$$

Equations 2.6 and 2.7 are valid for detunings much greater than the fine structure splitting. When the detuning becomes comparable to the fine structure splitting, the polarization of the light and the internal state of the atom becomes increasingly important. The spin-dependence of the dipole force (though not used in this work) is used to make state-dependent potentials [80, 115, 119, 133, 189, 220]. The equation describing the potential and the incoherent scattering rate for detunings comparable to the fine structure splitting:

$$U_{dip}(\vec{r}) = \frac{\pi c^2\Gamma}{2\omega_0^3}\left(\frac{2 + \mathcal{P}g_F m_F}{\Delta_{2,F}}+\frac{1 - \mathcal{P}g_F m_F}{\Delta_{1,F}}\right)I(\vec{r}) \tag{2.9}$$

$$\Gamma_{sc} = \frac{\pi c^2\Gamma^2}{2\hbar\omega_0^3}\left(\frac{2}{\Delta_{2,F}^2}+\frac{1}{\Delta_{1,F}^2}\right)I(\vec{r}). \tag{2.10}$$

Here $\mathcal{P}$ is the polarization of the light where $\mathcal{P}$ is 0, ±1 for linearly and circularly $\sigma^{\pm}$ polarized light. The detunings from the D1 and D2 line are $\Delta_{1,F}$ and $\Delta_{2,F}$ and $g_F m_F$ is the product of the Landé g-factor and the spin of the Zeeman state. Table 2.1 lists the scattering rates per unit dipole potential energy from the major optical potentials used in the experiment to provide a sense of scale for heating from the various applied fields.

Use	λ	Γ_{sc}/U_{dip} $(s^{-1})J^{-1}$
Dipole Trap	1064 nm	3.2e-6 $s^{-1}/(k_B \times nK)$
Optical Lattice	782.2 nm	0.044 s^{-1}/E_R
Disorder	532 nm	1.2e-5 $s^{-1}/(k_B \times nK)$

Table 2.1: Scattering rates in the experiments accounting for the D1, D2, and the 4S to 5P transitions. Rates are expressed in Hz per unit of potential depth per atom.

2.4.1 Optical Dipole Trap

The final stages of evaporative cooling are performed in an optical dipole trap. This trap is created by overlapping two foci of a linearly polarized, 1064 nm laser beam as shown in Fig. 2.9. The beam is created from a single spatial mode, multi-frequency Nd:YAG fiber laser (IPG Photonics 20W). The beam is recycled to make both foci with a continuous beam path, and care is taken to minimize interference between the two foci. The coherence length of the laser is only a few centimeters and the beam path between foci is

roughly a meter, but minimizing polarization overlap between the beams is crucial for minimizing heating. Due to spatial constraints, the crossing angle is sixty degrees in the horizontal plane. The principle axes of the trap fall along the x-, y-, and z-directions in the experiment with the trap taking a prolate spheroidal shape elongated in the x-direction. The beam waists are chosen to have an $1/e^2$ radius of 90 microns. A typical evaporation benchmark after spin mixing is $N \approx 400,000$ and $T \approx 1\mu K$ at $\bar{\omega} = 2\pi 97Hz$. The lowest entropy gases are produced near a trap frequency $\bar{\omega} = 2\pi 81Hz$, with $N \approx 45,000$ and $T/T_F \approx 0.17$.

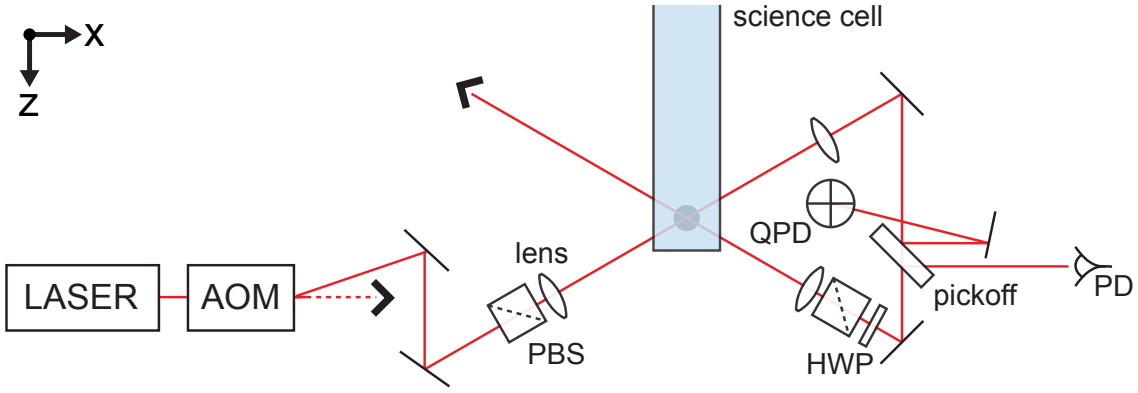

Figure 2.9: Schematic of dipole trap optics for intensity control and position stabilization. A wedged pickoff is used to sample the beam after the first pass through the science chamber. One beam is sent to a quadrant photodiode for position servoing, and the other beam is sent to a photodiode for intensity servoing. Polarization optics ensure that the two foci have minimal interference.

The IPG fiber laser can produce a maximum of 20 Watts of optical power, but when run at maximum power these lasers have short service lives. These lasers slowly degrade in peak power until no output is produced; three have failed in the experiment in six years of operation. Current best practice is to operate the laser at roughly half of its maximum power to extend the lifetime of the system.

2.4.2 Beam Pointing Stability and AOM Thermalization

Intensity control of the dipole trap laser is achieved by actively servoing the modulation power of an acousto-optic modulator. The first order diffracted beam is used to create a crossed dipole trap while the un-diffracted beam is not used. Several watts of RF power are used to generate the radiofrequency standing wave in the tellurium dioxide AOM crystal, and heating from this RF drive creates a thermal gradient inside the crystal. This thermal gradient results in a spatially varying refractive index in the AOM that causes both the diffracted and un-diffracted beams to deflect as shown in Fig. 2.10. As the thermal gradient varies in time as the dipole beam is turned on and off, no stable equilibrium is met in the crystal and the beam deflects in a hysteretic fashion. The magnitude of the deflection depends on the size of the thermal gradient and the

properties of the modulating material. For passively cooled TeO_2 and glass based modulators, deflections at the 100 microradian level are typical [162]. Germanium modulators have observed deflections at the multi-milliradian level [96] and are typically cooled to limit this effect. The timescale for the thermal pointing drift is set by the timescale for creating the thermal gradient in the crystal and is typically on the order of 1 s. An example of the deflection seen in our apparatus is shown in Fig. 2.10. The origin of this effect was explored in Ref. [96], where the authors showed that reversing the direction of thermal gradient in the modulating crystal reverses the direction of the deflection.

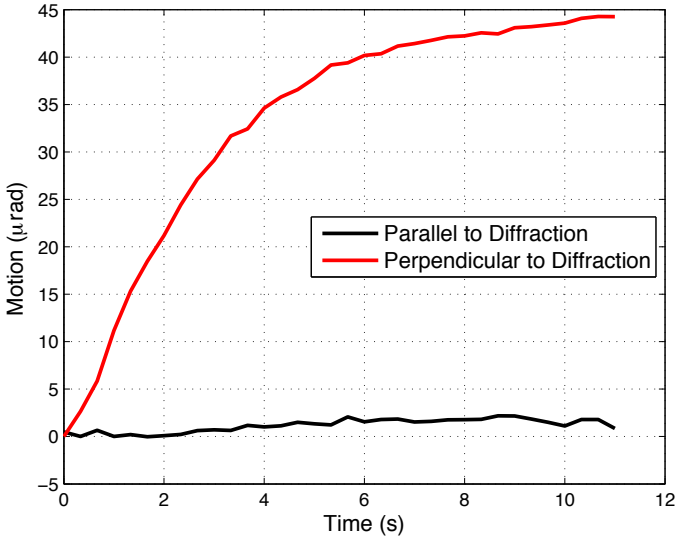

Figure 2.10: Deflection of the dipole trap beam due to thermally induced refraction in the intensity servo AOM. Deflection of the beam positions is shown in time both along and perpendicular to the direction of diffraction with $1W$ of RF power at the AOM. The time constant for equilibration of the temperature gradient is roughly $2.5s$, and deflection of the beam is primarily along the direction of diffraction. The pointing of the beam is measured by shining the beam on a CCD camera position $1m$ from the diffracting AOM.

Several methods exist for countering thermal beam steering in AOMs. Ref. [96] retroreflected the diffracted beam through the AOM to reverse the thermal steering and succeeded in reducing deflection by a factor of ten with a loss of a quarter of the optical power. Fiber coupling the diffracted beam provides the most straightforward solution, but requires sacrificing at least 20% of the power due to fiber coupling inefficiency. Non-linear effects in the fiber can cause problems for high beam powers, and large core-diameter fibers such as photonic bandgap fibers can be used to reduce these problems. Active stabilization of the thermal gradient in the crystal can also be attempted by applying an external heat load to the crystal with an ohmic heater or by driving the crystal with an additional RF source whose diffracted orders can be separated from the primary diffracted beam.

We chose to actively stabilize the beam pointing by varying the RF drive frequency of the AOM. Deflection perpendicular to the direction of diffraction is minimal, and fine control in the direction of diffraction can be achieved by adjusting the RF drive frequency. The position of the dipole beam is monitored by a quadrant photodiode (Pacific Silicon QP50-6SD2), and a simple analog circuit controls the voltage to a VCO generating the RF drive such that the error signal from the quadrant photodiode is fixed. The optical setup is sketched in Fig. 2.9. The response of the feedback circuit is limited to keep the bandwidth below the trap frequency over the power range used to avoid parametric excitation of the dipole trap modes and associated heating. The error signal for the position servo circuit is $\approx 18mV/\mu m/W$. Typical minimum optical power at the end of evaporation is $300mW$, affording a $6mV/\mu m$ error signal. This is well above the level of offsets introduced in the analog servo or via ground loops and position stability greater than $1\mu m$ is easily achieved. A comparison of the pointing stability with and without the pointing servo is shown in Fig. 2.11; the dipole beam focal waist is $90\mu m$. Implementing this servo has greatly improved the short time-scale number and temperature stability of the experiment.

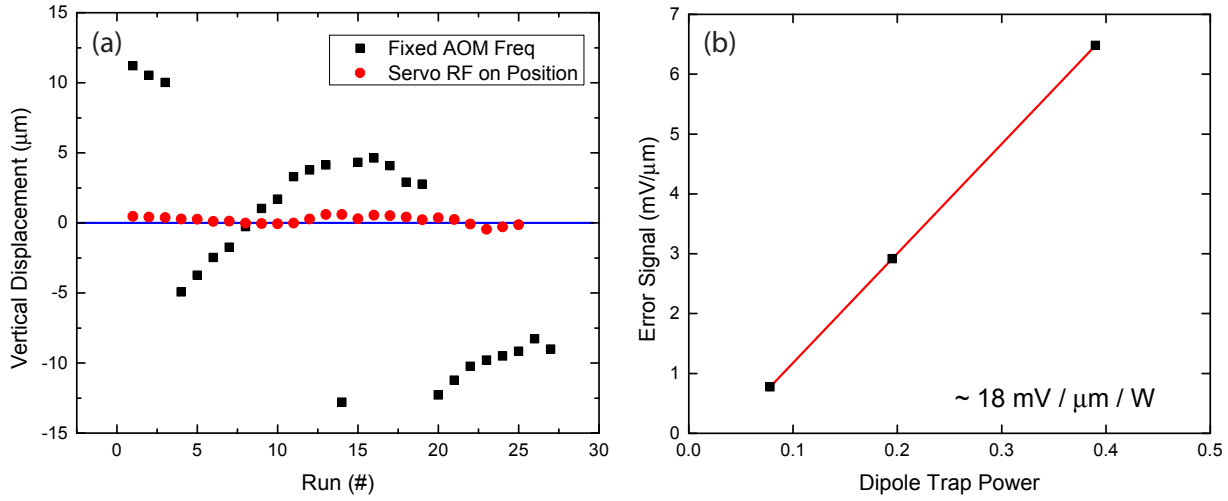

Figure 2.11: Pointing stability of the dipole trap with fixed and actively controlled RF drive frequencies. (a) The focal position of the first pass of the dipole trap is measured at the positions of the atoms at the end of a 90 second experimental sequence. With a fixed RF drive frequency, thermal effects cause the position of the focus to drift over time (black squares). Large jumps can be observed in the position when the experiment is not run continuously. The position of the dipole focus can be actively stabilized by controlling the AOM drive frequency (red circle) to achieve micron level stability of the focus. (b) The figure of merit for the feedback is the size of the error signal for a given displacement. For this implementation, the error signal is $18mV$ per μm motion per Watt of optical power. At the lowest powers used in the experiment, the error signal is $6mV/\mu m$ of motion.

2.4.3 Optical Lattice

We generate a three-dimensional, cubic optical lattice with three pairs of linearly polarized, counter-propagating laser beams at 782.2 nm as described in Ref. [100]. The lattice beams are arranged to be approximately orthogonal, and interference between the beams is reduced by minimizing their polarization overlap. Frequency shifts of (+80, +83, and -80 MHz [100]) are introduced between the beams to time-average any residual interference. The lattice light is generated from a Tekhnoscan TIS-SF-07 Ti:Sapphire laser pumped with 12W of 532 nm light generated by a Coherent Verdi V18 with a maximum power at 782 nm of 1.2 Watts. Each lattice beam is fiber coupled through a single-mode, polarization maintaining fiber to shorten the beam path and increase the pointing stability.

Calibration of the lattice potential is performed by modulating the lattice depth to drive atoms between bands. This spectroscopic techniques measures the location of several band gaps in 1D, and these transitions are related to the lattice depth as described in Sections 5.2 and 5.2.1. Each beam is intensity stabilized and focused to a 130 micron $1/e^2$ radius at the atoms. Alignment and calibration of the lattice potential is stable over a month at the five percent level. Further details of the physics and properties of the gas in the lattice are described in Chapter 5.

2.5 Raman Transitions

Raman transitions are state changing, two photon processes in which quantum amplitude is coherently transferred through an intermediate level. These transitions are distinct from single photon processes as the transition energy and recoil momentum can be controlled independently, and transitions between states with the same parity become possible. Additionally, the two laser fields can drive transitions at either their sum or difference frequencies, providing access to momentum selective, radiofrequency transitions as well as high energy optical transitions such as those used to create Rydberg states. The independent control over energy and recoil momentum has made Raman transitions a powerful tool for manipulating quantum gases where, for example, they have been used to probe excitations in strongly interacting Bose [49] and Fermi gases [59], generate synthetic gauge fields [120], and as the first demonstrated method of cooling quasimomentum in an optical lattice [26].

In this work we drive stimulated, Λ-type transitions as sketched in Fig. 2.12 to change both the internal state and momentum state of a gas of atoms. Population is driven from $|a\rangle$ to $|b\rangle$ by absorption from beam 1 and emission in beam 2; here we consider the Stokes process where $\omega_1 > \omega_2$. This provides an energy change of $\hbar\,\delta\omega$ and momentum change of $\boldsymbol{\delta k}$ satisfying the following relationship:

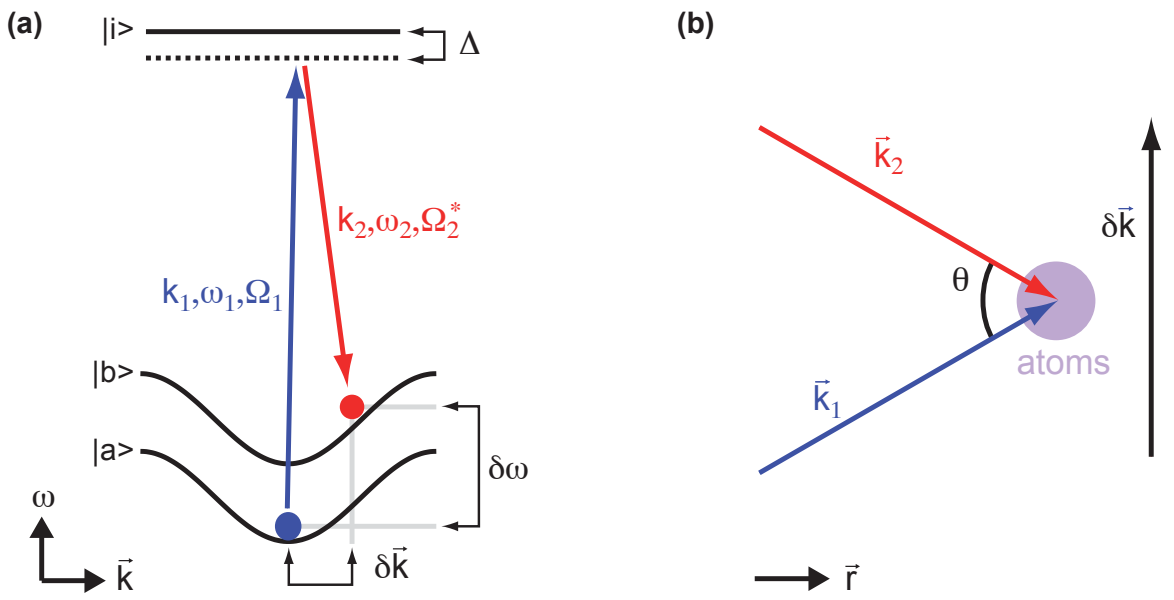

Figure 2.12: Illustration of momentum and energy transfer in a two-photon process. (a) Driving fields are applied at frequencies ω_1 and ω_2 to drive a transition from state $|a\rangle$ to $|b\rangle$ through the intermediate level, $|i\rangle$. Each of the laser fields is detuned from the intermediate level by Δ. (b) A net momentum is imparted after the transition given by the difference of the Raman beam wavevectors, $\delta\vec{k} = \vec{k}_1 - \vec{k}_2$. The full angle between the two beam is labeled as θ.

$$\delta\omega = \omega_1 - \omega_2 \tag{2.11}$$

$$\boldsymbol{\delta k} = \boldsymbol{k}_1 - \boldsymbol{k}_2. \tag{2.12}$$

Here 1 and 2 index the Raman fields, and $|a\rangle$ and $|b\rangle$ indicate momentum states in two different bands. Each beam is detuned from the intermediate atomic level, $|i\rangle$ by a detuning Δ, and the electric field is

$$\boldsymbol{\mathcal{E}}(t) \;=\; E_1 \cos\left(\boldsymbol{k_1}\cdot\boldsymbol{r} - \omega_1 t\right)\hat{\boldsymbol{e}}_{\boldsymbol{1}} \;+\; E_2 \cos\left(\boldsymbol{k_1}\cdot\boldsymbol{r} - \omega_2 t\right)\hat{\boldsymbol{e}}_{\boldsymbol{2}}. \tag{2.13}$$

The momentum difference imparted in Λ-type transitions in which $|\vec{k}_1| \approx |\vec{k}_2| = k_R$ is controlled by the angle between the two Raman beams such that $|\delta\vec{k}| = 2k_R \sin(\theta/2)$ where the θ is the angle between the beams. Raman transitions with co-propagating beams impart zero momentum while counter-propagating beams impart the maximum change of $2k_R$. The Hamiltonian is set by the electric dipole interaction with

the laser fields:

$$\mathcal{H} = -\frac{E_1}{2}\left(e^{i\omega_1 t} + e^{-i\omega_1 t}\right)\hat{\boldsymbol{e}}_{\mathbf{1}} \cdot \boldsymbol{d} - \frac{E_2}{2}\left(e^{i\omega_2 t} + e^{-i\omega_2 t}\right)\hat{\boldsymbol{e}}_{\mathbf{2}} \cdot \boldsymbol{d}. \tag{2.14}$$

Here we have made the dipole approximation and ignore spatial dependence of the electric field. Starting with all amplitude in $|a\rangle$, the Schroedinger equation is used to determine the evolution of the quantum populations. Only the terms $\left\langle i \left| \boldsymbol{e}_{\mathbf{1}} \cdot \hat{\boldsymbol{d}} \right| a \right\rangle$ and $\left\langle b \left| \boldsymbol{e}_{\mathbf{2}} \cdot \hat{\boldsymbol{d}} \right| i \right\rangle$ having non-zero weight are considered. Here $\boldsymbol{d} = e\boldsymbol{r}$, the single photon matrix elements are $\Omega_1 = E_1 e \langle i | \hat{\boldsymbol{e}}_{\mathbf{1}} \cdot \boldsymbol{r} | a \rangle e^{i\phi_1}/2$ and $\Omega_2 = E_2 e \langle i | \hat{\boldsymbol{e}}_{\mathbf{2}} \cdot \boldsymbol{r} | b \rangle e^{i\phi_2}/2$, e is the electric charge of the electron, and $\hat{\boldsymbol{e}}_{\mathbf{1}}$ and $\hat{\boldsymbol{e}}_{\mathbf{2}}$ are unit vectors for the electric field of Raman beams 1 and 2. These are used to write a set of coupled differential equations for the amplitudes c_a and c_b of states $|a\rangle$ and $|b\rangle$ as in Ref. [215]:

$$i\hbar \frac{d}{dt} c_a = \frac{|\Omega_1|^2}{\Delta} c_a + \Omega_R c_b \tag{2.15}$$

$$i\hbar \frac{d}{dt} c_b = \Omega_R^* c_a + \frac{|\Omega_2|^2}{\Delta} c_b. \tag{2.16}$$

The detuning between the initial and the intermediate state is defined as $\Delta = \omega_1 - \omega_{ai}$, and c_a and c_b are the probability amplitudes in $|a\rangle$ and $|b\rangle$. This is initially a three level problem involving amplitude in $|a\rangle$, $|b\rangle$, and $|i\rangle$, and the rotating wave approximation is made in a frame rotating with Δ with rapidly oscillating terms ignored. In the limit of large Δ, the amplitude in the excited state can be adiabatically eliminated. This reduces the three level problem to an equivalent two-level system [195, 36, 75]. This approximation breaks down when the single photon Rabi rates or ω_{ab} is of the same order as Δ, and the system ceases behaving as an equivalent two-level system [159]. The diagonal elements in this problem (the AC Stark shift of each state) can be eliminated by redefining the shifts into the energies of states a and b. The coupling element between $|a\rangle$ and $|b\rangle$ found through adiabatic elimination of the excited state $|i\rangle$ provides the Rabi rate, Ω_R.

$$\Omega_R = -\frac{\Omega_2^* \Omega_1}{\Delta} \tag{2.17}$$

The dipole matrix elements connecting the atomic levels $|J\rangle$ and $|J'\rangle$ (J is the total angular momentum of the electron) can be calculated in connection with the measured atomic linewidth [193].

$$|\langle J \,||er||\, J' \rangle|^2 = \frac{2J'+1}{2J+1} \frac{3\pi\epsilon_0 \hbar c^3 \Gamma}{\omega_0^3} \tag{2.18}$$

Here Γ is the linewidth of the transition, $\omega_0 = \omega_J - \omega_{J'}$, ϵ_0 is the permittivity of free space, and the double bars indicate that spin is ignored.

2.5.1 Two-Frequency Raman Transitions

Raman transitions are used in this thesis to rapidly generate relative motion between two spin components in a lattice gas as described in Sec. 6.3. A sketch of the Raman optics used to accomplish this is shown in Fig. 2.13 in which a single frequency laser beam is divided into two beams with independent frequency offsets provided by acousto-optic modulators. Phase modulation can also be applied equally to both beams with an electro-optic modulator—the consequences of this are described in the following section. The Raman light is generated from a single 770nm laser (New Focus VII TLB-6900) detuned $\approx$ 40 GHz from the D1 transition at 389,326.2 GHz. Modulation is provided by an EOM (Newport 4421-01 @ 650 MHz) operated at 632.25 MHz and AOMs (Gooch and Housego R23080-1-LTD) operating at a nominal frequency of 80 MHz. The combination of AOMs and EOMs allows for fast switching between transitions with $\delta\omega$ from DC to 10 MHz and in a 10 MHz window around twice the EO modulation frequency with no physical changes to the optics. The EOM is resonant and runs at a fixed frequency while the AOMs are driven by direct-digital synthesizers that allow for fine frequency control and easy generation of phase coherent frequency sweeps. The power in each beam is intensity stabilized by actively servoing the RF power in the AOM diffracted orders.

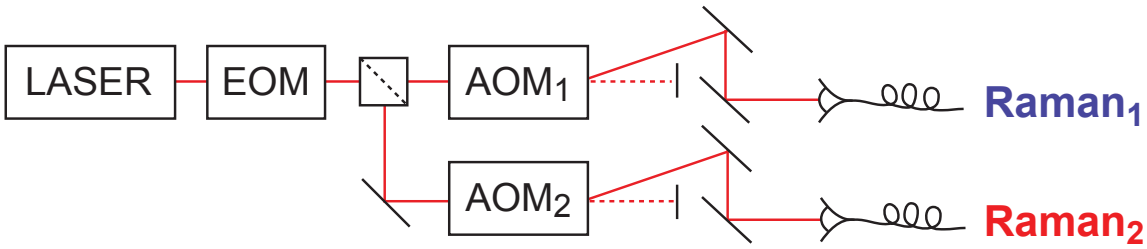

Figure 2.13: Raman optics for generating Zeeman state and hyperfine state changing transitions in potassium. The two Raman beams are generated from a single laser detuned 40 GHz from the ^{40}K D1 line. The frequency difference between two laser beams is generated by a pair of AOMs and an EOM. If only the AOMs are driven, $\delta\omega$ covers a range from zero to several MHz. The EOM provides a fixed offset to drive transitions at the GHz level with no changes to the optics. The frequency composition of the phase modulated beams is illustrated in Fig. 2.16.

The two Raman beams are focused onto the atoms with an angle separating the beams of 30 degrees; this provides a $\delta k = 2|k|sin(30°/2)$, which corresponds to $q_B/2$ in the 782.2 nm lattice or an energy scale of 100 nK in the trap. The beams are focused onto the position of the atoms over 760 mm, and the orientation provides a δk in the y-direction. The sign of the impulse is set by the relative detuning of the two beams. The beam are each focused to a $1/e^2$ radii of 170 microns at the atoms which provides adequate

intensity uniformity over the in-trap distribution with nominal radii of 10 to 15 microns. The intensity of the beams are actively controlled by sampling a fraction of the Raman light in each beam after the fiber with a photodiode and actively servoing this value against a computer controlled setpoint. Intensity control for pulses shorter than the inverse of the intensity servo bandwidth is achieved by adjusting the beam powers within the servo bandwidth while one of the AOMs is detuned sufficiently far from resonance (so that the Raman process is far off resonant). The detuned AOM is then jumped to resonance for the pulse duration. This enables the production of 20 μs long pulses with highly reproducible transition probabilities as shown in Fig. 2.14.

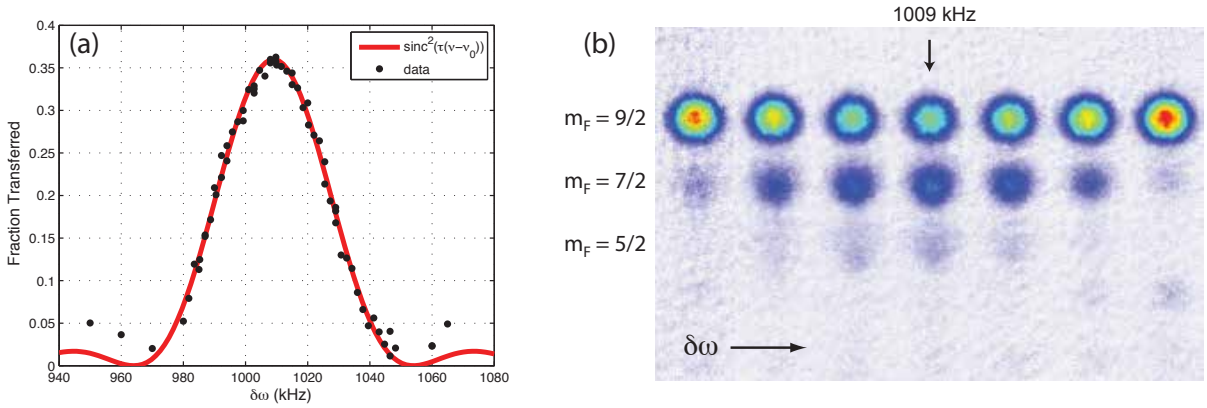

Figure 2.14: Measurement of Raman lineshape using a spectrally broad pulse. (a) Raman lineshape for a 20 μs pulse driving atoms from an initially spin polarized, $m_F = 9/2$ gas to $m_F = 7/2$ in the F = 9/2 manifold. Fit to data is a sinc squared function with $\tau = 22$ μs and $\nu_0 = 1009$ kHz. (b) Spin separated images showing transition occupation as the Raman detuning is varied. Transitions between Zeeman levels at low magnetic fields are degenerate and population in $m_F = 5/2$ is non-negligible.

Sample images using 20 μs Raman pulses to create a spin-mixture from a polarized $|9/2, 9/2\rangle$ gas are shown in Fig. 2.14—the bandwidth of the transition is much larger than the thermal width of 20 kHz, and the transition is not momentum selective. Copies of the original gas are created in lower Zeeman states with a displacement in momentum equal to δk. Changing the frequency difference of the Raman pulse allows us to map the lineshape of the transition by measuring the fraction of atoms transferred versus $\delta\omega$. The square pulse windowing in time produces a sinc squared lineshape which matches well with the experimental data. Longer adiabatic-rapid passage sweeps can be used to generate momentum selective transitions, as shown in Fig 2.15. The sweeps in this figure cover 5 kHz and remove a section of atoms near zero velocity along the y-direction. This requires absolute magnetic field stability at the 4 milliGauss level to repeatedly transfer from a given momentum range in the gas. Additionally, the degeneracy between transition energies between neighboring Zeeman levels at low magnetic fields allows for multiple transitions and population of

spin states other than $m_F = 7/2$. At the fields explored here, the non-linear Zeeman effect is weak enough that Raman transitions between adjacent Zeeman levels are all degenerate. This can easily be avoided by working at higher magnetic fields to reduce the ten level problem to just two. For the work presented in Sec. 6.3, the transferred fraction to $|9/2, 7/2\rangle$ is fixed at $\approx 35\%$ and minimal population is transferred to lower spin states.

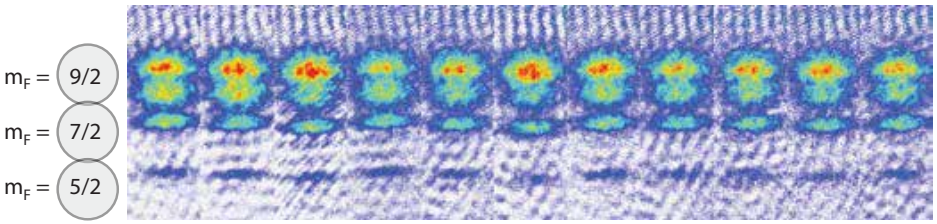

Figure 2.15: Stability of momentum selective Raman transitions in the experiment. Spin separated images (similar to Fig. 2.14) show a momentum selective transition moving atoms near zero vertical velocity from the $m_F = 9/2$ gas to $m_F = 7/2$ and $m_F = 5/2$. Performance of this process is strongly dependent on magnetic field stability—the 5 kHz wide sweep corresponds to 4 mGauss of field. Raman transition was performed by a 0.5 ms sweep at 10 kHz/ms and $\delta\omega = 993$ kHz at a magnetic field of 3.2 Gauss. The nominal position of each spin component is indicated by the gray circles.

2.5.2 Raman Transitions with Phase Modulated Beams

The single-laser, dual-AOM setup used to drive Raman transitions shown in Fig. 2.13 is easily modified to drive GHz level transitions between hyperfine levels in potassium with the addition of a phase modulating EOM. The EOM creates a comb of frequency harmonics in both Raman beams with peaks separated by the EOM modulation frequency. Pairs of comb peaks from the two beams can coherently drive Raman transitions spanning larger frequency differences than are possible with a dual-AOM setup. Additionally, the same optics used to drive kHz- to MHz-level transitions can also drive GHz level transitions (if the EOM is driven) with no physical changes to the optical hardware.

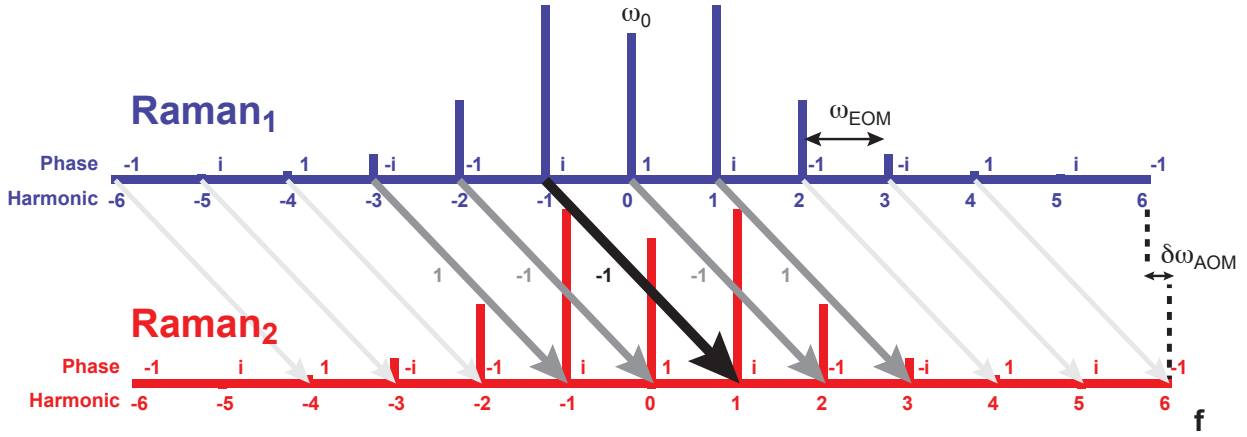

Figure 2.16: Frequency spectrum and multi-path interference in Raman transitions driven by phase modulated beams. Frequency spectra are drawn for two phase modulated Raman beams ($m = \pi/2$), including offsets provided by AOMs. The comb of frequency harmonics is shown with the phase of each harmonic labeled relative to the carrier; the height of each harmonic peak is proportion to the electric field amplitude. Modulation parameters are chosen to drive lambda-type Raman transitions where light is absorbed from harmonic n of Raman$_1$ and emitted into harmonic $n+2$ of Raman$_2$. The amplitude of these transitions is indicated by gray-scale arrows, where the relative phase of the two-photon process is marked in the center of each arrow. All paths with $\delta n = 2$ are adjusted to satisfy the resonance condition, and interference between these transitions leads to an effective two-photon Rabi rate that depends on the modulation amplitude.

Phase modulation of the light modifies the time variation of the electric field such that $\mathcal{E}(t) = E\hat{e}\,\cos(\omega t)$ becomes $E\hat{e}\,\cos(\omega t + m\cos(\omega_m t))$, where ω_m is the modulation frequency and m is the modulation angle. Modulation modifies the frequency spectrum of the beam by introducing sidebands offset from the carrier by integer multiples of the modulation frequency. A sample spectrum for the two Raman beams after phase modulation is shown in Fig. 2.16 including offsets introduced from the AOMs. The origin of the frequency harmonics can be seen from the identity $e^{im\cos(\phi)} = \sum_{n=-\infty}^{\infty} i^n J_n(m) e^{in\phi}$ where modulation is expanded in terms of Bessel functions of the first kind. The electric field from the two phase modulated beams can be written as follows.[1]

[1]Note that $J_n(m) = (-1)^n J_n(-m)$ and $e^{-im\cos(\phi)} = \sum_{n=-\infty}^{\infty} i^{-n} J_n(m) e^{-in\phi}$.

$$\boldsymbol{\mathcal{E}_1}(t) = E_1\hat{\boldsymbol{e}}_\mathbf{1}\ \cos\left(\omega_1 t + m\ \cos\left(\omega_m t\right)\right) \tag{2.19}$$

$$= \frac{E_1\hat{\boldsymbol{e}}_\mathbf{1}}{2}\left(e^{i(\omega_1 t + m\ \cos(\omega_m t))}\ +\ e^{-i(\omega_1 t + m\ \cos(\omega_m t))}\right) \tag{2.20}$$

$$= \frac{E_1\hat{\boldsymbol{e}}_\mathbf{1}}{2}\sum_{n_1=-\infty}^{\infty} J_{n_1}(m)\left(i^{n_1}e^{i(\omega_1+n_1\omega_m)t}\ +\ i^{-n_1}e^{-i(\omega_1+n_1\omega_m)t}\right) \tag{2.21}$$

$$\boldsymbol{\mathcal{E}_2}(t) = E_2\hat{\boldsymbol{e}}_\mathbf{2}\cos\left(\omega_2 t + m\ \cos\left(\omega_m t\right)\right) \tag{2.22}$$

$$= \frac{E_2\hat{\boldsymbol{e}}_\mathbf{2}}{2}\sum_{n_2=-\infty}^{\infty} J_{n_2}(m)\left(i^{n_2}e^{i(\omega_2+n_2\omega_m)t}\ +\ i^{-n_2}e^{-i(\omega_2+n_2\omega_m)t}\right) \tag{2.23}$$

The two frequency combs produced by phase modulation are offset by the difference in the AOM modulation frequency, $\delta\omega_{\mathrm{AOM}} = \omega_{\mathrm{AOM}_2} - \omega_{\mathrm{AOM}_1}$. We drive transitions with pairs of these combs teeth, such light is absorbed from the n-th harmonic of Raman_1 and emitted into the $n+2$-th harmonic of Raman_2; and the transition is on resonance for $\omega_b - \omega_a = 2\omega_{\mathrm{EOM}} + \delta\omega_{\mathrm{AOM}}$. The AOMs are necessary in this scheme to break the the degeneracy between absorbing from Raman_1 and emitting into Raman_2 and absorbing from Raman_2 and emitting into Raman_1. The energy difference between these two paths is seen by summing the frequency differences as

$$\delta\omega_{n_1-n_2=+2} = 2\ \omega_{\mathrm{EOM}} + (\omega_{\mathrm{AOM}_1} - \omega_{\mathrm{AOM}_2}) = 2\ \omega_{\mathrm{EOM}} - \delta\omega_{\mathrm{AOM}} \tag{2.24}$$

$$\delta\omega_{n_1-n_2=-2} = 2\ \omega_{\mathrm{EOM}} - (\omega_{\mathrm{AOM}_1} - \omega_{\mathrm{AOM}_2}) = 2\ \omega_{\mathrm{EOM}} + \delta\omega_{\mathrm{AOM}}, \tag{2.25}$$

and

$$\delta\omega_{n_1-n_2=-2} - \delta\omega_{n_1-n_2=+2} = 2\delta\omega_{\mathrm{AOM}}. \tag{2.26}$$

In practice, the frequency difference between the $\delta n = +2$ and -2 is limited to 20 MHz by the bandwidth of the AOMs. Large frequency difference could also be obtained by changing the AOM modulation order selected in one of the beam paths, but eliminates the benefit of rapidly switching between single MHz- and GHz-level transitions.

Interference between all transitions with $\delta n = +2$ in this scheme contributes to the total Rabi rate, and the balance of the interference depends strongly on the modulation index. The Rabi rate for each transition

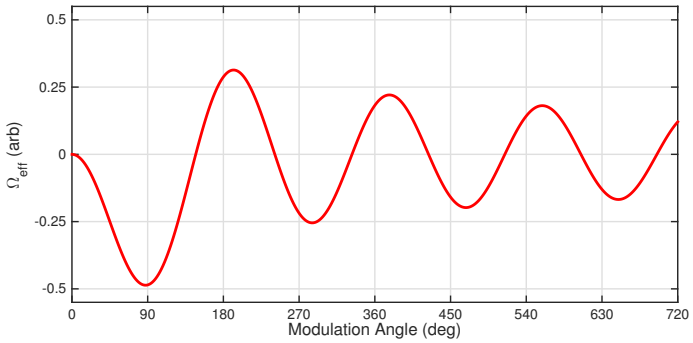

Figure 2.17: Rabi rate as a function of modulation angle in Raman transitions with phase modulated beams. The comb of peaks in Fig. 2.16 creates a series of transitions from harmonic peaks that differ by an index of +2. The interference between these peaks leads to an effective Rabi rate that depends on the modulation angle. The maximum Rabi rate occurs for a modulation angle of $\approx 90°$.

is defined as in Eq. 2.17, and the total rate can be found by summing over all complex rates with $\delta n = +2$.

$$\Omega_R = \frac{E_2 E_1}{4\Delta} \sum_{n_1=-\infty}^{\infty} \sum_{n_2=-\infty}^{\infty} i^{n_1}(-i)^{n_2} J_{n_1}(m)\ J_{n_2}(m) \langle b\,|\hat{\boldsymbol{e}}_{\boldsymbol{2}} \cdot \vec{r}|\, i\rangle \langle i\,|\hat{\boldsymbol{e}}_{\boldsymbol{1}} \cdot \vec{r}|\, a\rangle\, \delta_{n_1+2,n_2} \tag{2.27}$$

Here, δ is the Kronecker delta symbol imposing the condition that $n_2 = n_1 + 2$ to satisfy the resonance condition. The sum over all possible pairs of transitions can be taken using the identities $J_\nu(m_1 \pm m_2) = \sum_{n=-\infty}^{\infty} J_{\nu\mp n}(m_1) J_n(m_2)$ and $J_{-n}(x) = (-1)^n J_n(x)$. From these, the total rate is found as

$$\Omega_R \propto \frac{E_2 E_1}{4\Delta} J_2(2m). \tag{2.28}$$

The final Rabi rate is a function of the modulation angle due to a complicated interference of all the possible $\delta n = 2$ transitions as shown in Fig. 2.17. For maximum Rabi rate, m should be set to approximately 90°. Similar Raman transition schemes using phase modulated beam are described in Refs. [90, 116].

2.6 RF Electronics

A variety of radio-frequency and microwave signals are required to drive optical modulators and to create time varying optical and magnetic fields. RF signals at frequencies below 250 MHz are created using direct digital synthesizers (DDSs) due to the convenience of accurately generating both single frequencies and phase coherent frequency sweeps. Signals above this cutoff are produced via voltage controlled oscillators (VCOband where absolute frequency control is necessary, the VCO signals are divided and phase locked to a DDS. All timings and clock signals used in the experiment are referenced to a master clock signal produced by a 10 MHz distribution amplifier (Stanford Research Systems FS730). This distribution amplifier is

Use	Device
Clock Distribution	Analog Devices AD9516 - 14 channel programmable distribution amplifier
RF Source	Analog Devices AD9959 - 500 MHz DDS, 4 channels
RF Source	Analog Devices AD9854 - 300 MHz DDS with phase coherent frequency sweeps
Phase Locked Loop	Analog Devices ADF4007 - 7.5 GHz bandwidth
Variable attenuator	Analog Devices ADL5330 - 60dB range VGA, 10 - 3000 MHz
RF Switch	Minicircuits ZX80-DR230-S+ - TTL controlled RF switch
RF Amplifier	Minicircuits ZHL-1-2W - 2 Watt amplifier 0 to 500 MHz
Microwave Amplifier	Minicircuits ZHL-10W-2G+ - 10 Watt amplifier, 800 - 2000 MHz

Table 2.2: Radio-frequency and microwave electronics used in this experiment.

stabilized to a rubidium stabilized crystal oscillator for improved short-term stability and to a 1 pulse-per-seconds source generated from GPS for long-term stability. A list of standard RF electronics is provided in Table 2.2.

The optical power in the dipole trap, disorder, lattice, and Raman beams are actively servoed in the standard manner with AOMs. Each beam is passed through an AOM aligned to optimize diffraction into a particular diffraction order, and the beam's optical power is monitored using a wedged pickoff and a photodiode. The RF drive power of the AOM is servoed such that the optical power matches a computer controlled setpoint as shown in Fig. 2.18. The servos are simple integrator circuits built around low-offset audio op-amps. Importantly for optimal servo behavior, the maximum RF power at the AOM should be adjusted such that the diffraction efficiency as a function of drive power is monotonic over the entire gain range of the variable gain attenuator (VGA) used to modulate the drive power. Overdriving the AOM can cause the diffraction efficiency to fall with increasing drive power and cause the servo gain to change sign. A host of thermal effects can lead to significant beam pointing drift as described in Section 2.4.2.

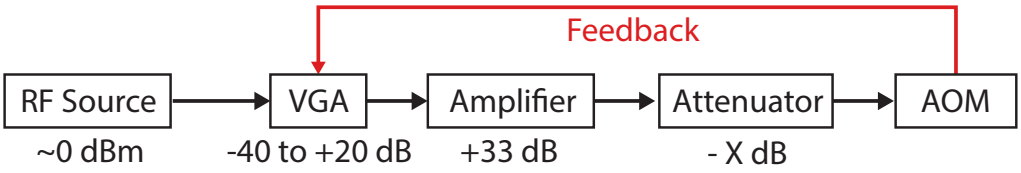

Figure 2.18: Radio frequency signal chain for active intensity stabilization of laser beam power. The final attenuator is adjusted to ensure diffraction efficiency is a monotonic function of RF drive power.

2.7 Imaging

At the end of each experimental sequence, an image is taken of the gas to measure its density or momentum distribution. These images are taken in time of flight expansion using absorption imaging with a resonant

laser beam. The partial absorption of the probe beam is used to generate a column-integrated map of the atomic density. In this procedure, the atoms are released from the trapping potential and allowed to freely expand for a given expansion time. Resonant light is applied and the shadow cast by the atoms is imaged onto a CCD camera (Princeton Instruments Pixis 1024BR). Two subsequent images are taken to acquire the light intensity without atomic absorption and the background with no applied light. These are called the atom image $\mathcal{A}$, the light image $\mathcal{L}$, and the background image $\mathcal{D}$, respectively.

$$\mathcal{OD} = \mathsf{log}\left(\frac{\mathcal{A}-\mathcal{D}}{\mathcal{L}-\mathcal{D}}\right) \quad \text{where} \quad \begin{cases} \mathcal{A} &= \text{atom image, resonant light} \\ \mathcal{L} &= \text{light image, no atoms} \\ \mathcal{D} &= \text{dark image, background} \end{cases} \tag{2.29}$$

Resonant light is absorbed proportionally to the column integrated density in the gas quantified as the optical depth ($\mathcal{OD}$). The areal density of atoms is found by dividing the $\mathcal{OD}$ by the atomic scattering cross section. For the imaging using resonant light, the scattering cross section is given as $\sigma_{\rm sc} = 3\lambda^2/2\pi$ which for the ^{40}K D2 line at 766.7 nm is $1/(0.53\mu m)^2$. The image is binned into pixels at the camera, and the number in each pixel is $N_{\rm px} = \mathcal{M}^2\ \mathcal{OD}/\sigma_{\rm atom}$. The magnification $\mathcal{M}$ is the area of a pixel in the object plane. The primary imaging system in the experiment has a magnification of 3.2 microns per pixel and the optics can resolve features as small as 2 microns. The imaging exposure is taken over 25 microseconds to limit motion blur and heating during the probe time, and the light intensity is adjusted to minimize saturation effects. Absorption is a non-linear process with a scattering rate set by the ratio of the intensity I to the saturation intensity I_{sat}.

$$\Gamma_{\rm sc} = \frac{\Gamma}{2}\frac{I/I_{\rm sat}}{1+I/I_{\rm sat}} \tag{2.30}$$

Here Γ is the natural linewidth of the transition, and $I_{\rm sat} = \pi hc\Gamma/3\lambda^2$ on resonance for circularly polarized light. Heating during the exposure can also cause non-linear absorption due to the atoms Doppler shifting out of resonance, as described in Ref. [112]. The saturation intensity measured with our system corresponds to 14,000 counts per pixel in the camera as shown in the saturation plot in Fig. 2.19. Imaging can be performed at intensities well below this quantity so that minimal non-linear effects are seen in absorption, or the probe power can be increased well above I_{sat}. A compromise between increasing signal-to-noise and non-linear absorption exists with increasing probe intensity, and images are taken at high or low intensity depending on the requirements of the experiment.

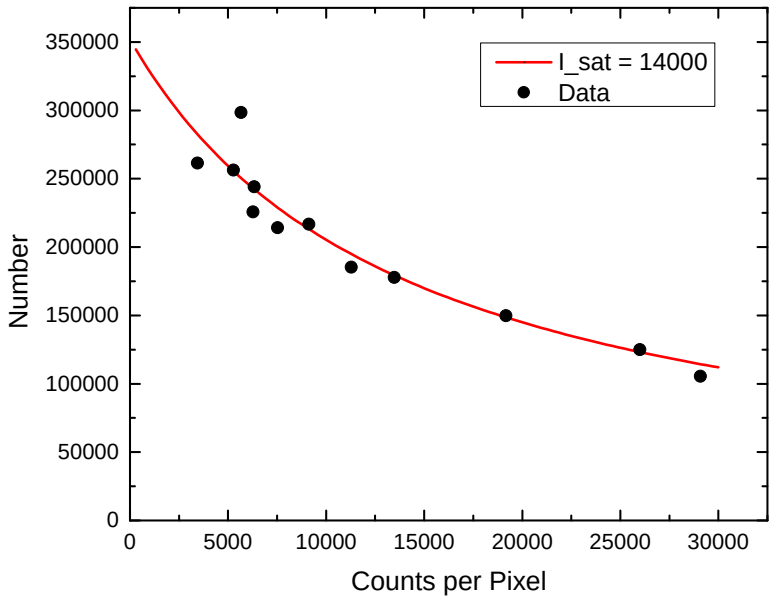

Figure 2.19: Saturation effects in the primary imaging system. Images are taken of similarly prepared gases with varying probe intensities. The effective cross section is related to the average number of counts per pixel on the camera. The saturation intensity of 2.2 mW/cm^2 corresponds to 14000 counts per pixel. The red line is a fit to the data using the formula in Eq. 2.30, and the number plotted is the apparent value determined from the OD images.

2.7.1 Gram-Schmidt Fringe Removal

Etaloning between parallel optical surfaces creates deep fringes in the imaging probe beam. Small vibrations in the apparatus cause the fringe pattern to shift and change shape between exposures, and this misalignment creates high spatial-frequency fringes in the optical depth images as shown in Fig. 2.20. The changes in the probe beam between images can be reduced by shortening the time between images. Experiments in Hamburg have found temporal correlation between images can change on ms timescales and that this effect can be exaggerated by adding acoustic noise to their environment [105]. These fringes are a false signal and can modify the results of fitting to small features or affect the accuracy in determining the position of the gas. We use a simple post-correction procedure to reduce the effects of non-ideal light images by building a reconstructed light image from a pre-calculated basis of possible light images and the fringe pattern in the atom image. This method is based on work in Ref. [23].

To accomplish the reconstruction of the best light image, we start with a basis set of images taken from the experiment, typically 50 to 500 images. We create a mask $\mathcal{M}$ that is zero in the signal region of the image and one elsewhere, as in Fig. 2.20e. The set of possible light images, $\mathcal{L}_i$, where i indexes the images with

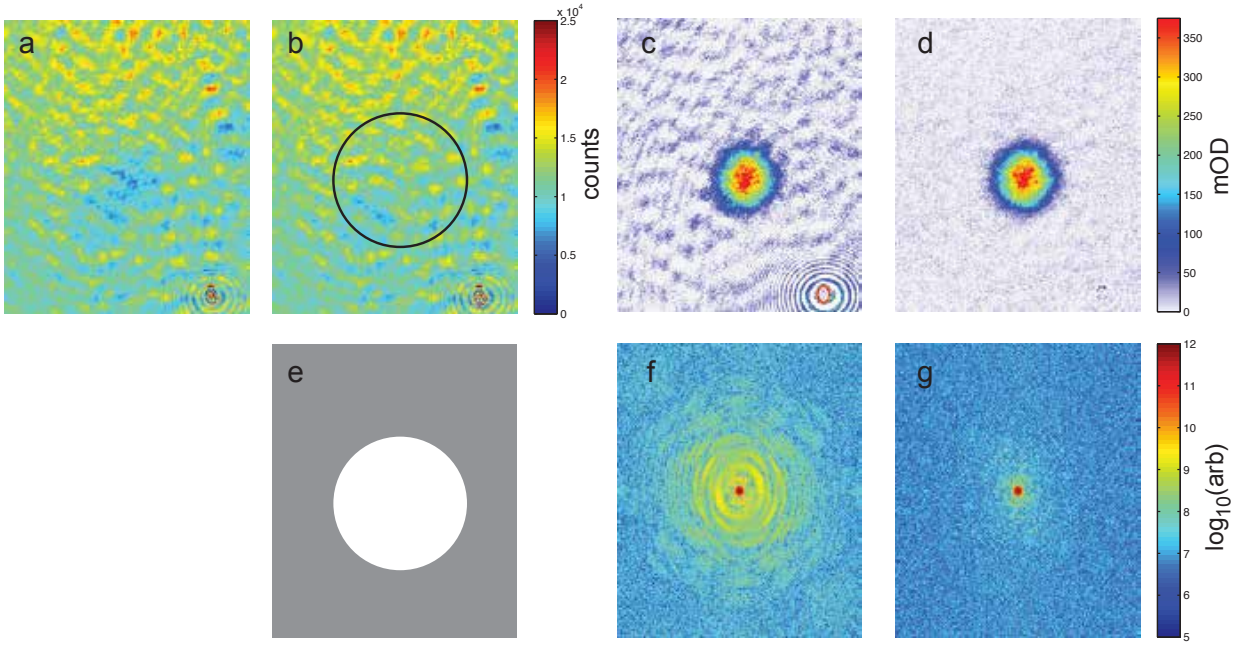

Figure 2.20: Improvement in optical depth image from defringing algorithm. (a-b). Atom and Light images used to produce the optical depth image in (c). A basis of possible light images was created using a large set of light images and the mask in (e). The circle indicates the region where the signal appears. (d) The corrected image after defringing procedure shows a marked reduction of fringes. (f-g) The power spectra for images in (c) and (d). Here defringing has removed artificial high frequency weight from the signal.

the signal region masked is then made into an orthonormal basis, $\mathcal{B}_k$, using Gram-Schmidt diagonalization.

$$\mathcal{B}_k = \mathcal{L}_k - \sum_{j<k} \mathcal{B}_j \frac{\tilde{\mathcal{L}}_k \cdot \tilde{\mathcal{B}}_j}{\left|\tilde{\mathcal{B}}_j\right|^2} \text{ , where } \quad \tilde{\mathcal{A}}_i \equiv \mathcal{M}\mathcal{A}_i \quad \text{and} \quad \tilde{\mathcal{B}}_i \equiv \mathcal{M}\mathcal{B}_i. \tag{2.31}$$

The evaluation time of this procedure scales as the square of the number of images, and can be resource intensive for large images and large basis sets. Once the basis has been created, the reconstructed light image, $\mathcal{R}_i$ is calculated by summing over the basis images with a weighting given by the inner product between the masked regions of the atom image and each basis image.

$$\mathcal{R}_i = \sum_j \mathcal{B}_j \frac{\tilde{\mathcal{A}}_i \cdot \tilde{\mathcal{B}}_j}{\left|\tilde{\mathcal{B}}_j\right|^2} \tag{2.32}$$

The optical depth images is then calculated using the computed best light image.

$$\mathcal{OD}_i = \log\left(\frac{\mathcal{A}_i}{\mathcal{R}_i}\right) \tag{2.33}$$

The result of this procedure shows a dramatic reduction in the high-frequency fringes in the images as is

evident in the power spectrum in Fig. 2.20(g). The statistical properties of the noise can also be analyzed before and after the defringing procedure (as in Ref. [105]) to show a recovery of the Poisson distributed shot noise in the image as the size of the basis set grows.

Chapter 3

Controlled Disorder from Optical Speckle

Optical speckle is used to create a well characterized, spatially disordered potential for exploring Anderson localization and transport in disordered lattices. This section details how variable-scale speckle is produced in the experiment and summarizes the statistical properties of speckle including its intensity distribution, autocorrelation, and power spectrum. Ex situ measurements of a three-dimensional speckle field are discussed and compared with analytic predictions. Details of the experimental implementation, methods for alignment to the ultracold gas, and systematics in calibrating the absolute potential height are discussed.

Speckle is a popular method for generating controlled disorder in ultracold gas experiments and has been used to observe Anderson localization in 1D [18], the superfluid to Bose-glass transition in the disordered Bose-Hubbard model [158], coherent backscattering in 2D [84], and quantum transport through disordered channels [104]. The work in this thesis focuses on 3D Anderson localization using a single-beam speckle pattern to create a disordered potential in free space and the transport measurements in 3D disordered lattices created by superposing speckle on a 3D optical lattice. Other sources of controlled disorder and quasi-random disorder have been implemented in ultracold gas experiments including incommensurate lattices [177] used to realize the Aubré-Andre model in 1D [177], periodically-pulsed potentials realizing the kicked rotor [143, 25, 58], multi-species or spin-dependent experiments [56], and arbitrary optical potentials using holography or masks [157]. Each of these methods has advantages and disadvantages given technical constraints of producing and calibrating the disordered potential.

3.1 Statistical Properties of Speckle

Speckle is produced by the interference of monochromatic waves with random phases and is ever-present when a coherent source such as laser beams, radio waves, or sound waves scatters from a rough surface. The interference pattern produced from this scattering has characteristic light and dark patches called speckles with well defined statistical properties and spatial correlations controlled by the random nature of the scattering process. The properties of speckle including its correlation properties are covered in great detail

in Ref. [64], and this chapter summarizes the aspects most necessary for understanding the experimental work presented in Chapters 4 and 6.

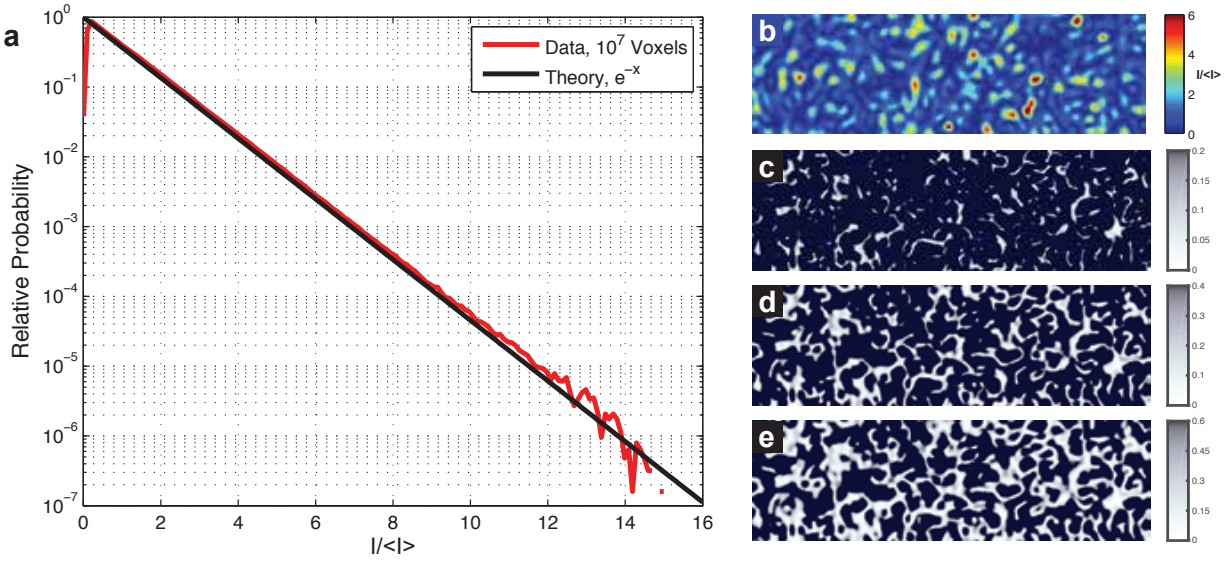

Figure 3.1: Speckle intensity probability distribution and percolation in 2D. (a) The exponential probability distribution for intensity is shown for the 3D speckle scan discussed in Sec. 3.5. Agreement between measurement and the predicted scaling is seen over six decades! (b) Example 2D slice through the 3D speckle scan shows a typical speckle intensity maps. The field of view is 8 by 50 microns. (c-e) Disordered potentials created from blue-detuned (repulsive) speckle have percolation transitions in 2D as the low intensity regions are disjoint for energies less than half of the mean intensity. Above this intensity, a percolation transition occurs when these regions begin to connect. At higher energies, the disjoint regions connect and classically allowed paths connect all of space. This percolation transition is illustrated graphically by adjusting the upper limit of the grayscale color map to 0.2, 0.4, and 0.6 of the mean intensity in (c), (d), and (e).

We create a speckle pattern by imprinting spatially varying, random phases over a laser beam with a diffuser. The diffuser employed is a rigid polycarbonate sheet stamped with a random pattern, but the details of the diffuser are unimportant for the nature of the speckle produced. The electric field after the diffuser is found by summing over the large number of random phases produced in the diffuser plane—this random phasor sum gives electric field amplitudes:

$$A = \frac{1}{\sqrt{N}} \sum_{i=1}^{N} a_i e^{i\phi_i}. \tag{3.1}$$

For a sufficiently large number of random phases produced by the diffuser, the central limit states that the sum will converge to a Gaussian distribution. The intensity is the square modulus of the electric field; and given this condition, the intensity will be exponentially distributed in space, where the width of the

exponential is set by the mean intensity $\langle I \rangle$:

$$P(I) = \frac{\exp\left(-I/\langle I \rangle\right)}{\langle I \rangle}. \tag{3.2}$$

Images of an example speckle intensity map in 2D are shown in Fig. 3.1. The distribution of intensities is plotted from a 3D scan of speckle taken with a microscope and a CCD camera. From this data, the intensity distribution is shown to scale exponentially over six orders of magnitude. Deviations from the ideal exponential distribution are seen at low intensity due to spatial averaging in the speckle imaging system and dark counts in the camera. The formation of a speckle pattern can be easily explored in 2D with a simple 1 line computer program (speckle in 3D with the typical imaging geometry is more complicated and requires use of Fresnel transform as described in Sec. 3.2). Using the MATLAB code below, one introduces random phases over a 64 x 64 wide aperture. Speckle is created in an imaging geometry by taking the Fourier transform of the aperture plane to find the amplitude in the image plane, and the intensity is found by taking squaring the modulus of the amplitude. When the random phases are sampled evenly over 2π or a large multiple of 2π, a speckle pattern is created; and for less random sampling, the imaging system simply focuses the light to a small spot.

```
>> imagesc(abs(fftshift(fft2(exp(-2*pi*1i*rand(2^6)),2^11,2^11))).^2)
```

We use a speckle potential to create a three-dimensional disordered potential for exploration of Anderson localization with ultracold atoms. To perform these experiments, a potential is required that generates localization without classical trapping. Conveniently, the percolation transition for speckle in 3D is found numerically at $4(1) \times 10^{-4}$ of the mean intensity [163, 185] and can be ignored for the potential heights employed in this work. The percolation energy scale in speckle originates from optical vortices, lines of darkness in the optical field about which the phase of the light winds by an integer multiple of 2π. Speckle fields are permeated by optical vortices that meander through the speckle field taking random walks in space [149]. For a repulsive speckle potential, these vortices are the classical absolute minimum energy paths through space and connect large areas of the potential. Surprisingly, it is possible for vortices to form loops and knots by winding upon themselves [16, 111]. These closed vortex loops are the source of the percolation energy scale in 3D. In 2D, the average height of saddle points controls the percolation transition at the much higher value of $\langle I \rangle \approx 0.52$, as indicated graphically in Fig. 3.1 [188, 208].

3.2 Speckle Intensity Autocorrelation and Power Spectrum

The characteristic size of the speckle features is determined by the optical intensity autocorrelation function. This section details the calculation of the autocorrelation function for uniformly and Gaussian illuminated lens with random phases introduced across the aperture. Equivalence is shown between the autocorrelation function and the imaging spot produced via a lens with a similarly illuminated aperture. We will also calculate the power spectrum of the intensity, which is relevant for understanding dynamics of a wave scattering in a speckle potential. These calculations are based on a derivation found in Ref. [64], where more details on the statistical properties of speckle can be found. Previous theoretical and experimental work exploring speckle correlation properties in the deep Fresnel zone can be found in Refs. [61, 126]

The autocorrelation function of the intensity $\mathrm{I}(\vec{r})$ is defined as a convolution integral of the speckle intensity field with itself:

$$C_{\mathrm{I}}(\vec{\Delta r}) \equiv \int \mathrm{I}(\vec{r})\ \mathrm{I}(\vec{r}+\vec{\Delta r})\ d\vec{r}. \tag{3.3}$$

The intensity autocorrelation, C, can be related to the complex correlation coefficient of the field, μ. Here the complex field is $A(\vec{r})$ and $\mathrm{I} = |A|^2$. In general, the correlation of two intensities can be related to the correlation of the field amplitudes A_1 and A_2 as

$$C_{12} \ = \ \langle \mathrm{I} \rangle^2 \left(1+\mu_{12}^2\right) \quad \text{where} \quad \mu_{12} \ \equiv \ \frac{\langle A_1 A_2^* \rangle}{\sqrt{\langle |A_1|^2 \rangle \langle |A_2|^2 \rangle}}. \tag{3.4}$$

The angled brackets $\langle ... \rangle$ indicate spatial averaging over $\vec{r}$. For calculating the autocorrelation of the speckle field, $A_1 = A(\vec{r})$ and $A_2 = A(\vec{r}+\vec{\Delta r})$. We first calculate the complex field produced from a lens with illumination $\mathrm{I}(\alpha,\beta)$ where α and β parameterize the surface of the lens. The field from the lens is a sum of spherically expanding rays emanating from the imaging aperture and can be expressed as shown in Ref [20].

$$A(x,y,z) \ = \ -i\frac{e^{i2\pi z/\lambda}}{\lambda z} e^{i\frac{\pi}{\lambda z}\left(x^2+y^2\right)} \iint_{-\infty}^{\infty} a(\alpha,\beta)\ e^{i\frac{\pi}{\lambda z}\left(\alpha^2+\beta^2\right)}\ e^{-i\frac{2\pi}{\lambda z}(\alpha x+\beta y)}\ d\alpha\ d\beta \tag{3.5}$$

Here f is the focal length of the lens, λ is the wavelength of the light, and $a(\alpha,\beta)$ is the electric field across the aperture. A coordinate system is adopted with z along the axis of the lens and x and y in the same plane of the lens. To find the intensity correlation function we will start by evaluating the complex correlation

coefficient. The integral for numerator of the complex correlation coefficient takes the form

$$\Big\langle A(\vec{r})\ A^*(\vec{r}+\vec{\Delta r})\Big\rangle = \Big\langle \iiiint A(\alpha_1,\beta_1,x,y)\ A^*(\alpha_2,\beta_2,x+\Delta x,y+\Delta y)\ \delta(\alpha_1-\alpha_2)\ \delta(\beta_1-\beta_2)\ d\alpha_1\ d\beta_1\ d\alpha_2\ d\beta_2\Big\rangle. \tag{3.6}$$

The integral here is over all points on the scattering surface for the two amplitudes considered. The random phase introduced on the $(\alpha_i,\ \beta_i)$ scattering surface is delta function correlated. This correlation is expressed in Eq. 3.6 with the Dirac delta functions $\delta(\alpha_1-\alpha_2)$ and $\delta(\beta_1-\beta_2)$, and integration over the delta functions reduces the dimensionality of the amplitude autocorrelation integral. With Eq. 3.5, the numerator of the complex correlation coefficient can be found in terms of the properties of the imaging system:

$$\Big\langle A(\vec{r})\ A^*(\vec{r}+\vec{\Delta r})\Big\rangle = \iint A(\alpha,\beta,x,y)\ A^*(\alpha,\beta,x+\Delta x,y+\Delta y)\ d\alpha\ d\beta \tag{3.7}$$

$$= \frac{1}{\lambda^2 z^2}\iint I(\alpha,\beta)\ e^{-i\frac{2\pi}{\lambda z}(\alpha\Delta x+\beta\Delta y)}\ d\alpha\ d\beta. \tag{3.8}$$

This allows us to write down the intensity autocorrelation function using Eq. 3.4. Here the axial distance is taken as the focal length of the lens f, and

$$\frac{C_I(\vec{\Delta r})}{\langle I\rangle^2} = 1+\left(\frac{\iint I(\alpha,\beta)\ e^{-i\frac{2\pi}{\lambda f}(\alpha\Delta x+\beta\Delta y)}\ d\alpha\ d\beta}{\iint I(\alpha,\beta)\ d\alpha\ d\beta}\right)^2. \tag{3.9}$$

Note that the intensity correlation function of speckle near the focus of an imaging system is 1 plus the Fourier transform of the intensity across the imaging aperture squared, namely the correlation function is exactly the spot size of the equivalent imaging system without random phases imprinted across the beam. This is physically intuitive—the random phasor sum is limited by the same principle that governs Gaussian beams as their high spatial-frequency bounds are set by the fundamental properties of diffraction.

The intensity correlation function can be easily calculated for a uniformly illuminated aperture in 3D following the example of Refs. [64] and [20]. Here we consider a circular aperture of radius a and a lens of focal length f; the integral in Eq. 3.9 can be rewritten in terms of dimensionless variables

$$u \equiv \frac{2\pi}{\lambda}\left(\frac{a}{f}\right)^2\Delta z \quad \text{and} \quad v \equiv \frac{2\pi}{\lambda}\left(\frac{a}{f}\right)\Delta r, \tag{3.10}$$

where $\Delta r = \sqrt{\Delta x^2 + \Delta y^2}$ and the integral expressed as

$$\frac{C_I(\vec{r})}{\langle I \rangle^2} = 1 + \left(e^{i\left(\frac{f}{a}\right)^2 u} \int_0^1 J_0(v\rho) e^{-\frac{1}{2} i u \rho^2} \rho d\rho \right)^2 . \tag{3.11}$$

Here $J_0(x)$ is a Bessel function of the first kind of order 0 and argument x. This integral takes simple analytic forms along the axial and transverse directions of the speckle shown here for a potential of mean height Δ:

$$C_I(\Delta z, \Delta r = 0)/\Delta^2 = 1 + \mathsf{sinc}^2\left(\frac{\Delta z}{4}\right) \tag{3.12}$$

$$C_I(\Delta z = 0, \Delta r)/\Delta^2 = 1 + \left(\frac{J_1(v)}{v}\right)^2 . \tag{3.13}$$

Along the axial direction, the correlation function is the same as Fraunhofer diffraction from a rectangular aperture, and in the plane of the lens, the correlation function is the same as the Fourier transform of the circular aperture, or an Airy disc. The shape of the correlation function is shown in Fig. 3.2 with slices along the u and v axes.

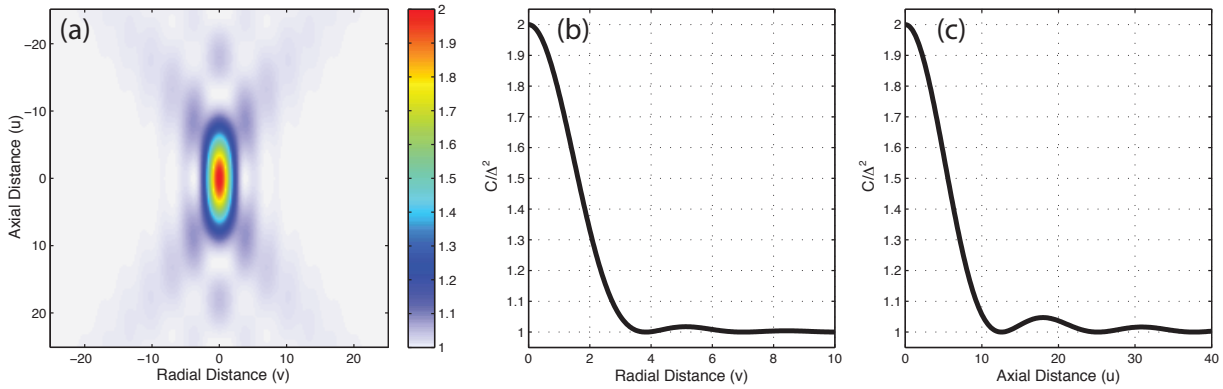

Figure 3.2: Autocorrelation of speckle intensity for a uniformly illuminated aperture. (a) Correlation function expressed in Eq. 3.11 is shown with respect to the dimensionless variables u and v. Slices of the correlation function are plotted along the radial (b) and axial (c) directions in the speckle.

For a Gaussian illuminated aperture, the correlation function can be expressed again by integrating Eq. 3.4 with the appropriate illumination function, and the correlation function takes the form associated with a focused Gaussian beam following the work of Ref. [164]:

$$C(\Delta x, \Delta y, \Delta z)/\Delta^2 = 1 + \frac{1}{1 + 4\Delta z^2/\sigma_{||}^2} \exp\left[-\frac{(\Delta x^2 + \Delta y^2)/(\sigma_\perp^2)}{1 + 4\Delta z^2/\sigma_{||}^2} \right] . \tag{3.14}$$

In connection with Gaussian optics, $\sigma_{||} = 4\lambda_L f^2/\pi w^2$ and $\sigma_\perp = \lambda_L f/\pi w$. The power spectrum is calculated

as the Fourier transform of the correlation function:

$$\tilde{C}(\Delta k_x, \Delta k_y, \Delta k_z)/\Delta^2 = \delta^3(\Delta k_x, \Delta k_y, \Delta k_z) \; + \; \frac{\pi^{3/2}\sigma_\perp^2\sigma_{||}}{\sqrt{(\sigma_\perp \Delta k_x)^2 + (\sigma_\perp \Delta k_y)^2}} \times \\ \exp\left[-\frac{1}{4}\left((\sigma_\perp \Delta k_x)^2 + (\sigma_\perp \Delta k_y)^2 + \frac{(\sigma_{||}\, \Delta k_z)^2}{(\sigma_\perp \Delta k_x)^2 + (\sigma_\perp \Delta k_y)^2}\right)\right]. \tag{3.15}$$

The shape of the intensity autocorrelation and power spectrum are shown in Fig. 3.3. As each of these quantities is calculated within the paraxial approximation, there is no weight in the power spectrum along the axis of speckle. The shape of the power spectrum governs scattering from the speckle potential, and the consequences of this shape are discussed in detail at the end of Sec. 4.8. One might expect the paraxial approximation to do a poor job in representing an imaging system with an $f/\#$ close to 1, but the comparison of measured to calculated intensity correlation functions with zero free parameters in Figure 3.10 shows good agreement.

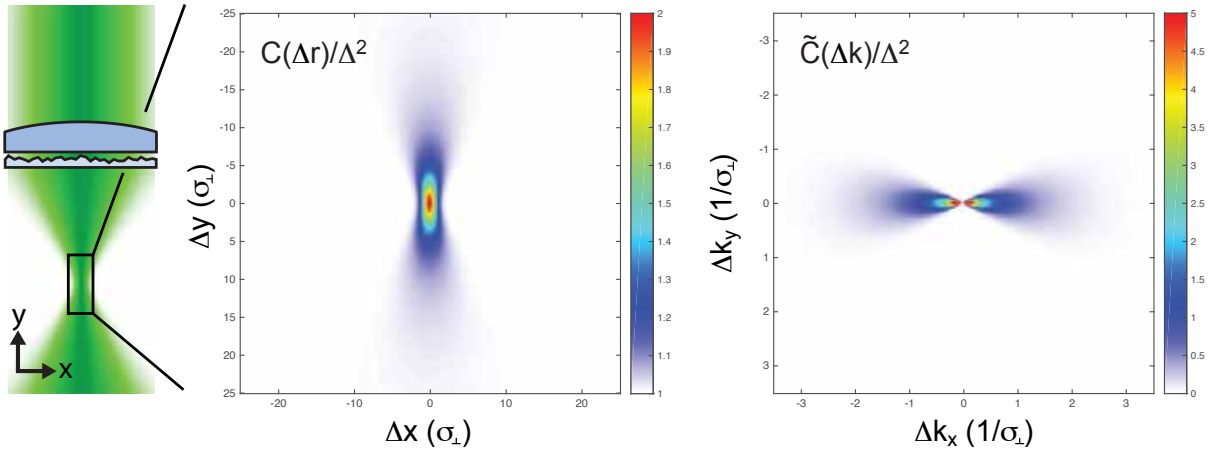

Figure 3.3: Calculated speckle autocorrelation and power spectrum for a Gaussian illuminated aperture. Intensity autocorrelation function $C(\vec{\Delta r})/\Delta^2$ and power spectrum $\tilde{C}(\vec{\Delta k})/\Delta^2$ are shown for speckle with an anisotropy factor of $\sigma_{||}/\sigma_\perp = 5.8$.

3.3 Experimental Realization

We create speckle in an imaging geometry as shown in Fig. 3.4. A collimated, 532 nm laser beam with a waist ($1/e^2$ radius) of 6.7 mm is focused through a high numerical aperture lens (Lightpath Photonics GPX15-15, f = 15 mm, clear aperture of 13 mm, and back focal length of 12.24 mm) and a diffuser (Luminit L.5P1-10, 0.5° FWHM divergence angle) which imprints random phases across the beam. The 532nm beam

is produced by a Coherent Verdi V18 with 6 W dedicated for the speckle. Intensity control is provided by modulating the beam with an AOM (IntraAction Corp); the first order diffraction peak is coupled through a single-mode, polarization-maintaining fiber to minimize beam pointing drift. Total efficiency through the fiber and AOM is greater than fifty percent. Scattering in the fiber limits the maximum output power of the two meter fiber to approximately 2 W.

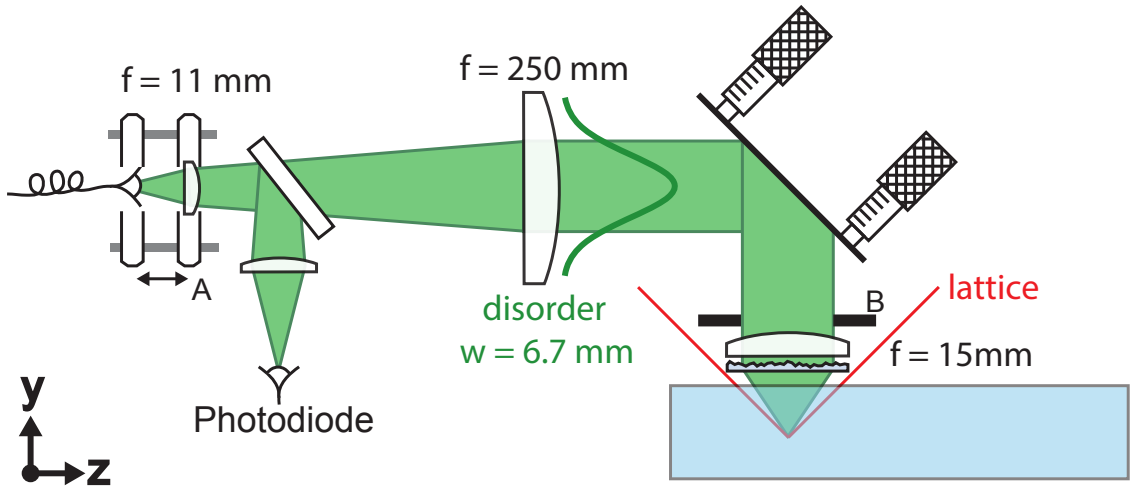

Figure 3.4: Sketch of apparatus for generating controlled disorder. A Gaussian, 532 nm laser beam is launched from a single mode fiber and collimated by two lenses. The effective numerical aperture of the focusing lens can be adjusted to control the correlation length of the speckle by varying the collimated beams waist at (A) or by apodizing the beam at the focusing lens (B). The high numerical-aperture focusing lens and the diffuser (jagged surface) sit immediately above the vacuum chamber (blue rectangle) and focus the light onto the position of the atoms. The 532nm beam is sampled with a wedged pickoff after the fiber cage, and this light is used to actively stabilize the beam power.

The light is launched from the fiber and collimated by two lenses in a manner that affords direct control over the collimated beam diameter. The first lens after the fiber is an 11mm, f/2 aspheric lens (Thorlabs C220TMD-A) and the second is a 250 mm, 2 inch diameter plano-convex spherical lens. Adjusting the position of the short focal length aspheric lens (point A in Fig. 3.4) sets the beam size at the large diameter lens while the large diameter lens collimates the beam. The shift in the asphere position does not significantly affect the output beam collimation.

Spatial alignment of the disorder focus is controlled via two systems. The focusing lens is mounted in a threaded tube with 100 threads per inch, affording half turn adjustments of 125 microns along the axis of the focus. The threaded tube mates with a flexure mount attached to the support structure of the QUIC trap; details are provided in Ref. [100]. The flexure mount (Fig. 3.5) offers coarse adjustment of the speckle focal position transverse to the direction of propagation. The arms of the flexure mount are limited by spatial constraints of the mounting hardware and were found to be hysteretic with poor isolation between the two

directions of motion. To overcome this limitation, alignment in the focal plane is performed by tilting the mirror closest to the focusing lens. This allowed for fine-scale, repeatable adjustment of the focal position.

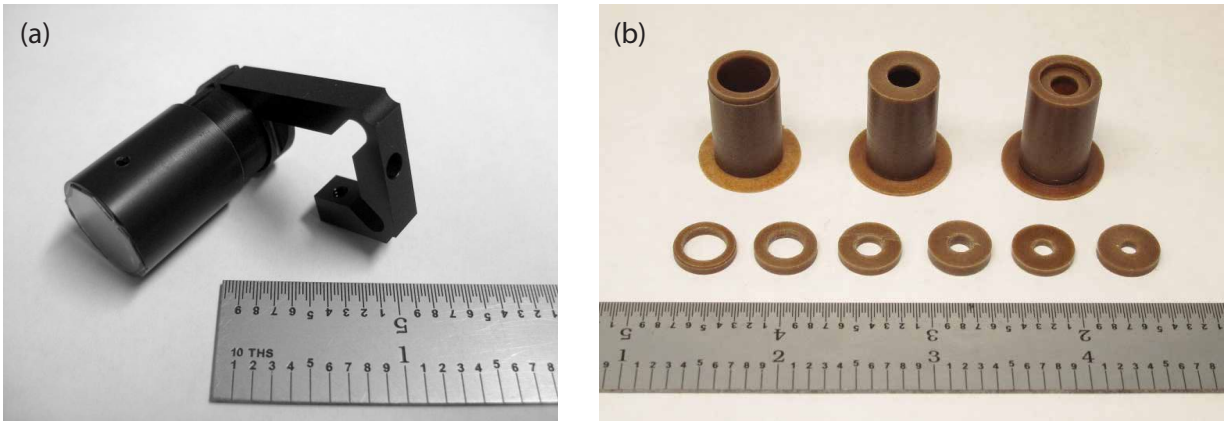

Figure 3.5: Speckle focusing lens hardware. (a) Flexure mount with threaded lens tube holds the speckle focusing lens and diffuser. (b) Tophat-shaped apertures fit inside the lens tube restricting the clear aperture of the lens to afford control of the speckle correlation length.

The size of the speckle correlation function is controlled by varying the effective numerical aperture of the speckle focusing lens. The intensity autocorrelation in this geometry is the same as the spot produced by the imaging system without the diffuser as discussed in Sec. 3.2. Control over the lens illumination is achieved by varying the waist of the collimated, Gaussian beam incident on the focusing lens or by apodizing the beam at the lens (point B in Fig. 3.4). In practice, it is more reproducible to apodize the beam at the lens, and a series of apertures were machined to fit into the focusing lens tube as shown in Fig. 3.5. These apertures rest above the front surface of the focusing lens and are geometrically constrained to be concentric with the lens.

3.4 Speckle Alignment and Calibration

Alignment of the speckle is performed by pulsing the speckle potential and measuring diffraction of the Fermi gas from the potential. Starting with a cold (typically 200 nK gas), pulsing the speckle potential broadens the momentum distribution of the gas inversely proportional to the speckle correlation length. For the anisotropic potential employed in the experiment, the transverse correlation length is at least a factor of five shorter than the axial correlation length, and diffraction along the speckle axis is minimal. Diffraction in the transverse direction from the speckle field gives a direct alignment signal as the amount of diffraction increases with decreasing correlation length and increasing disorder height. Starting with a fixed

temperature gas, the speckle focus[1] is moved in three dimensions to maximize the diffraction signal using the last mirror to control the focal position in the x- and z-directions and the threaded lens tube to control the y-direction.

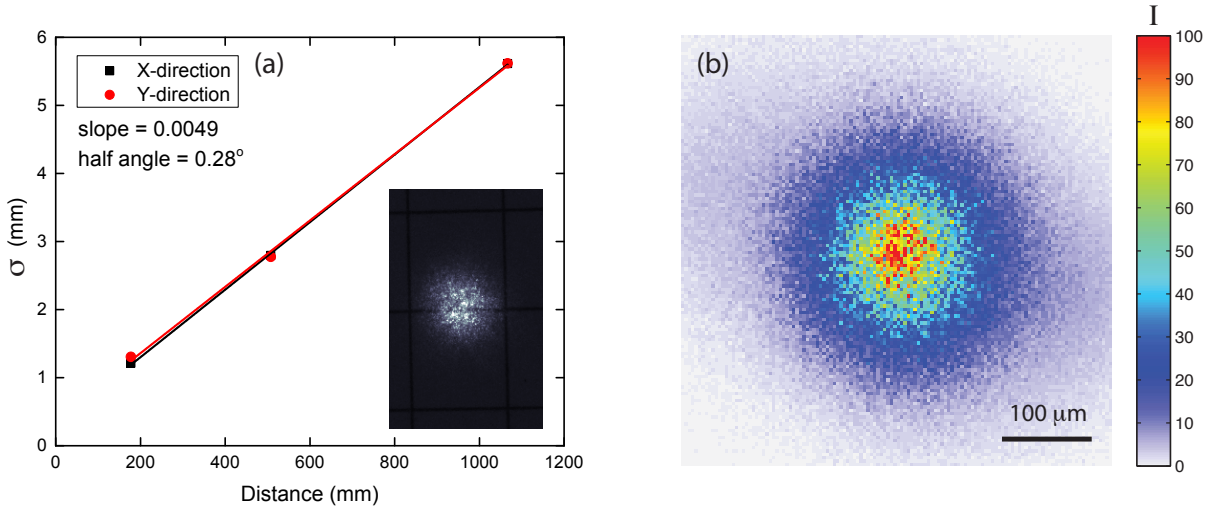

Figure 3.6: Ex situ calibration of diffuser angle and speckle intensity envelope waist. (a) A collimated laser beam is sent through the diffuser and its RMS width is measured at several distances to determine the diffuser angle. The inset shows the speckle imaged on a sheet of graph paper. (b) Image of speckle focus in the geometry shown in Fig. 3.4 where the intensity envelope has an $1/e^2$ radius of $\approx 125\mu m$.

The mean height of the speckle potential, Δ, is inferred based on measured values of the 532nm beam power and waist, calculations of the beam truncation at the focusing lens, and measurement of the speckle envelope waist at the atoms. The beam waist at the focusing lens was measured by imaging the beam on a sheet of graph paper and the waist is found to be 6.7 mm with high accuracy. The total power in the beam before the lens was measured by focusing the beam onto a calibrated optical power meter, and the power at the atoms is estimated to be 8% lower due to reflections from the glass cell. The fraction of light transmitted through the lens aperture is calculated from the aperture diameter and disorder beam waist using Eq. 3.16. This formula assumes the beam is centered on the lens, and misalignment here contributes to the systematic uncertainty in the mean disorder potential.

$$P_{\text{transmited}} = \int_0^{r_{max}} 2\pi r \frac{2P_{\text{total}}}{\pi w^2} e^{-\frac{2r^2}{w^2}} dr \tag{3.16}$$

The transverse waist of the disorder envelope at the position of the atoms is measured by pulsing the disordered potential and observing the impulse given to a hot gas. The impulse is proportional to the derivative of the speckle envelope, and the waist is found to be between 170 and 180 microns based on

[1]Speckle is always in focus. For simplicity, this document labels the region where the speckle has the finest correlation length as the speckle focus.

repeated measurements using this procedure as described in Ref. [100]. The size of the speckle envelope at the focus is determined by the diffuser angle and the focal length of the lens (the spot size of the imaging system is two orders of magnitude smaller than the beam waist). The diffuser angle is measured to be 0.66° FWHM (nominally 0.5°) as shown in Fig. 3.6. The disorder lens back focal length and the diffuser's divergence angle predict a $1/e^2$ radius of the speckle envelope of $w \approx 125$ microns, significantly smaller than the measured value and corresponds to a factor of 2 underestimation of the predicted mean speckle intensity. Measurements of the focal waist using an identical ex situ optical setup find beam waists in agreement with those predicted from the diffuser angle. The discrepancy between the predicted waist and those measured with the above technique has not been resolved, and direct measures of the mean speckle potential should be developed to directly address this discrepancy. For calculating the speckle height in published data, the waist measured by deflection of the atoms of 170 microns was used to calculate Δ. Experimental calibration of the speckle amplitude is not achieved, and the systematic uncertainty in the disorder height is quoted at 40%.

3.5 Three-Dimensional Scans of Speckle Potentials

Three-dimensional scans of speckle potentials were performed using an ex-situ replica of the speckle optics in the experiment to compare measured intensity autocorrelation functions and power spectra to predicted values and to calibrate the speckle correlation length for the variable scale localization measurement in Chapter 4. Scans were performed by mounting a 60x microscope objective on a manual translation stage. Positioning of the microscope along the speckle focus was controlled with a differential micrometer with half micrometer steps, and the microscope provided a magnification of 66 nanometers per pixels as calibrated by imaging a 1951 Air Force resolution target. The camera used was a PointGrey Chameleon monochrome (Sony ICX445 CCD) with a pixel pitch of 3.75 microns and total area of 1280 by 960 pixels. The 3D scans were built from a series of roughly 70 images stacked on regular intervals of 0.5 to 5 microns. The imaging microscope was moved between images using the manual translation stage, and vibrations in this process caused the microscope position to jitter slightly between frames and resulted in sub pixel misalignment between images. This jitter was removed by calculating the correlation function between adjacent frames to determine the offset between images, and then correcting the offset using the Fourier shift theorem to perform arbitrary shifts of the imaged speckle field. Typical jitter between frames was less than half a pixel, and up to 10 pixels net displacement was seen across an entire scan—likely the result of the speckle propagating slightly off-axis from the microscope. Three dimensional scans were performed for aperture diameters from

3.5 to 15 mm for an input beam waist of 6.7 mm, identical to the experimental configuration. Slices through the reconstructed speckle field for different effective numerical aperture imaging systems are shown in Fig. 3.7.

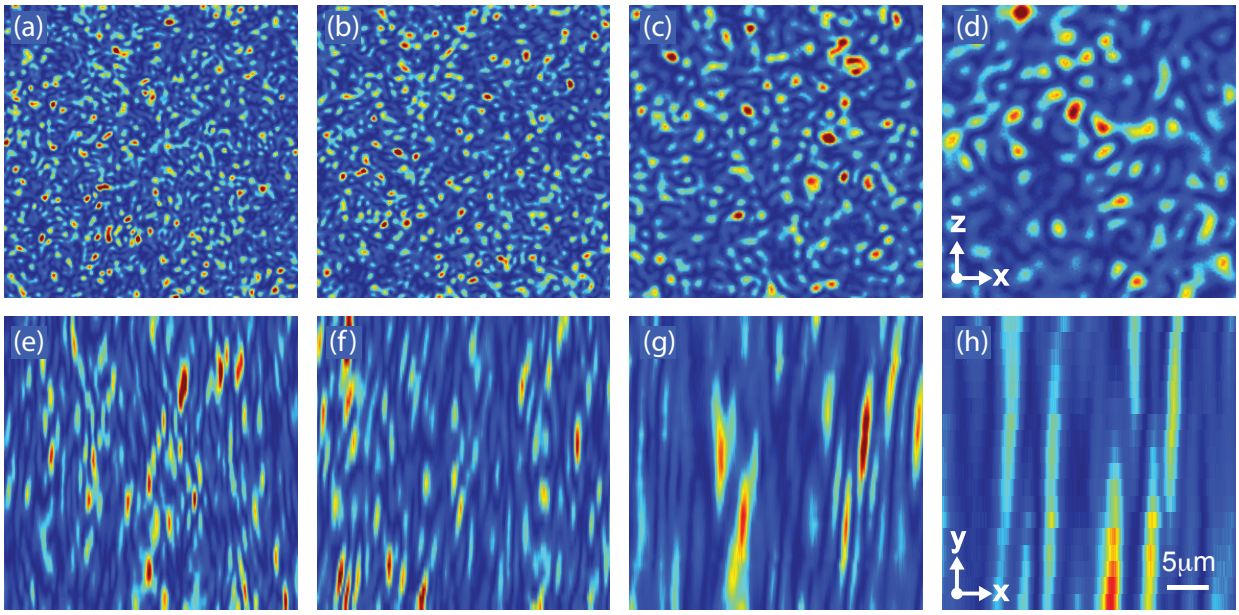

Figure 3.7: Three-dimensional scans of speckle potentials with variable correlation lengths. Slices of these scans are shown here for four different correlation lengths in the x-z (transverse-transverse) and x-y (transverse-axial) planes. The field of view in each image is 35 x 35 microns, and the false color scale extends from zero to five times the mean intensity. Images (a-d) are slices in the speckle focal plane, while (e-h) are reconstructed by stacking many 2D images of the speckle together. The speckle correlation length was varied by stopping-down the pupil of the focusing lens with circular apertures with diameters of 15 (a,e), 11.7 (b,f), 7.9 (c,g), and 4.7 mm (d,h).

Evaluation of the autocorrelation of the speckle scans was performed using the convolution theorem. It is possible to perform the convolution directly, but it is numerically faster to use fast Fourier transforms. The power spectrum of the potential is found by taking the square modulus of the Fourier transform of the potential such that $\tilde{C}_I(\mathbf{\Delta k}) = |\mathcal{F}[I(\mathbf{\Delta r})]|^2$, and the autocorrelation is the inverse Fourier transform of the power spectrum as $C_I(\mathbf{\Delta r}) = \mathcal{F}^{-1}[\tilde{C}_I(\mathbf{\Delta k})]$. Results for $C_I(\mathbf{\Delta r})$ and $\tilde{C}_I(\mathbf{\Delta k})$ over the range of speckle scanned is shown in Fig. 3.9. These data show the expected behavior of the correlation function growing with the effective $f/\#$ of the imaging system. Both the autocorrelation and the power spectrum are azimuthally averaged.

The measured correlation functions are compared with analytic predictions for a uniformly illuminated circular aperture from Eq. 3.11 in Fig. 3.10. The beam illuminating the focusing lens has a waist of 6.7 mm, and truncation of the intensity by the variable apertures means that the lens pupil is neither uniformly

Aperture (mm)	w_x (μm)	w_z (μm)	w_y (μm)	$(w_x w_y w_z)^{1/3}$
15.0	0.63 ± 0.012	0.62 ± 0.01	3.14 ± 0.04	1.07 ± 0.01
11.7	0.69 ± 0.02	0.72 ± 0.02	3.84 ± 0.08	1.24 ± 0.03
9.8	0.84 ± 0.02	0.81 ± 0.02	5.32 ± 0.09	1.54 ± 0.04
8.0	0.91 ± 0.01	0.91 ± 0.01	8.47 ± 0.07	1.91 ± 0.02
6.4	1.11 ± 0.03	1.14 ± 0.03	14.06 ± 0.15	2.61 ± 0.12
5.7	1.27 ± 0.06	1.27 ± 0.03	17.18 ± 0.19	3.03 ± 0.22
4.7	1.53 ± 0.05	1.47 ± 0.05	24.81 ± 0.1	3.82 ± 0.36
4.5	1.49 ± 0.06	1.50 ± 0.05	24.9 ± 0.31	3.82 ± 0.42
3.4	1.83 ± 0.05	1.79 ± 0.01	35.87 ± 0.53	4.90 ± 0.45

Table 3.1: Summary of measured speckle intensity autocorrelation widths. Intensity autocorrelation data were fit to a Gaussian function to extract the waist (twice the RMS radius) of $C_I(\delta \mathbf{r})$ along the x-, y-, and x-directions. The aperture diameters measured correspond to a range of $f/\#$ from ≈ 1.1 to 4.8. These data are plotted in Fig. 3.8.

or Gaussian illuminated. Despite this, good quantitative agreement is found between the measured and predicted correlation functions. Exact reproduction of the side lobes is complicated by the technical problems including the depth of focus of the microscope objective, imperfect alignment of the microscope along the speckle axis, and motion in the imaging optics during the speckle scan. A summary of the autocorrelation data and power spectra are shown in Fig. 3.9 for the aperture diameters explored, covering a range of $f/\#$ from ≈ 1.1 to 4.8. To simplify analysis of the correlation function, we fit each measured autocorrelation function to a Gaussian surface function to extract the $1/e^2$ radii for each distribution. A summary of this data are list in Table 3.1 and plotted in Fig. 3.8. Interpolation between the data presented in these graphs is used to generate the geometric mean correlation length used in the observation of Anderson localization in variable scale speckle described in Chapter 4.

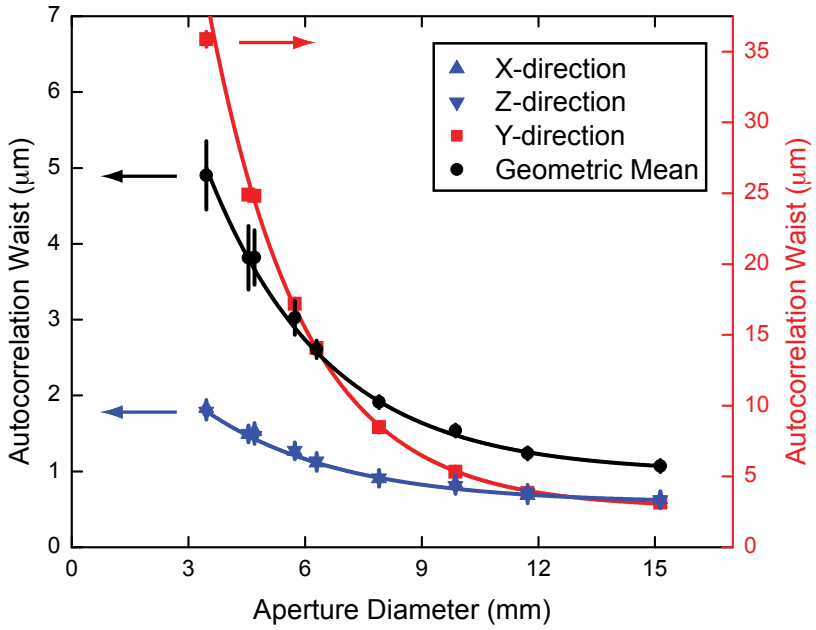

Figure 3.8: Measured autocorrelation waists for ex-situ 3D scans of variable-scale speckle. Data are plotted from Gaussian fitting to 3D reconstructed speckle intensity maps with the values listed in Table 3.1. Lines are interpolations used to determine the correlation values for aperture diameters not directly measured, and error bars represent the uncertainty in the Gaussian fit.

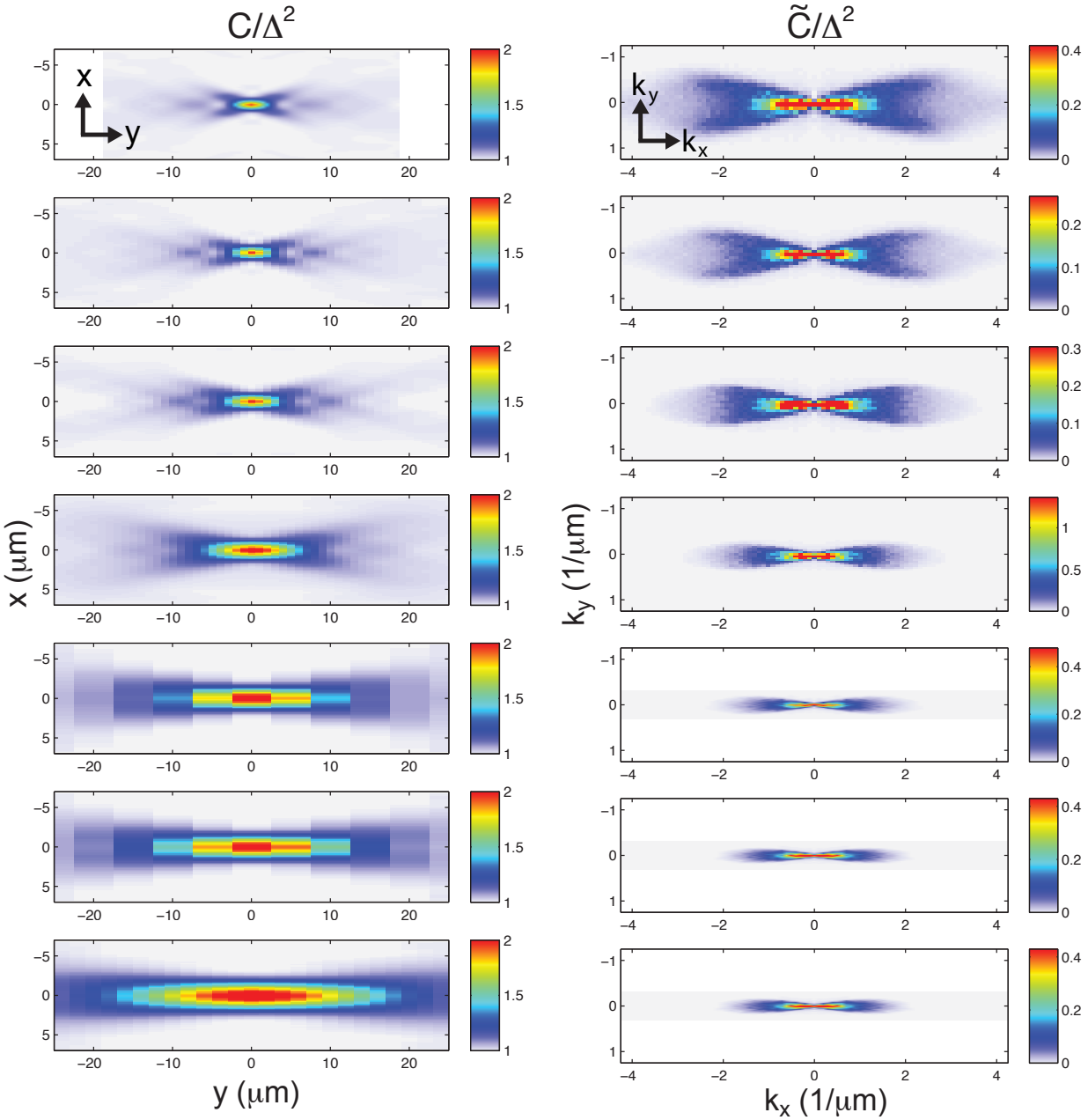

Figure 3.9: Autocorrelation functions and power spectrum for ex situ scans of variable-scale speckle. Intensity autocorrelations $C_I(\mathbf{r})$ and power spectra $C(\tilde{\mathbf{k}})$ are calculated from scans containing $\approx 10^7$ voxels. Speckle with variable correlation lengths are created by reducing the effective numerical aperture of a speckle imaging lens with circular apertures. Data sets are shown for aperture diameters of 15.0, 11.7, 9.8, 8.0, 6.4, 5.7, and 4.7 mm for the setup described in Fig 3.4.

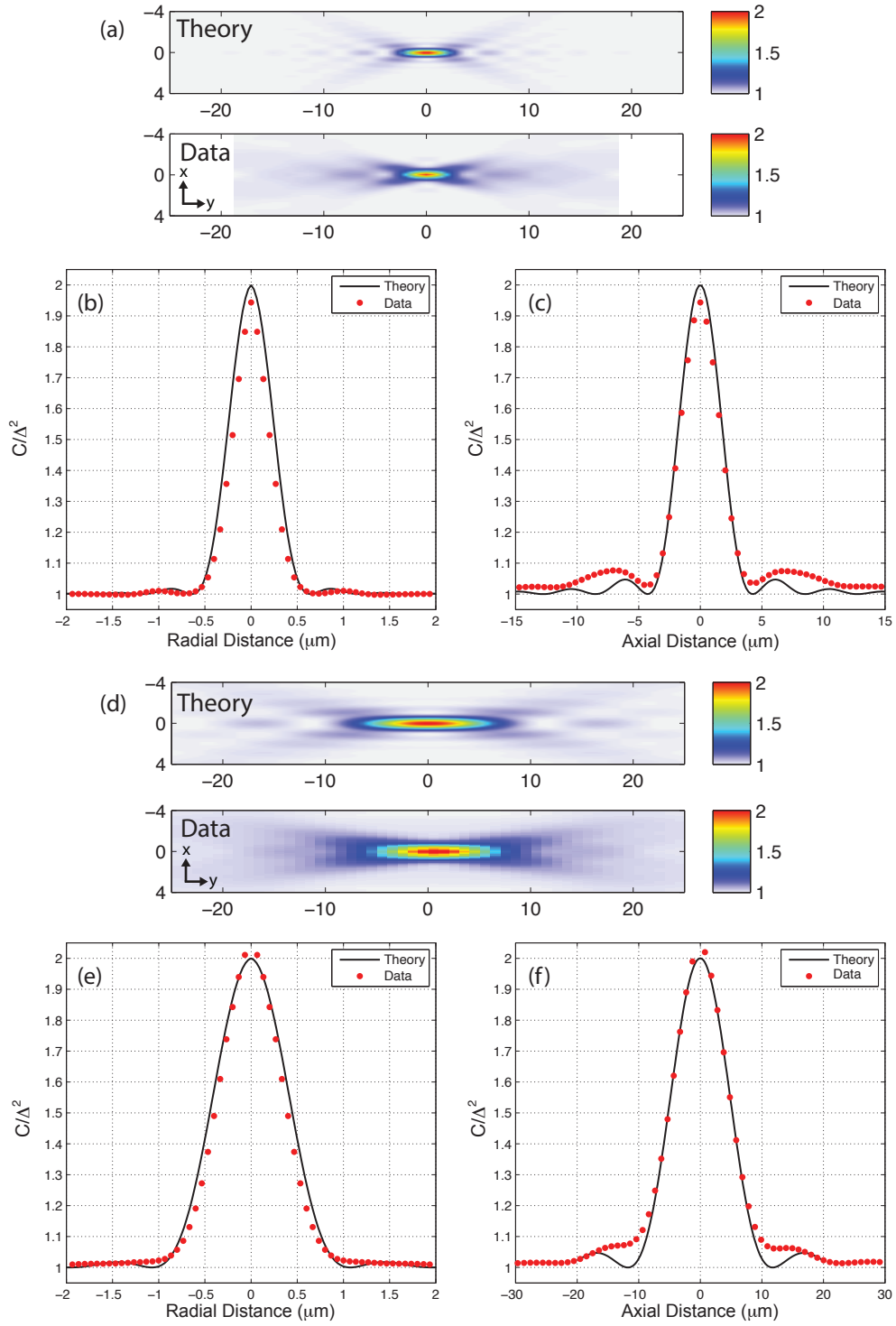

Figure 3.10: Detailed comparison of measured speckle autocorrelation distributions to theoretical prediction for uniformly illuminated circular apertures. Autocorrelation data are azimuthally averaged. Axial-transverse slices of the three-dimensional distribution are shown for for 15 (a-c) and 7.9 mm (d-f) aperture diameters. Theory images and curves are generated with zero free parameters using Equations 3.11, 3.12, and 3.13. These equations assume uniform illumination of the speckle focusing lens.

Chapter 4

Anderson Localization in Variable-Scale Speckle

4.1 Introduction

This chapter covers measurements on three-dimensional localization of an ultracold, non-interacting Fermi gas in a disordered potential created from optical speckle. Bimodal behavior is observed in the atomic density profile after expansion into the disorder. High energy atoms are observed to expand quasi-ballistically, while low energy atoms adopt a localized, anisotropic density profile whose shape is fixed in time. A disorder dependent mobility edge separating the two components is found relative to the atom's single-particle energy scale. Additionally, the shape and spatial extent of the localized gas is studied as a function of the temperature of the gas, the mean disorder height, and the disorder correlation length. The observed bimodal behavior and measured density profile are averaged over a thermal distribution of single-particle energies that complicates the interpretation of the data on both a quantitative and qualitative level, and two additional measurements were performed to probe the nature of the single-particle states in speckle disorder. First, the spatial extent of the single-particle localized states is probed by quenching the localized profile and observing the resulting dynamics. Second, an external force is applied to the localized gas to probe the stability of marginally localized states. These measurements are published in Refs. [102, 131, 132] and are discussed in part in Stan Kondov's dissertation [100]. The data on the response to an external force are unpublished.

Comparisons with other published theoretical and experimental work in the field are made where possible with emphasis given to theoretical work by Marie Piraud, R. Kuhn, and Cord Müller, as well as experimental work led by the Fred Jendrzejewski. A central point of this discussion is the lack of agreement between our observation and theoretical predictions for the length scale of localization in these systems. Our observations indicate significant occupation of localized states with length scales hundreds of times longer than the disorder correlation length. Predictions from weak scattering and the Born approximation suggest localization lengths scale more comparable to the disorder correlation length. The validity of the weak scattering approximation in these calculations is discussed and related to the measurements presented in this chapter. Generically,

one expects the weak scattering approximation to fail exactly in the regime of Anderson localization where the Ioffe-Regel criterion is satisfied, and theoretical tools that go beyond the Born approximation may be required to understand the phenomena of localization in correlated disorder.

4.2 Background

Anderson localization is an interference phenomenon in which waves fail to propagate in a disordered medium. Localization arises from multi-path interference and can be viewed as an extreme example of coherent backscattering or weak localization. In weak localization, one considers numerous trajectories available in a disordered medium. Paths that form loops have time-reversed duals as shown in Fig 4.1. If these dual paths are phase coherent, the paths will positively interfere with an amplitude twice the incoherent sum of the two paths. This modifies the diffusion constant, D, in the medium such that $D \to D - \delta D$. The size of δD is controlled by the Boltzmann mean free path and the wavelength of the particle. Anderson localization occurs when the perturbation to the diffusion constant becomes as large as the constant itself and motion arrests.

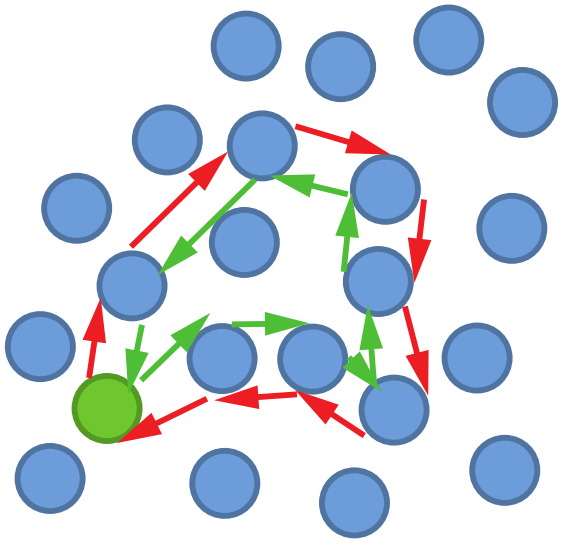

Figure 4.1: Illustration showing self-interference in a disordered scattering medium. A wave starting at the green point can travel the clockwise (red) and anti-clockwise (green) paths in the disorder. If these paths interfere coherently, the return probability ($I = |A_+ + A_-|^2 = 4|A|^2$) is twice larger than an incoherent sum over the two paths ($I = |A_+|^2 + |A_-|^2 = 2|A|^2$) where A is the amplitude for a given path. This increase in return probability has an associated reduction in transport called weak localization.

The dimensionality of the scattering medium is critically important to the behavior of localization. Again borrowing from the picture of weak localization and arguments from Bergmann [15] and Langer

and Neal [110], interference is necessarily stronger in lower dimensions. Considering the formation of self-interfering loops from the perspective of random walks, one must ask what the return probability is for a random walk. This probability diverges for 1D and 2D systems, while remaining finite for dimensions greater than 2; this implies that self-interference is infinitely strong in low dimensions and that localization will take on dimension-dependent behavior. Indeed, it is found that for uncorrelated disorder in 2 and lower dimensions, all waves become Anderson localized for arbitrarily small disorder, and localization is not guaranteed for $d > 2$. In systems such as the 3D speckle considered here, a mobility edge (or edges) in energy exists separating localized from extended states. This concept was formalized using the concept of the dimensionless Thouless conductance in the scaling theory of localization introduced by the "gang of four" in Ref. [2].

The field of Anderson localization is active, with hundreds of research articles published on the topic every year. Work on strong or Anderson localization began with a paper on the "Absence of diffusion in certain random lattices" by Phillip Anderson in 1958 [6] and has grown significantly through numerous theoretical advances and observations, as shown in Fig. 4.2. The majority of these works focus on theoretical or numerical treatments of the phenomenon and its role in observations in materials. Direct observations of the effect in the solid state are complicated by electron-electron and electron-phonon interactions, and it is only in the last twenty years that work with photons [30, 213, 183, 200, 148, 58, 108, 25], microwaves [52], acoustics waves [76], and more recently ultracold gases [177, 18] has allowed for detailed tests of localization and coherent backscattering in interaction-free environments. Reviews of Anderson localization can be found in [103, 2, 144, 203, 201, 113, 146, 107, 1] and in many other places. This chapter discusses localization in 3D with ultracold Fermi gases. Concurrent work with Bose gases can be found in Refs. [83, 82, 84, 184]. Anderson localization has recently been exploited to increase the resolution in endoscopic fiber imaging; disordered fiber bundles have been used to transmit an image localized in 2D in the random fiber to increase the resolution and minimize the pixelation present in these applications [89].

4.3 Observation of 3D Anderson Localization

We localize matter waves in a three-dimensional disordered potential produced from optical speckle in which both the properties of the speckle and the matter waves are controlled to explore dynamics and localization in three-dimensional disorder. This section details the experimental preparation to observe localization and the essential behaviors of the observations. This information is partially repeated from Ref. [100] with the inclusion of new measurements and comments where our understanding has improved or changed.

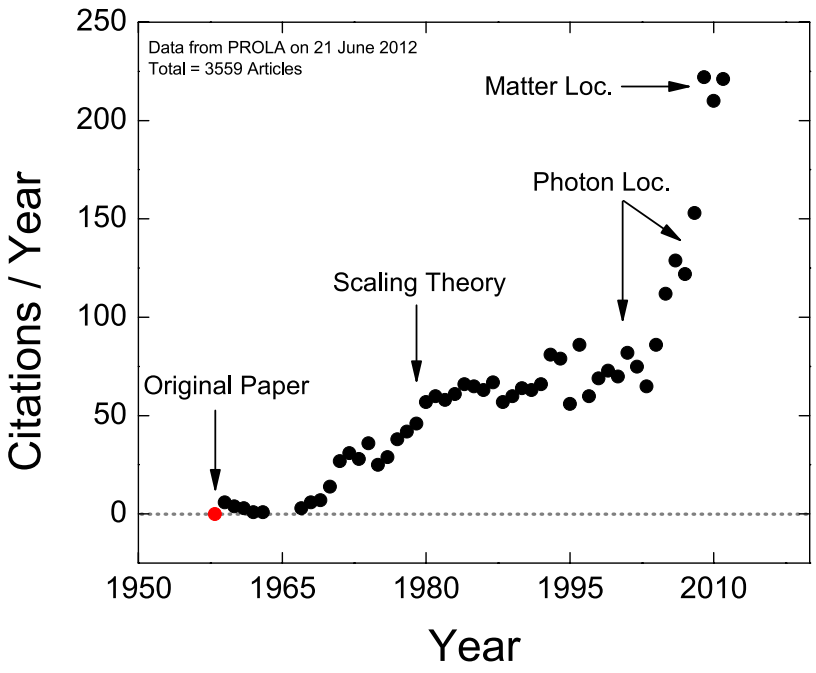

Figure 4.2: Timeline showing citations of Anderson's 1958 paper proposing disorder-induced localization. Citations of Ref. [6] are binned by year using data from the APS Journal Archive and important developments in the field are labeled. Use of only the APS archive underestimates the total number of citations by approximately a factor of two according to Google scholar.

Optical speckle provides a well characterized source of correlated disorder that is both easy to create and control. Chapter 3 provides a detailed introduction to the properties of speckle and the specific implementation employed for this work. To summarize that chapter, we create a three-dimensional speckle field from 532 nm light generating a repulsive potential characterized by its mean height, Δ, and the geometric mean of the RMS widths of the speckle intensity autocorrelation function, $\bar{\zeta} = (\zeta_x \zeta_y \zeta_z)^{1/3}$. Varying the effective numerical aperture of the speckle imaging optics allows for control of $\bar{\zeta}$ from 1.2 to 5.8 μm. The speckle potential exists in a finite volume of space, and the intensity is modulated by a gaussian envelope with a waist ($1/e^2$ radius) of 170 μm in the focal plane and a Rayleigh range of 400 μm along the axis of the focus. The power in the speckle beam is actively stabilized to minimize the statistical uncertainty in Δ between measurements. Within experimentally available parameters, values of Δ between 0 and 1000 $k_B \times nK$ are achieved. A number of systematic errors, including the size of the speckle envelope and total power at the atoms, contributes to a 40% systematic uncertainty in Δ.

A spin-polarized gas of ultracold ^{40}K atoms is our source of non-interacting matter waves. The atoms are prepared at temperatures from 170 to 1500 nK using standard cooling techniques described in Chapter 2.1 and are composed of the $|F = 9/2, m_F = 9/2\rangle$ and $|F = 9/2, m_F = 7/2\rangle$ spin states in ^{40}K. The $m_F = 7/2$ atoms are removed after cooling to create a non-interacting, spin-polarized gas. S-wave collisions are

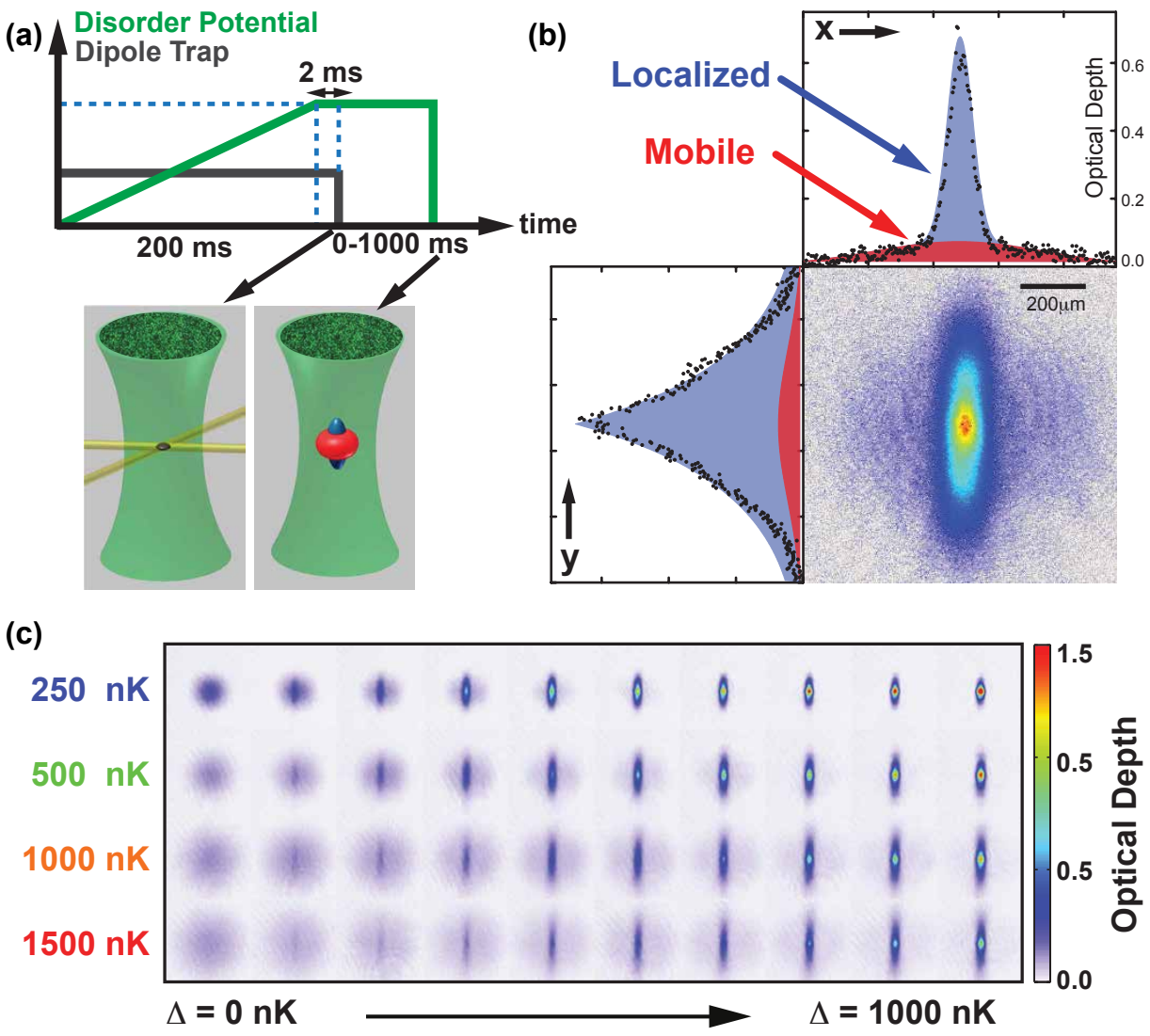

Figure 4.3: Experimental procedure for observing dynamics and localization in the speckle potential. (a) Atoms are loaded into a speckle potential while in a crossed-beam optical trap. The trap is suddenly removed and the atoms are allowed to expand into the speckle for a hold time from 0 to 1000 milliseconds. (b). A two-component profile is observed composed of localized and mobile atoms. The mobile component (red shaded area) expands quasi-ballistically, and the localized component (blue shaded area) assumes a fixed profile in time. (c) Time-of-flight images at 20 ms showing the emergence of an anisotropic localized profile as disorder is introduced for four different temperature gases.

forbidden in the polarized gas due to quantum statistics, and energetics suppresses p-wave and higher angular momentum collision channels. The p-wave cross section scales as T^2 below the p-wave barrier at 130 μK, and at 200 nK the single-state p-wave scattering cross section is 10,000 time smaller at 200 nK than the s-wave cross section between two different spin states [42]. Single-state spin polarization is achieved at an efficiency greater than 65:1. Effects of quantum degeneracy and Pauli blocking are minimal, as the ratio of the temperature to the Fermi temperature is at least 0.5 for all data and the gas can be well approximated by

Boltzmann statistics. Since the gases are thermal, they contain a continuous distribution of single-particle energies and deBroglie wavelengths $\lambda_{dB} = h/\sqrt{2\pi m k_B T}$. For the temperatures explored here of 170 to 1250 nK, the mean λ_{dB} varies from 620 to 250 nm.

The experimental sequence for observing localization is shown in Fig. 4.3. The non-interacting, spin-polarized gas is held in a harmonically confining dipole trap, and the speckle potential is introduced using a linear ramp of the 532 nm laser power over 200 ms to the fixed value corresponding to the required Δ. After a 2 ms delay, the dipole trap is suddenly removed and a magnetic gradient field is applied to balance the atoms against gravity using the coil detailed in Section 2.3.3. The atoms are allowed to expand into the speckle potential for a hold time, τ, up to $1s$. At the end of this period, a column-integrated, absorption image is taken of the density profile in the speckle. Sample density profiles are shown in Fig. 4.3 for different gas temperatures and disorder strengths for $\tau = 20ms$. A bimodal behavior is observed composed of mobile and localized atoms. The mobile component of the gas expands in an isotropic, quasi-ballistic fashion from the in-trap position with a thermal velocity that exceeds that of the parent gas. The localized component expands briefly and then assumes a fixed, anisotropic profile in time. We interpret the division between the two components as a mobility edge and the localized component as a truncated thermal average of single-particle Anderson localized states in the speckle potential.

The localized gas takes on a shape set by the in-trap spatial distribution and the dynamics within the disorder. Profiles of the gas in Fig. 4.4(a) at τ of 0, 40, and $140ms$ show the in-trap density profile and the shape of the localized profiles without the mobile component—here the mobile component has been subtracted or has sufficiently low optical depth to be ignored. The localized profile in the x-direction is minimally broadened from the in-trap Gaussian distribution. Nominal values for the in-trap RMS widths of the gas are $\sigma_x \approx 30\mu m$ and $\sigma_y \approx 15\mu m$, and the observed profile widths are within a few microns of the non-disordered values in the x-direction. As such, the localization lengths in this direction are interpreted to be much smaller than the trapped size of the gas. Along the y-direction, the axis of the speckle focus, the localized gas extends over several hundred microns. The gas expands initially and then assumes a profile with a fixed shape. The amplitude of the profile decays in time as atoms slowly leave the localized component, and the density profiles are seen to differ only by a scaling factor during this process as shown by the profiles at 40 and $140ms$ in Fig 4.4. The profiles appear exponential in shape along the y-direction. Single-particle Anderson localized states are generically expected to have exponentially decaying envelopes, but interpretation of the observed profiles is complicated by the truncated thermal distribution of single-particle states of which they are composed. Several predictions for this shape from weak scattering theory are discussed at the end of this chapter. Each density profile is fit to a heuristic surface fit to extract the

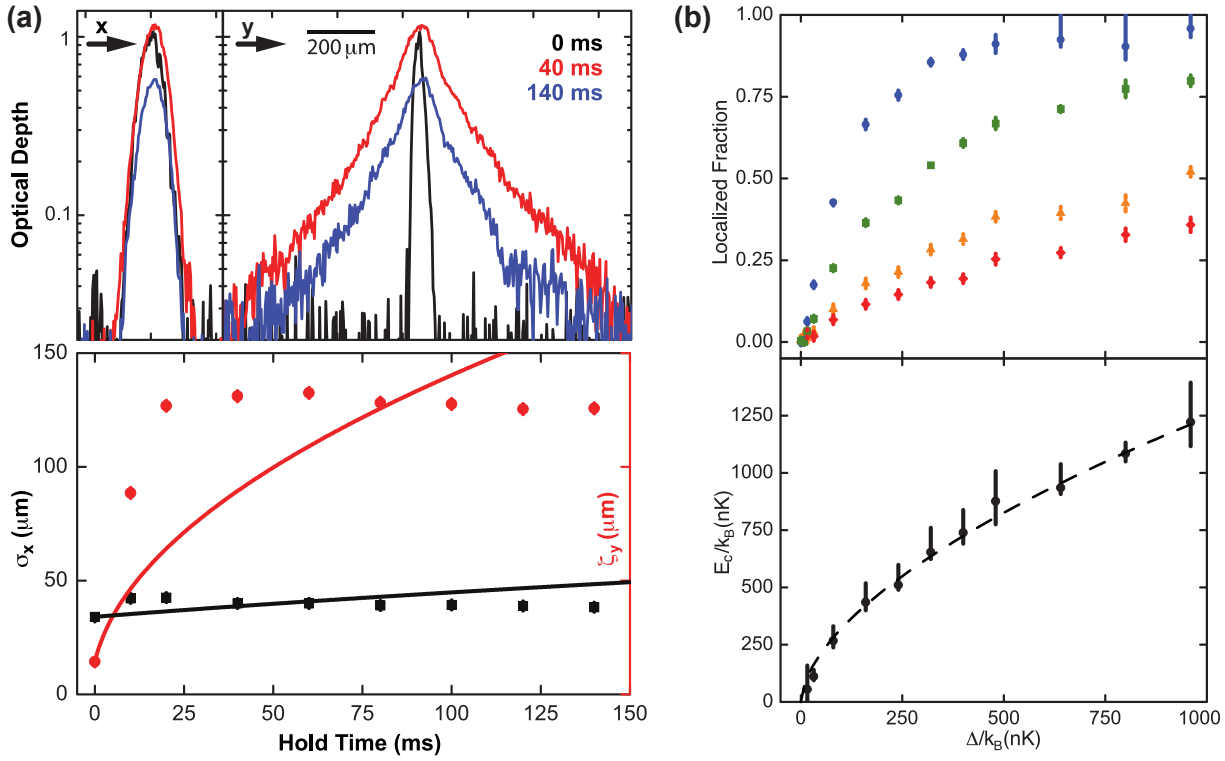

Figure 4.4: Details of the localized gas density profile and fraction of atoms localized. (a) The upper graphs show slices through the gas along the x- and y-directions for hold times in the disorder of 0, 40, and 140ms. The black line at 0 ms hold time indicates the in-trap size of the gas and its optical depth has been scaled by a factor of 15 so that it can be shown on the same scale. Slices show that the density profile adopts an exponential profile along the y-direction, while little motion is observed in the x-direction. The localization length and rms size are plotted versus hold time in the speckle potential. The localization length along y and the rms size along x quickly adopts stationary values. Solid lines are classical expansion dynamics predicted by solving Newton's equations in speckle and differ greatly from the observed data. (b) For localization data taken at various temperatures and disorder strengths, the fraction of atoms in the localized state is measured using a two-component fitting procedure for 240 nK (blue circles), 480 nK (green squares), 1130 nK (orange triangles), and 1470 nK (red diamonds) measured after 20ms hold time. These four data sets are converted to a mobility edge through the known energy distribution. Error bars indicate the range of values found. The dashed line is a power law fit with exponent of 0.59 $\pm$0.02.

RMS size of the gas along the y-direction to provide a metric representative of the size of gas. The fitting procedure is described in detail in the following section.

Interpretation of the localization length data is complicated by the range of single-particle energies and localization lengths in the gas. The fraction of atoms f that are localized by the disorder depends on the average disorder potential and the temperature of the gas. Data shown in Fig. 4.4(b) for $\bar{\zeta} = 1.2\mu m$ show the fraction of atoms in the localized state at $\tau = 20$ ms. The single-particle energy distribution for each gas is known via imaging the momentum distribution of the gas after release from the trap. Using the free particle density of states $g(\epsilon)$ and the Boltzmann distribution of energies, we find the mobility edge E_c as

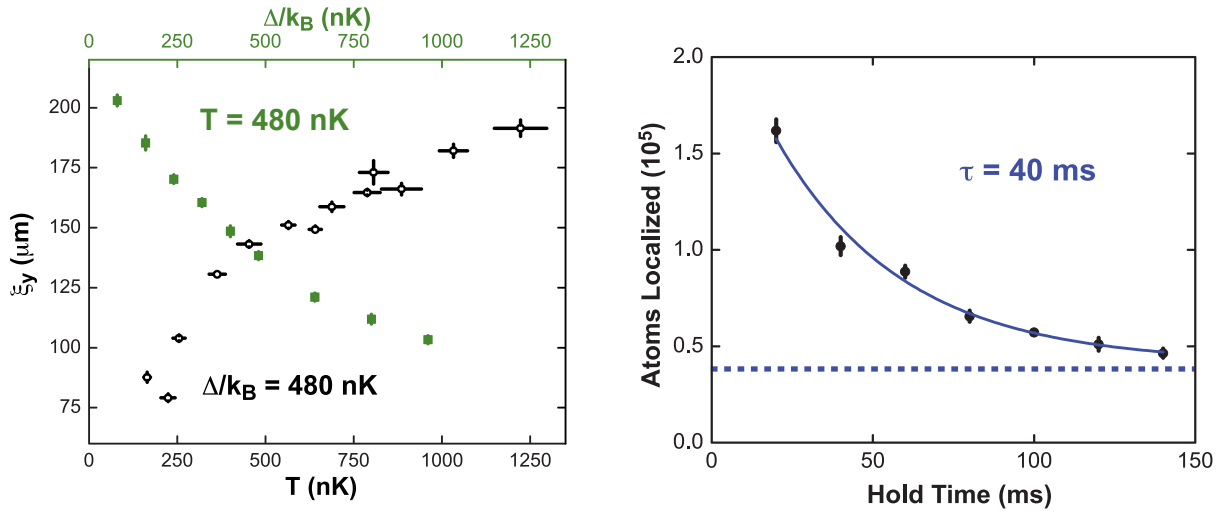

Figure 4.5: Scaling of localization length with temperature and disorder strength, and details of the decay of the localized state. (a) Scaling of localization length with temperature at fixed disorder strength (open circles) and with disorder at fixed temperature (green squares). (b) Decay of the localized state in hold time. The total number of atoms in the localized state exponentially decreases with a finite offset.

the cutoff required to match the measured f:

$$f = \frac{\int_0^{E_c} g(\epsilon)\ P(\epsilon) d\epsilon}{\int_0^{\infty} g(\epsilon)\ P(\epsilon) d\epsilon} = \frac{2}{\sqrt{\pi (k_B T)^3}} \int_0^{E_c} \sqrt{\epsilon}\ e^{-\epsilon/(k_B T)}\ d\epsilon. \tag{4.1}$$

This procedure is used to find the critical energy for each measured fraction of localized states in Fig. 4.4 for the four separate temperatures probed. The four sets of critical energies collapse onto a single curve with a power law scaling of $E_c \propto \Delta^{0.59\pm0.02}$. Predictions from self-consistent Born approximation and weak-scattering theory calculations suggest a scaling of $E_c \propto \Delta^2$ [216, 106, 164]. Differences may arise from detailed properties of scattering in our speckle geometry or failures in the approximations employed in these calculations, as discussed in Sec. 4.9. The expected trends that the localization length should decrease with increasing disorder and decreasing temperature are both present as shown in Figure. 4.5. Direct comparison with theory is possible due to the known thermal energy distribution in the gas, but thermal averaging complicates direct interpretation of the single-particle behavior.

4.4 Fitting Procedure for Localized Gas

To extract length scales and populations of the mobile and localized gases, the optical depth images acquired after expansion in the speckle potential are fit to a two-component density profile. The mobile component contains high energy atoms that expands quasi-ballistically and are fit to a 2D gaussian. The localized

component's density profile is a convolution of the in-trap size of the gas with a thermal distribution of localized states below a critical energy. Due to the anisotropy of the speckle potential, the gas is observed to expand appreciably only along the axis of the speckle. The localized profile is fit to a function, $\rho_{\mathcal{L}}$, that is Gaussian in the x-direction and a stretched exponential in the y-direction. The optical depth of the image, $\mathcal{OD}$, is the sum of the localized and mobile component distributions, $\rho_{\mathcal{L}}$ and $\rho_{\mathcal{M}}$:

$$\mathcal{OD} \;=\; \rho_{\mathcal{M}} + \rho_{\mathcal{L}} \quad \text{where} \quad \begin{cases} \rho_{\mathcal{M}} = \; \mathcal{OD}_{\mathcal{M}} \; \exp\left(-\frac{x^2}{2\sigma_x^2} - \frac{y^2}{2\sigma_y^2}\right) \\ \rho_{\mathcal{L}} \;=\; \mathcal{OD}_{\mathcal{L}} \; \exp\left(-\frac{x^2}{2\sigma_x^2} - \left|\frac{y}{\xi_y}\right|^{\beta}\right). \end{cases} \tag{4.2}$$

The stretched exponential allows the shape of the localized fitting function to evolve continuously from the in-trap Gaussian profile ($\beta = 2$), to a simple exponential ($\beta = 1$), and to a localized profile with stretched tails ($\beta < 1$). The RMS size of the gas is related to the stretched localization length, ξ_y and the stretched exponent β as

$$\sigma_y = \xi_y \sqrt{\frac{\Gamma(1+3/\beta)}{3\;\Gamma(1+1/\beta)}}. \tag{4.3}$$

Here $\Gamma(h)$ is the Gamma function of argument h. The relation between ξ_y and the RMS size is a numerical prefactor that depends on β. For $\beta = 2$ (gaussian) $\sigma_y = \xi_y/\sqrt{2}$, for $\beta = 1$ (simple exponential) $\sigma_y = \sqrt{2}\;\xi_y$, and for $\beta = 0.5$ (extremely stretched exponential) $\sigma_y = 30\sqrt{30}\;\xi_y \approx 11\xi_y$.

This two-component fitting function captures much of the observed shape of both the mobile and localized components, but it must be emphasized that the fitting function for the localized component is entirely heuristic. The goal of the fitting procedure is to extract a length scale from the density profile (namely the RMS size of the gas), and the simplest functional form that described the shape of the data was chosen. The RMS size of the gas can also be extracted from the image directly ($\sigma = \sqrt{\sum x^2 f(x) / \sum f(x)}$) with no assumption on the shape of the gas. Pixel shot noise in regions of low signal and high x^2 prevents a stable value of the second moment from being found as the averaging window size is varied. This motivates the use of a fitting function and requires a functional form to be chosen.

Without a detailed simulation of scattering and localization in a speckle potential, it is not possible to predict the thermally averaged density profile of the gas. The stretched exponential fit captures much of the shape of the gas, and it is possible to construct this profile from a weighted sum of simple exponentials ($\beta = 1$). Column integration in the imaging procedure adds complexity in relating the density profile of the gas to theory. For example, in the case of simple exponential ($\beta = 1$) density profiles (as might be expected for localization), the observed line-of-sight integrated image becomes rounded at the origin and broadened

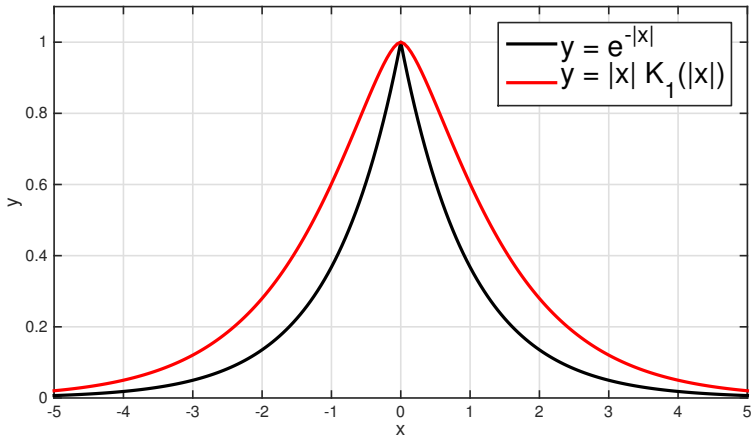

Figure 4.6: Comparison of an exponential profile before and after column integration. Fine detail such as the sharp peak in the exponential profile (black line) is obscured by column integration and the column-integrated profile (red line) appears wider than the underlying distribution. These effects complicate interpretation of the observed density profiles and comparison with theory.

by the column integration as shown in Fig. 4.6. The exponential density profile after column integration in the $z-$direction is as

$$\mathcal{OD}(x) \;\propto\; \int_{-\infty}^{\infty} e^{-|\mathbf{r}|} dz \;=\; 2\,|x|\,K_1\left(|x|\right), \tag{4.4}$$

where $K_1(x)$ is the modified Bessel of the first kind of argument x.

4.5 Localization in Variable-Scale Speckle

The central point of this chapter is to discuss localization in speckle disorder of variable scale. Localization in three dimensions is controlled by the interplay of the particle's wavelength and the Boltzmann mean-free-path. In the speckle disorder explored here, the mean free path is a function of both the disorder potential energy and correlation properties, as described in Sec. 4.8. We perform experiments with a fixed, thermal distribution of single-particle wavelengths and fixed mean disorder height to measure the role of the speckle correlation length in controlling the onset of localization and the localization length scale. The role of correlation in disordered potentials is an area of active research, and measurement of this scaling is an important test for theory. Measurements presented here are distinct from experiments on the localization of light in three-dimensional semiconductor powders [213, 191, 127], as spatial correlations in the speckle disorder are important and absorption in the scattering medium is absent.

Experiments using variable-scale speckle were performed with a fixed temperature gas and a fixed mean disorder potential energy while the geometric mean correlation length was varied by a factor of 4. A spin-

polarized gas of ^{40}K atoms in the $|9/2, 9/2\rangle$ state was prepared in an optical trap at a temperature of 174 $\pm$ 4 nK and trap frequencies of $\omega_x = 2\pi 25Hz$ and $\omega_y = \omega_z = 2\pi 95Hz$. The mean speckle potential energy Δ was set to 220 $k_B \times nK$. The correlation length was varied by reducing the illumination of the speckle imaging lens with circular apertures of diameters from 3.6 to 13 mm. At each value the total optical power transmitted through the focusing lens was fixed and the input power adjusted based on the known beam waist and aperture diameters. Correcting the beam power with aperture diameter introduces a 10% statistical uncertainty in Δ between disorder realizations. A 40% systematic uncertainty in Δ also exists as discussed in Sec. 3.4. The statistical uncertainty in Δ is negligible for the interpretation of data here due to the weak scaling with disorder amplitude as shown in Fig. 4.5.

The apertures allowed for variation of the f/# of the imaging system from 1.1 to 4. The speckle correlation length as measured by the $1/e^2$ radii of the intensity autocorrelation function varied from $\zeta_x = 0.6$ to 1.8 microns and $\zeta_z = 3.1$ to 37 microns, while the geometric mean spanned from $\bar{\zeta} = 1.1$ to 4.8 microns. The envelope of the speckle potential has a roughly Gaussian profile in the focal plane with 170 micron waist independent of the aperture diameter set by the diffuser angle and the focal length of the speckle imaging lens. The Rayleigh range along the axis of the speckle focus varies from 400 to 1200 microns, linearly growing in proportion to the f/# of the imaging system. Other details of the speckle potential are covered in Chapter 3, including ex-situ measurements of the variable scale speckle and a detailed description of the intensity autocorrelation function.

Representative data exhibiting localization in variable-scale speckle are shown in Fig. 4.7. These data are similar to the fixed correlation data presented in Sec. 4.3, in which the size of the localized gas is fixed at the in-trap value in the x-direction and grows in the y-direction in time until a stable profile is reached. The size of the localized component grows with the disorder correlation length, and the shape of the gas changes from close to exponential behavior observed in the $\bar{\zeta} = 1.2\mu m$ data. The density profile of the gas develops longer tails as the correlation length grows, and a stretched exponential fit was employed to describe the shape of the data and extract the RMS size of the gas in the y-direction. Localization in this potential is again interpreted from measurements of the axial RMS size of the gas in time. For each correlation length probed, the gas expands initially with an RMS size that grows linearly in time until a plateau is reached and the size is roughly constant over a period of several hundred milliseconds. The transient period of expansion increases with disorder correlation length and corresponds to a thermal velocity of 480 nK, more than a factor of two higher than the temperature of the gas.

Reduced data from the eight correlation lengths explored shows scaling of the axial RMS size, the fraction of atoms localized, and the shape of the gas versus $\bar{\zeta}$ in Fig. 4.8. Stable values for each correlation length are

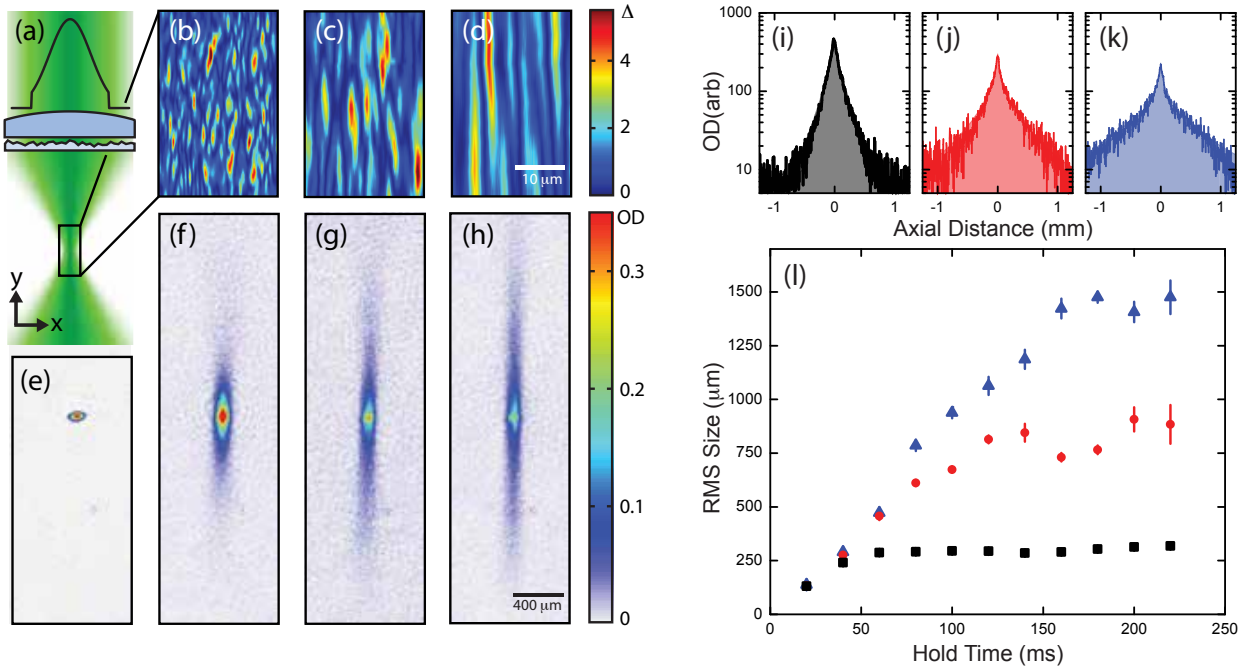

Figure 4.7: Summary of localization and dynamics in variable-scale speckle. (a) Imaging geometry used to control optical speckle correlation length with a variable aperture, high numerical aperture lens, and diffuser. (b-d) Measured speckle intensity field in the axial-transverse (x-y) plane near the focus, reconstructed from ex situ 3D scanning. (e) In-trap density profile of the gas before release into the speckle potential with imaging laser detuned to limit probe beam saturation. (f-g) Images of the gas after expanding in the speckle potential for $\tau = 160$ ms, showing that the size of the localized state grows with speckle correlation length. (i-k) Slices through the density profiles in (f-h) show how the shape of the localized gas evolves as the speckle correlation length is changed. (l) The RMS size of the gas is extracted using the fitting procedure described in Sec. 4.4 to show the dynamics as the localized state forms. At each correlation length, there is a period of quasi-linear expansion followed by a plateau of the RMS size. The speckle correlation length for the data are $\bar{\zeta}$ of 1.2, 2.4 and 3.8 μm for (b)(f)(i) black squares, (c)(g)(j) red circles, and (d)(h)(k) blue triangles, respectively. The temperature of the gas is 175 nK and $\Delta = 220\ k_B \times nK$.

found by averaging over measurement taken at τ from 160 to 220 ms where there is a plateau in σ_y for all data. For these data, the correlation length grows roughly linearly with $\bar{\zeta}$, and a power law fit through the data finds $\sigma_y \propto \bar{\zeta}^{1.22\pm0.06}$ as shown in Fig. 4.8. The fraction of atoms localized at each value of $\bar{\zeta}$ is roughly constant at 30% at $\tau = 160$ ms. This indicates that the single-particle mobility edge is roughly constant across the range of correlation lengths probed, and the distribution of single-particle energies that form the localized gas can be approximated as constant. This allows for comparisons to be made of the observed, thermally averaged length scale. Weak scattering theory predicts that the single-particle localization lengths should scale as $\zeta E^2/\Delta^2$ in the limit where the wavelength is much larger than the inverse speckle correlation length and the particle energy much less than the mobility edge, E_c. The atomic wavevector is estimated at $\lambda_{dB} \approx 700\ nm$, which is smaller than the range in $\bar{\zeta}$ employed in this measurement. The decay from the localized states is similar over the range of correlation lengths probed. Fig. 4.9 shows the fraction localized

as a function of time for three representative correlation lengths—each decays from a maximum localized fraction near 70% to 30% over a period of 200 ms. Surprisingly, there is no discernible variation across the data set, indicating that leakage likely occurs uniformly across the gas and not in the tails of the distribution where the largest variation in the disorder potential envelope is seen.

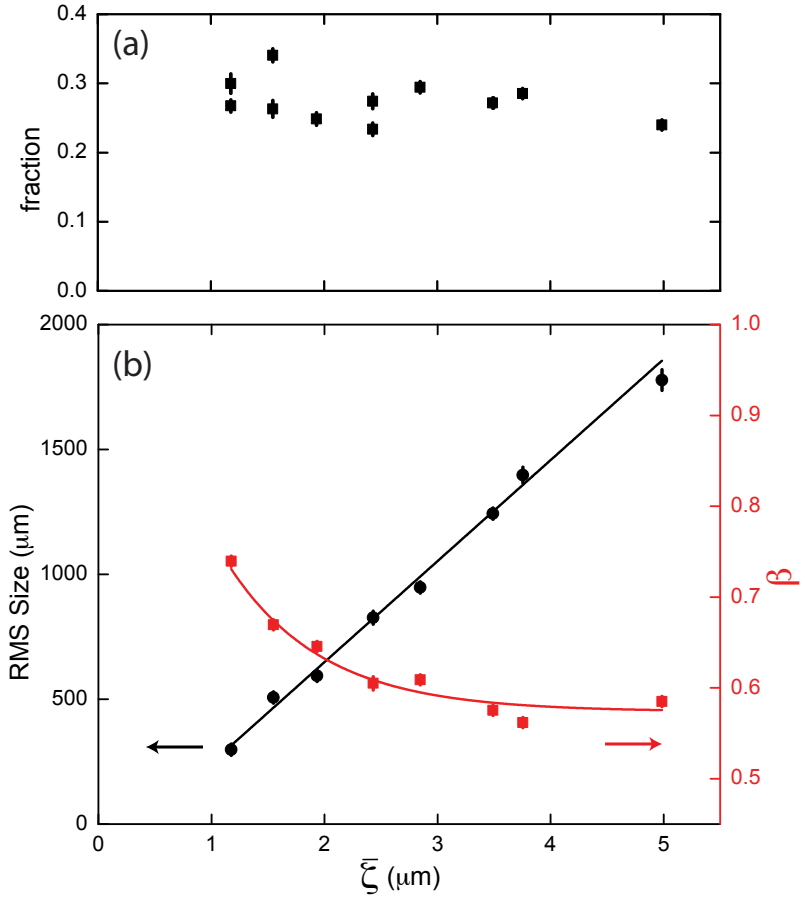

Figure 4.8: Summary of localized component size and population as the speckle correlation length $\bar{\zeta}$ is varied from 1.2 to 5 μm. (a) The fractional population in the localized component measured at $\tau = 160$ ms is measured to be approximately 30%, independent of the correlation length for the parameters explored. (b) The RMS size is measured to grow with $\bar{\zeta}$ as the stretched exponent, β, from the fitting procedure decreases. Error bars indicate the standard error of the mean and each point is the average of 20 measurements.

4.6 Quench of the Localized Density Profile

The spatial extent of the localized profiles we observe are much larger than predicted by weak scattering theory, as discussed in Sec. 4.8. The density distributions are averaged over several 10^5 atoms, and it is natural to ask whether the size of the single-particle states is comparable to the thermally averaged profile or not. Each single-particle wavefunction is expected to have an exponentially decaying envelope in space, and

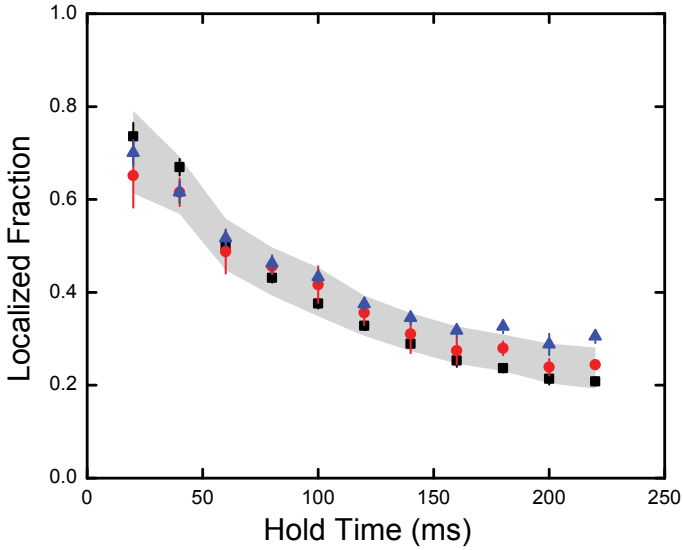

Figure 4.9: Fraction of atoms in the localized component for variable-correlation length data. Data are $\bar{\zeta}$ of 1.2 (black squares), 2.4 (red circles) and 3.8 (blue triangles) μm, the same colors as in Fig. 4.7. The gray band contains the scatter from all 8 data sets.

two simple interpretations could explain the observed profiles. First, the single-particle states could possess localization lengths comparable to the observed σ_y with largely overlapping spatial profiles centered on the in-trap position of the gas. In this case, the observed profile would be a thermal average of the single-particle localized states. Second, the single-particle localization lengths are comparable to $\bar{\zeta}$ with mean positions sparsely distributed in space. In this scenario, σ_y is indicative of the dynamics as the localized state is formed in the speckle.

To distinguish between these scenarios we perform a quench of the localized density profile that removes a quarter of the atoms from the gas in a spatially-selective manner and observe the resulting dynamics. This measurement is performed with a spin-polarized gas at 220 nK with disorder correlation $\bar{\zeta} = 1.2\ \mu m$ with amplitude $\Delta = 660\ k_B \times nK$. The gas is allowed to evolve in the speckle for 60 ms such that the localized profile has time to fully develop. A chirped microwave-frequency magnetic fields is applied over 2 ms to drive a portion of the $|9/2, 9/2\rangle$ atoms for $y > 0$ to $|7/2, 7/2\rangle$ via adiabatic rapid passage. Spatial selectivity is provided by the gradient magnetic field used to levitate the $|9/2, 9/2\rangle$ atoms. Atoms in $|7/2, 7/2\rangle$ are accelerated at 16/9 g and leave the region of interest in the experiment within 7.5 ms. To quantify the asymmetry of the gas, we fit the lower and upper half of the gas separately to a simple exponential profile to obtain exponential decay lengths $\xi_y^>$ and $\xi_y^<$ for $y > 0$ and $y < 0$, respectively. Similarly, occupation in the two halves of the gas is measured as $N_>$ and $N_<$.

The results of the density quench are shown in Fig. 4.10. The length scale for the quenched half of the gas

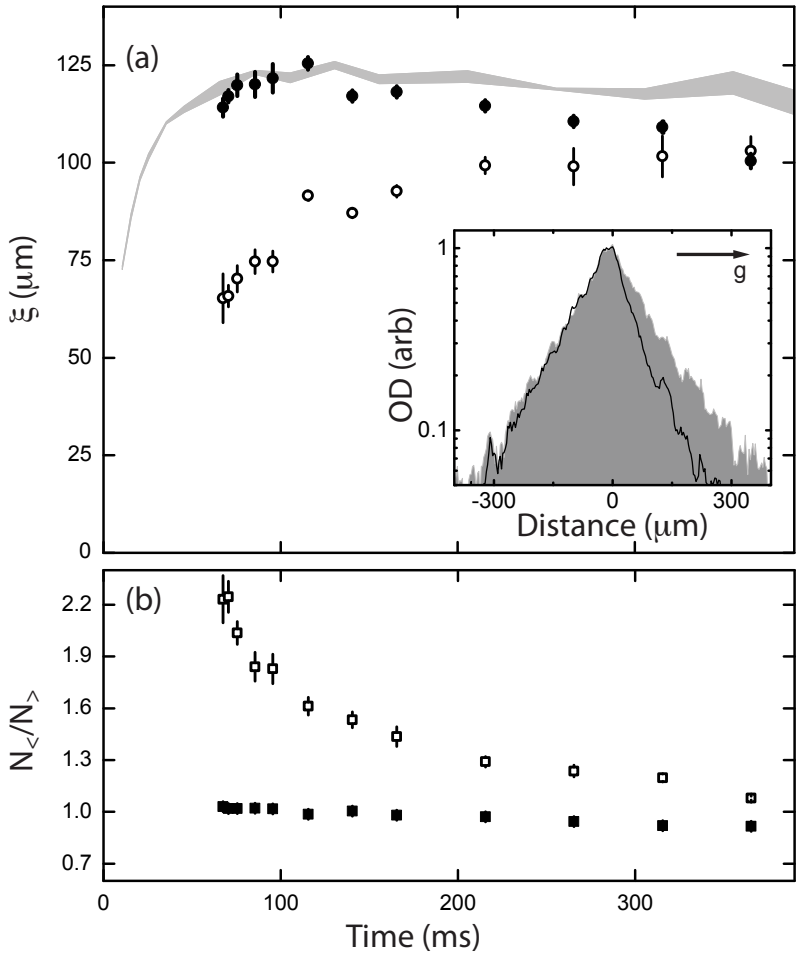

Figure 4.10: Quench of the localized density profile and dynamics showing reformation of the localized state. (a) A microwave sweep is applied at $\tau = 60$ ms that removes a portion of the upper half of the gas (y $>$ 0). Each half of the gas is fit independently with a simple exponential, and the length scales are plotted as function of time. Open circles, $\zeta_y^<$, indicate data for y < 0 and closed circles, $\zeta_y^>$, for y > 0. The gray band shows symmetric localization length without the quench applied. The inset shows the optical depth along the y-direction for the unperturbed (grey) and quenched (black line) gases at $\tau = 60$ ms. (b) Occupation ratio of the lower and upper half of the localized for the quenched (open squares) and unperturbed (filled squares) gases.

$\xi_y^>$ drops by a factor of two from its unperturbed value immediately after the quench. The gas then exhibits a slow relaxation toward the unperturbed, fixed value of ξ_y as it slowly redistributes over 300 ms. The values of $\xi_y^>$ and $\xi_y^<$ converge at long times indicating transport of atoms between the two halves. This transport is also evident in the plot of the population ratio between the two halves, $N_</N_>$ which starts near 2 following the quench and approaches unity, again over a period of several hundred milliseconds. The long-time symmetric length scale after the quench tends to a value slightly smaller than without the quench. From these data we can rule out the scenario of small, spatially-sparse localized states. Under this scenario, the single-particle states uninvolved in the quench would have been unaffected, and no reëquilibration would have been seen.

Conclusively confirming (or disproving) the large localization length scenario is unfortunately not possible with this data. Further energy-resolved studies that avoid the problem of thermal averaging are required before firm conclusions should be drawn. Of note is the timescale of reëquilibration and the residual trapping from the magnetic gradient coil (see Sec. 2.3.3); both are of order several hundred milliseconds. The degree to which these are related is currently unknown. The energy scale of the residual trapping potential along they y-direction over 1.5 mm is similar to the temperature of the gas, but this force does not explain the majority of the short-time dynamics observed. The exact interplay of this residual magnetic potential and localization should be explored using techniques similar to Ref. [40].

4.7 Applying a Force to the Localized Gas

As a subsequent test of the localized states in speckle, an external force was applied to a localized gas. The goal of this measurement is to observe the fraction of atoms that remain localized and the dynamics after the force is applied. This experiment was performed using the same techniques as the previous localization measurements. A 250 nK, spin-polarized gas was released into the speckle potential with $\bar{\zeta} = 1.2\mu m$ and $\Delta = 1000\ k_B \times nK$ with a gradient magnetic field applied to balance the force of gravity. The external force was applied by reducing the levitation magnetic field gradient to recover a set fraction of the gravitational force. Absorption images of this procedure are shown for forces equivalent to 0, 0.08, and 0.16 of gravity in Fig. 4.11. The mean disorder potential, correlation length, and the gas temperature were chosen near experimental extremes to create a small initially localized gas with minimal spatial variation in the magnetic gradient.

The dynamics after applying a force to the localized gas presents an interesting story. In the case where no force is applied, the same behavior is seen as in previous measurements. Atoms slowly leak out of the localized profile over a period over several hundred milliseconds while the shape of the gas is essentially fixed in time. The timescale for atom loss here is longer than the value observed in Fig. 4.9 due to the larger value of Δ employed. For the case of a weak applied force, as in Fig. 4.11(b), the shape of the gas changes dramatically in time as atoms away from the central peak are preferentially stripped from the localized state. At long times, the gas shrinks dramatically along the y-direction and assumes a shape similar to the in-trap density profile (as shown in Fig. 4.7). The effect is more pronounced for a larger applied force, and the rate at which atoms are stripped from the localized gas increases with the remaining atoms assuming a shape that mimics the in-trap profile. The stability of the remaining localized atoms in Fig. 4.7(c) where $F/mg = 0.16$ is higher than observed in other localized gases, indicative of their smaller spatial extent.

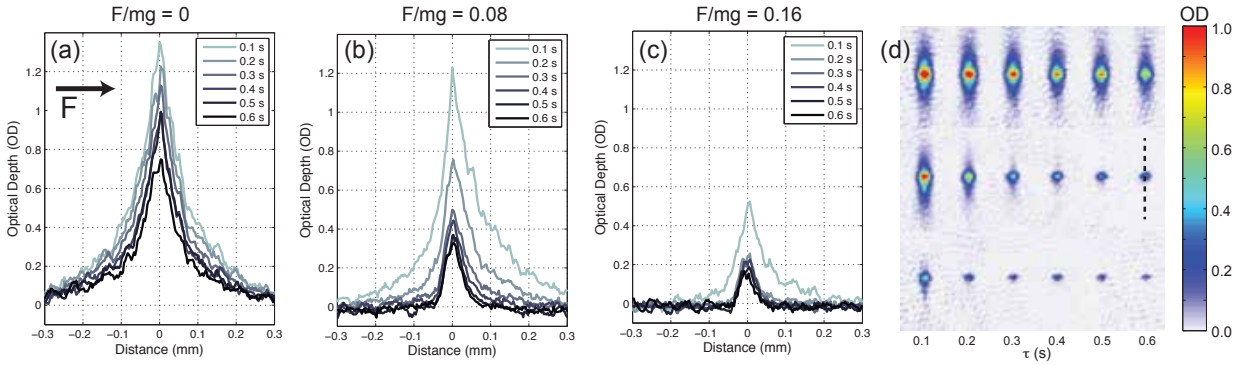

Figure 4.11: Applying a DC force to the localized gas. A 250 nK gas was released into speckle with $\Delta = 1000$ $k_B \times nK$ and $\bar{\zeta} = 1.2\mu m$. Applying a force causes atoms that are more weakly localized to be stripped from the localized state and leave the field of view. (a-c) Vertical slices through the gas are shown for $\tau = 0.1$ to 0.6 s in the speckle with applied force $F/mg = 0$, 0.08, and 0.16. The slice is taken through each profile, as indicated by the dotted line in (d). (d) Absorption images showing the dynamics in the presence of a uniform force for $F/mg = 0$ (top row), 0.08 (middle row), and 0.16 (bottom row).

These measurements imply that atoms with longer correlations lengths are more weakly localized and can be easily stripped from their localized states with an applied force. One expects states proximal to the mobility edge with long localization lengths to be less strongly localized, as large phase gradients can accumulate across their wavefunction. Analogously, lower energy atoms with shorter localization lengths are more likely to remain localized in the presence of an applied force. Future studies of localization without fine energy resolution could use this technique to strip away atoms with large spatial extent that may be sub-diffusive or marginally localized. The applied force could then be removed, and the dynamics of the remaining atoms studied. These data also provide insight into the role the non-uniform levitating force plays in the measurement. The minimum applied force in this measurement is more than a factor of ten larger than the non-uniformity in the force from the magnetic levitation coil, but these data imply that a small fraction of the localized atoms will be stripped out of the localized component by the residual force. For the sub percent variation in the levitation field, this effect is likely to only be relevant at the longest time scales measured.

4.8 Comparison with Theoretical Predictions of 3D AL

4.8.1 Müller & Shapiro Result

Müller and Shapiro present a simple argument that suggests stretched exponential density profiles used to described the observed localized profiles can arise from diffusive dynamics in speckle with generic, power law scaling of the diffusion constant with energy. This sections summarizes their Comment [147] and our Reply

[132]. First, Gaussian density profiles under diffusive expansion evolve without changing shape; their RMS size grows as the square root of time, $\sigma(t)^2 = \sigma(0)^2 + 2Dt$. Integrating over a Boltzmann energy distribution, the size in time can be expressed as

$$n(\vec{r},t) = C\int dE \frac{\nu(E)}{(4\pi D_E t)^{d/2}} \mathsf{exp}\left(-\frac{r^2}{4D_E t} - \beta E\right), \tag{4.5}$$

assuming zero initial size. Here $\nu(E)$ is the density of states, C is a normalization constant, and D_E is an energy dependent diffusion constant. Under the assumption of a power law scaling of the diffusion constant, $D_E \propto \hbar E^a/m$, and the density profile will be sharply peaked in the center due to slowly diffusing atoms. Long tails will form, composed of the higher energy particles with their associate higher diffusion constants. Of note from this comment is the limiting functional form for the density in the tails of the distribution which takes the following form:

$$n(\vec{r},t) \sim \mathsf{exp}\left(-|r/s(t)|^{2/(a+1)}\right). \tag{4.6}$$

Here $s(t)$ provides a length scaling as a function of energy, temperature, and time. This form of $n(\vec{r},t)$ is a stretched exponential with the stretched exponent $\beta = 2/(a+1)$. Müller and Shapiro propose a weak-scattering scaling of $D(E) \propto E^{5/2}$ similar to the findings in Ref. [164] which results in $\beta = 4/7$, not dissimilar from the value of β found in Fig. 4.8.

The key point made in the Reply to Müller and Shaprio's comment is that the stretched exponential fitting function is a convenient tool used to extract the RMS size from noisy data, and this model is not necessarily representative of the underlying shape of the tails in the column integrated density profile. Use of the stretched exponential function was motivated by the ease in representing the profile as it expanded from the in-trap Gaussian distribution and to describe the non-exponential profiles seen at longer correlation lengths as described in Sec. 4.4. To emphasize this point, a characteristic density profile from the tails of the distribution (data from Fig. 4.7(i)) was fit to both a simple exponential and a power law at distances greater than 300 microns from the gas center. These fits as shown in Fig. 4.12 demonstrate no quantitative difference in the goodness of two fits. Fits to a stretched exponential profile fail due to the low signal-to-noise ratio of the data.

Additional factors contribute to the complexity of the density profiles and their interpretation including anisotropy in the speckle correlation function, atom loss, line-of-sight integration, spatial variation in the speckle intensity, non-linear absorption in imaging, and residual confinement from the anti-gravity coil. Theoretical focus on this experiment would be better placed in exact simulations of the experimental details,

at minimum including a more complete picture of scattering in speckle. Comparison to the full expansion and stabilization of the density profile would also be productive in drawing conclusions from the data. Given the continuous distribution of energies present, one can expect that all phenomena from localization, sub-difussive transport, diffusive transport, super-diffusive transport, and ballistic transport to be present. All of these will complicate the interpretation of the tails of the distribution. Any future experiment to study the energy dependent behavior of localization would be well advised to use a narrower energy distribution than was possible in the above described experiments.

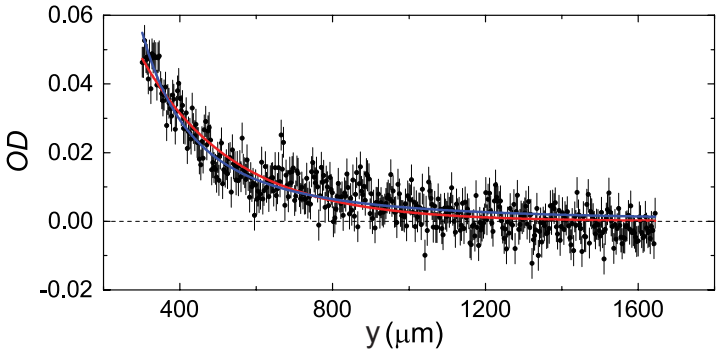

Figure 4.12: Tails of localized density profile compared to exponential and power law fits. The reduced χ^2 for the exponential fit (red data) for $y > 0$ and $y < 0$ are 1.09 and 1.14, and the reduced χ^2 for the power law fit (blue data) for $y > 0$ and $y < 0$ are 1.14 and 1.02. Data are repeated from Fig. 4.7(i) at greater than 300 microns from the center position, and error bars indicate the statistical uncertainty at each point.

A secondary point raised in this Comment relates to the large RMS sizes observed in the measurement. RMS sizes of the localized gas on the order of 1 mm are reported, and it is claimed that these length scales are only attainable for atoms in an energy interval proximal to the mobility edge where the localization length should diverge. Previous experiments in 1D [18] observed localization lengths also on the mm scale for similarly sized disorder, indicating that the Anderson localization can occur over several thousand speckle correlation lengths, similar to the observation presented here. Measurements presented here occur at higher temperature, disorder amplitude, and dimensionality. Interference, the origin of Anderson localization, is inherently weaker in 3D, and it is natural to expect longer localization lengths.

4.8.2 Kuhn and Müller Result

Work by Kuhn and Müller in Ref. [106] explores coherent matter wave transport in speckle potentials. In this work, a diagrammatic Green's function approach is used to calculate scattering and Boltzmann transport mean free paths in two- and three-dimensional speckle. Weak scattering from the potential is assumed. The speckle employed in this work is three-dimensional and isotropic with a potential autocorrelation function

$\langle V(r+\delta r)V(r)\rangle_r = sin(k_L\delta r)/(k_L\delta r)$, where k_L is the wavevector of the speckle light. This speckle is different than the anisotropic speckle we employed and can be generated from interference over a uniformly illuminated 4π solid angle. Here, the zero of potential energy has been chosen such that its mean value is zero, and the potential autocorrelation at large radii tends to zero instead of $\langle V_R\rangle^2$.

We extract scaling laws from Kuhn and Müller's theoretical treatment of localization to determine the localization length as a function of particle energy (E), correlation length ($\zeta = 1/k_L$), the disorder correlation energy ($E_\zeta = \hbar^2/m\zeta^2$), disorder amplitude ($\Delta$), Boltzmann mean free path (ℓ_B), and the elastic scattering mean free path (ℓ_s). Equations 41, 64, and 76 from Ref [106] shown below express the localization length in terms of these quantities:

$$\frac{1}{k\ell_s} = \pi\frac{\Delta^2}{E_\zeta^2}\left[\frac{1}{(k\zeta)^3}\Theta(k\zeta-1)+\frac{1}{(k\zeta)^2}\Theta(1-k\zeta)\right] \tag{4.7}$$

$$\ell_B = \frac{3}{2}\ell_s\left[(k\zeta)^2\Theta(k\zeta-1)+\Theta(1-k\zeta)\right] \tag{4.8}$$

$$L_{loc} = \frac{\frac{3}{2}\ell_B}{\frac{3}{\pi}-k^2\ell_b^2}. \tag{4.9}$$

Combining the above equations provides the scaling of the localization length L_{loc} in terms of Δ, ζ, and E; where Θ is the Heaviside step function:

$$L_{loc} = \begin{cases} \left[\frac{3}{4}\frac{\hbar^3\sqrt{2mE}}{\Delta^2 m^2\zeta^2}\Big/\left(1-\left(\frac{3}{\pi}\frac{\hbar^4E^2}{m^2\Delta^4\zeta^4}\right)\right)\right], & k\zeta<1 \\ \left[3\frac{E^2\zeta}{\Delta^2}\Big/\left(1-\left(\frac{24}{\pi}\frac{E^5\zeta^2 m}{\hbar^2\Delta^4}\right)\right)\right], & k\zeta>1. \end{cases} \tag{4.10}$$

For much of the variable correlation length data explored, $k\zeta > 1$ and the length scale of localization is predicted to scale linearly with ζ for $E^5/(E_\zeta\Delta^4) << 1$. We relate this theoretical result for isotropic disorder to our measurement in anisotropic disorder by comparing the scaling against the geometric mean of the correlation lengths employed, $\bar{\zeta}$. The variable scale data indicates a roughly linear scaling with $\bar{\zeta}$ as shown in Fig. 4.7 with $\sigma_y \propto \bar{\zeta}^{1.22\pm0.06}$. The validity of the Born approximation used to generate this scaling in Eq. 4.10 is discussed in detail in Sec. 4.9. How reasonable the comparison of the scaling against $\bar{\zeta}$ in an anisotropic medium to predictions from an isotropic theory is unknown, but numerical work beyond the Born approximation suggests that the exact shape of the correlation function is less relevant than its spatial extent [41]. Use of the geometric mean instead of, for example, the simple mean is standard in reducing an anisotropic quantity to an isotropic one.

Kuhn also proposed a simple geometric measure that relates the Boltzmann and scattering mean free

paths in an isotropic scattering medium. The ratio of these two quantities measures how quickly a system will lose memory of its initial state. For systems with no memory, the ratio is unity, as each scattering event erases knowledge of the previous state. For systems with only small angle scattering, the ratio can be large, and many scattering events are required to randomize the initial motion. The power spectrum of the scattering medium can be sampled over an elastic scattering sphere to determine the on-shell scattering rate as described in detail in Sec. 4.8.3, but this measure contains no information about the degree of randomness introduced by the scattering process. Anderson localization is governed by the Boltzmann mean free path rather than the elastic scattering mean free path, so understanding the relationship between these two quantities is critically important for understanding localization in speckle. Kuhn suggests that the average over the cosine of the scattering angles, weighted by the value of the speckle power spectrum at each angle, quantifies the degree of randomness introduced in scattering as

$$\frac{\ell_B}{\ell_s} = \frac{1}{1 - \left\langle \cos(\theta_{\mathbf{k}-\mathbf{k}'}) \tilde{C}(\mathbf{k}-\mathbf{k}') \right\rangle_{\boldsymbol{k'}}}. \tag{4.11}$$

Here $\boldsymbol{k}$ is the initial vector, $\boldsymbol{k'}$ is the set of final states, θ is the angle between $\boldsymbol{k}$ and $\boldsymbol{k'}$, and $\left\langle F(\mathbf{x})\ \tilde{C}(\mathbf{x}) \right\rangle_{\boldsymbol{k'}}$ indicates averaging $F(\mathbf{x})$ over the elastic scattering surface, $\boldsymbol{k'}$, as in Sec. 4.8.3. Considering limiting cases, if only forward scattering is present, $\langle \cos(\theta) \rangle_{\boldsymbol{k'}} = 1$ and ℓ_B is infinite, and if every possible $\boldsymbol{k'}$ is equally probable, $\langle \cos(\theta) \rangle_{\boldsymbol{k'}} = 0$ and $\ell_s = \ell_B$.

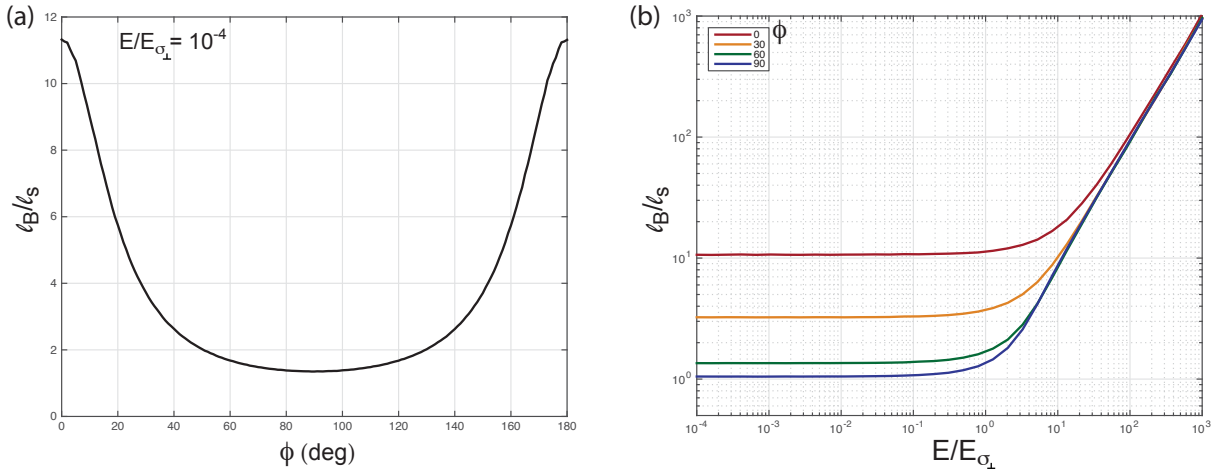

Figure 4.13: Energy and angle dependent relationship between ℓ_B to ℓ_s in 3D speckle. (a) Low energy limit of ℓ_B/ℓ_s calculated from Eq. 4.11 at $E/E_\sigma = 10^{-4}$ as a function of the k-vector polar angle, ϕ ($\phi = 0$ is along the axial direction of the speckle). Vectors in the transverse plane of the speckle scatter into a larger volume than those propagating on axis. (b) This ratio is calculated as a function of particle energy for four representative values of ϕ. At high energies, forward scattering dominates and all curves asymptote to the same line. Typical energies in the experiment are of order E_σ.

The angular dependence of the ℓ_B/ℓ_s ratio is plotted in Fig. 4.13 for the single beam speckle power spectrum, as written in Eq. 3.15. Several interesting properties of scattering from speckle are apparent in this graph. First at low energies, there is a large anisotropy between scattering along the axial and transverse directions in speckle. This anisotropy will cause a rapid pumping of motion into the axial direction, as forward scattering is greatly preferred along this axis, and scattering from the transverse plane scatters into all directions. This may have strong implications for localization in 3D speckle and explain the extreme anisotropy in localization length scales between the axial and transverse directions observed in our measurements. This can be understood graphically by considering the spherical sections of the speckle power spectrum shown in Fig. 4.16. From these images it is clear that more randomness is introduced in low energy scattering in the x-z plane than along the y-direction, where only a small fraction of the elastic scattering surface focused around forward scattering contains any weight. At high energies, $\ell_B/\ell_s \approx E/E_\sigma$ and forward scattering dominates all other processes. This can be easily understood as the spherical scattering surface at high energies can be approximated as integral over the power spectrum in a plane passing through the origin and perpendicular to the initial k-vector. The k-vector sets the scale of $\mathsf{cos}(\theta)$ relative to the fixed speckle power spectrum, and the integrand will decrease inversely proportional to $|\mathbf{k}|^2$ or E. Large ℓ_B/ℓ_s at high energies will cause localization lengths and the role of finite size effects in experiments to increase. Importantly, the ratio ℓ_B/ℓ_s given by evaluating $\langle\mathsf{cos}(\theta)\rangle$ over the scattering sphere is strictly valid for isotropic scattering media, and Eq. 4.13 is used in the case of anisotropic speckle as a qualitative measure of the randomness introduced via elastic scattering rather than as a strict equality.

4.8.3 Piraud & Sanchez-Palencia: On-Shell Scattering

Work led by Marie Piraud explores diffusion and localization in a speckle potentials in one, two, and three spatial dimensions using a mixture of numerical and analytical techniques. Her work is found in a number of papers including Refs. [166, 165, 167, 168] and summarized in Ref. [164]. In this section I will discuss her calculation of the single-scattering timescale and relationship of this timescale to the elastic scattering mean free paths in speckle disorder. This calculation is based on Fermi's golden rule and uses the speckle power spectrum $\tilde{C}(\boldsymbol{k})$ (the Fourier transform of the intensity autocorrelation function) as the elastic scattering vertex connecting an initial state $\mathbf{k}$ to the set of final states $\mathbf{k}'$ with the same energy as $\boldsymbol{k}$. This elastic scattering process is illustrated in Fig. 4.14 in 2D, where the set of possible final states $\boldsymbol{k'}$ exist on a spherical surface of radius $k_E = |\boldsymbol{k}| = \sqrt{2mE/\hbar^2}$ and are driven by spectral weight in the potential sampled from $\boldsymbol{\delta k} = \boldsymbol{k} - \boldsymbol{k'}$ (a sphere tangent to the origin with center at $-\mathbf{k}$). The total scattering rate is found by integrating over this surface (indicated by the angle brackets):

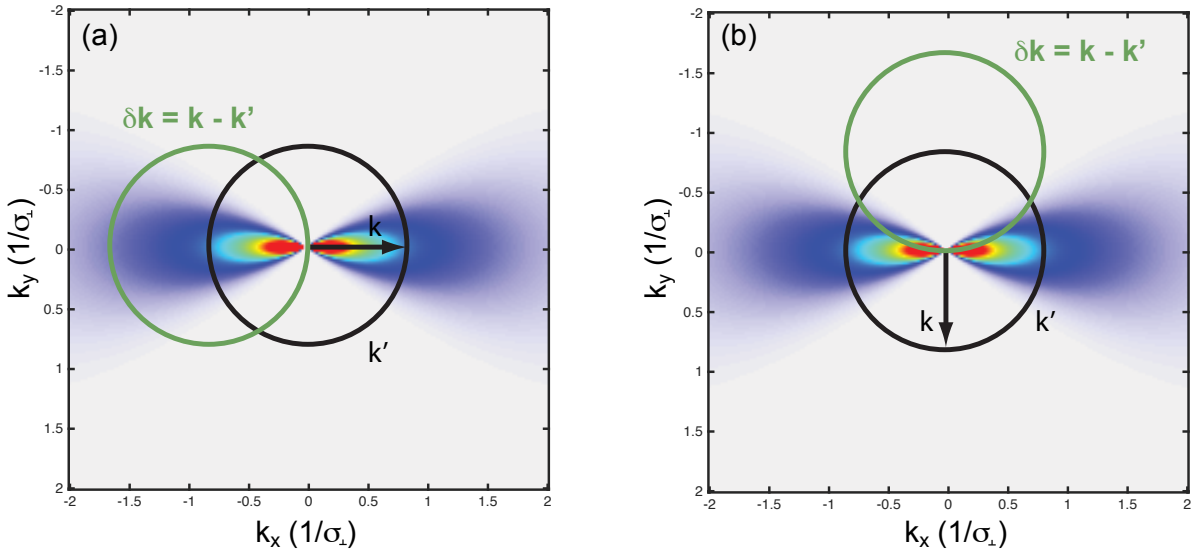

Figure 4.14: Illustration of elastic scattering surface from speckle in three-dimensions. The speckle power spectrum takes a figure-8 shape in the axial-transverse plane of the speckle focus. Here the speckle is propagating along the y-direction and the power spectrum is azimuthally symmetric about this axis. Elastic scattering of state $\boldsymbol{k}$ (black arrows) to $\boldsymbol{k}'$ from the potential requires weight in the power spectrum at $\boldsymbol{\delta k} = \boldsymbol{k} - \boldsymbol{k}'$. A sphere of possible $\boldsymbol{k}'$ (black circles) states exists with radius $|\boldsymbol{k}|$. The single scattering rate can be estimated by integrating over the sphere of possible $\boldsymbol{\delta k}$ (green circles) shown here for initial states along the x- and y-directions in (a) and (b), respectively. See Fig. 4.15 for surface projections of the power spectrum for representative k-vectors.

$$\tau_s(E, \mathbf{k}) = \frac{\hbar}{2\pi \left\langle \tilde{C}(\mathbf{k} - \mathbf{k}') \right\rangle}. \tag{4.12}$$

Here the integration volume extends over the k' elastic scattering sphere—this introduces an energy conserving delta function and the integral can be rewritten as

$$\left\langle \tilde{C}(\mathbf{k} - \mathbf{k}') \right\rangle = \int \frac{d^3\mathbf{k}'}{(2\pi)^3} \tilde{C}(\mathbf{k} - \mathbf{k}') \delta \left[E - \epsilon(\mathbf{k}) \right] \tag{4.13}$$

$$= \frac{m k_E}{\hbar^2} \int \frac{d\Omega}{(2\pi)^3} \tilde{C}(\mathbf{k} - \mathbf{k}'). \tag{4.14}$$

The power spectrum for the single beam speckle is discussed in detail in Sec. 3.2 and is

$$\begin{aligned}\tilde{C}(k_x,k_y,k_z) =& \frac{\pi^{3/2}V_R^2\sigma_\perp^2\sigma_{||}}{\sqrt{(\sigma_\perp k_x)^2+(\sigma_\perp k_y)^2}}\times \\ & \exp\left[-\frac{1}{4}\left((\sigma_\perp k_x)^2+(\sigma_\perp k_y)^2+\frac{(\sigma_{||}\ k_z)^2}{(\sigma_\perp k_x)^2+(\sigma_\perp k_y)^2}\right)\right].\end{aligned} \tag{4.15}$$

For the finest correlation length speckle in this thesis, $\sigma_{||}/\sigma_\perp = 5.8$ and this value of the speckle anisotropy is used for the remainder of this discussion. The power spectrum can be redefined to remove the potential height such that $\tilde{C}(\mathbf{k}) \equiv V_R^2\ \tilde{c}(\mathbf{k})$ and the elastic scattering time calculated as

$$\tau_s(E,\mathbf{k}) = \frac{\hbar E_{\sigma_\perp}}{V_R^2}\frac{(2\pi)^2/k_E\sigma_\perp}{\int d\Omega_{\hat{k}'}\tilde{c}(\boldsymbol{\delta k})/\sigma_\perp^3}\ . \tag{4.16}$$

The integral in Eq. 4.16 depends on both the k-vector's magnitude and direction, as shown in Fig. 4.15. These surface maps of the power spectrum are sampled over the k-vectors' associated elastic scattering surfaces, and the graphs directly show the possible transitions and their relative probabilities. As discussed in Sec. 4.8.2, forward scattering is strongly preferred for motion along the y-direction and for high values of $\mathbf{k_E}$.

The elastic scattering time calculated from Eq. 4.16 using the power spectrum in Eq. 4.15 is plotted in Fig. 4.16. Surprisingly, the low energy ($k\sigma_\perp << 1$) behavior shows minimal angular anisotropy in the scattering rate ($\tau_x/\tau_y \simeq 1.002$), and the timescale plateaus in this regions. At $E/E_{\sigma_\perp} \sim 1$ the scattering timescales begins increasing and anisotropy emerges between the axial and transverse directions in the speckle. In the high energy limit, the timescale grows linearly with k_E and the anisotropy saturates at $\tau_{E,\perp}/\tau_{E,||} = \frac{\sqrt{\pi}}{2}\frac{\sigma_{||}}{\sigma_\perp}$. This limit arises from integrating the power spectrum in the transverse-transverse and axial-transverse planes, and the elastic scattering mean free time scales as $E^{1/2}$ for E/E_σ greater than 10.

Combining the calculation of the elastic scattering mean free time with the calculated ratio ℓ_B/ℓ_s from Sec. 4.8.2, we make an estimation of the Boltzmann scattering mean free path as $\ell_B = v\tau_s(\ell_B/\ell_s)$. Using the typical value of $\Delta = 200\ k_B \times nK$ and $E_\sigma = 170\ k_B \times nK$, the trends in Figures 4.16 and 4.13 are combined to find characteristic value ℓ_B. Sampling the value along the axis of the speckle, values of ℓ_B of 0.2, 0.8, 6.5, and 250 microns are found for $E/E_\sigma = 0.1$, 1, 10, and 100, respectively. This analysis demonstrates that the typical Boltzmann mean paths ($E \approx E_\sigma$) are on the same order as the correlation length and of the typical λ_{dB}. The scaling of ℓ_B grows quickly with energy with a high energy scaling of $\ell_B \propto E^2$; this scaling could have significant implications for localization as ℓ_B approaches the size our system. For almost all atoms in the thermal distributions used, $E \ll 10E_\sigma$ and typical ℓ_B are 1 or 2 orders of magnitude smaller than the

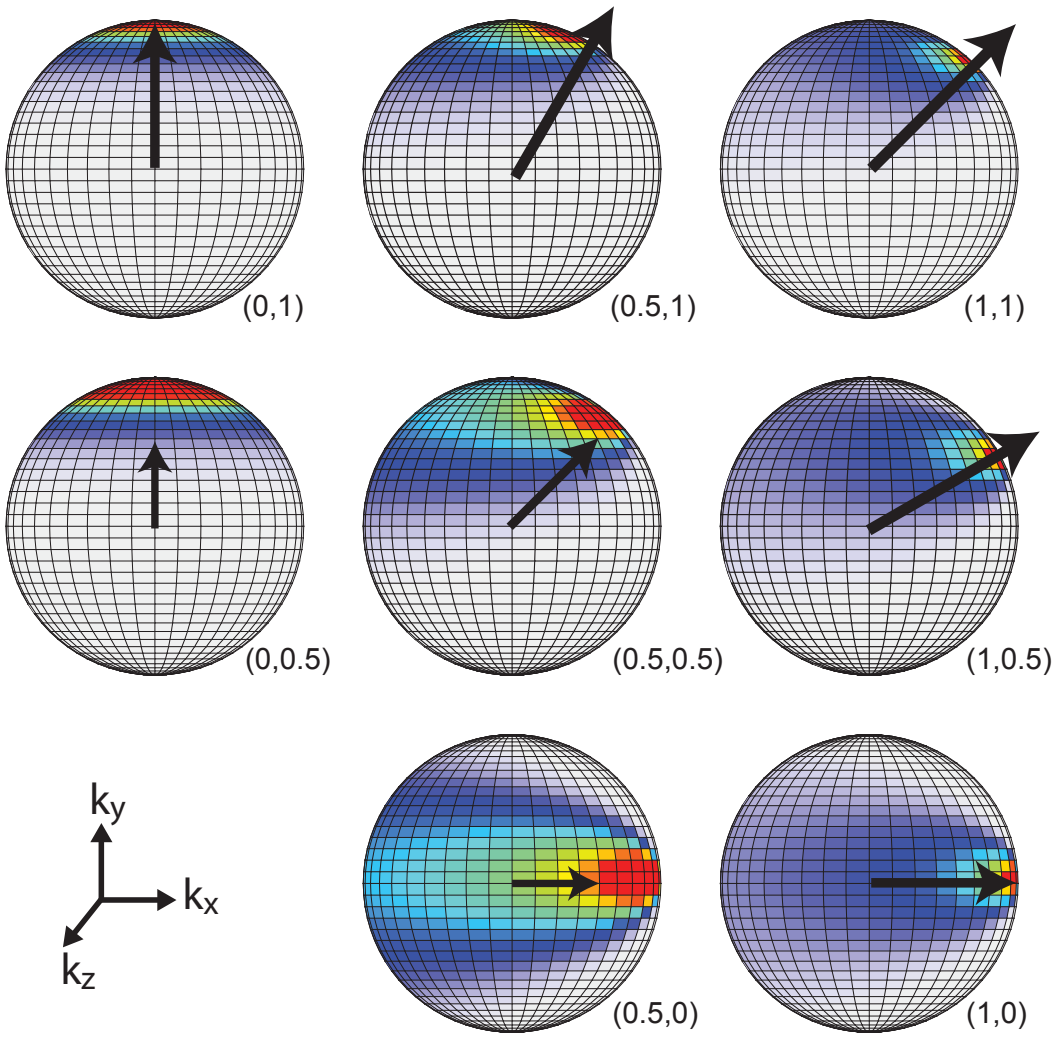

Figure 4.15: Illustration of power spectrum of speckle sampled over elastic scattering surfaces for several initial k-vectors. Vectors are in units of $(k_x/\sigma_\perp, k_y/\sigma_\perp)$ with size and direction indicated by black arrows and the coordinates written in parentheses.

system's size. For the longer $\bar{\zeta}$ speckle explored, a significant fraction of the atoms sample the high-energy limit of ℓ_B and finite system sizes may play a significant role.

4.8.4 Piraud & Sanchez-Palencia: Quantum Diffusion

Piraud calculates diffusion constants for atoms in speckle potentials in Ref. [166], and direct comparisons can be made between thermally averaged density profiles generated from these predicted diffusion constants and measured optical depth images from the experiment. Piraud's calculation considers incoherent transport in the speckle for the single-beam speckle for $\sigma_{||}/\sigma_\perp = 5.8$, corresponding to $\bar{\zeta} = 1.2\ \mu m$: the shortest correlation length explored here. Boltzmann diffusion constants are found by solving the Bethe-Salpeter

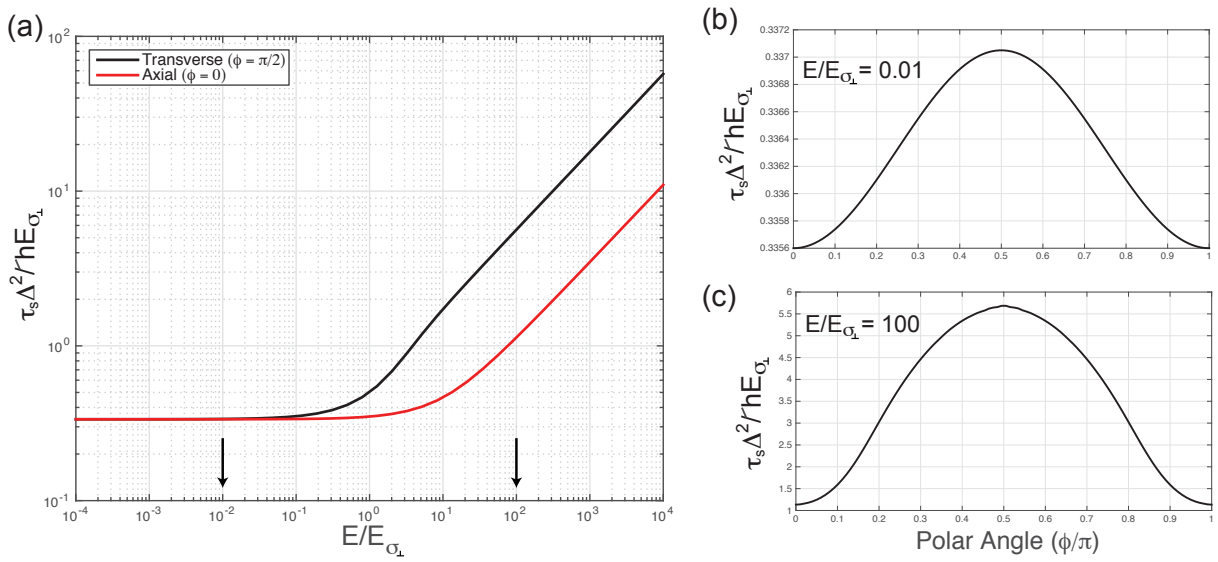

Figure 4.16: Fermi's Golden Rule calculation of the mean time between scattering events in speckle disorder. (a) The dimensionless, elastic scattering timescale ($\tau_s \Delta^2/\hbar E_\sigma$) is plotted versus the energy of the particle along the transverse- (black line) and axial-directions (red line) in speckle. (b-c) Show the orientation dependence of the elastic scattering timescale at E/E_σ of 0.01 and 100, as indicated by the arrows in (a). The anisotropy at low energies is exceedingly small and grows to a fixed value at high energies. The polar angle is measured from the axis of the speckle such that $\phi = 0$ is on axis. This image is based on a figure from Ref. [164]. Typical energies in the experiment are of order E_σ.

equation using the speckle power spectrum to describe the four-point scattering vertex connecting states $\boldsymbol{k}$ and $\boldsymbol{k}'$. The diffusive motion found is observed to divide along the natural axes of the speckle (the x- ,y- , and z-directions) with anisotropy between motion in the axial and transverse directions set by the ratio of the on-shell scattering weight.

Boltzmann diffusion constants are extracted graphically from Fig. 2 of Ref. [166]. Approximate numerical values for the diffusion constants are listed below.

$$\frac{m\ \mathtt{D_{xz}(E)}}{h}\left(\frac{\mathtt{V_R}}{E_{\sigma_\perp}}\right)^2 = 0.236\ \left(\frac{\mathtt{E}}{\mathtt{E}_{\sigma_\perp}}\right) + 0.46\ \left(\frac{\mathtt{E}}{\mathtt{E}_{\sigma_\perp}}\right)^{5/2} \tag{4.17}$$

$$\frac{m\ \mathtt{D_y(E)}}{h}\left(\frac{\mathtt{V_R}}{E_{\sigma_\perp}}\right)^2 = 2.36\ \left(\frac{\mathtt{E}}{\mathtt{E}_{\sigma_\perp}}\right) + 4.6\ \left(\frac{\mathtt{E}}{\mathtt{E}_{\sigma_\perp}}\right)^{5/2} \tag{4.18}$$

For $\bar{\zeta} = 1.2\mu m$, $\mathtt{E}_{\sigma_\perp} = 170\ k_B \times nK$. Predicted density profiles are calculated numerically with the known particle number and density of states. The time evolution is calculated using Gaussian solutions to the diffusion equation ($\frac{\partial \rho}{\partial t} = \mathtt{D}\nabla^2\rho$) whose RMS size grows as $\sigma_i(t) = \sqrt{\sigma_i^2(0) + 2D_i t}$. Integration over the

thermal distribution of energies allows for direct calculation of the optical depth image:

$$\mathcal{OD} \propto \iint P(E)\rho(r,E)dEdz = \int dE \left[\frac{2}{(k_B T)^{3/2}}\sqrt{\frac{E}{\pi}}e^{-\beta E}\right]\left[\frac{N}{2\pi\sigma_x(t)\sigma_y(t)}e^{-\frac{x^2}{2\sigma_x^2(t)}-\frac{y^2}{2\sigma_y^2(t)}}\right]. \quad (4.19)$$

Comparison between the predicted profiles based on diffusion and the experimental observation are shown in Fig. 4.19. The largest similarity between experiment and theory is the evolution of the central density in time which falls at roughly the same rate in both tests. The shape of the gas in the x-direction is also similar, but this is largely due to the smaller diffusion constant in this direction and the gas remains roughly fixed at the in-trap distribution. Diffusive dynamics fails to capture the shape of the observed density profiles in the y-direction; the data are roughly exponential and the theory is not. The diffusive profiles fail to show a division of the gas into two components with clearly separated (localized and mobile) behavior as is seen at lower disorder strengths, the diffusive profiles expands more slowly than the data over the time range probed, and the simulation predicts that the RMS size will grow without bound in time in disagreement with the data. The lengths scales obtained from the diffusion simulation are not dissimilar to the measured values, and this may warrant further studies in the future. Drawing distinction between slowly diffusing and localized atoms is difficult with the large energy spread of states involved in this measurement. Future work to distinguish between these two alternatives would benefit from narrower energy distributions to aid in direct comparison of single-particle behavior.

4.9 Comment on the Validity of the Born Approximation

The vast majority of theoretical work exploring scattering and localization in speckle potentials focuses on the weak scattering limit and the self-consistent theory of localization [205, 206], including the works discussed here by Kuhn and Piraud. Perturbations to the diffusion constant from scattering in speckle are found by considering a limited number of terms in the Born series, and the convergence of this series and the accuracy of the approximation hinges on high order terms rapidly trending to zero. This section examines the validity of these approaches by comparing the approximation's figures of merit to experimentally relevant parameters. A brief discussion of recent numerical work that explores transport in speckle beyond the weak scattering limit is also included.

Both Kuhn and Piraud present figures of merit that determine the regime of validity of their calculations. Kuhn presents a simple energetic argument in Ref. [106] comparing the energy of the particle to a critical energy set by the ratio of the mean disorder height squared and the speckle energy scale for isotropic

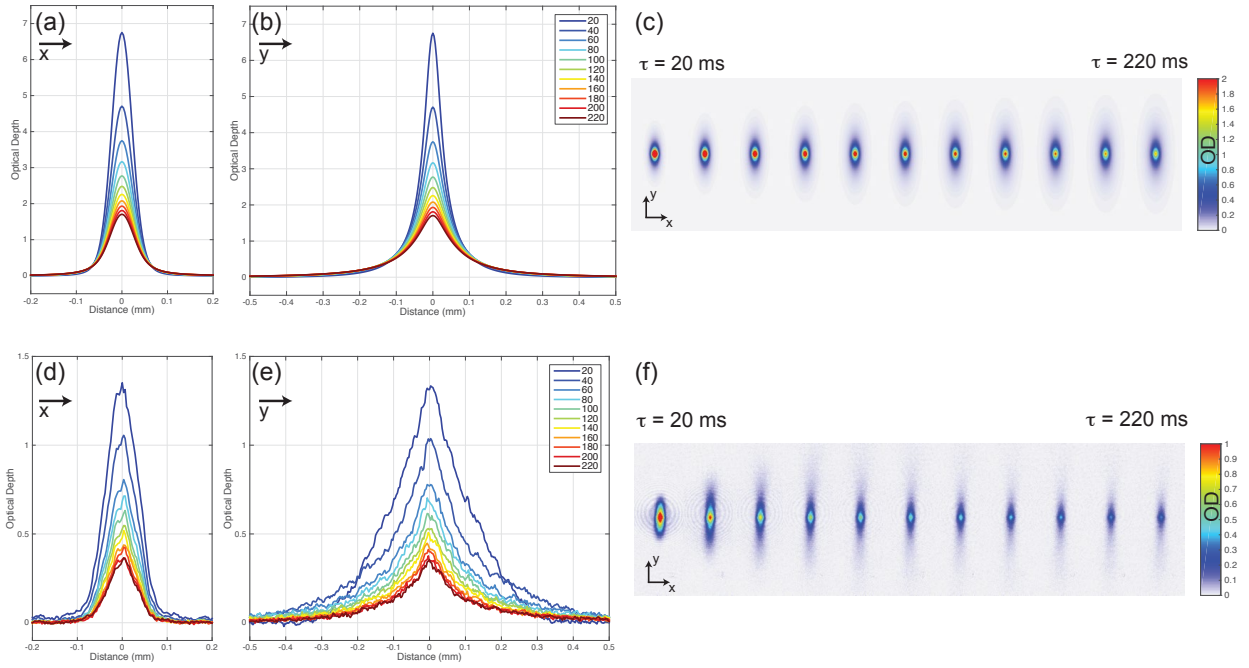

Figure 4.17: Comparison of measured optical depth profiles to profiles generated from predicted diffusion constants and known energy distribution of a 220 nK thermal gas with 1.6 $\times 10^5$ atoms in speckle disorder with $\Delta = 220\ k_B \times nK$ and $\bar{\zeta} = 1.2\mu m$ for τ from 20 to 220 ms. (a-c) Slices in the x- and y-direction and calculated optical depth images show the predicted distribution from Piraud's predicted diffusion constants. (d-f) Measured dynamics are shown over the same spatial scale. Note the difference in the optical depth scale between the measured and predicted profiles. The predicted diffusive profiles are reminiscent of the measured profiles but fail to capture the long tails in the y-direction, the bimodal behavior observed at short τ, and the plateau in RMS size at large τ.

disorder, $E_\Delta = \Delta^2/E_\zeta$. Here $E_\zeta = \hbar/(m\sigma^2)$, and σ is the isotropic characteristic length of the disorder correlation function studied. The weak scattering approximation is claimed to be valid when $E \gg E_\Delta$, and the breakdown of the approximation is connected directly to the mobility edge such that $E_c = E_\Delta$ in three-dimensions. For the shortest correlation length probed, E_ζ is 170 $k_B \times nK$, Δ varies from 0 to 1000 $k_B \times nK$, and the gas temperature varies from 170 to 1500 nK. For the high temperature data, this criteria is satisfied for 95% of the gas at $\Delta = 200\ k_B \times nK$ and 5% for $\Delta = 200\ k_B \times nK$. For the low temperature range, 90% of the gas satisfy $E > E_\Delta$ at $\Delta = 200\ k_B \times nK$, but 0% satisfy the condition for $\Delta = 200\ k_B \times nK$. Very little of the data has $E \gg E_\Delta$, and the predicted scaling of $E_c \propto \Delta^2$ is not seen. The measured scaling is $E_c \propto \Delta^{0.6}$, as shown in Fig. 4.4. This prediction also suggests that the mobility edge should shift as E_ζ is varied. For the variable correlation length data, the geometric mean of the correlation length is varied by a factor of 4 corresponding to a change of E_ζ by a factor of 16. No shift in the mobility edge with changing correlation length is observed for this data, in stark contrast to the predicted behavior.

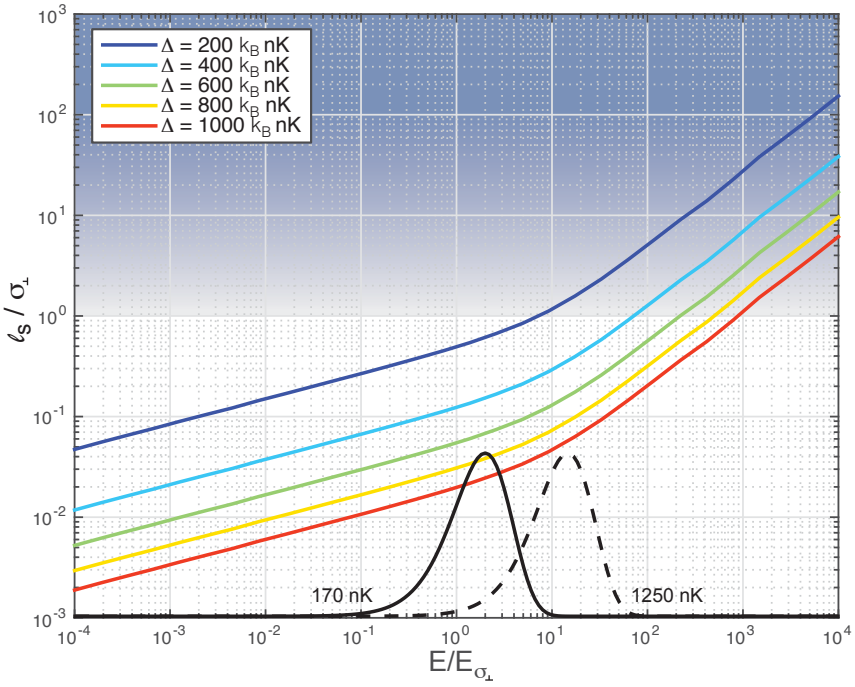

Figure 4.18: Regime of validity of the Born approximation for representative disorder and single-particle energy scales. The ratio $\ell_s/\sigma_\perp$ is plotted for scattering along the axial direction of the speckle for Δ from 200 to 1000 nK; ℓ_s is calculated as the product of τ_s and the thermal velocity, where τ_s is calculated as in Fig. 4.16. The weak scattering approximation is valid in the shaded area for $\ell_s/\sigma_\perp \gg 1$, as claimed by Ref [164]. The black solid and dashed curves show probability distributions for representative thermal distributions explored in the measurements presented here, on a linear scale. For the data presented here, there is little overlap with the regime of validity of weak scattering except for the highest temperature and lowest disorder strengths explored.

In Piraud's work, the Born approximation is declared valid when the elastic scattering mean-free-path is much longer than the speckle correlation length, $\ell_s \gg \sigma_\perp$ [164]. The elastic scattering mean-free-path is calculated as the product of the elastic scattering mean-free-time, τ_s and the thermal velocity of the atoms. The Fermi's golden calculation detailed in Sec. 4.8.3 can be used to calculate τ_s by integrating the spectral weight on the elastic scattering surface set by $\boldsymbol{k}-\boldsymbol{k}'$ and the thermal velocity is known. The ratio of $\ell_s/\sigma_\perp$ is plotted in Fig. 4.18 for relevant disorder heights; also included are sample single-particle energy distribution spanning the temperature range explored in our measurements. For $\Delta > 200\ k_B \times nK$, the elastic scattering mean free path is less than the speckle correlation length for all but the highest energy particle used, and the usefulness of Born approximation is called into question.

Recent work by Delande and Orso [40] employs a transfer-matrix approach to go beyond the approximations used in self-consistent calculations. This work is based on the development of the scaling theory of localization by Kramer and MacKinnnon [125] and extends these methods to speckle potentials. Delande and

Orso consider both red- and blue-detuned potentials and find that the mobility edge scaling is overestimated in both cases by the self-consistent theory, and that the mobility edge scales differently for attractive or repulsive speckle. Both of these findings differ from the prediction of the self-consistent theory and indicate that more detailed calculations are required to understand localization in these systems. The calculations employed for the transfer-matrix approach requires fine discretization of the speckle potential and massive computation resources. These results are computed in a quasi-1D geometry on an m-by-m bar extended along one direction. The mobility edge found for the blue detuned speckle always lies below the mean value of the disorder potential in direct disagreement with Piraud's work. The scaling of this quantity is not discussed in detail. Additionally, the location of the mobility edge is not found to be strongly dependent on the exact shape of the intensity autocorrelation function and is set primarily by the characteristic width of the correlation function.

4.10 Thoughts on Other Experimental Observations of 3D Anderson Localization

Work led by Fred Jendrzejewski has explored localization in three dimensions with ultracold bosons in Refs. [83, 82]. For these measurements, fine-grained disorder is created by interfering two speckle patterns propagating at right angles with identical polarization vectors. This creates a disorder potential with correlation lengths that are more isotropic than is produced in a single-beam speckle pattern. Their experiment begins with an interacting BEC of ^{87}Rb. To make the gas non-interacting, the condensate is released from the trapping potential and allowed to expand until the density has fallen sufficiently that interactions can safely be ignored. At this point the disorder potential is applied instantaneously and the resulting dynamics are observed. A two-component behavior is also observed in which a fraction of the gas diffuses from the central positions while the remainder is localized by the disorder. Distinguishing between the two components depends strongly on theoretical modeling of the dynamics in the disorder and a heuristic analysis of the energy shift provided by sudden application of the speckle disorder. Jendrzejewsi also published very clean evidence of coherent backscattering in a quasi-2D speckle in Ref. [84]. In this experiment, a gas was created with a very narrow velocity distribution using delta-kick cooling after creating a BEC. The gas was then allowed to evolve in a speckle potential and a backscattering peak observed. The dynamics of this backscattered peak are used to extract scattering and decoherence times in the speckle potential. Agreement is found between the experiment and the theoretical and numerical predictions in Ref. [27], but no discussion is provided as to the relevance of these methods for comparison with work on 3D localization in speckle potentials.

Recent unpublished work by the LENS group has studied localization with a non-interacting BEC of ^{39}K with the assistance of a Feshbach resonance [184]. These experiments also employ a crossed beam speckle potential; but instead of snapping the potential on, they ramp the disorder on while tuning the scattering length to zero. This avoids the poorly understood, heuristic energy shift introduced in Ref. [83]. They identify diffusive, sub-diffusive, and localized behaviors based on the growth of the gas's RMS size in time, and they identify a sharp mobility edge separating localized from sub-diffusive behavior. The location of their mobility edge is 20% higher than predicted by self-consistent approaches, but the discrepancy may be explained by differences in the speckle correlation function employed. This work is strongly focused on connecting localization theory and experiment, and it will be exciting to see how it develops.

4.11 Conclusions

In observing the dynamics of a non-interacting Fermi gas in 3D speckle disorder, we find behavior qualitatively similar to scenario of Anderson localization. Anderson localization predicts that localized and extended states will exist in a three-dimensional disordered potential, with these two phases separated by a mobility edge (or edges) in energy. We observe the gas divide into two components after release into the disorder. One component expands ballistically and rapidly leaves the field of view. The other expands anisotropically before assuming a fixed profile in the disorder. These two components correspond to extended and localized states in the speckle. The mobility edge separating the two components is related to a single-particle energy scale, which is found to depend strongly on the disorder amplitude and weakly on the disorder correlation length for the parameters explored.

The length scale of the localized gas is measured as the disorder amplitude, the temperature of the initial gas, and the speckle correlation length are varied. The qualitative scaling of the localized gas size follows intuition as the size decreases with increasing scattering rates from the disorder, i.e. increased disorder amplitude and decreasing temperature and disorder correlation length. Comparison of the single-particle localization length scaling with disorder amplitude and gas temperature is complicated by the shift in mobility edge for the variable-temperature and variable-Δ data. Data taken over a factor of four in disorder correlation length shows minimal shift in the mobility edge and allows for comparison to weak scattering theory. Qualitative agreement of the localization length scaling is achieved with predictions from weak scattering, but quantitative agreement between our observation and predicted localization length are separated by a large margin. This disagreement is not resolved, and the validity of the weak scattering approximation in this regime is suspect for much of the data explored. Complexity introduced by thermal

averaging of the density profiles and the finite size of the speckle correlation could also play a role in the disagreement.

Further experiments were performed to test the stability of the localized gas by quenching the density profile and applying an external force. In the quench measurement, atoms were selectively removed from the localized gas and allowed to reëquilibrate. Over a period of several hundred milliseconds, they were observed to reform the initial density profile, indicating that the localized profiles are not composed of micron-scale, sparsely distributed single-particle localized states and that the single-particle localization lengths are related to the measured thermally averaged quantity. Additionally, an external force was applied to the localized gas by reducing the force required to levitate the atoms against gravity. States localized over long length scales were quickly stripped out of the localized component, and the remaining gas assumed a shape similar to the in-trap profile indicating the most strongly localized states have localization lengths much shorter than the thermally averaged profiles. This reinforces the view that a majority of the atoms are proximal to the mobility edge where they are expected to have long localization lengths. Large quantitative gaps remain between theory and experiment, but there is hope that recent experimental and more realistic numerical simulations will bridge the divide.

Chapter 5

Fermions in Optical Lattices

This chapter provides a summary of the essential physics needed to understand the transport experiments performed in Chapter 6 on ultracold atoms in three-dimensional optical lattices. A brief explanation is provided of the Hubbard model and band structure in 1D. The rest of the chapter focuses on inferring thermodynamics quantities in the lattice from known constraints on entropy and atom number. The subtleties of performing experiments in trapped versus isotropic systems will also be discussed.

5.1 Realizing the Hubbard Model

The Hubbard model is a minimal model for electronic solids that considers a system of two fermionic states on a lattice with nearest-neighbor hopping and on-site interaction energy [71, 77, 88]. The role this model plays in highly-correlated electronic phenomena such as high-temperature superconductivity [204, 194, 124] and T-linear resistivity [35, 47] is a topic of active and spirited research. This model has been explored through theoretical and numerical techniques for more than fifty years, but direct comparisons to theory in the solid state are complicated by incomplete knowledge of the underlying Hamiltonian and coupling to an external heat bath provided by electron-phonon scattering. Recent advances in the production of low entropy quantum gases and the introduction of optical lattices with the ability to directly measure and modify the underlying Hamiltonian have allowed for quantum simulation of this model and its equivalent for bosons [68, 9, 86, 19, 180, 198]. This has generated a great experimental effort with quantum lattice gases in dozens of labs around the world. These experiments provide direct tests of the Hubbard model and strongly-interacting quantum matter in general.

The Fermi-Hubbard model is written in second quantization notation in Eq. 5.1, where $\hat{c}_{i,\sigma}$ ($\hat{c}^{\dagger}_{i,\sigma}$) are the annihilation (creation) operators on site i with spin σ, $\hat{n}_{i,\uparrow}$ is the number operator on site i with spin $\uparrow$, t is the tunneling energy, U is the interaction energy, and $< ij >$ indicates that the sum is taken only over nearest neighbors on the lattice. Here t is used for the tunneling energy to avoid confusion with the

superexchange energy scale $J = t^2/U$. This Hamiltonian is illustrated graphically in Figure 5.1:

$$\hat{H}_{\mathrm{FH}} = -t \sum_{\langle ij \rangle, \sigma} \left(\hat{c}^{\dagger}_{i,\sigma} \hat{c}_{j,\sigma} + \hat{c}^{\dagger}_{j,\sigma} \hat{c}_{i,\sigma} \right) + U \sum_{i} \hat{n}_{i,\uparrow} \hat{n}_{i,\downarrow}. \tag{5.1}$$

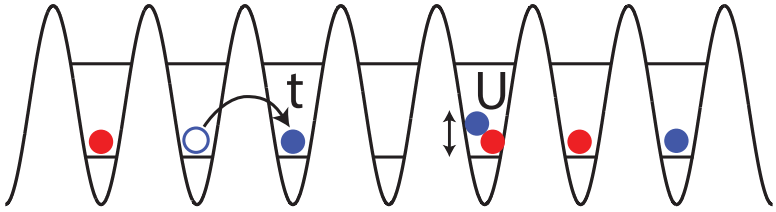

Figure 5.1: Illustration representing the tunneling and interaction energies in the Hubbard model. Here the red and blue circles represent atoms with up- and down-spins. The horizontal lines represent different bands within the lattice. For the temperatures explored in this work, we explore only the ground band.

All experiments with quantum gases are performed in the presence of a trap. In this experiment, and most others, the trap is harmonic confinement provided by a combination of Gaussian optical potentials used to cool and trap the atoms and to produce the lattice potential. A few specialized experiments have engineered trap potentials such as box or flat-bottomed potentials for achieving more isotropic system [62] or to remove entropy from a certain region of the system [73]. The effect of the harmonic confinement is to create a site dependent energy offset in the Hamiltonian as written in Eq. 5.2. This energy offset creates spatial variation in both number and entropy density—the consequences of this will be explored in the thermodynamic calculations presented in this chapter.

$$\hat{H}_{\mathrm{FH+Trap}} = \hat{H}_{\mathrm{FH}} + \sum_{i,\sigma} \epsilon_{i,\sigma} \hat{n}_{i,\sigma} \quad \text{where} \quad \epsilon_{i,\sigma} = \frac{1}{2} m \omega^2 r^2 \tag{5.2}$$

A great deal has already been achieved in exploration of the Hubbard models with ultracold gases. Bosonic systems have observed the superfluid-Mott insulating phase transition [68], strong synthetic magnetic fields have been created [4, 3, 141, 199], and quantum gas microscopes have directly imaged individual site occupations [9, 186, 209]. Fermi gases in optical lattice have also observed the Mott insulator transition [86] and numerous studies of transport dynamics have been performed in these systems [180, 67, 28, 95, 154, 54]. The future of fermions in optical lattices will certainly involve searches for very low entropy phases such as the anti-ferromagnetic state [73], while other work will focus on understanding processes of relaxation, thermalization, and the role of disorder in the presence of strong-interactions, in line with the original proposal for the creation of these systems as quantum simulators [81].

5.2 Band Structure

Particles in a lattice have broken continuous spatial symmetry, and the parabolic dispersion of free space is replaced by a band structure. Positions in the lattice are periodic after displacement by an integer number of lattice sites, and momenta are restricted to take on values with absolute value less than $q_B = h/\lambda$, where λ is the wavelength of light used to generate the lattice and is twice the lattice spacing. More precisely, any momentum value not in the range from $-q_B$ to q_B can be mapped back into this zone. This restricted momentum value is called crystal momentum or quasimomentum. Examples of the energy bands that form are shown in Fig. 5.2. The maximum quasimomentum introduces an energy scale for the lattice called the recoil momentum, E_R. This corresponds to the energy an atom would gain by absorbing a lattice photon, and is approximately $h8kHz$, or 390 $k_B \times nK$, for ^{40}K in a $\lambda = 782.2nm$ lattice:

$$E_R = \frac{q_B^2}{2m} = \frac{h^2}{8md^2}. \tag{5.3}$$

For the optical lattice potentials explored here, the potential is sinusoidal in space as

$$V_{\text{lattice}} = -s\Big(\mathsf{cos}^2(k_L x) + \mathsf{cos}^2(k_L y) + \mathsf{cos}^2(k_L z)\Big), \tag{5.4}$$

with $k = 2\pi/\lambda$, s is in the lattice depth, and the potential is attractive. The problem is separable in the spatial dimensions, and we find the wavefunctions and energies in this potential by solving Schroedinger's equation in one dimension. From Bloch's theorem (see Ref. [8], for example), solutions should take the form

$$\psi(r) = e^{iq\cdot r} u_{n,q}(r), \tag{5.5}$$

where $u_{n,q}(r)$ has the lattice periodicity, n is the band index, and q is the quasimomentum. We expand both the wavefunction and the lattice potential in a series expansion in terms of $K = 2nk$, where n is an integer:

$$u_{n,q}(r) = \sum_K c_K(q) e^{iK\cdot r} \quad \text{and} \quad V(r) = -\frac{s}{4}\left(e^{i2k\cdot r} + e^{-i2k\cdot r} + 2\right). \tag{5.6}$$

The only terms that survive leave a system of equations:

$$\left(\frac{\hbar^2(q+K)^2}{2m} - E(q)\right) c_K(q) + \frac{s}{4}\Big(c_{K-2k}(q) + c_{K+2k}(q)\Big) = 0. \tag{5.7}$$

This system of equations can be solved numerically for each value of q after truncating the series to a finite number of terms, typically ten. Sample one dimensional band structures are shown in Fig. 5.2. Notice that,

as the lattice depth is increased, the band become flatter and the band gaps increase. This process can be generalized to three dimensions with a higher dimensional system of equations to solve. The lattices used in this thesis (aside from disorder effects) are separable and the band structure can be found by summing three one-dimensional band structures. Numbering of the band indices is done by enumerating all possible three dimensional states and ordering them in energy.

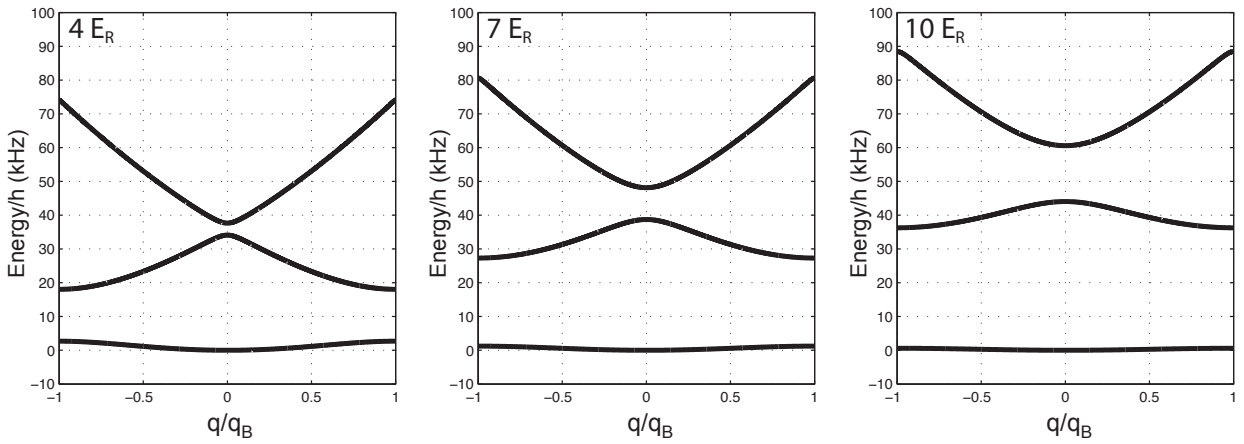

Figure 5.2: Lowest three energy bands calculated in one dimension for lattice depths of s = 4, 7 and 10 E_R. The lowest energy point is set to zero.

The Bloch wavefunctions, the eignenstates of the system, can be reconstructed with the coefficients $c_K(q)$ and are delocalized in space. In the tight binding limit, it is convenient to consider states localized to individual lattice sites; and the states, called Wannier functions, are formed from a superposition of Bloch states. A Wannier wavefunction w_n (with band index n) at position x_i is formed:

$$w_n(x - x_i) = \sum_q e^{iq(x-x_i)} u_{n,q}(x). \tag{5.8}$$

We can use these Wannier functions to calculate the values of the tunneling and interaction energies in the lattice. As shown in Eq. 5.9 and 5.10, t is given by the energy to tunnel from site i to site j, and the interaction energy U is given by the inter-atomic scattering length weighted by the density squared on a lattice site.

$$t_{ji} = \int dx\ w_j^*(x - x_i) \left[-\frac{\hbar^2}{2m} \frac{\partial^2}{\partial x^2} + V(x) \right] w_i(x - x_j) \tag{5.9}$$

$$U_i = \frac{4\pi\hbar^2 a_s}{m} \int dx\ |w(x - x_i)|^4 \tag{5.10}$$

s (E_R)	t (E_R)	U (E_R)	U/t
4.0	0.0862	0.1995	2.314
4.5	0.0754	0.2261	2.998
5.0	0.0661	0.2528	3.827
5.5	0.0579	0.2793	4.821
6.0	0.0509	0.3056	6.006
6.5	0.0448	0.3317	7.408
7.0	0.0395	0.3574	9.057

Table 5.1: Isotropic Hubbard parameters for ^{40}K atoms in a 782.2nm optical lattice.

These expressions have analytic forms in the tight-binding limit. A comparison between the band structure calculation with the deep-lattice limit is shown in Fig. 5.3. For the parameters explored in Chapters 5 and 6, these approximations,

$$t = \frac{4E_R}{\sqrt{\pi}} s^{3/4} e^{2\sqrt{s}} \quad \text{and} \quad U = \frac{4\pi\hbar^2 a_s}{md^3} s^{3/4} \left(\frac{\pi}{2}\right)^{3/2}, \tag{5.11}$$

are not valid.

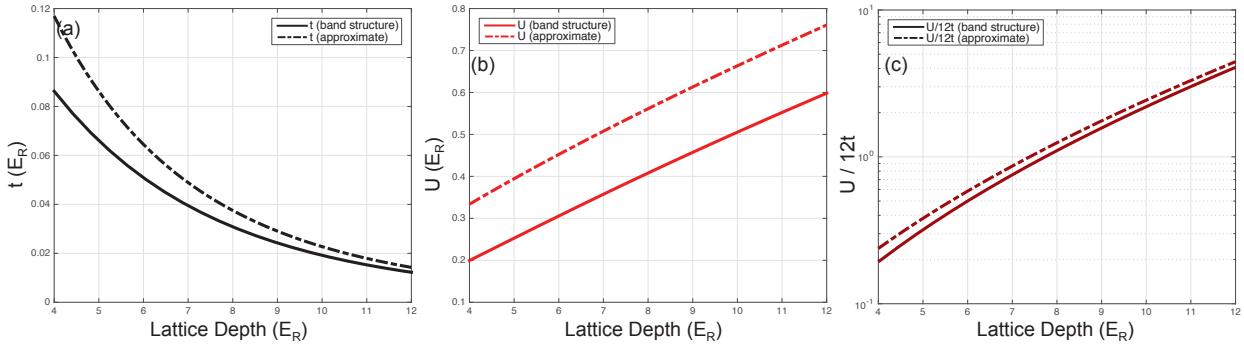

Figure 5.3: Comparison of the tunneling and interaction energies in the Hubbard model from the numerical band structure calculation to analytic results in the deep-lattice limit. The tunneling energy t, interaction energy U, and the ratio of $U/12t$ are shown in (a-c).

The ground band can be approximated by the tight binding dispersion:

$$\epsilon(q) = 2t\left[1 - \cos\left(\pi \frac{q}{q_B}\right)\right] \tag{5.12}$$

All experiments performed in this thesis have lattice depths between 4 and 7 E_R. To keeps all particles confined to the ground band, several criteria must be met: the energy gap to the second band must be higher than the temperature, and the maximum energy between two colliding particles in the ground band must be less than the lowest energy in the in the first excited band. This energy condition can be written

in terms of the quasimomentum state and band occupancy number in a matrix of six numbers. The energy of that state will be labeled as

$$\epsilon \begin{pmatrix} q_x & q_y & q_z \\ n_x & n_y & n_z \end{pmatrix} \tag{5.13}$$

The condition on collisional energies for the system to remain single band is

$$2\,\epsilon \begin{pmatrix} q_B & q_B & q_B \\ 0 & 0 & 0 \end{pmatrix} = 24t < \epsilon \begin{pmatrix} q_B & 0 & 0 \\ 1 & 0 & 0 \end{pmatrix}. \tag{5.14}$$

This condition is satisfied for lattice depths greater than 3.74 E_R. Another consideration is that the next-nearest neighbor tunneling parameter should not be too great. For a lattice depth of $4E_R$, this quantity is 7% of the nearest-neighbor tunneling energy [135], and the system realizes a single-band, tight-binding model.

5.2.1 Lattice Alignment and Calibration

The 3D retroreflected optical lattice is aligned to the position of the atoms in the optical dipole trap. Sag in the dipole trap causes the position of the atoms to change as the trap frequency is reduced, with a displacement of the trap center of g/ω^2. Here g is the gravitational acceleration and ω is the trap frequency along the direction of gravity. Before aligning the lattice to the position of the atoms, the geometric mean of the trap frequencies is chosen that provides the desired occupation in the center of the lattice gas for a given number and entropy per particle. The trap is then re-compressed to this value after the final stage of evaporation in the optical trap such that the trap center before loading into the lattice is fixed. For lattice experiments in this thesis, the final geometric mean trap frequency in the optical trap is chosen to be $\approx 2\pi\ 85Hz$. Sag can also be removed with a magnetic field gradient that counteracts gravity for a given spin-state, but this method is not ideal for spin-mixed lattice experiments.

The lattice is composed of three pairs of retroreflected beams, and each pair is aligned to the fixed atom position in two stages. Initially, the retroreflected beam paths are blocked and the forward direction of each lattice beam is pulsed on for 2 milliseconds at near maximum power. This provides a large trapping potential that will impart a position-dependent impulse onto the atom gas. The center-of-mass velocity acquired by the gas is indicative of the slope of the trapping potential–forming the derivative of a Gaussian as the beam is swept over the atoms as shown in Fig. 5.4(a). The shape of this excursion can be fit to the expected function to extract the optimally aligned position. In practice, it is has proven better to minimize

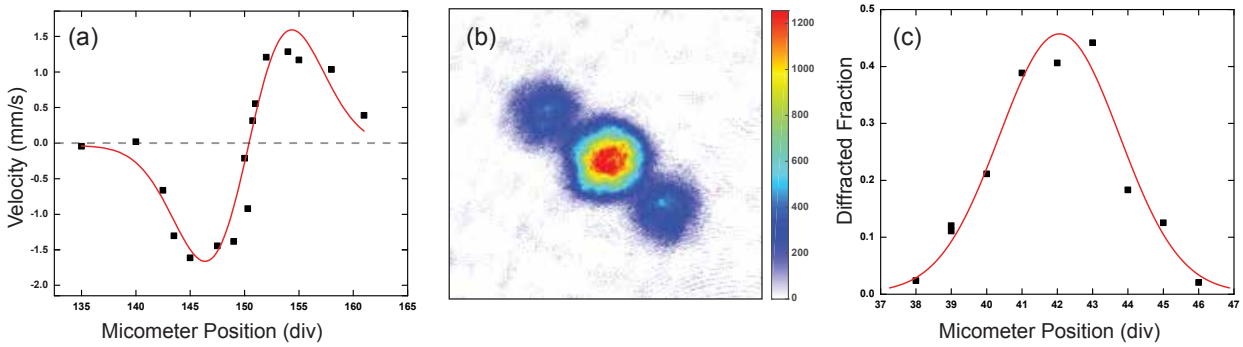

Figure 5.4: Example data showing alignment of a retroreflected optical lattice beam. (a) The forward direction of each lattice beam is aligned by pulsing the beam on for a short period of time (typically 2 ms) with the retroreflected path blocked. The gradient of the dipole potential creates a force on the atoms and the deflection of the gas is used as an alignment signal. Each beam is adjusted by two differential micrometers on the closest mirror to the atoms. (b) Alignment of the retroreflected beam is achieved by diffracting the atoms from the lattice potential. Each retroreflected pair is pulsed on for 200 μs, and a momentum of $\pm 2\hbar k_L$ is given to the diffracted orders. (c) The fraction of atoms in the diffraction peaks is measured as the retroreflected beam position is varied. The measured curve will be symmetric with respect to the aligned position, though it may not necessarily appear as a single peak.

the excursion from zero motion during this process as the response to the impulse is not guaranteed to be symmetric about the zero motion.

After the forward pass beams have been aligned using the impulse method, the retroreflected beams are aligned by diffracting the atoms from the lattice potential. Each pair of lattice beam is pulsed on for 200 μs, and atoms are diffracted by the lattice potential into momentum states at integer multiples of $2\hbar k_L$ as shown in Fig. 5.4(b). The fraction of atoms diffracted is a function of the lattice depth, and the graph of diffracted fraction vs beam position will form a symmetric pattern centered on the aligned position as shown in Fig. 5.4(c). This pattern is not guaranteed to be singly-peaked, as shown in Ref. [100]. Pulse edges are made as sharp as possible by turning on and off the beam by rapidly switching the RF power to the AOM outside the servo bandwidth of the intensity servo using a DDS.

Calibration of the lattice depth in many BEC experiments is performed using Kapitza-Dirac diffraction from the optical standing wave. In these experiments, all atoms can be condensed into the $q = 0$ state and the fraction of atoms diffracted directly related to the lattice depth [152, 57]. In Fermi gases, the spread of quasimomentum makes interpretation of the fraction of atoms diffracted more complicated, and calibration is performed by lattice modulation spectroscopy. In this scheme, the lattice intensity is modulated at the few percent level to drive transitions between bands [197, 97, 99]. This process adds heat to the gas and is manifested as a loss feature in the gas. Energy added to the gas by driving atoms to higher bands, and the decay process allows the gas to heat and atoms to escape from the trap. The modulation period can

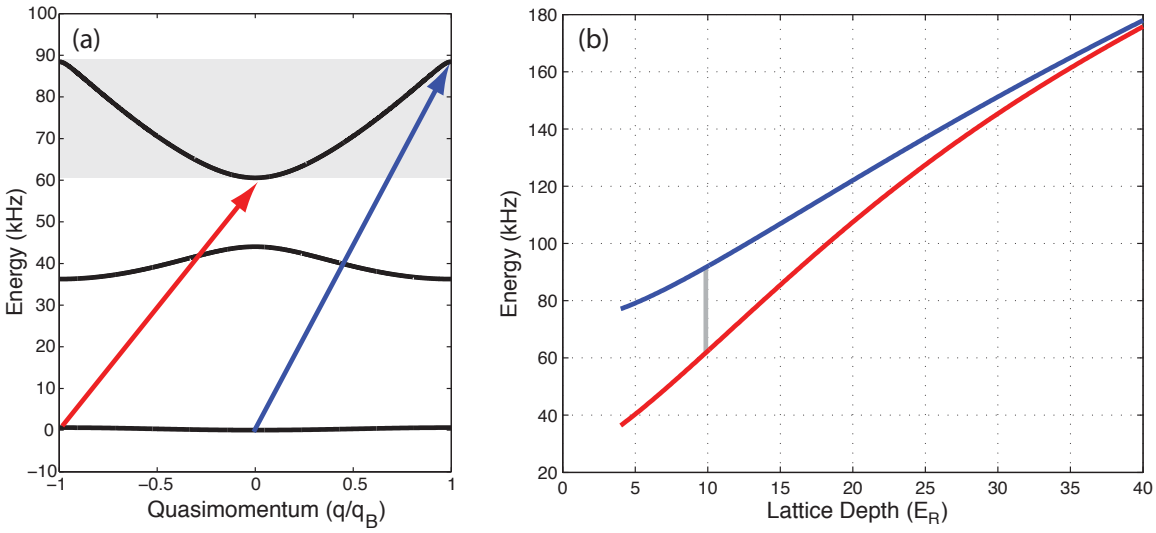

Figure 5.5: Calibration of latice depth using one dimensional band structure. (a). The band structure (black) is shown for s = 10 E_R. Modulating the lattice potential depth drives atoms between bands. Only certain transitions are possible set by symmetry and the lattice band structure. For atoms in the ground band, the lowest energy allowed, inter-band transition (red arrow) is $|n = 0, q = -q_B\rangle \rightarrow |n = 2, q = 0\rangle$. A range of transitions exists to the second excited band (shaded area), and the highest energy transition (blue arrow) is $|n = 0, q = 0\rangle \rightarrow |n = 2, q = q_B\rangle$. (b.) The lowest and highest frequency transitions between n=0 and n=2 are shown for a range of lattice depths. The lower frequency transition is not used for calibration as there is not always appreciable population at the band edge. The grey line represents the possible transitions in a 10 E_R lattice shown in (a).

be increased until the desired signal-to-noise ratio of the loss feature is achieved. Due to the parity of the on-site wavefunctions, the easiest transitions to parametrically drive are from the ground to the second excited band as illustrated in Fig. 5.6. The absolute low- and high-frequencies bounds are set by transitions from $|n = 0, q = -q_B\rangle \rightarrow |n = 2, q = 0\rangle$ and $|n = 0, q = 0\rangle \rightarrow |n = 2, q = q_B\rangle$, respectively—here n indexes the lattice band. A typical spectroscopy feature from lattice modulation spectroscopy is shown in Fig. 5.6, showing loss as this band of transitions is traversed. Importantly, the high-frequency edge of this feature is sharp and can be used to define the energy of the $|n = 0, q = 0\rangle \rightarrow |n = 2, q = q_B\rangle$ transition. This energy is directly related back to the lattice depth as shown in Fig. 5.5(b). The low-frequency transition is not sharply defined due to low population at the band edge and lack of thermalization into these states. The sharp, high-frequency edge in the modulation spectrum can also be used to fine tune the lattice retroreflected beam alignment as shown in Fig. 5.6(b). The modulation frequency can be set slightly below this edge and the loss signal will disappear as the beam is moved away from alignment such that the lattice depth falls and the modulation frequency is in the gap between bands. This creates an arbitrarily narrow alignment feature that is directly related to the lattice depth.

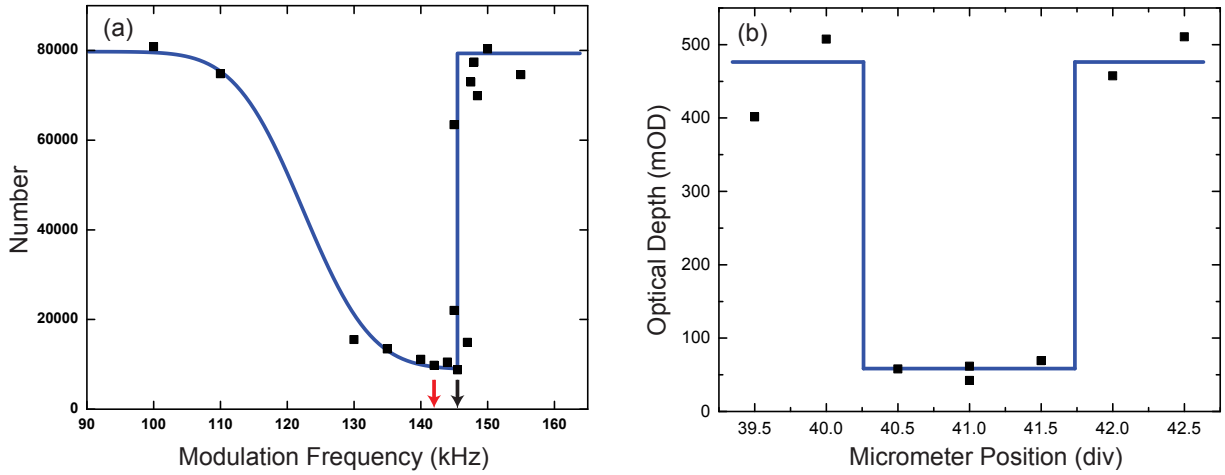

Figure 5.6: Calibration of lattice depth using lattice modulation spectroscopy. Atoms are heated by driving interband transitions as shown in Fig. 5.5 and leave the trapping volume. (a) The lattice intensity is modulated at the few percent level and a loss feature (black squares) is seen over a range of frequencies. The sharp edge of the loss feature at $\approx 146kHz$ (black arrow) corresponds to the largest frequency that can drive transitions from the ground to the second excited band (blue arrow in Fig 5.5) and represents a lattice depth of $s \approx 27E_R$. (b) This sharp loss feature can also be used to quickly optimize the retro beam alignment. With the modulation frequency set slightly below the sharp loss feature (red arrow), the retro beam can be translated and the band gap probed, as a direct measure of the lattice depth. Alignment is achieved in the center of the high-loss (maximum lattice depth) region. The blue lines are guides to the eye showing expected behavior.

5.2.2 Imaging Projection of the First Brillouin Zone

Images of lattice gases shown in this thesis are taken after bandmapping and time-of-flight expansion. The bandmapping process is a technique for mapping quasimomentum states in the lattice onto momentum states in the trapping potential by adiabatically reducing the lattice potential such that quasimomentum states in the n-th band are mapped onto free particle states in the n-th Brillouin zone [91, 66]. This process has been successfully employed to visualize the Brillouin zones in both Bose and Fermi gas optical lattice experiments [65, 98]. In this process, the lattice is turned off using a linear intensity ramp with a timescale slow compared to inverse of the band-gap and fast relative to the trapping period and the bandwidth. Typical ramps times are 200 μs; limitation in the intensity servo bandwidth limit the linearity of the ramp and the profile typically takes a quasi-exponential profile in time. The process of bandmapping is not perfect and the adiabaticity criterion for accurate mapping of the states fails near the band edges. This failure is discussed in detail in Ref. [134] through numerical simulation of the dynamics during bandmapping. The conclusion of this work is that bandmapping works well for low quasimomentum states but generally fails for states near the band edge. This has important implications for using the bandmapped quasimomentum distributions for

thermometry, and significant error using this method is found for thermal gases $kT/t > 7$.

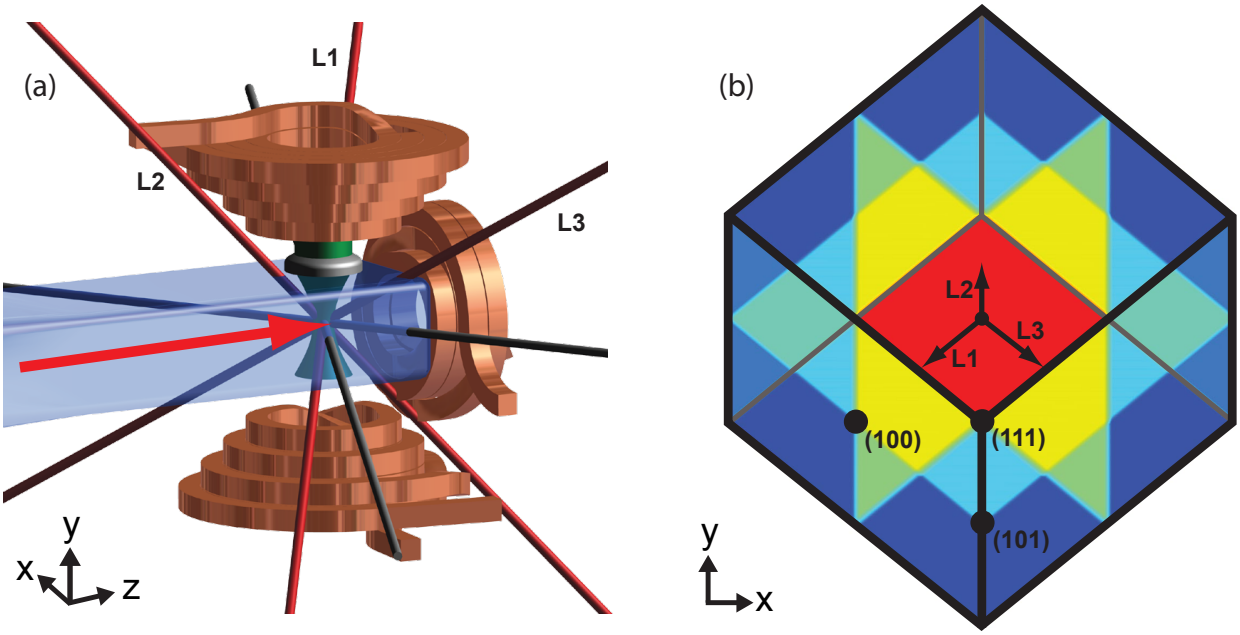

Figure 5.7: Schematic showing orientation of lattice beams relative to the imaging axis and vacuum chamber. (a) Rendering of science cell and surrounding magnetic trap shows the relative orientation of the lattice beams (red, labeled L1-L3), optical trap beams (gray), and the disorder (green). The atom gas is located at the intersection of these beams. The imaging beam (red arrow) travels through the atoms and the Ioffe coil (rightmost coil) to an imaging system that transfers the light to a CCD camera. (b) Atoms occupy the 1st Brillouin zone, which is a cube in momentum space. This cube is rotated relative to our imaging axis, and the projection in our imaging plane is a hexagon. The colors in this figure label the symmetric planes ($q = 0$ and $q = q_B$) in the first BZ, and the boundary of the volume is marked with black lines. Specific points have been labeled for clarity.

The imaged quasimomentum distributions after bandmapping lie within a cubic volume representing the first Brillouin zone. For all gas temperatures explored in this work, the atoms occupy only the lowest band and thus populate only the first Brillouin zone. Interpretation of our images is complicated by the relative orientation of the lattice axes to the imaging axis as illustrated in Fig. 5.7(a). The lattice beams do not fall along any of the primary axes of the experiment and are arranged such that one of (111) directions in the lattice falls roughly along the y-axis of the experiment. Imaging is performed along the z-axis, and column integrated images of the cubic first Brillouin zone appear as a hexagon in projection. Figure 5.7(b) graphically illustrates the orientation of different symmetric planes in the first Brillouin zone as they appear in the imaging projection. Subsequent bandmapped images indicate the boundaries of this volume with a hexagon.

5.3 Thermodynamics in Optical Lattices

Direct probes of temperature in 3D optical lattices are a topic of active research. A detailed review of the problems associated with thermometry and cooling in strongly-correlated lattice systems can be found in Refs. [136, 135]. The present state of the art is to infer thermodynamic quantities in the lattice from measured values in a harmonic trap where direct probes of temperature and entropy exist. The lattice loading process is typically assumed to be isentropic, but heating from off resonant scattering and non-adiabaticity in the ramp cause this assumption to be violated at some level. The entropy introduced in the loading process can be estimated by measuring entropy in a harmonic trap before and after quasi-adiabatically turning on and off the lattice potential, and the entropy in the lattice can be assumed to lie between these two values, with the average of the "round-trip" entropy providing the best estimation of the entropy in the lattice. Currently, the best direct measures of temperature in an optical lattices use the spatial distribution of atoms as a measure of entropy including work studying number fluctuation in 2D gas microscope [10] and spin gradients in the presence of a magnetic field gradient [210].

In this section, we explore four separate approximations used to estimate the temperature in an optical lattice, given known constraints on entropy, number, lattice, and trapping parameters. These approaches start in the non-interacting ($U = 0$) and atomic ($t = 0$) limits. These limits fail to capture behavior for the range of Hubbard parameters, particle number, and entropy explored in this work, and two approaches beyond these extreme limits are discussed, including the Hartree-Fock method that introduces interactions into the non-interacting limit and the high-temperature series expansion, which introduces tunneling into the atomic limit. The regimes of potential validity of each method is indicated in Fig. 5.8 as a function of lattice depth. Importantly, the applicability of a given method will depend on more than just the ratio of U/t, as will be discussed in the following sections.

The same techniques are applied for inferring temperature and chemical potential in the lattice in each of the four approaches discussed. This process is outlined here, and the fine details of the implementations and validity will be discussed on an individual basis. First, a grand potential is defined such that

$$\Omega = U - TS - \mu N \quad \text{where} \quad -\beta\Omega = \mathsf{log}(Z), \tag{5.15}$$

where U is the internal energy, T is the temperature, S is the entropy, μ is the chemical potential, N is the total number, $\beta = 1/k_B T$, and Z is the grand partition function. The details of the underlying Hamiltonian, $\mathcal{H}$, are contained within the grand partition function as $Z = \mathsf{Tr}[e^{-\beta\mathcal{H}}]$. Relations for N and S are found by

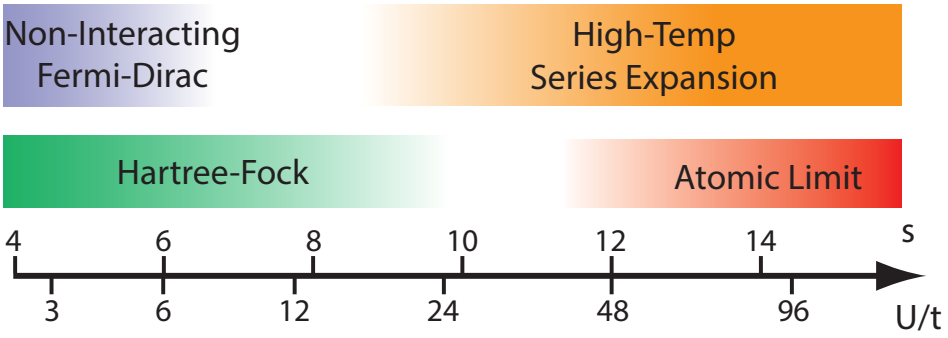

Figure 5.8: Regimes of potential validity for various statistical mechanics techniques in a lattice. Shaded areas indicate the range of utility of each approach for inferring temperature within the isentropic assumption. These regimes are not rigidly defined, as a function of lattice depth as the validity of each approach will depend on more than just the ratio of the Hubbard interaction to tunneling energy. For example, the high-temperature series is not convergent at low temperatures, and the non-interacting limit will fail progressively with increasing density.

taking partial derivatives of the grand potential with respect to μ and T, respectively:

$$N = -\frac{\partial \Omega}{\partial \mu} \ , \text{ and } S = -\frac{\partial \Omega}{\partial T}. \tag{5.16}$$

Values for temperature and chemical potential are found that satisfy the known constraints on number and entropy, N_0 and S_0. The unknown values of T and μ are found by constructing a 2D optimization problem in which the error functional represents the deviation from the known constraints:

$$\left|N_0 - N(\mu, T)\right| \ + \ \left|S_0 - S(\mu, T)\right| \ = \ 0. \tag{5.17}$$

The search for optimal T and μ is performed numerically until the required accuracy is achieved, and reconstructed density and quasimomentum profiles are generated from these inferred quantities.

5.3.1 Analytic Results for a Harmonic Trap

We will use the well known properties of a degenerate Fermi gas in a harmonic trap to infer thermodynamic quantities in the lattice. The relevant thermodynamics for the harmonically trapped system are briefly reviewed below, and more details can be found in Ref. [44]. The Hamiltonian for the harmonically trapped system is

$$H = \sum_{i=x,y,z} \left(\frac{p_i^2}{2m} + \frac{m\omega_i^2 x_i^2}{2} \right), \tag{5.18}$$

and relative populations of the states are given by the Fermi-Dirac distribution

$$f(\vec{x},\vec{p}) = \frac{1}{\mathrm{z}^{-1}e^{\beta H(\vec{x},\vec{p})}+1} \ , \text{ where } \mathrm{z} = e^{\beta\mu}. \tag{5.19}$$

Information is extracted from the gas by taking images after quickly removing the trapping potential and allowing the gas to expand in time-of-flight. After an expansion time, t, an absorption image is taken of the gas. In the infinite expansion time limit, the imaged distribution will be a direct mapping of the momentum distribution in the trap. At expansion times comparable to the trap period, the distribution will be indicative of both the the spatial and momentum distributions of the trapped gas. Importantly, the shape of the gas does not change during time-of-flight, as the Hamiltonian is quadratic in both x and p. The functional form of the probability distribution acquired by integrating out either the spatial or the momentum components will necessarily be identical. This means that in expansion the shape of the gas (aside from any imaging non-idealities) does not change, and the expansion time can be chosen to maximize signal-to-noise and minimize saturation effects. In the infinite expansion time limit, the imaged column integrated momentum profile will take the form

$$n(\vec{p_x},\vec{p_y}) = \frac{1}{h^3}\int d^3\vec{x}\ d\vec{p_z}\ f(\vec{x},\vec{p}). \tag{5.20}$$

This integral gives a surface function as

$$OD = A\frac{\mathsf{Li}_2\left[-\mathrm{z}\ e^{\left(-\frac{(x-x_c)^2}{2\sigma_x^2}-\frac{(y-y_c)^2}{2\sigma_y^2}\right)}\right]}{\mathsf{Li}_2[-\mathrm{z}]}, \tag{5.21}$$

where z is the fugacity, μ is the chemical potential, and $\mathsf{Li_n}[\mathsf{z}]$ is the Poly-Logarithmic function of order n. The necessary thermodynamic variables are extracted by fitting to this function through standard least-squares optimization. Relations for number, entropy per particle, and temperature follow; σ is the root-mean-square size, λ is the wavelength of the imaging transition, and M is the magnification[1] of the imaging system:

[1]The magnification here is the area of an imaging pixel in the object plane of the imaging system, which for our primary imaging system is $(3.2\mu m)^2$/px.

$$N = A\sigma_x\sigma_y M^2 \frac{2\pi}{3\lambda^2} \frac{2\pi \mathsf{Li}_3[-\mathrm{z}]}{\mathsf{Li}_2[-\mathrm{z}]} \tag{5.22}$$

$$\frac{S}{k_B N} = 4\frac{\mathsf{Li}_4(-\mathrm{z})}{\mathsf{Li}_3(-\mathrm{z})} - \mathsf{Log}(\mathrm{z}) \tag{5.23}$$

$$k_B T = \frac{m\omega^2\sigma_i^2}{(1+(\omega \mathsf{t})^2)}. \tag{5.24}$$

The level of degeneracy characterized by the ratio T/T_F can be determined in two ways. Consistency between these two method should be verified to check for imaging non-idealities. First, T/T_F is a monotonic function of the fugacity measured directly from the shape of the momentum profile. This technique works best for T/T_F values between 0.1 and 0.5 (when the momentum profile differs significantly from the Gaussian, non-degenerate limit, and the fugacity function has not drastically diverged as shown in Fig. 5.9). This degeneracy factor can also be found directly by calculating the temperature from the size of the gas in expansion and the Fermi temperature from knowledge of the number and trap frequencies. Care should been taken to avoid imaging saturation and Doppler shift problems [112], as this will reduce the observed number of atoms and shift the calculated value of E_F.

$$\frac{T}{T_F} = \left(\frac{1}{6\ \mathsf{Li}_3(-\mathrm{z})}\right)^{\frac{1}{3}} \tag{5.25}$$

$$\frac{T}{T_F} = \frac{m\omega^2\sigma_i^2}{1+(\omega \mathsf{t})^2} \frac{1}{\hbar\bar{\omega}\,(6N)^{1/3}} \tag{5.26}$$

$$E_F = k_B T_F = \hbar\bar{\omega}(6N)^{1/3} \quad \text{where} \quad \bar{\omega} = (\omega_x\ \omega_y\ \omega_z)^{1/3} \tag{5.27}$$

Below $T/T_F \approx 0.1$, the shape of the gas does not change significantly, and limitations due to the signal-to-noise ratio in typical imaging systems inhibit accurate determination of T/T_F in this regime. Creating gases with $T/T_F \ll 0.1$ to explore the anti-ferromagnetically ordered state in the Hubbard model is a central goal in the quantum simulation community, and the lowest reported degeneracies have $T/T_F \approx 0.05$ [72, 73], with Ref. [74] reporting the first hint of anti-ferromagnetic correlations at a temperature 1.4 time times the Neel transition temperature.

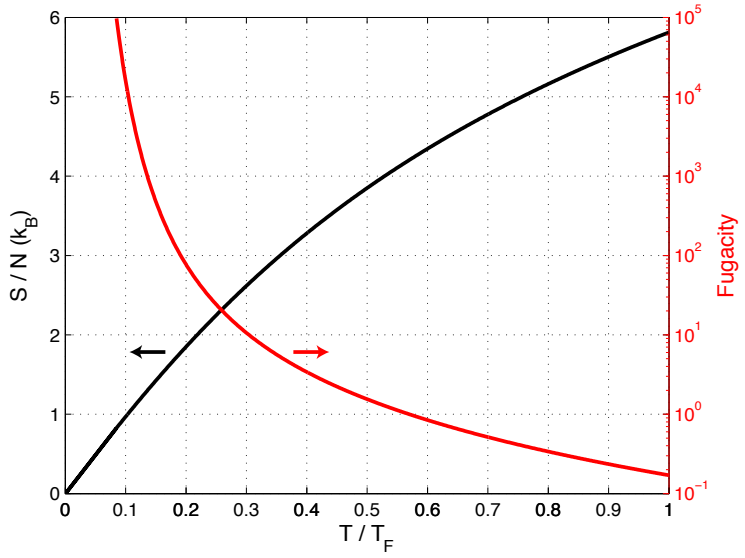

Figure 5.9: Relationship between T/T_F, S/N, and fugacity in a harmonically trapped system. The fugacity diverges rapidly below $T/T_F \approx 0.1$, and accurate determination of temperature from the shape of the optical depth images is difficult in this region.

5.3.2 Fermi-Dirac Statistics in a 3D Lattice

We start by considering a single-component, non-interacting lattice gas in the grand canonical ensemble. The Hamiltonian for the system is

$$H_{\mathsf{FD}} = \sum_{i=x,y,z} \left[2t \left(1 - \cos\left(\pi \frac{q_i}{q_B} \right) \right) + \frac{m\omega_i^2 x_i^2}{2} \right]. \tag{5.28}$$

Here we have taken the result from tight binding for the lattice dispersion, where t is the nearest-neighbor tunneling energy, and the harmonic trap frequency is ω. We only concern ourselves with states in the ground band, where q_i is in the range of $-q_B$ to q_B, and the bandwidth is $12t$. The grand potential for a single-component Fermi gas takes the form

$$-\beta\Omega = \sum_{\{\vec{x},\vec{q}\}} \log\left(1 + e^{\beta(\mu - \epsilon(\vec{x},\vec{q}))} \right), \tag{5.29}$$

as each state is either singly occupied or empty. The sum over all points in energy phase space is written as $\{\vec{x},\vec{q}\}$, and $\epsilon(\vec{x},\vec{q}) = \sum_{i=x,y,z} \left[2t \left(1 - \cos\left(\pi \frac{q_i}{q_B} \right) \right) + \frac{m\omega_i^2 x_i^2}{2} \right]$. Equations for number and total entropy follow from Eq. 5.16. Naturally, the occupation formula is the Fermi-Dirac distribution:

$$N = -\frac{\partial \Omega}{\partial \mu} = \sum_{\{\vec{x},\vec{q}\}} \frac{1}{e^{\beta(\epsilon(\vec{x},\vec{q})-\mu)}+1} = \sum_{\{\vec{x},\vec{q}\}} f_{\mathrm{FD}}(\epsilon(\vec{x},\vec{q}),T,\mu) \tag{5.30}$$

$$S/k_B = -\frac{\partial \Omega}{\partial T} = \sum_{\{\vec{x},\vec{q}\}} \left[\mathsf{log}\left(1+e^{\beta(\mu-\epsilon(\vec{x},\vec{q}))}\right) - \frac{\mu-\epsilon(\vec{x},\vec{q})}{T} \frac{1}{1+e^{\beta(\epsilon(\vec{x},\vec{q})-\mu)}} \right] \tag{5.31}$$

$$= \sum_{\{\vec{x},\vec{q}\}} S_{\mathrm{FD}}(\epsilon(\vec{x},\vec{q}),T,\mu). \tag{5.32}$$

The sums are converted to integrals with volume elements such that $dxdq = h$ in the semi-classical approximation:

$$N = \frac{1}{h^3} \int d^3\vec{q} \int d^3\vec{x}\ f_{\mathrm{FD}}(\epsilon(\vec{x},\vec{q}),T,\mu) \tag{5.33}$$

$$S/k_B = \frac{1}{h^3} \int d^3\vec{q} \int d^3\vec{x}\ S_{\mathrm{FD}}(\epsilon(\vec{x},\vec{q}),T,\mu). \tag{5.34}$$

These 6 dimensional integrals are reduced to 2 dimensional integrals by assuming radial symmetry in the x coordinate, and by making a variable substitution in q. In the spatial coordinates, $\int d^3\vec{x}$ becomes $\int 4\pi r^2 dr$ as is normally done; this is an approximation, and more careful treatment of this energy should be employed when necessary. We define $\epsilon_q = \sum_{i=1,2,3}[1-\mathsf{cos}(\pi q_i/q_b)]$ and $P(\epsilon_q)$ as the probability of a given value of the quasimomentum sum, with $P(\alpha) \equiv \int d^3\vec{q}\ \delta(\alpha-\epsilon_q)$, where δ is a Dirac delta function (this is analogous to a density of states in q). Using these definitions, we rewrite the thermodynamic integrals as

$$N = \frac{1}{h^3} \int P(\epsilon_q)\ d\epsilon_q \int 4\pi r^2 dr\ f_{\mathrm{FD}}\left(\frac{1}{2}m\omega^2 r^2 + 2t\ \epsilon_q,\ T,\ \mu\right) \tag{5.35}$$

$$S = \frac{1}{h^3} \int P(\epsilon_q)\ d\epsilon_q \int 4\pi r^2 dr\ S_{\mathrm{FD}}\left(\frac{1}{2}m\omega^2 r^2 + 2t\ \epsilon_q,\ T,\ \mu\right). \tag{5.36}$$

This rewriting of the thermodynamic integrals allows for fast numerical evaluation of Eq. 5.17 to solve for T and μ. Example code used to solve this problem is shown in Appendix C.1 for the non-interacting method and the Hartree-Fock method described in the next section.

Using this method, the temperature and chemical potential in the lattice are calculated while matching the number and total entropy in the gas. Sample profiles in space and quasimomentum are shown in Fig. 5.10 in an $s = 4E_R$ lattice with 20,000 atoms for S/N ranging from 1 to 4 k_B, corresponding to a range of T/T_F from 0.1 to 0.5. These profiles show the expected behavior that as the temperature rises, the

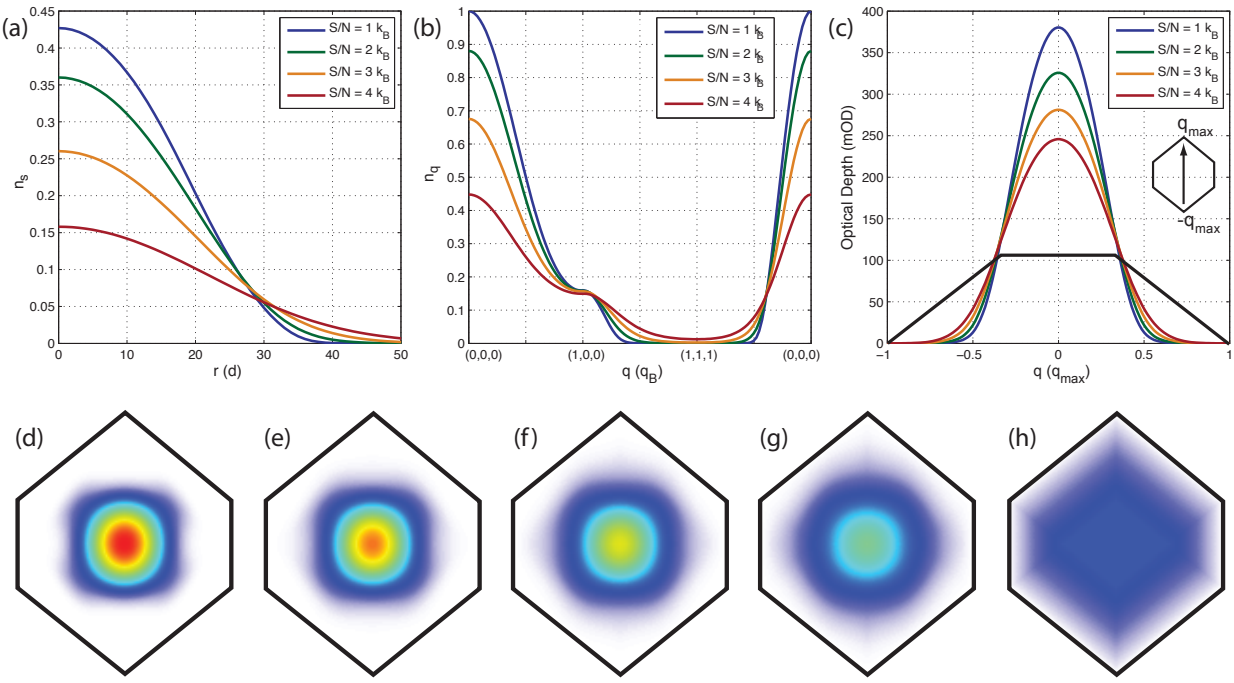

Figure 5.10: Non-interacting Fermi-Dirac calculation of the spatial, quasimomentum, and bandmapped optical depth for an $s = 4E_R$ lattice gas. (a) The occupation per spin state is plotted for an entropy of 1-4 k_B per particle. (b) The quasimomentum distribution is plotted along the standard trajectory in a 3D Brillouin zone. (c) Slices through column integrated bandmapped quasimomentum profile for the imaging projection described in Sec. 5.2.2 are generated at 10ms TOF. Vertical slices through the profile are shown as indicated by the inset; here $q_{\max} \approx \sqrt{3}q_B$. An infinite temperature gas is shown for completeness (black trace). (d-h) Full column integrated images are shown relative to the outline of the first Brillouin zone in projection for S/N = 1, 2, 3, and 4 k_B and for infinite temperature. The total number for these data is 20,000 atoms, harmonic confinement is $2\pi 100$ Hz, and $E_F \approx 5.7t$.

peak density decreases and the quasimomentum distribution broadens. Additionally, there is appreciable population along the band edge, but very little at the extreme points of the Brillouin zone. These data correspond to experimentally accessible values of entropy and number. The quasimomentum distributions acquired with the experiment have a non-trivial projection in imaging as described in Section 5.2.2, and sample profiles are shown to make the connection between the underlying and observed distributions.

In these thermodynamic calculations and the lattice transport experiment presented in Chapter 6, the single particle bandwidth, $12t$, is the dominant energy scale. For understanding the occupation and quasimomentum distributions in the lattice, all parameters should be viewed in relationship to the bandwidth. As we explore lattice depths from $s = 4$ to 7 E_R, the absolute value of $12t$ changes by more than a factor of two, and this changes the balance between the tunneling and confinement energies in the lattice, the location of the Fermi energy for a given number, and the distribution of quasimomentum. Importantly, it is not possible to create identical profiles in position and quasimomentum as the lattice depth is varied as the balance of

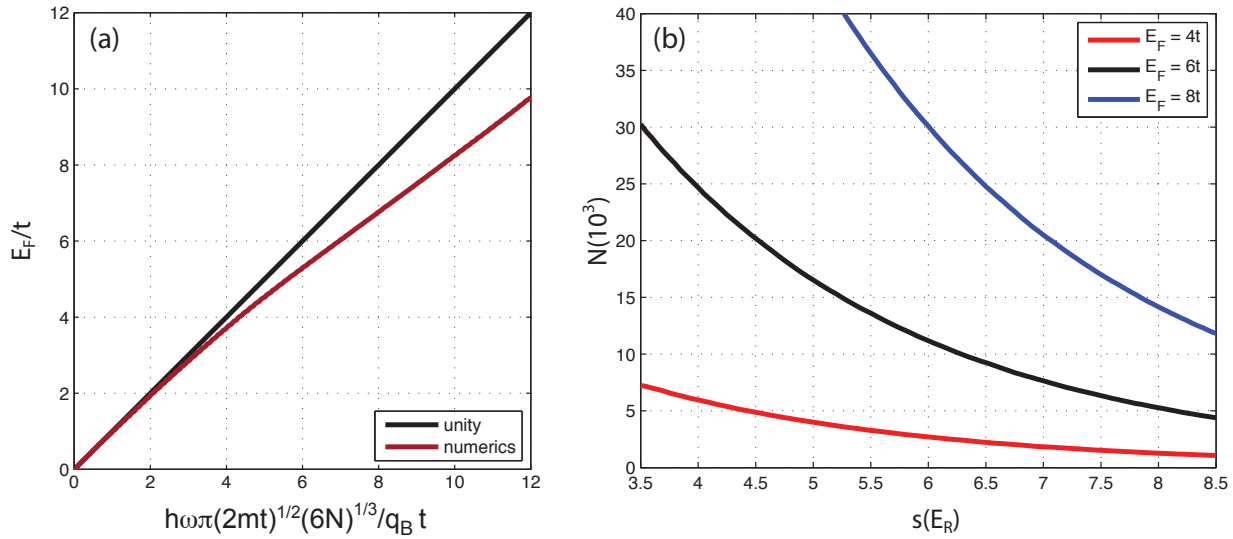

Figure 5.11: Comparison of Fermi energy in lattice versus particle number. (a) Comparison of Fermi energy in a 3D lattice with harmonic confinement to the Fermi energy scaling calculated in the effective mass limit. Each axis is normalized by the tunneling energy. (b) Number scaling with varying lattice depths for the Fermi energy fixed to $4t$, $6t$, and $8t$.

the bandwidth, confinement energy, and Fermi energy change. To explore this idea, we calculate the Fermi energy as a function of the lattice depth. In a harmonic potential, the Fermi energy $E_F = \hbar\bar{\omega}(6N)^{1/3}$ depends only on the trap frequency and number per spin state as in Eq. 5.27. We can extend this formula to the lattice dispersion in the effective mass limit by finding the curvature of the dispersion at $q = 0$. In this limit, the effective mass $m^* = q_B^2/(2\pi^2 t)$ and effective trapping frequency $\bar{\omega}^* = \bar{\omega}\sqrt{\frac{m}{m^*}}$. Using these approximations, the Fermi temperature in the effective mass limit is dependent on the trap frequency, the mass, the tunneling energy, and the particle number as

$$E_F = \hbar\bar{\omega}^*(6N)^{1/3} \;=\; \hbar\bar{\omega}\frac{\pi}{q_B}\sqrt{2mt}(6N)^{1/3}. \tag{5.37}$$

The value of the Fermi energy outside this limit can be calculated in the usual fashion by integrating the number of states below a given energy as

$$N_{E<E_F} = \frac{1}{h^3}\int d^3\vec{q}\int d^3\vec{x}\;\; \Theta(E_F - \epsilon(\vec{x},\vec{q})) \tag{5.38}$$

Here Θ is the Heaviside step function and $\epsilon(\vec{x},\vec{q})$ is the particle energy as a function of $\vec{x}$ and $\vec{q}$. The deviation of the Fermi energy from the effective mass scaling is shown in Fig. 5.11, and the number to match E_F to set fractions of the bandwidth is shown for the range of lattice depths explored is also shown. The variation in number required to fix E_F at a set fraction of the bandwidth can be quite large—for example, data taken

from $s = 4$ to $7E_R$ at $E_F = 6t$, N must vary from 24,500 to 7,600.

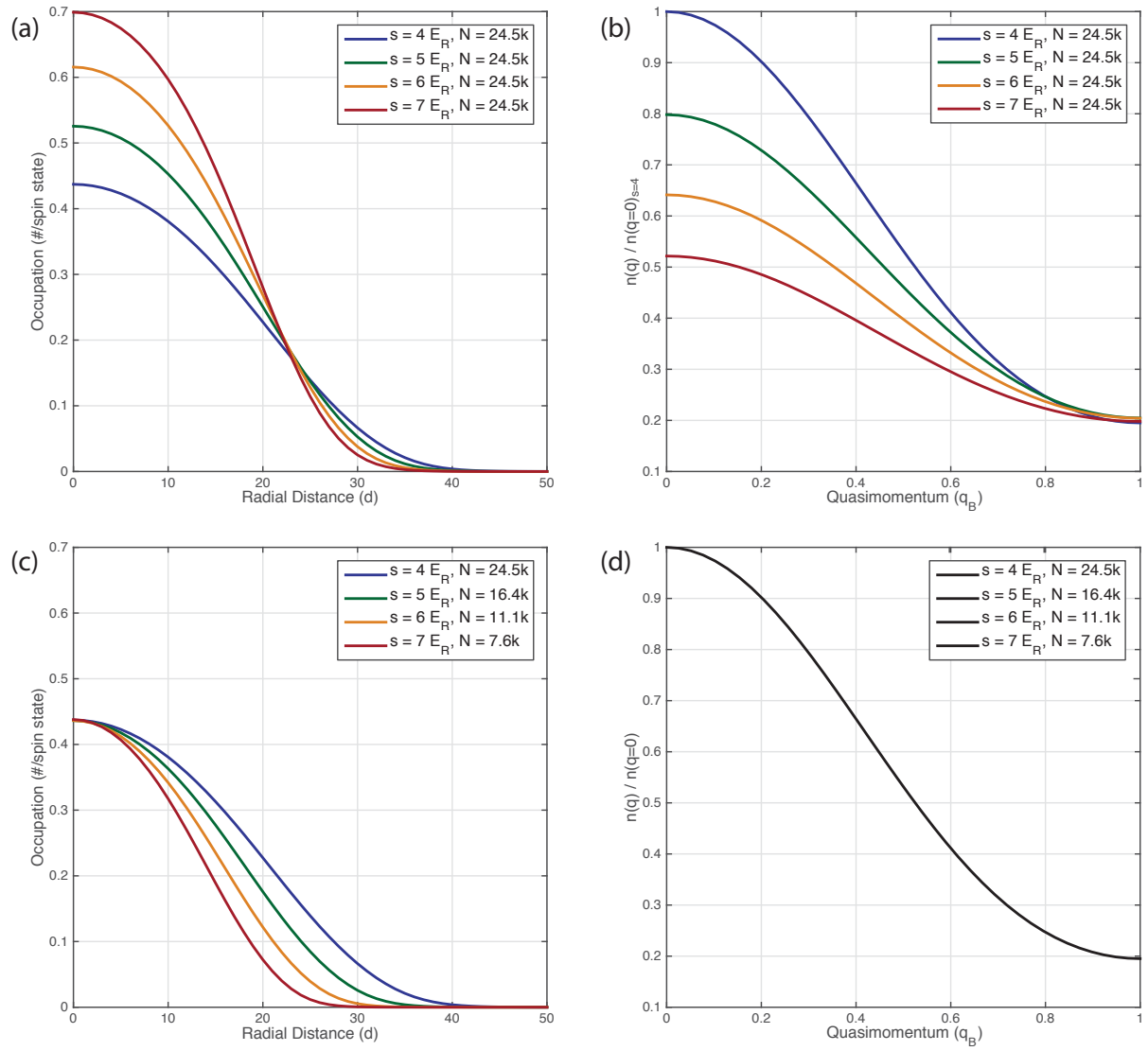

Figure 5.12: Non-interacting statistical mechanics comparison of spatial and quasimomentum distributions for $s = 4$ to $7E_R$ lattice gases at fixed N and fixed E_F/t. Thermodynamic profile are calculated assuming $S/N = 1.5$ and 2π 100 Hz harmonic confinement. (a-b) Profiles at fixed number N show variation in central filling and band population as lattice depth is varied. The quasimomentum distributions in (b) are normalized by the $s = 4E_R$ value at $q = 0$, and the profiles are plotted along a lattice direction. (c-d) Profiles adjusted such that $E_F = 6t$ show identical central filling, and the quasimomentum profile for these data are identical within the non-interacting assumption.

Data taken at constant E_F/t allows for gases with fixed central occupation and quasimomentum distribution to be created across a range of lattice depths. Figure 5.12 shows a comparison between the spatial and quasimomentum profiles of lattices gases with fixed atom number and fixed E_F/t for $s = 4$ to $7E_R$ and $S/N = 1.5$. The gases at fixed atom number show a large variation in central occupation and in the

uniformity of filling across the Brillouin zone. The thermodynamic profiles calculated for fixed E_F/t show identical quasimomentum distribution and central occupations; the only variation present within the non-interacting calculation is the RMS size of the gas in space, which must vary due to the change in number. Example thermodynamic quantities and comparison with values calculated after adding interactions with the self-consistent Hartree-Fock method are listed for relevant lattice depths and S/N for $E_F = 6t$ in Table 5.2.

5.3.3 Hartree-Fock

Interactions can be added into the non-interacting Fermi-Dirac calculation by including a density dependent energy offset. This approach is called the self consistent Hartree-Fock method, and requires iteratively solving for the density profile to determine the thermodynamic variable T and μ given the isentropic assumption and constraints on N and S. This approach has been successfully employed with Bose lattice gases [174, 118, 117, 122] where the validity of this method is based on agreement seen for experiments with large atom number in harmonic traps. The method is known to fail near the superfluid-Mott insulator phase transition [202], but this is irrelevant for the work done here.

We consider a two-component Fermi gas with an interaction energy U between the two components. The calculation is performed by considering only a single spin state, with interaction energy $U/2$ for each spin; and the Hamiltonian (for a single spin) is modified to be

$$H_{\mathsf{HF}} = H_{\mathsf{FD}} + \frac{U}{2} n(\vec{x}, T, \mu) \tag{5.39}$$

$$n(\vec{x}, T, \mu) = \frac{d^3}{h^3} \int d^3\vec{q}\; f_{\mathrm{FD}}(\epsilon_k, T, \mu). \tag{5.40}$$

This modifies the optimization problem stated in Eq. 5.17, as the density-dependent interaction energy is a function of both T and μ, and the equations for N and S stated in Eq. 5.33 and 5.34 are rewritten as

$$N = \frac{1}{h^3} \int d^3\vec{q} \int d^3\vec{x}\; f_{\mathrm{FD}}\big(\epsilon_k + \frac{U}{2} n(\vec{x}, T, \mu), T, \mu\big) \tag{5.41}$$

$$S = \frac{1}{h^3} \int d^3\vec{q} \int d^3\vec{x}\; S_{\mathrm{FD}}\big(\epsilon_k + \frac{U}{2} n(\vec{x}, T, \mu), T, \mu\big). \tag{5.42}$$

This represents a set of equations that can be solved iteratively to converge on the correct values of T and μ, and the computer code used to accomplish this is listed in Appendix C.1. In this computation, we define

a density profile that is iterated such that in iteration i the density profile is found by optimizing Equations 5.41 and 5.42 using the density from iteration $i-1$. This procedure is repeated until a stable profile is found. In practice, the computation starts with $U = 0$ and progressively increases the strength of the interactions until the desired value is reached, and iteration is stopped when the change in the measured value of T and μ reaches the desired precision.

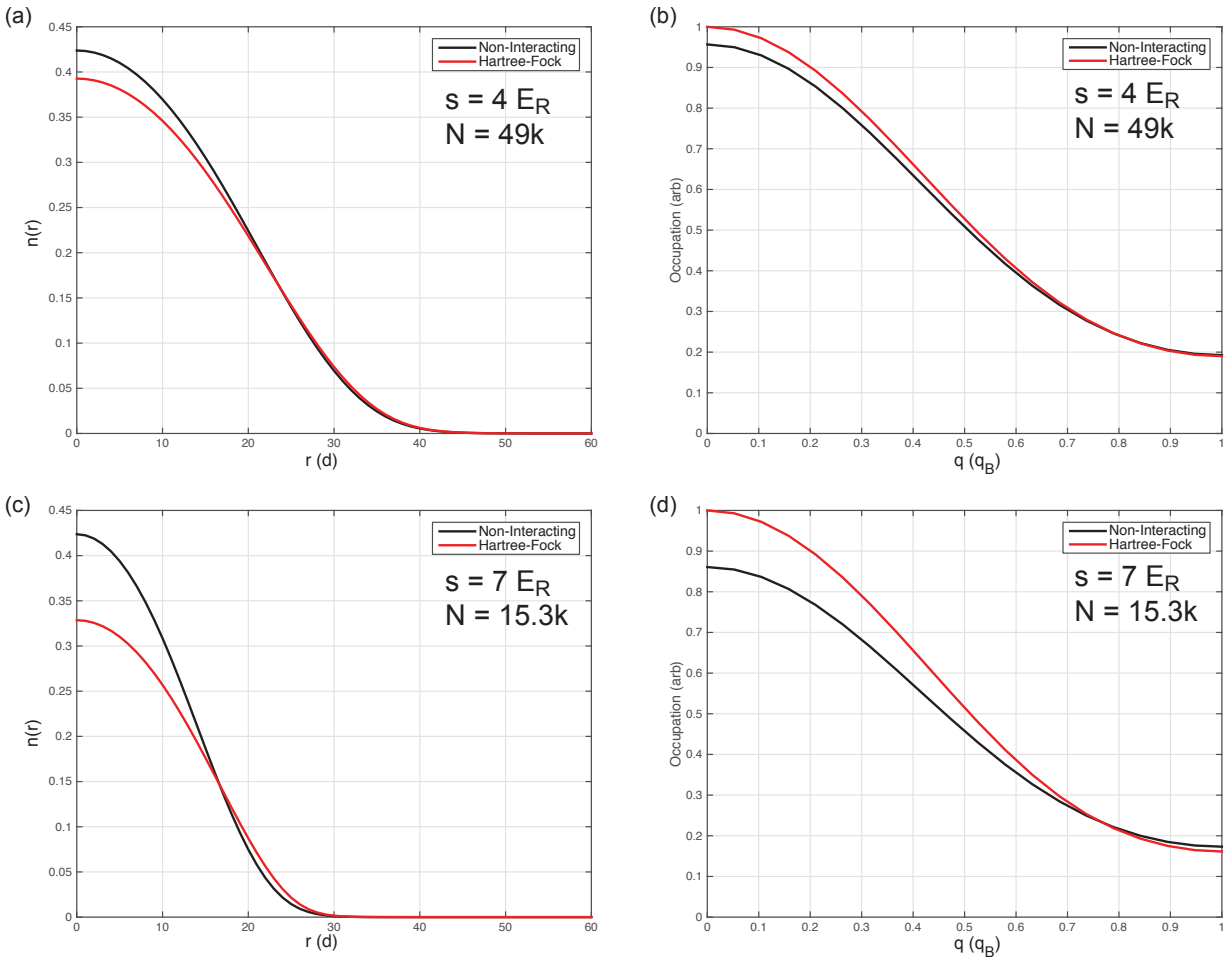

Figure 5.13: Comparison of spatial and quasimomentum distribution calculated in the non-interacting (black lines) and Hartree-Fock (red lines) limits. Comparison between numerically computed density profiles in lattice using a self-consistent, non-interacting calculation (black line) and an analogous Hartree-Fock calculation including the effects of interactions (red line). Parameters for this calculation are $E_F = 6t$ and S/N = 1.7 k_B per particle, and an external confinement of 2π $100Hz$. For the $s = 4E_R$ data, $t = 0.0862$ E_R and $U = 0.200$ E_R, and for $s = 7E_R$ data, $t = 0.0395$ E_R and $U = 0.357$ E_R.

A comparison between Hartree-Fock and non-interacting Fermi-Dirac predictions are shown in Fig. 5.13 for lattice gases with $s = 4$ and $7E_R$, E_F fixed at $6t$, and $S/N = 1.7k_B$. These traces show the expected effects from introducing interaction—the spatial profile broadens and the quasimomentum distribution narrows. This effect is more pronounced in the $s = 7E_R$ example, since U/t is roughly four times the value at

Input Parameters			Non-Interacting Fermi Dirac				Hartree-Fock			
s (E_R)	S/N	N_{tot}	T/t	μ/t	$n_s(0)$	$\frac{n_q(q_B)}{n_q(0)}$	T/t	μ/t	$n_s(0)$	$\frac{n_q(q_B)}{n_q(0)}$
4	1	49.0k	0.53	5.81	0.47	0.19	0.52	6.03	0.43	0.18
5	1	32.8k	0.53	5.81	0.47	0.19	0.51	6.15	0.41	0.17
6	1	22.2k	0.53	5.81	0.47	0.19	0.49	6.33	0.38	0.16
7	1	15.2k	0.53	5.81	0.47	0.19	0.48	7.56	0.35	0.14
4	2	49.0k	1.17	5.14	0.40	0.21	1.11	5.35	0.37	0.20
5	2	32.8k	1.17	5.14	0.40	0.21	1.08	5.48	0.35	0.19
6	2	22.2k	1.17	5.14	0.40	0.21	1.04	5.65	0.34	0.18
7	2	15.2k	1.17	5.14	0.40	0.21	1.00	5.88	0.31	0.17
4	3	49.0k	2.08	3.50	0.28	0.27	2.01	3.69	0.27	0.26
5	3	32.8k	2.08	3.50	0.28	0.27	1.96	3.83	0.26	0.25
6	3	22.2k	2.08	3.50	0.28	0.27	1.90	4.01	0.25	0.25
7	3	15.2k	2.08	3.50	0.28	0.27	1.84	4.24	0.24	0.24

Table 5.2: Comparison of non-interacting and Hartree-Fock statistical mechanics in a lattice with $E_F = 6t$. Within the isentropic assumption, thermodynamic quantities are calculated using harmonic confinement of $2\pi 100Hz$. Key points to note are that the non-interacting parameters are the same for a given S/N across the range of lattice depths. The difference between the non-interacting and Hartree-Fock calculation is minimal in the expected region of high entropy and low lattice depth. All values are calculated to an accuracy of ± 1 in their least significant digit. Number in this table is the total of a 50/50 mixed gas of two spins.

$4E_R$. At this lattice depth, the non-interacting limit overestimates the central occupation by more than 50 percent. This is to be expected—the lattice greatly increases the role of interaction and they should not be ignored! Table 5.2 presents the results from non-interacting and Hartree-Fock calculations of thermodynamic quantities across a range of lattice depths and entropies typical of experimental values for E_F fixed at $6t$. These values reinforce the behavior seen in Fig. 5.13 in that the non-interacting calculation increasingly fails at higher lattice and lower entropies per particle—the cases in which the density and U/t are least negligible. Comparisons to measured bandmapped quasimomentum images are provided in Chapter 6, and results shown in Figure 6.6 indicate that these distributions can largely be explained within the Hartree-Fock method described here.

5.3.4 Caveats to the Non-Interacting and Hartree-Fock Methods

There are several important caveats to the non-interacting and Hartree-Fock methods presented here. First, the semi-classical approximation underestimates the number of states available in the lattice plus trap system as described in Sec. 5.4.2. The underestimation of the available states effects both the location of the Fermi energy and the inferred value of the chemical potential. The error introduced in these approximations is quantifiable by performing analogous thermodynamic calculations using the exact eigenstates, and errors at the 20% to 30% level are expected in μ and E_F for the range of parameters explored. Second, since the

states used in the Hartree-Fock method are not the exact eigenstates, interactions are introduced in the approximation differently than they exist in reality. This introduces an unquantified error that is difficult to evaluate in the absence of quantum Monte Carlo calculations. Finally, neither of these approximations captures correlations between spin states that emerge at low entropies. For example, anti-ferromagnetic correlation does not appear in either of these methods.

5.3.5 Atomic Limit

In the deep lattice limit, tunneling can be ignored and interactions are the dominant energy scale. The zero tunneling limit is named the atomic limit, and thermodynamic properties are straightforward to compute within the local density approximation. We consider a two component ($\uparrow\downarrow$), interacting Fermi gas with interaction energy U, and N particles on a lattice with temperature T. The partition function on an individual lattice site is given by summing over grand canonical weights for the four possible spin occupation configurations (00), (10), (01), and (11):

$$Z_0 = 1 + 2\mathrm{z} + w\mathrm{z}^2 \quad \text{where} \quad \mathrm{z} = e^{\beta\mu} \quad \text{and} \quad w = e^{-\beta U} \tag{5.43}$$

The partition function is spinless and occupation on a site can be 0, 1, or 2. The grand potential is determined by summing over all lattice sites in the system, i,

$$-\beta\Omega = \sum_i \mathsf{log}\left(Z_0\right). \tag{5.44}$$

Equations for total number and entropy on a lattice site are given by taking the derivatives of Eq. 5.44 with respect to chemical potential and temperature:

$$N = -\frac{\partial\Omega}{\partial\mu} = \sum_i \frac{2\mathrm{z} + 2\mathrm{z}^2 w}{Z_0} \tag{5.45}$$

$$S = -\frac{\partial\Omega}{\partial T} = k_B \sum_i \left[\mathsf{log}(Z_0) - \frac{2\mu\mathrm{z} + (2\mu - U)\mathrm{z}^2 w}{T Z_0}\right]. \tag{5.46}$$

These equations fully characterize the atomic limit in an isotropic system for dimensionless variables μ/U and $k_B T/U$. The behavior of the on-site occupation, and entropy per particle are shown for four values of T/U in Fig 5.14. At low temperature in these plots, Mott plateaus become sharply defined where the occupation plot shows integer filling and the entropy plot shows plateaus at $k_B\mathsf{log}(2)$ and 0. At higher temperature, the effects of interactions become less apparent, and the Mott plateaus begin to lose contrast.

The entropy per particle is greatest in regions where particle number fluctuations are highest—at low fillings and between Mott plateaus.

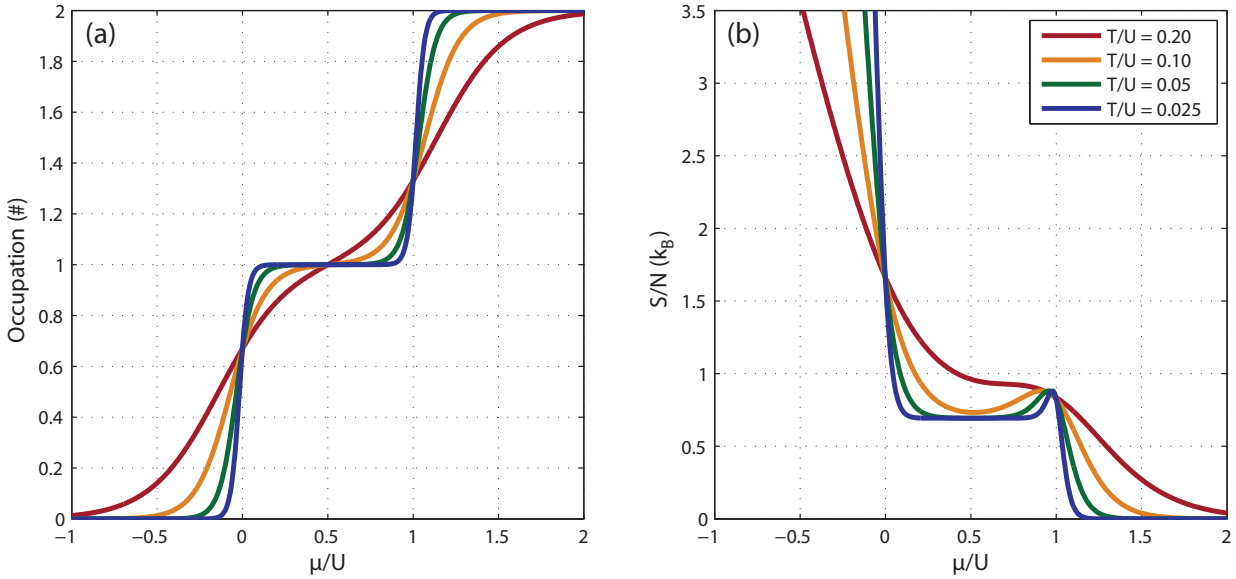

Figure 5.14: Site dependent occupation and entropy per particle in the atomic limit.Temperature dependence of occupation number per site (a) and the entropy per particle (b) in the atomic limit. Plateaus in number and entropy are clearly visible at integer fillings, showing both Mott and band insulating regimes. Notice that entropy per particle at unity filling approaches $k_B \log(2)$ due to the two possible spin configurations. The atomic limit is spinless, so the site occupation can be 0, 1, or 2.

The harmonic trapping potential is considered by taking the local density approximation in which the chemical potential acquires a spatially dependent shift given by the confinement energy:

$$\mu_i = \mu - \frac{1}{2} m\omega^2 r_i^2. \tag{5.47}$$

Within this approximation, T and μ can be calculated for a lattice gas with known entropy and atom number. This is performed in the same fashion as the non-interacting Fermi-Dirac and Hartree-Fock methods described earlier in this Section; here Equations 5.45 and 5.46 are summed to satisfy the known constraints on particle number and entropy. Sample density profiles within the local density and isentropic loading approximations are shown in Fig 5.15 for $S/N = 1$ and 2. The lowest reported S/N in an atomic Fermi gas with $S/N \approx 0.4 k_B$ [73], and $S/N \approx 1 k_B$ represents the practical limit of most experimental efforts. Mott plateaus in density are clearly visible for profiles at $S/N = 1 k_B$, but not in the higher temperature plot. The plots emphasize the strong dependence on the lattice profile of the total number of particles. Additionally, the Mott lobes shown here are far less clear than those observed in BEC lattice experiments in which S/N can be much less that $1 k_B$, as shown in Ref. [10], for example.

Atomic limit calculations are not used to infer quantities in this thesis, but the graphs in Figure 5.14 are a valuable tool for understanding some of the differences between trapped and uniform systems. From the perspective of the local density approximation, the chemical potential axes in this figure can be viewed as a rescaled radial position (with $r = 0$ at $\mu_{\max}$) that progresses to lower values of μ as the radius increases. This creates non-uniform distribution for both occupation and entropy. While it is obvious in the trapped system that the density should be spatially varying, the entropy term is less obvious. The general behavior is to have much of the total entropy of the gas stored at its periphery where number fluctuations are greatest.

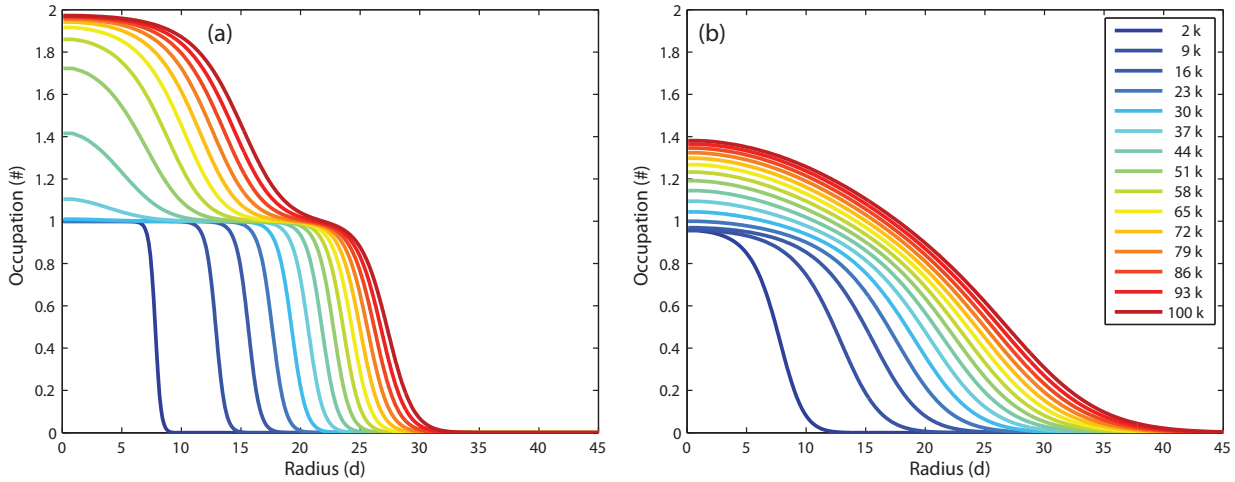

Figure 5.15: Radial density profiles in the atomic limit with the local density approximation shown for S/N = 1.0 k_B (a) S/N = 2.0 k_B (b). Traces correspond to total particle numbers from 2000 to 100,000 for a 3D lattice. The ratio of confinement to interaction energy, $m\omega^2 d^2/2U$, is 0.0022. The color scale is shared.

5.3.6 High-Temperature Series Expansion

The atomic limit can be extended by including non-zero tunneling terms as a series expansion in t/T. This is called the high-temperature series expansion, and this method is employed in a similar fashion to the atomic limit procedure presented earlier to infer thermodynamic quantities in lattice with known entropy and atom number. Here the grand potential takes the form

$$-\beta\Omega/N \;=\; \mathsf{log}\left(Z_0\right) + \sum_{r=2}^{\infty} (\beta t)^r Z_0^{-r} A_r\left(\mathrm{z}, e^{\beta U}\right), \tag{5.48}$$

where the functions A_r depend on the coordination number of the lattice and the possible interaction graphs. The methods for calculating A_r are described in Ref. [150]. To second order, the grand potential becomes

$$-\beta\Omega = \mathsf{log}\left(Z_0\right) + 3\left(\frac{\beta t}{Z_0}\right)^2 \left(2\mathrm{z}(1+w\mathrm{z}^2) + \frac{4\mathrm{z}^2}{\beta U}(1-w)\right). \tag{5.49}$$

From this approximate grand potential, expressions for the local N and S are found using expressions analogous to Equations 5.45 and 5.46.

The high-temperature expansion has a limited regime of convergence, and as its name implies, the expansion fails at temperatures when $\beta t > 1$. The exact regions of convergence depend on both the temperature and chemical potential, and a detailed study of the convergence of the series expansion to tenth order in comparison with dynamical mean-field theory can be found in Refs. [38, 87, 85]. One benefit of the series expansion is that it works well at half filling, where dynamical mean-field theory fails. This expansion fails to converge across the entire range of data presented in Chapter 6 and is not used.

5.4 Eigenstates in a Lattice with Harmonic Confinement

The quantum states in a lattice with harmonic confinement are fundamentally different from the Bloch waves in an isotropic lattice. Bloch wavefunctions extend over all of space with the form $\psi(r) = e^{ikr}u(r)$, where $u(r)$ has the same periodicity as the lattice [8]. Adding a harmonic trapping potential removes the spatial symmetry of the system and introduces a new energy scale set by the confinement. The wavefunctions in this new potential have features of both the Bloch waves from the lattice and of the quantum harmonic oscillator. The low energy states in this potential have wavefunctions that are simply the harmonic oscillation states modulated by the lattice potential, as shown in Fig. 5.16a. The 1D Schroedinger equation is solved for the lattice with harmonic confinement using the code modified from Appendix I.4.1 of Ref. [135].

5.4.1 Relevance of Localized States

The competition between tunneling and harmonic confinement causes the high energy states to take a form that is spatially localized at the edges of the gas with minimal weight in the center of the trap, as shown in Fig. 5.16(b). This happens when the harmonic confinement energy of the state exceeds the single-particle bandwidth of $4t$. The center region of the trap for these high energy states is energetically forbidden and the wave function is exponentially suppressed in the center of the trap, leaving little probability for transport between the edges of the gas. The energy levels of trapped systems can be classified into low and high energy states based on the ratio of the confinement and tunneling energy scales. This ratio,

$$q = \frac{4t}{\frac{1}{2}m\omega^2 d^2}, \tag{5.50}$$

sets the location of the first quantum state localized to the edges of the trap. Reference [173] give this critical

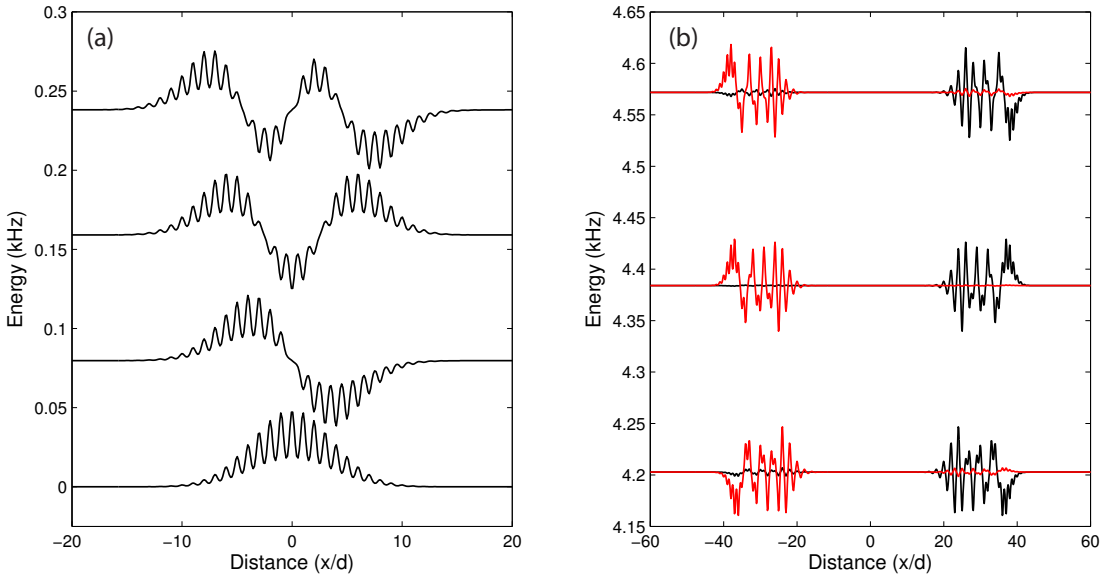

Figure 5.16: Quantum states in a 1D lattice with harmonic confinement. (a) Probability amplitude of four lowest energy states in 4 E_R, 1D lattice plus harmonic confinement of $2\pi 100$ Hz. Wave functions were calculated numerically using the method of finite differences on the Schroedinger equation. Each state is vertically offset by its energy. (b) Probability amplitude of localized states in same potential. n = 62, 64, 66 (black) and n = 63, 65, 67 (red). The high energy localized states are not symmetric about the center of the system and do not support transport across the entire system.

quantum number separating low from high energy states as

$$n_c \simeq 2||\sqrt{q/2}||. \tag{5.51}$$

The double bars indicate rounding to the closest integer. Fig. 5.17 shows the probability density for the lowest hundred energy states for lattice depths of 4 and $7E_R$. The state corresponding to critical quantum number calculated from Equation 5.51 is shown in red.

The effects of the localized state were first observed by looking at dipolar oscillations of a Fermi gas in a 1D optical lattice [142]. These states were later directly observed by radio-frequency spectroscopy [151] proving that a spatially dependent energy gap exists in these systems. It is also important to note that while these states are localized to the edge of the gas, the states do not have zero conductivity and can support motion around the edge of the gas, as was observed in Refs. [161, 175]. This effect is striking in one dimension where the number of non-localized states is very low, but it has also been observed in higher dimensions [198].

For the transport experiments considered in Chapter 6, it is important to ask whether these states play a significant role. Data in these experiments is taken in a $2\pi 100Hz$ trap for $s = 4$ to $7E_R$. The critical quantum

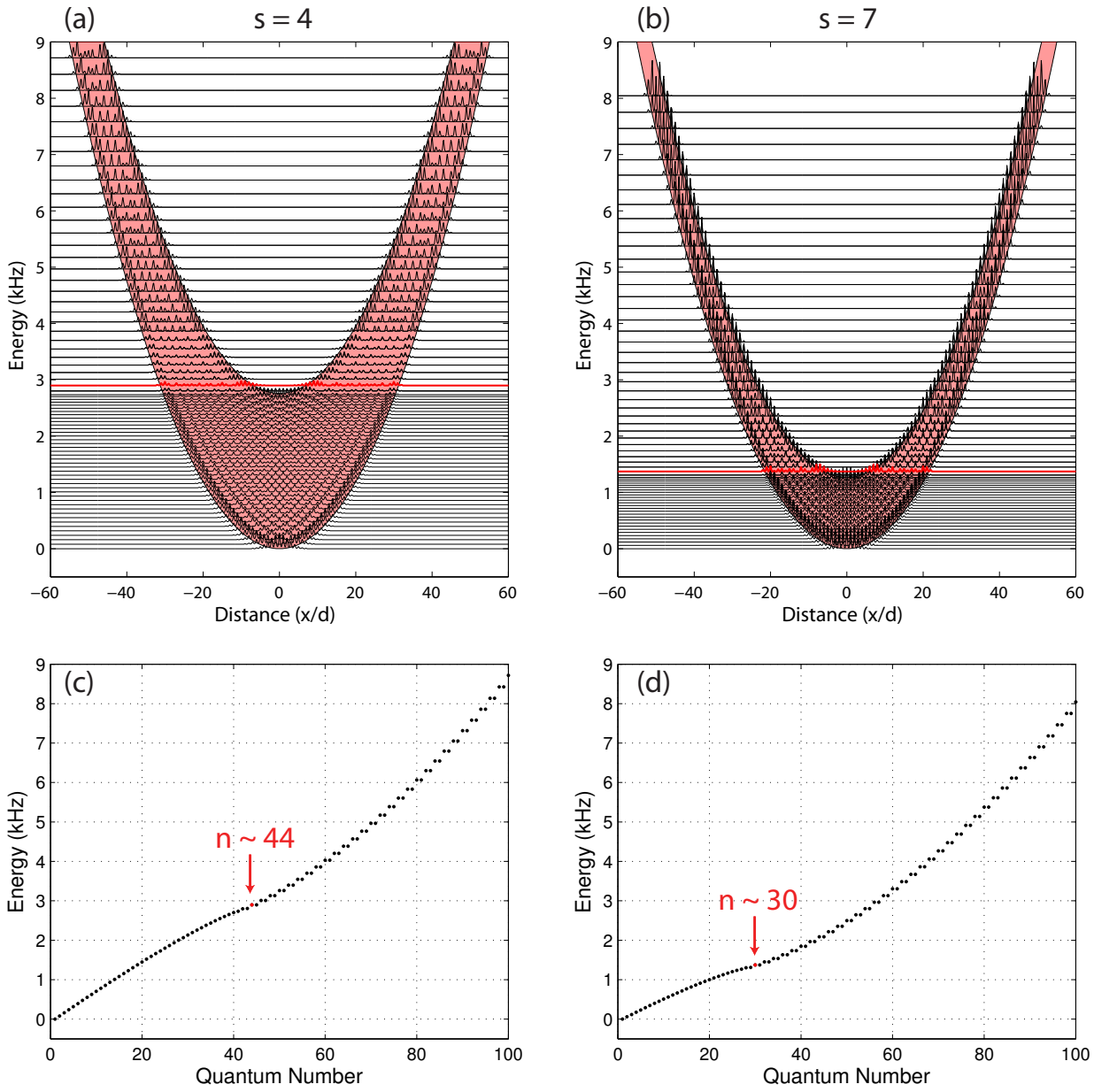

Figure 5.17: Energy spectrum in 1D lattice with harmonic confinement. (a,b) The first 101 eigenstates for potassium atom in a 1D lattice with depths of 4 and $7E_R$ and harmonic confinement of $2\pi 100$ Hz are calculated numerically. The probability density of each state is plotted with an offset given by the energy of each state. States below a critical energy are extended across the system, while the remainder have their probability amplitude confined to the edges of the system. The classically allowed phase space corresponding to energies within the bandwidth of $4t$ above the trap energy is shaded in red. The first localized state for $n = n_c$ is labeled in red. (c,d) The dispersion relation of these states is shown. Low energy scaling is consistent with the spacing of harmonic oscillator levels. The first localized state is again indicated in red, with this number decreasing at higher lattice depths.

number for these data vary from $n_c = 44$ and 30, respectively, indicating a span from 85,000 and 27,000 states per spin that allow for full transport in 3D at $s = 4$ and $7E_R$. The number of non-localized states

becomes rapidly lower at higher lattice depths as the bandwidth shrinks relative to the confinement energy. The fraction of localized states occupied can be evaluated within the Hartree-Fock calculation (presented in Section 5.3.3) by counting the number of states whose energy exceeds the bandwidth. This fraction can be defined as $f_{\rm loc} = N(E > 12t)/N_{\rm tot}$, and the number of localized states can be evaluated through an integral similar Equation. 5.41 as

$$N(E > 12t) \;=\; \frac{1}{h^3}\int d^3\vec{q}\int d^3\vec{x}\;\; \Theta\big(\epsilon_k + \frac{U}{2}n(\vec{x}) - 12t\big)\;\; f_{\rm FD}\big(\epsilon_k + \frac{U}{2}n(\vec{x}), T, \mu\big). \tag{5.52}$$

Here, the Heaviside step function Θ limits the integral to only states with energies that exceed the bandwidth. Appreciable population of these states is predicted for $s \geq 6E_R$ for the transport data presented in Section 6.2. The limitations of these states against transport in 3D are an open question, as these states are restricted to move around the periphery of the gas.

5.4.2 Exact Number Distribution vs. the Semi-Classical Approximation in 3D

The semi-classical approximation used to perform the thermodynamic integrals for self-consistently determining temperature and chemical potential in the lattice plus trap system divides phase space into volumes of $d^3x\, d^3q = h^3$. In this approximation, one quantum state fits into each voxel, and the energy of that states is calculated from the sum of its kinetic and potential energy in the non-interacting limit described in Sec. 5.3.2. The error introduced by this approximation can be estimated by comparing the energy spectrum from the semi-classical approximation to that found from the exact solution of the Schroediger equation. The exact energy spectrum of the 3D system is calculated by solving the 1D Schroedinger equation, enumerating all possible 1D occupation numbers in 3D, and ordering the states by total energy. Figure 5.18 plots the number of available states less than the Fermi energy from the semi-classical approximation and the exact solution of the lattice with harmonic confinement. This figure shows that the semi-classical approximation underestimates the number of available states at all energies with the largest fractional error at low E_F. The fractional error decreases with increasing Fermi energy, and for $E_F = 6t$, the error is at the 30% level. The self-consistent approach for finding T and μ in the lattice plus trap detailed in Sec. 5.3 can be performed using the exact eigenstates. For typical experimental parameters, the temperature calculated using the exact and semi-classical states can be used interchangeably within the experimental uncertainty in N and S/N. Significant differences arise in the determination of μ between the two methods. This is expected given the large fractional errors in total number shown in Fig. 5.18(b).

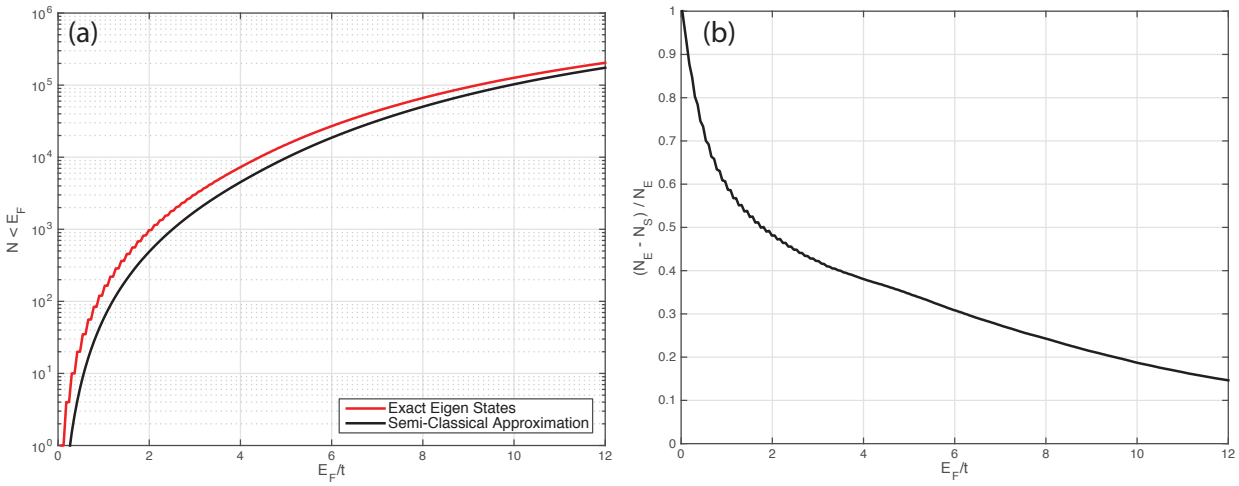

Figure 5.18: Comparison of exact eigenstates and semi-classical distribution of states in a 3D lattice with harmonic confinement. Calculations of these distributions are performed with $s = 4E_R$ and $\omega = 2\pi 110$ Hz, radially symmetric confinement. Exact eigenstates are calculated using the 1D method assuming separability in 3D. (a) The number of states (for a single-spin component) is plotted versus the Fermi energy from both the semi-classical and the exact methods. The semi-classical approximation underestimates the number of available states at all energies. (b) The fractional error of the semi-classical approximation is plotted versus Fermi energy. Here, the number of states are N_S from the semi-classical method and N_E from the exact Eigenstates in 3D; the fraction error from the semi-classical approximation is $(N_E - N_S)/N_E$. For $E_F = 6t$ the error is $\approx 30\%$. As expected, the error introduced by the semi-classical approximation decreases at higher E_F.

Chapter 6

Transport Experiments in Lattices

6.1 Motivation and Introduction

This chapter describes experimental studies of the transport behavior of strongly correlated gases in optical lattices. This work is motivated by the many open questions surrounding the field of strongly correlated materials that exhibit, for example, the phenomena of high-temperature superconductivity [114], heavy fermion superconductivity [194, 160], T-linear resistivity at low temperatures [24], and giant magneto-resistance [53]. The goal of quantum simulation with optical lattices is to realize one of the simplest strongly-interacting Hamiltonians, namely the Hubbard model, in a well controlled and characterized manner and to ask what physics can be produced from this minimal model. From this starting point, complexity can be introduced in a controlled manner and direct comparisons can be made between experiment and theory. Experiments performed with cold atoms should not be thought of as direct tests of materials; rather, they are the present state-of-the-art sandbox for testing models of strongly correlated materials.

In materials where strongly correlated phenomena are present, competition between electron-electron and electron-phonon interactions, kinetic energy, and disorder may lead to a number of distinct low entropy phases. The phase diagram for the cuprate high-temperature superconductors shown in Fig. 6.1 beautifully illustrates this point. At low temperature and half filling, the cuprates (and the Hubbard model) form an anti-ferromagnetic Mott insulator as the spin-spin and on-site interactions dominate the tunneling energy and effect of thermal fluctuations—these interactions are sufficiently strong that the anti-ferromagnetic phase survives to three hundred Kelvin. Doping away from half-filling disrupts the anti-ferromagnetic state and creates several metallic states at high temperature. At low temperatures, two superconducting "domes" arise for a range of doping in hole- and electron-doped materials, and the largest motivating factor for studying these materials is their high critical temperatures. At optimum doping, several cuprate and iron-based superconductors have critical temperatures above 100 Kelvin. This high critical-temperature for superconductivity and the lack of an underlying microscopic physical model has motivated a huge amount of interest in this class of materials.

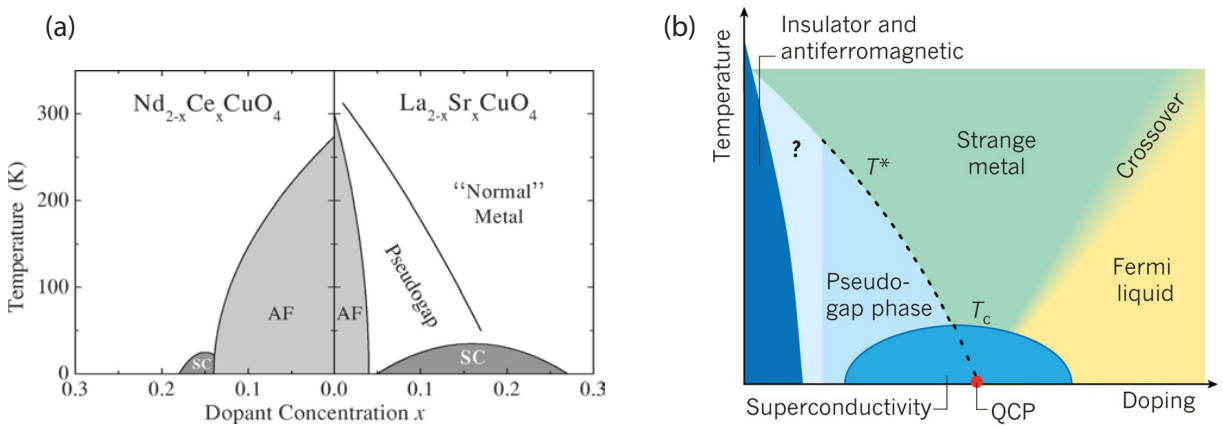

Figure 6.1: Phase diagram for the hole- and electron-doped cuprate superconductors. (a) Several low temperature phases appear as the cuprate doping is changed including the superconducting (SC), antiferromagnet (AF), and metallic states. (b) An expanded view of the hole doped side of the phase diagram shows the division of the metallic regime into the well understood Fermi liquid and areas of active research, including the strange metal and pseudogap phases. These figures are reproduced from Refs. [34] and [204].

At temperatures higher than those supporting antiferromagnetism and superconductivity, there are several metallic phases, including the pseudogap and strange metal regimes. Importantly, these phases are less well understood than the superconducting state [114, 79], and it is hoped that an improved microscopic model of these regimes will inform our understanding of superconductivity in these materials. The pseudogap phase is characterized by a partially gapped Fermi surface and conductivity that varies along different crystal directions. It is possible that pre-formed Cooper pairs in this state lead to this behavior [39], and related work with ultracold gases studying the BEC-BCS crossover [172, 222, 29, 21, 155, 221] may be relevant. Recent experiments have shown that relaxation rates of quasiparticles in the pseudogap regime follow a Fermi-Liquid T^2 relaxation rate [140], but aspects of these experiments are not consistent with predictions from Fermi-Liquid and raise additional questions. The strange metal occurs at temperatures above T^* (higher than the pseudogap state) and is so named because it has T-linear scaling of its resistivity [35, 24] and other properties divergent from Fermi liquid theory.

Doping is adjusted in the cuprates to modify the charge carrier density to access the superconducting regime. This process inherently introduces disorder as atomic substitutions have been made in the lattice. This disorder may play a significant role in these materials [139, 31, 32, 33], and while theoretical predictions expect disorder to destroy the d-wave paring in the cuprates, measurements indicate that the low-energy excitations are protected from the effects of disorder [60]. Strontium ruthenate, another novel superconductor, has triplet π-wave pairing symmetry with a quantum critical point that can be tuned via an external magnetic field. This critical point is highly sensitive to disorder, and superconductivity is only

seen in extremely clean samples [123, 124]. The anomalous behavior in the cuprates and the sensitivity of the ruthenates to disorder motivates further study in the controlled environment afforded by ultracold gases in optical lattices.

Work in this chapter explores the analog of the strange metal regime in the Hubbard model. Two series of experiments are described that probe the role of disorder, interactions, and relaxation dynamics, motivated by the open questions described above. The first set of measurements examines the response of a gas in a disordered lattice to an external impulse. In this measurement we find disorder-induced localization and an interaction driven metal-insulator transition. We also explore the temperature dependence of localization, motivated by predictions that many-body localized states have a critical temperature below which there is zero conductivity. This work is published in Reference [101]. Theoretical analysis of these results by Vito Scarola [179] has shown this observation is consistent with Anderson localization of Hubbard quasiparticles and is discussed in depth. The second group of measurements explores the relaxation of non-equilibrium quasimomentum distributions over a range of interaction strengths and degeneracy. This work relates to fundamental questions about the origins of resistance in strongly correlated materials. All experiments we discuss here involve gases with entropy per particle much higher than the majority of condensed matter experiments—temperatures at their lowest will be a tenth of the Fermi temperature. Recently, experiments in a compensated optical lattices are approaching the Neel temperature where antiferromagnetic correlations are observed at $T/T_F \approx 0.05$ [73].

6.2 Localization in a Disordered Lattice

6.2.1 Properties of the Disordered Lattice

We create an optical lattice with controlled disorder by superposing optical speckle on a three-dimensional optical lattice. The speckle is generated from a high numerical aperture imaging system using 532 nm light and a holographic diffuser to imprint random phases across the beam creating a random, repulsive potential. The statistical properties of the speckle intensity are known from ex-situ measurements and knowledge of the speckle imaging system, as described in detail in Chapter 3. The full numerical aperture of the speckle imaging system is used to create fine correlation length speckle. The intensity autocorrelation function is cylindrically symmetric about the axis of propagation, with autocorrelation lengths of 310 nm radially and 1600 nm axially. To minimize the correlation length along any lattice direction, the speckle propagates vertically in the experiment, roughly along the (111) direction in the lattice similar to experiments with bosons in disordered optical lattices [211, 156, 135]. This orientation allows for uncorrelated Hubbard

parameters along each of the lattice directions [212].

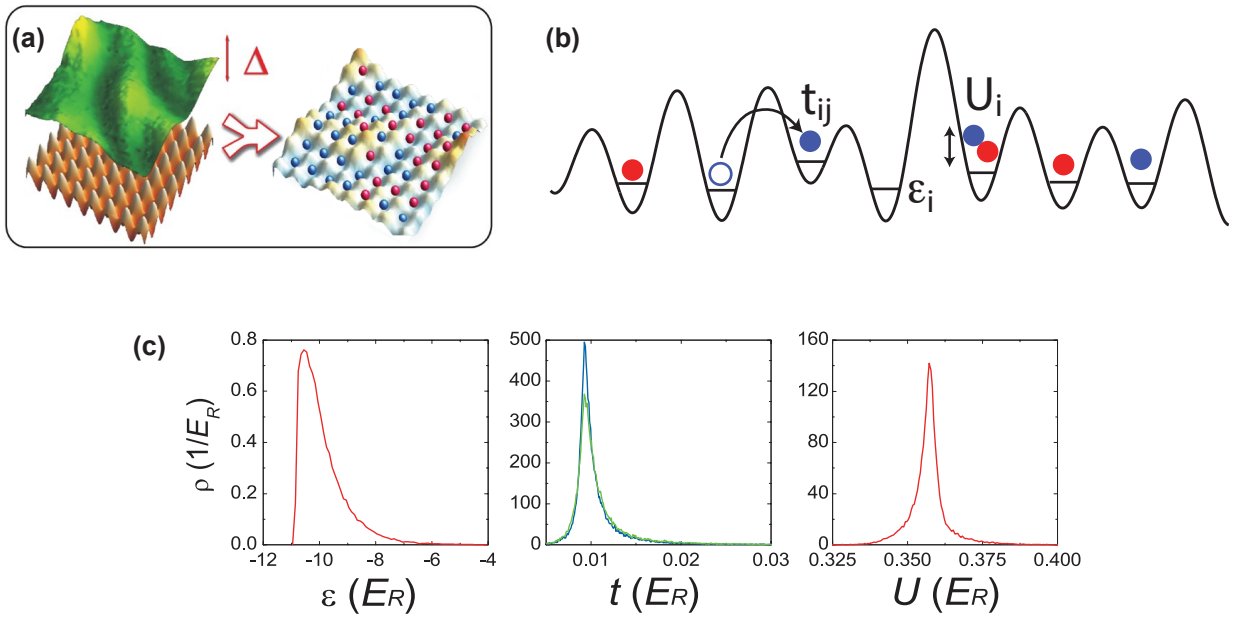

Figure 6.2: Illustration representing the tunneling and interaction energies in the disordered Hubbard model. (a) Disorder is added to the optical lattice by superposing a three-dimensional optical speckle field (green) on the simple cubic lattice. A two-dimensional slice of the resultant potential is shown in false color on the right, where the red and blue spheres indicate the location of atoms with spin up and down. (b) A 1D slice of the lattice indicates that the tunneling, interaction, and occupation energies become site dependent in the disordered lattice. (c) The Hubbard parameters probability distributions in the disordered lattice are shown for a $s = 14E_R$ lattice with $\Delta = 1E_R$; here ρ is the probability density. Each parameter is broadened by the disorder, with the largest effect on the occupation and tunneling energies, which are diagonal and off-diagonal disorder. Hubbard parameter probability distributions are reproduced from Ref. [212].

Adding disorder to the lattice causes the Hubbard parameters to become site-dependent and broadens the distributions of tunneling, interaction, and on-site energies from their isotropic values, as shown in Fig. 6.2. The disordered Hubbard model is written in Eq. 6.1, where t_{ij} is the tunneling energy between sites i and j, $\hat{c}^\dagger_{j\sigma}$ ($\hat{c}_{j\sigma}$) are fermion creation (annihilation) operators for spin σ on site i, U_i is the interaction energy on site i, $\hat{n}_i = \hat{c}^\dagger_{i\sigma}\hat{c}_{i\sigma}$ is the number operator for site i with spin $\sigma =\uparrow$ or $\downarrow$, ϵ_i is the occupation energy on site i, and $1/2m\omega^2 r_i^2$ is the harmonic confinement provided by the trap:

$$H_{\mathrm{DFHM}} = -\sum_{<ij>,\sigma} t_{ij}\left(\hat{c}^\dagger_{j\sigma}\hat{c}_{i\sigma} + h.c.\right) + \sum_i U_i \hat{n}_{i\uparrow}\hat{n}_{i\downarrow} + \sum_{i,\sigma}\left(\epsilon_i + \frac{1}{2}m\omega^2 r_i^2\right)\hat{n}_{i,\sigma}. \tag{6.1}$$

The distributions of these disordered parameters are calculated numerically using the known lattice and disorder distributions, as described in Ref. [212]. The largest effect of the disorder is to broaden the occupation and tunneling energy distributions—creating both diagonal and off-diagonal disorder—while

the interaction energy is minimally affected by the disorder. The distribution of t and U broaden about their isotropic values, while the distribution of on-site energies is shifted to higher energies with a standard deviation approximately set by Δ, as shown in Figure 6.2(c). None of the Hubbard parameters in this model are spin dependent.

The trapping potential in these experiments creates spatial variation in occupation and entropy, as discussed in detail in Chapter 5. The phases produced in the lattice depend strongly on the interplay of the harmonic confinement, bandwidth, and the chemical potential—a beautiful example of this is the wedding-cake structure observed in BEC optical lattice experiments in which Mott insulator regions of progressively smaller occupation are surrounded by a shell of superfluid [63]. The confinement, bandwidth, and number can be encapsulated in a single quantity called the characteristic density $\tilde{\rho} = \frac{N}{2N_0}$, where $N_0 = \frac{4\pi}{3}\left(\frac{12t}{m\omega^2 d^2}\right)^{3/2}$. Here d is the lattice spacing. Defining a global phase for the system allows a zero temperature phase diagram to be drawn for the trapped Hubbard model as a function of only $\tilde{\rho}$ and the ratio U/t, as shown in Fig. 6.3. For low U/t, the system divides into a metallic state labeled "L" in analogy to Fermi liquids and a band insulator "B" for higher number. All experiments presented in this chapter take place in the "L" regime with $\tilde{\rho} < 5$ and $U/t < 12$. For $U > 12t$ regions of Mott and band insulator form in the gas, and depending on the number of atoms in the experiment, the central region can have occupation of 1 or 2 atoms per site as shown in the atomic limit profiles shown in Figure 5.15. Work using dynamical mean field theory to explore the Hubbard model at half filling has shown that aspects of this diagram may be incorrect, and the zero temperature Mott insulator regime may be larger than previously expected [128]. Additionally, the definition of $\tilde{\rho}$ is not standardized, and several similar expressions can be found in the literature [175, 176, 87, 181].

The speckle potential has finite extent in space, and the intensity envelope is uniform to within a few percent over the lattice gas. As described in Chapter 3, the speckle intensity envelope has a Gaussian waist ($1/e^2$ radius) of 170 microns in the x-z plane of the experiment and a Rayleigh range of 400 microns along the y-direction. This waist of the speckle is directly measured in the experiment by pulsing the speckle potential and observing the impulse given to a hot gas. The measured deflection in position can be translated into a local mean gradient in the intensity [100]. Typical lattice gases explored in this work have radial occupations that extend across 20 to 30 lattice sites—this is less than a tenth of the measured waist, and the speckle envelope is effectively infinite for our system size. The mean speckle intensity Δ is inferred at the position of the atoms from knowledge of the beam power, beam waist, and clipping in the speckle imaging system. This value depends strongly on the waist on the speckle envelope, and the measured value for the waist used to calculate Δ disagrees with ex situ predictions as described in Chapter 3. From this we estimate a systematic uncertainty in the absolute speckle intensity of 40% and statistical uncertainty of 10%. In the future, direct

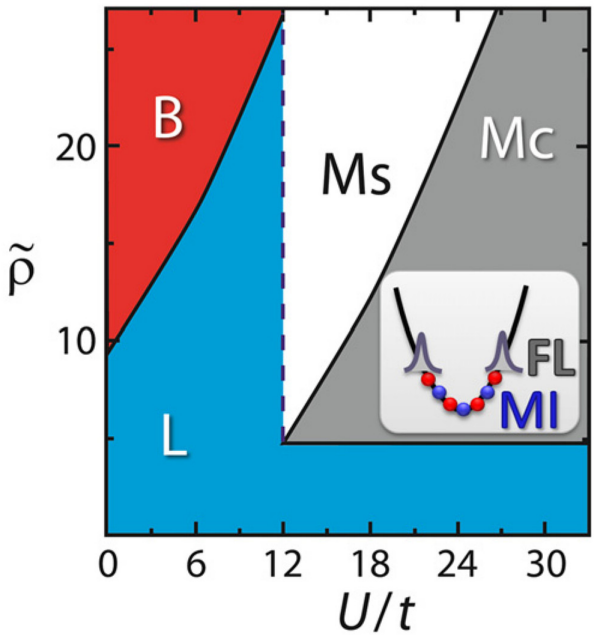

Figure 6.3: Zero temperature phase diagram for the Hubbard model in a harmonically trapped system. Phases are Fermi Liquid (L), band insulator (B), central Mott-insulator (Mc), and shell of Mott-insulator (Ms). Image reproduced from Ref. [136]. Results from dynamical mean field theory exploring the Hubbard model at half filling have indicated that the Mott insulator regime may extend to lower values that shown here [128].

measures to calibrate the the speckle intensity should be explored. One possible method for calibrating the absolute value of Δ would be to perform spectroscopy on a tightly confined 1D gas. The addition of speckle would create a known distribution of harmonic oscillator spacings whose mean value could be related directly to Δ.

6.2.2 Observing Localization

We probe the role of disorder in a strongly correlated lattice gas by measuring the response of the quasi-momentum distribution to an external force. If the gas is in a metallic or conducting state, a current will arise due to the external force, and the quasimomentum distribution will shift to acquire a non-zero average velocity. The extent of this response is related to the conductivity of the system. As disorder is applied to the system, states can become localized due to Anderson and other related types of localization, such as many-body localization [11, 12]. Here, we consider a single-band Hubbard system in which states begin localizing at the top and bottom of the band [103]. As the level of disorder increases, the two mobility edges will converge and the conductivity of the system will decrease. Conductivity in the system falls to zero when the two mobility edges cross such that all states in the band are localized. We observe analogous behavior

in a disordered optical lattice in which transport initiated by external force progressively decreases with increasing disorder. The conductivity at high disorders falls below our experimental resolution, and we associate this behavior with the localization of all states in the ground band. Our measurement of the transport has finite resolution, as in any measurement of conductivity, and we identify the minimal disorder necessary to localize the band when the measured velocity falls below our experimental resolution. To understand the phase diagram of localization in the disordered Hubbard model, we vary the mean disorder potential and the ratio of the Hubbard energies, U/t, to observe the interplay between disorder and interactions.

To achieve a strongly-interacting metallic state in the lattice, we first cool an equal mixture of atoms in two Zeeman states, $|9/2, 9/2\rangle$ and $|9/2, 7/2\rangle$, in an optical dipole trap, as described in Chapter 2.1. Thermodynamic properties of the gas are modified by adjusting the final stages of cooling to obtain the desired temperature, degeneracy, and number of atoms. Before loading into the lattice, the dipole trap is recompressed to give a mean trap frequency of $\bar{\omega} \approx 2\pi 80 Hz$; this is done to minimize the spatial redistribution that is required in loading the optical lattice and to control the characteristic density of the gas. After recompression, the lattice and speckle potentials are superposed on top of the dipole trap potential over a period of 150 ms via symmetric, exponential ramps of the potentials. We lack an accurate method to directly measure the thermodynamic properties in the lattice (as introduced in Section 5.3 and detailed in Reference [136]), and we infer thermodynamic quantities in the lattice assuming isentropic loading. The self-consistent Hartree-Fock method described in Section 5.3.3 is used to calculate the temperature and chemical potential of the lattice gas within this assumption, and this is used to determine the occupation in real and quasimomentum space. We explore lattice depths from 4 to 7 E_R such that $U < 12t$, and the ratio U/t varies from 2.3 to 9 (below the point at which a Mott insulator would form). The characteristic density of the gas is less than 5, the central filling varies from 0.35 to 0.55 atoms per spin state, and the mean disorder potential energy Δ varies from zero to $2E_R$. A list of the relevant properties are listed in Table 6.1.

A force is applied to the atoms after loading into the disordered lattice via a magnetic field gradient. The gradient is applied vertically in the laboratory frame—this lies roughly along the (111) direction in the lattice and corresponds to the y-direction in imaging. The impulse is applied for $2ms$ with a gradient of approximately $1.5G/cm$ based on the velocity observed in the clean lattice and the effective mass; this corresponds to a force roughly one quarter of gravity for the $|9/2, 9/2\rangle$ state. The magnetic moments of the two spin states differ slightly and the $|9/2, 7/2\rangle$ state feels a force that is $7/9^{\text{th}}$ as large as the stretched state. Relative displacement between the spin states during the impulse is estimated at less than $1\mu m$; this is negligible compared to a typical root-mean-square radius of $5\mu m$ in the lattice and the gases remain in contact during the impulse. The field gradient is chosen to maximize motion in a $4E_R$ lattice with no

disorder. A similar transport measurement with ultracold bosons was used to measure the superfluid–to–Bose-glass transition in a disordered Bose-Hubbard system [158, 138]; the location of the transition was consistent with quantum Monte Carlo predictions [70].

To observe the response of the lattice gas to the applied force, we measure the quasimomentum distribution $\tilde{n}(q)$ of the gas through bandmapping and absorption imaging in time-of-flight. Images showing this response and the redistribution of quasimomentum at $s = 4E_R$ and $\Delta = 0\text{-}2E_R$ are shown in Figure 6.4(b-c). Due to the imaging projection, the first Brillouin zone appears as a hexagon as described in Section 5.2.2. During bandmapping, both the lattice and the disorder are turned off using a linear ramp over $200\mu s$; this is adiabatic with respect to the band gap but faster than all other timescales in the system. Bandmapping is not a perfect process and fails at high quasimomenta [134]. This effect may diminish the observed signal for large amplitude impulses. The impulse used in this work is adjusted to maximize the observed displacement in quasimomentum. After bandmapping, the dipole trap is instantaneously removed, and the gas is allowed to expand for $10ms$. The observed quasimomentum distributions shift in response to the applied impulse as shown in Fig. 6.4. The center-of-mass of the quasimomentum distribution is extracted numerically from the image, and a velocity is calculated by subtracting the position of the gas after the impulse from the stationary gas and dividing by the $10ms$ expansion time. For this data, $q_B = 12.75mm/s$, and the maximum center-of-quasimomentum is $\approx 0.25q_B$. There is uncertainty in determining the position of the stationary gas due to changes in stray fields and drift in the position of the optical trap. This uncertainty is found to be $0.05mm/s$ by repeatedly measuring the position of the gas with no applied force and corresponds to a positional uncertainty in the trapped gas of $500nm$.

Data showing the response to the applied force across the range of lattice depth and disorder amplitude explored is summarized in Figure 6.4(d). For each data set, the center-of-mass velocity acquired during the impulse decreases with increasing Δ, atoms redistribute from low quasimomentum values to higher ones, and the amount of redistribution decreases with disorder strength. At lattice depths from 4 to $7E_R$, a regime in which v_{COM} falls below our experimental resolution is observed within the range of disorders probed. We fit the response to the applied force to an exponentially decaying function of the form

$$v_{\mathrm{com}}(\Delta) = Ae^{-\Delta/(\Delta_c \log(A/v_{res}))}. \tag{6.2}$$

This equation provides a heuristic fit that matches well with the observed data. From a single-particle perspective, a smooth decrease in the observed motion is expected with increasing disorder as disorder-induced localization progressively shifts the location of the mobility edges to include more of the band. Once the mobility edge has encompassed all available states, the system will become completely localized

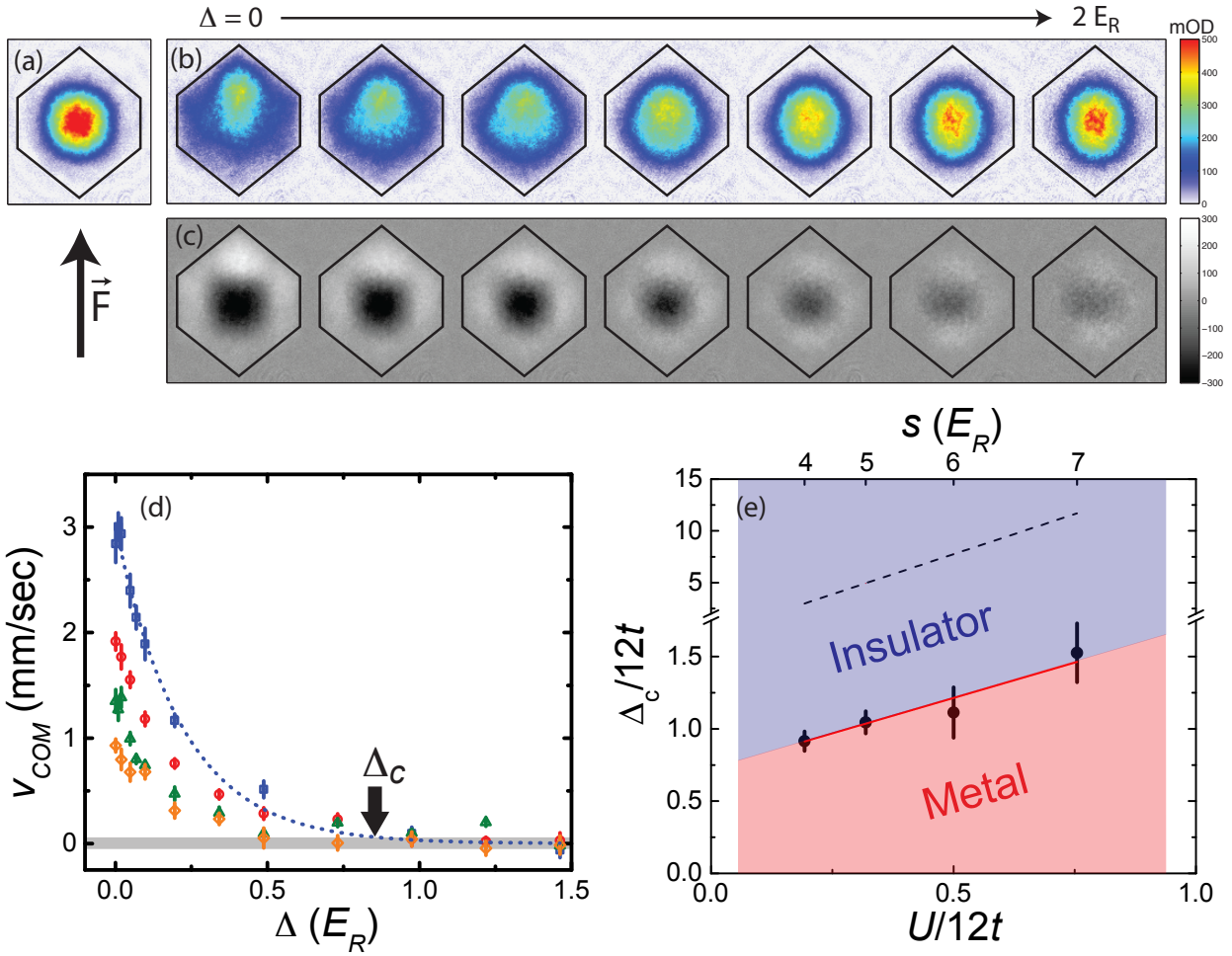

Figure 6.4: Response of a disordered lattice gas to an impulse. (a) Bandmapped image of a spin-mixed gas at s = $4E_R$, $\Delta = 0$. The first Brillouin zone is indicated by a black hexagon. (b) An external force ($\vec{F}$, black arrow) is applied to the gas, and the response in quasimomentum is shown for Δ = 0, 0.1, 0.2, 0.5, 0.75, 1.0, 1.5, and $2.0E_R$. (c) The redistribution of quasimomentum after the impulse is shown by subtracting the stationary gas from the images in (b). (d) The center-of-mass velocity after the impulse is plotted for lattice depths of $4E_R$ (blue squares), $5E_R$ (red circles), $6E_R$ (green triangles), and $7E_R$ (orange diamonds) as the disorder strength is varied. The response curves are fit to an exponential decay and a critical velocity Δ_c is found when this value falls below the experimental resolution (gray band). (e) The critical disorder strength required to arrest motion increases with interaction strength. The dashed line indicates the location of a percolation transition [70]; the red line is a linear fit to the critical disorder data.

with an associated critical disorder labeled Δ_c. We extract the location of Δ_c as the point where Eq. 6.2 crosses the experimental resolution of $v_{\rm res} = 0.05mm/s$. Several alternative methods for reducing the data were explored, and similar values for the critical disorder were found.

A phase diagram showing the location of the critical disorder separating localized vs. metallic regimes is plotted in Figure 6.4(e). The interactions are varied in the experiment by adjusting the lattice depth; and, in doing this, the bandwidth of the system also changes. To make fair comparison of quantities between

s	N (10^3)	$\bar{\omega}$ (Hz)	T/T_F (trap)	$\tilde{\rho}$	$n_r(0)$	$\frac{n_q(q_B)}{n_q(0)}$	T/t	μ/t	E_F/t	f_{loc}
4	37.0 ± 2.5	$2\pi 101$	0.14 ± 0.03	0.7	0.37	0.15	0.7	5.5	5.6	0.0001
5	41.2 ± 3.0	$2\pi 106$	0.18 ± 0.03	1.4	0.45	0.24	1.0	6.5	6.7	0.01
6	47.1 ± 6.5	$2\pi 110$	0.16 ± 0.02	2.7	0.58	0.33	1.1	8.4	8.1	0.04
7	48.7 ± 1.9	$2\pi 114$	0.17 ± 0.02	4.5	0.64	0.40	1.5	10.2	9.6	0.21

Table 6.1: Thermodynamic properties of the lattice gases shown in Figure 6.4. Value to the right of the double bars are inferred assuming isentropic transfer from the harmonic trap into the lattice with the Hartree-Fock method described in Section 5.3.3. The fraction of localized states is calculated using the inferred thermodynamic quantities and Eq. 5.52. Number in this table is the total of a 50/50 mixed gas of two spins.

different lattice depths, the critical disorder and interaction energy are each normalized by the single-particle energy scale of the system, the bandwidth. For a non-interacting gas, $\Delta_c/12t$ should be a fixed quantity. The normalized data in this figure show the location of the phase boundary depends on the interaction strength and indicates that we have observed an interaction-driven metal-insulator transition. The positive slope of the phase boundary states that more disorder is required to localize a more strongly interacting gas. This reinforces the intuitive picture that interactions tend to disrupt interference based localization, and that more disorder should be required to localize a more strongly interacting system. The slope of the phase boundary, as determined by a linear fit to the data, is greater than zero at the 3σ level at minimum. This uncertainty is estimated by generating a large number of measurement realities from the published data points assuming random sampling from each point's error bar. Each measurement reality is then fit with a linear regression, and the fraction of realities with slope greater than 0 is determined. For the data shown, the method indicates the probability that the slope is less than zero is one in four hundred.

Thermodynamic quantities are inferred for the data shown in Fig. 6.5 assuming isentropic transfer from the dipole trap into the lattice using the Hartree-Fock method described in Section 5.3.3. The values found in this procedure are listed in Table 6.1. These data are taken at roughly equal number, entropy per particle, and trap frequency; and as the lattice depth is increased from 4 to $7E_R$, the Fermi energy shifts almost by a factor of two. This causes the quasimomentum distribution to broaden as the ratio of E_F/t shifts with lattice depth; this process is described in greater detail in Figure 5.12. Images showing the quasimomentum distribution before and after the impulse are found in Figure 6.5, where broadening of the quasimomentum distribution with increasing lattice depth is evident. This is consistent with $n_q(q_B)/n_q(0))$ trending closer to unity with increasing lattice depth, as listed in Table 6.1. Due to this broadening of the momentum distribution with lattice depth, the maximum response in center-of-quasimomentum from the impulse also decreases. This is visible both in the traces in Figure 6.5(b) and in the reduced data in Figure 6.4(d).

Comparison of the bandmapped quasimomentum distribution at $\Delta = 0$ to Hartree-Fock based predictions

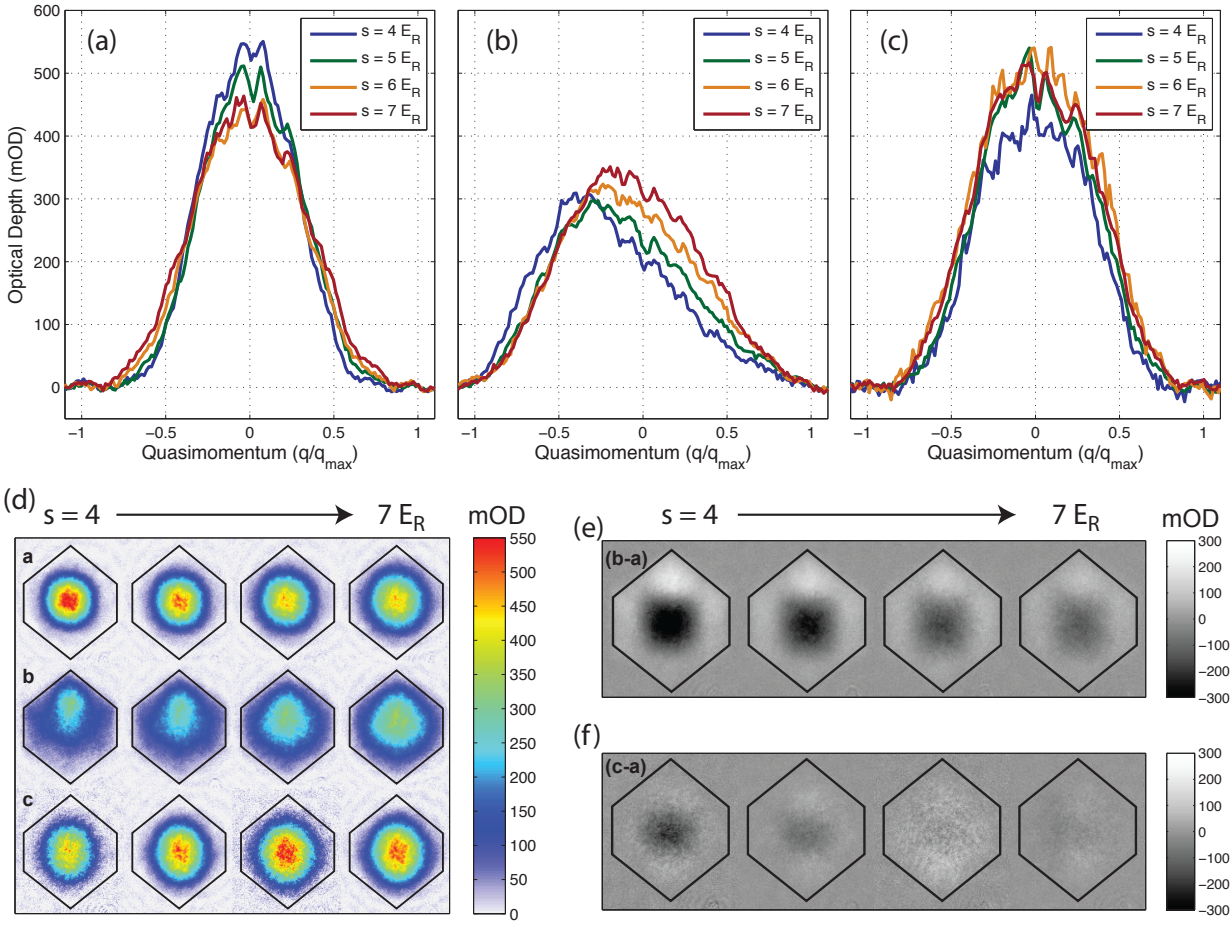

Figure 6.5: Variation in quasimomentum distribution with lattice depth in the disordered lattice transport data. Vertical traces plotted through the center of bandmapped quasimomentum distributions for $\Delta = 0$ with no impulse (a), $\Delta = 0$ with the impulse (b), and $\Delta = 1.5E_R$ with the impulse (c). The quasimomentum axis is defined as in Figure 5.10. Broadening of the quasimomentum distribution and reduced response with lattice depth are clearly visible in (a) and (b); broadening due to the disorder potential is minimal as shown in Fig. 6.11. (d) Full bandmapped images are shown for the quasimomentum distributions for (a), (b), and (c). The first Brillouin zone is indicated by a black hexagon. (e-f) The redistribution of quasimomentum induced by the impulse is shown by subtracting the quasimomentum distribution before the impulse for $\Delta = 0$ (e) and $\Delta = 1.5E_R$ (f).

are shown in Figure 6.6. The procedure used to generate these profiles is detailed in Section 5.3. Profiles using the measured harmonic trap entropy and number listed in Table 6.1 fail to reproduce the measured optical depth profiles. Column integrated distributions are produced as described in Section 5.7. Surprisingly, agreement is found to curves with $T/T_F = 0.35$ with no free parameters. These curves suggest that we may have systematically underestimated number or entropy per particle in the lattice. There are a number of problems with direction comparison to measured quasimomentum distributions as detailed in References [134, 136] as well as problems that arise due to finite time-of-flight, finite size of the lattice gas, and interactions during free expansion. Strong conclusions about entropy per particle should not be drawn from these profiles

alone.

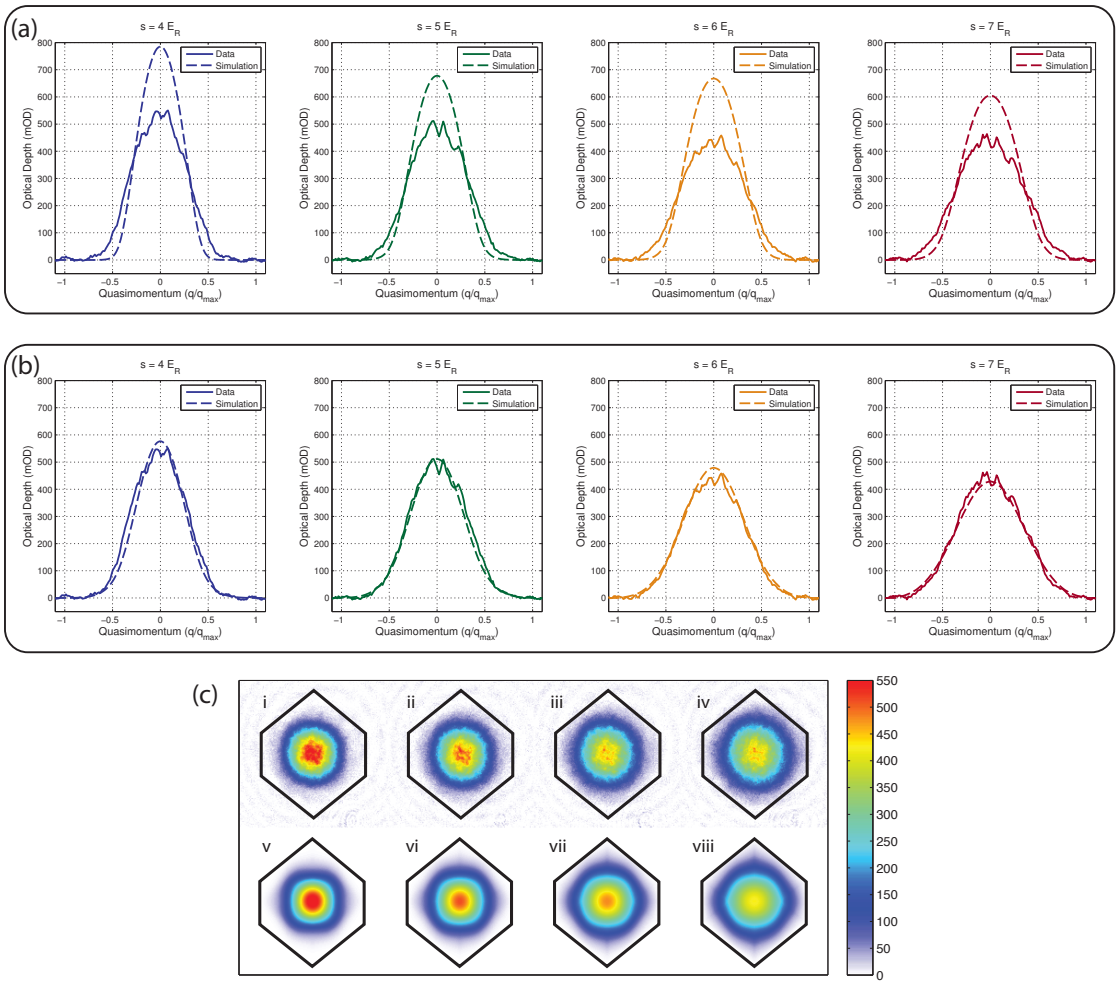

Figure 6.6: Comparison of measured quasimomentum distributions to predictions from Hartree-Fock calculations for spin-mixed gases in a non-disordered lattice. Optical depth images are calculated using the values for entropy and number from Table 6.1. The projection is taken along the imaging direction as shown in Section 5.7. (a) Hartree Fock calculation with S/N given by Table 6.1. (b) Hartree-Fock with $T/T_F = 0.35$. (c) Comparison of measured quasimomentum distributions to prediction for $T/T_F = 0.35$.

6.2.3 Many-Body Localization and Temperature Scaling

In order to better understand the localized state measured in Section 6.2, we measure the stability of the localized gas in the disordered lattice over a range in temperature. This is motivated by recent theoretical work by Basko and Altshuler which shows that localization in a strongly interacting system can survive at non-zero temperature in a process called many-body localization [11, 12, 13]. This unexpected result has sparked a number of theoretical and experimental efforts to explore this phenomenon. These results are surprising because the traditional view of low-temperature conductivity in disordered, interacting systems

is that conductivity will always be non-zero at finite temperature. In systems of localized states connected to an external bath (such as phonons), conductivity at finite temperature is known to scale proportional to $(T/T_0)^{\alpha}\, e^{-(T_0/T)^{1/(d+1)}}$. Here T_0 is a characteristic temperature, α is a constant, and d is the dimensionality. This phenomenon is called variable range hopping [144, 145, 187, 218], and the range of hopping is determined by a competition between the spatial overlap and activation energy for hopping between localized states in the material. In this scenario there is always finite conductivity at any non-zero temperature. Basko and Altshuler find that interactions do not always lead to a hopping-type behavior between localized states, and that the conductivity in an isolated quantum system with interactions can be zero at finite temperature.

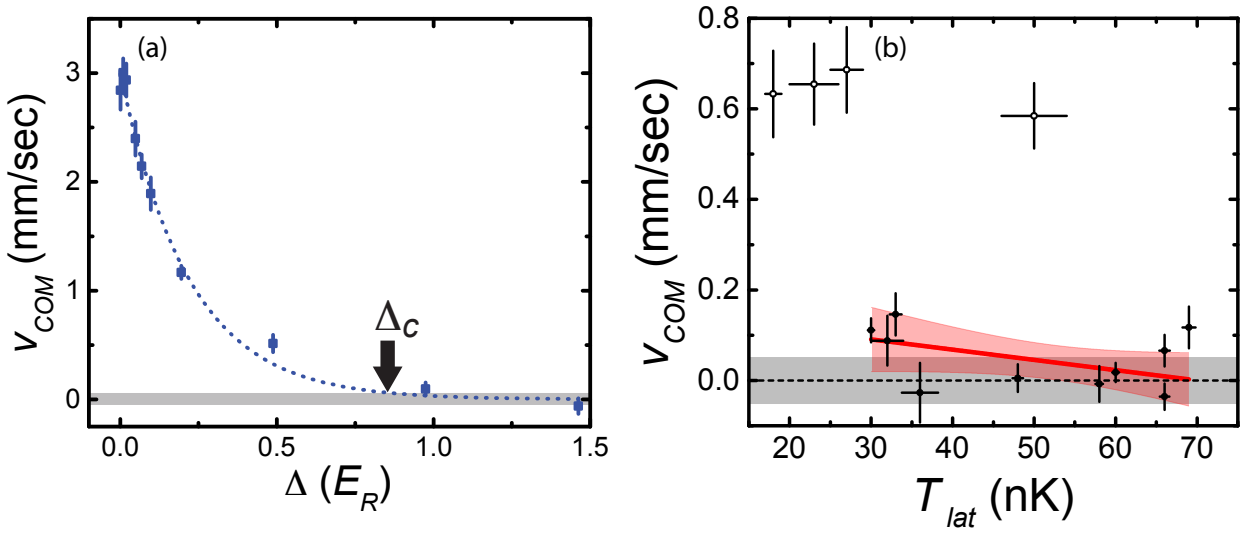

Figure 6.7: We explore the stability of a localized gas over a range of temperatures. (a) Center-of-mass velocity after an impulse in the disordered lattice (reproduced from Fig. 6.4). The motion falls below our resolution at $\Delta \approx 0.85 E_R$. (b) We measure the center-of-mass velocity acquired after applying an impulse to the gas for $\Delta = 1\ E_R$ (filled circles) and $\Delta = 0.4\ E_R$ (open circles). The red line is a linear fit to the data and the shaded area indicates the 95% confidence bound of the fit. The grey band indicates our uncertainty in measuring zero velocity. The temperature in the lattice is inferred from a Hartree-Fock calculation.

The work initiated by Basko and Altshuler on many-body localization offers a new paradigm in which an interacting system can remain localized at non-zero temperature. This theory considers a system of initially Anderson localized states in which interactions are introduced directly between the localized states (without mediation by phonons or connection to a heat bath) and asks if these interactions lead to a similar hopping-type conductivity as is generated in typical materials. Surprisingly, they find both insulating and conducting phases emerge separated by a mobility edge in temperature. The insulating phase is novel, as it has strictly zero conductance at non-zero temperature for short-range interactions. Subsequent work in random spin models demonstrated that a similar transition can survive even to infinite temperature [153].

Work on many-body localization relates to fundamental questions of ergodicity and thermalization in closed quantum systems [219, 169]. In the canonical ensemble, systems are connected with a thermal bath, and the bath sets the temperature of the system and ensures ergodicity. In closed quantum systems, such as experiments with ultracold gases, systems appear remarkably close to thermal states without the aid of an external bath. It is not obvious why a system under unitary time evolution should have this behavior; but it is believed that local subsystems can equilibrate, with their surroundings acting as a heat bath and that a thermal state will be approached after sufficient time—this is known as the eigenstate thermalization hypothesis [46, 192, 94]. Non-ergodicity has been explored in 1D nearly integrable cold atoms systems where atoms are taken far from equilibrium and observed not to relax in the quantum Newton's cradle [95].

Run	N (10^3)	T/T_F (trap)	$\tilde{\rho}$	$n_r(0)$	$\frac{n_q(q_B)}{n_q(0)}$	T/t	μ/t	E_F/t	f_{loc}
1392	14.7 ± 0.6	0.28 ± 0.03	0.28	0.18	0.08	1.0	3.4	4.6	0.00
1399	30.0 ± 0.9	0.40 ± 0.01	0.58	0.20	0.21	1.9	2.7	5.7	0.03
1400	24.8 ± 1.8	0.21 ± 0.02	0.48	0.27	0.11	0.9	4.4	5.4	0.00
1403	23.4 ± 1.6	0.38 ± 0.01	0.45	0.19	0.16	1.6	2.9	5.3	0.03
1409	19.1 ± 0.8	0.24 ± 0.01	0.37	0.22	0.09	0.9	3.9	5.0	0.00
1411	32.5 ± 1.2	0.29 ± 0.01	0.62	0.27	0.17	1.3	4.2	5.8	0.01
1415	35.2 ± 1.3	0.24 ± 0.01	0.68	0.30	0.16	1.1	4.7	5.9	0.01
1420	18.7 ± 0.6	0.22 ± 0.01	0.36	0.22	0.08	0.8	4.0	4.9	0.00
1425	34.4 ± 1.2	0.37 ± 0.01	0.66	0.23	0.21	1.8	3.3	5.9	0.05
1430	37.6 ± 1.3	0.36 ± 0.01	0.72	0.24	0.22	1.8	3.5	6.0	0.05

Table 6.2: Thermodynamic properties of lattice gases used in variable temperature transport measurement. Here $s = 4E_R$ and $\bar{\omega} = 2\pi 100$ Hz. Thermodynamic quantities were calculated using the method described in Section 5.3.3. Number in this table is the total of a 50/50 mixed gas of two spins, and central occupation values are listed per spin state.

We probe the stability of our localized state against variations in temperature in the lattice to look for behavior predicted for many-body localization. To realize a system analogous to the many-body localization scenario, we begin with Δ marginally higher than Δ_c such that all atoms are initially localized. We then perform transport measurements by applying an external force on the atoms and modify the temperature in the lattice while looking for small changes in conductivity. The temperature in the lattice is inferred within the isentropic loading assumption using the Hartree-Fock method used to self-consistently match the entropy and atom number in the harmonic trap. This process is described in Section 5.3.3. For this measurement, an equal mixture of two spin states is loaded into an $4E_R$ optical lattice with $\Delta = 1E_R$, marginally higher than $\Delta_c \approx 0.8E_R$. The force is applied with a magnetic field gradient for $2ms$, and the response of the quasimomentum distribution is measured via bandmapping and time-of-flight imaging. A summary of the thermodynamic quantities for this data is listed in Table 6.2.

Data showing the response to an external force are plotted in Figure 6.7. No change in the conductivity

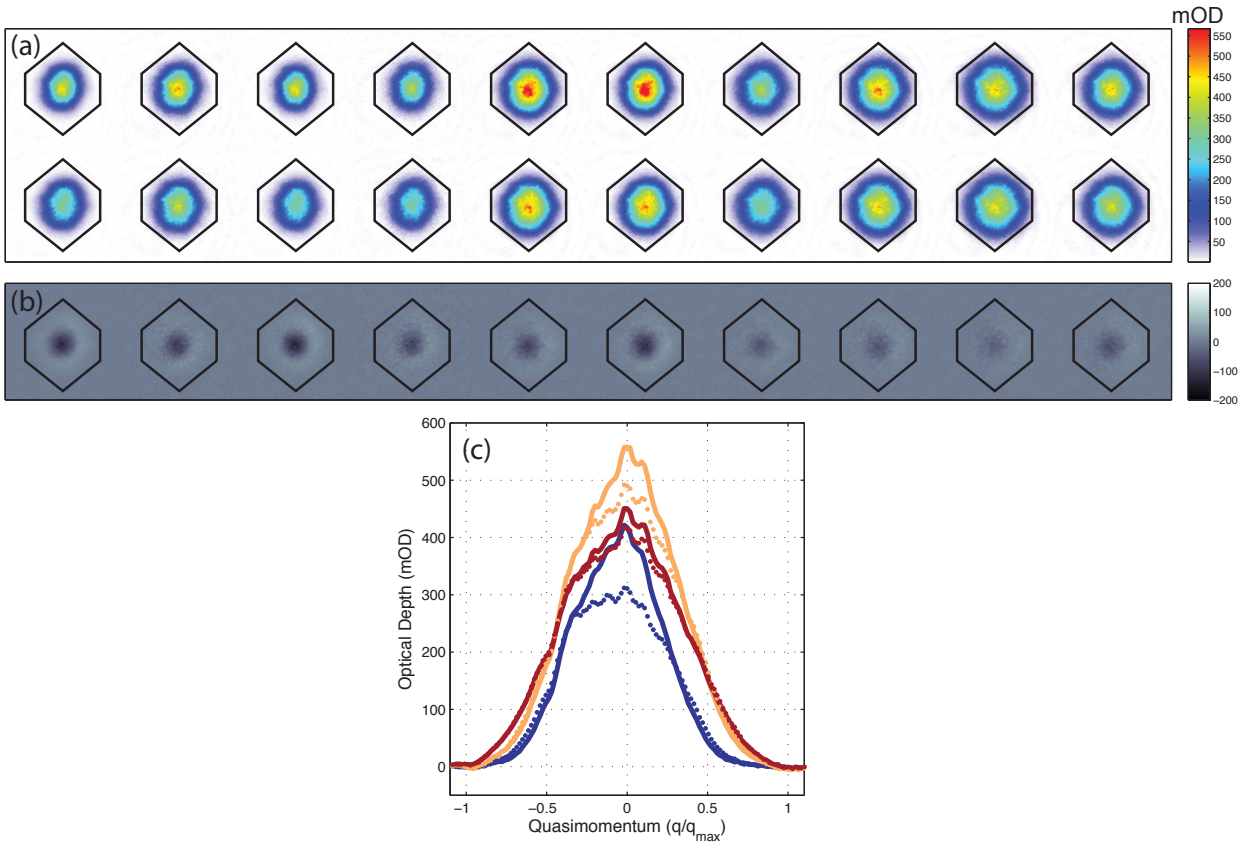

Figure 6.8: Summary of quasimomentum distributions exploring temperature dependence of marginally localized gas. (a) Quasimomentum distribution of lattice gases for s = $4E_R$ and $\Delta = 1E_R$ before (top row) and after (bottom row) applying an impulse. The first Brillouin zone is indicated by a black hexagon. (b) The redistribution in quasimomentum is shown by subtracting the stationary gas from the perturbed gas. (c) Representative vertical slices through the quasimomentum distributions in (a) indicate the response to the gas to the impulse. Solids lines are before the impulse, dotted lines are after the impulse. Blue, yellow, and red traces represent the low, intermediate, and high temperatures. Data are presented in the order in which they are listed in Table 6.2.

of the marginally localized gas is observed over a doubling of the temperature in the lattice. The data cover a range from 27 to 64 nK[1] and are fit to a line to extract a 95% confidence interval for the behavior. The confidence interval overlaps our zero velocity uncertainty band over the entire range of data. The error in determining zero is estimated by repeatedly measuring the position of gas with no impulse applied, and v_{res} corresponds to a thermal energy of 12 $k_B \times pK$, an incredibly tiny value compared to the ground bandwidth of $\approx 400 k_B \times nK$. This observation is consistent with the gas being many-body localized across the range in temperature explored. Whether a temperature induced mobility edge should be observed in this system is unknown. The many-body transition can be thought of in terms of energy density rather than temperature,

[1]The implementation of the Hartree-Fock calculation used to calculate the temperature for this data published in Ref. [101] (and shown in Fig. 6.7) double counted the interaction energy U. Our best estimations of temperature in the lattice for this data are listed in Table 6.2. No conclusions of the paper are modified by this change.

and this view may strongly affect how localization is discussed in trapped systems where there are necessarily local variation in energy density (see e.g. Figure 5.14). Additionally, within a single-band systems such as our disordered optical lattice, there is a maximum energy density that can be reached. If the critical energy density for transport lies above this maximum value, no transition will exist in the system. Measurements of the many-body nature of the system, such as those that probe the entanglement of the interacting state would allow stronger conclusion about the nature of the insulating state to be made. The properties of the gases used in this study are summarized in Table 6.2, and inferred profiles of these gases in position and quasimomentum are plotted in Fig. 6.9. Recent experiments from the Munich group have used the relaxation of a spin imbalanced charge density wave in a quasi-random 1D lattice, and related predictions of entanglement entropy in their system to claim observation of many-body localization in 1D [182]. Their results show that interactions tend to destabilize the localized phase, and that localization persists over a range of energy density, as is suggested by the work presented here.

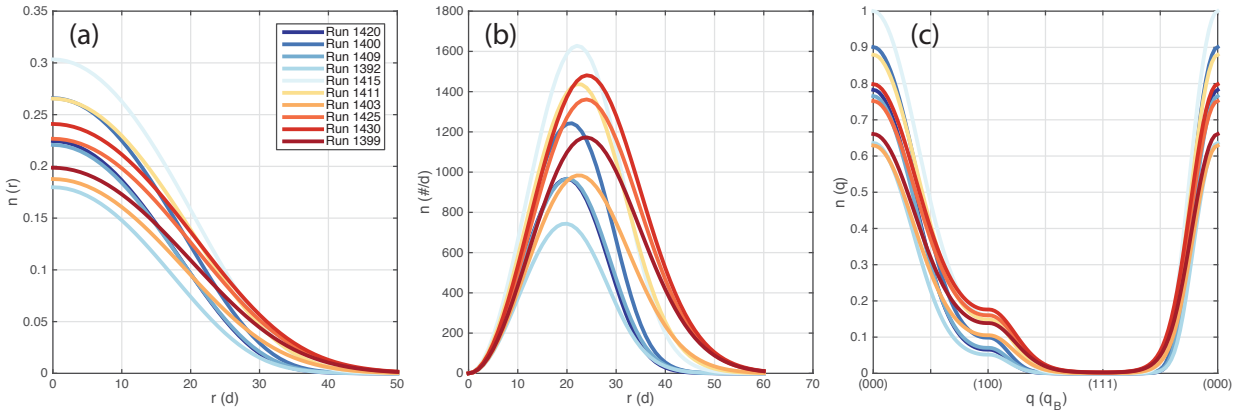

Figure 6.9: Spatial and quasimomentum distributions are calculated using the Hartree-Fock method for the data in Table 6.2. The color indicates temperature in the lattice with blue to red mapping from cold to hot and is shared between the figures. (a) Occupation per spin state as a function of radial distance. (b) Total number of atoms at a given radius; the region containing localized states is shaded in gray and account for at most 10 percent of the atoms. The radial density is calculated as $4\pi r^2 n(r)$. (c) Quasimomentum distributions are plotted along a representative trajectory through the Brillouin zone.

Additionally, we probe the temperature scaling of a conducting gas with $\Delta = 0.4\ E_R$ where v_{COM} is roughly a quarter of the $\Delta = 0$ value, as shown in Figure 6.7. The conductivity of this state is measured with the same magnetic field gradient impulse as the $\Delta = 1E_R$ data, and no temperature dependence in the conductivity is observed over a range of temperature from 20 to 50 nK. From the perspective of single-particle physics, this behavior is surprising. The initial state for $\Delta = 0.4E_R$ is conducting, implying non-negligible occupation of non-localized states. The relative occupation of states will vary with temperature, and hence the relative occupation of metallic and insulating states and the bulk conductivity will also change.

Expected behavior with $\Delta = 0$ is that v_{COM} will decrease with increasing temperature due to broadening of the quasimomentum distribution. The role of many-body interactions on the measurement at $\Delta = 0.4E_R$ is unknown, and connection with the picture of many-body localization is complicated due to the occupation on non-localized states.

6.2.4 Scarola and DeMarco Result

Recent work by Vito Scarola and Brian DeMarco [179] has numerically simulated transport of strongly-interacting fermions in a disordered lattice in the presence of diagonal disorder. This work is exceptional both in that it is not performed in a pertubative limit, but also in that it replicates a scaled version of the experiments presented here and allows for direct comparison of results. The calculation uses experimental values for entropy, particle number, trap frequencies, and lattice parameters to create a scaled system with size up to 11^3. The state is initialized using the high-temperature series expansion to eighth order and the local density approximation to self consistently generate thermodynamics quantities in the disordered lattice given the known experimental parameters. This is similar to the process described in Section 5.3.6. The series expansion has a limited range of convergence which constrains applicability to data with $t \ll U$ and $t \lesssim k_B T < 12t$. For the experiment, this limits comparison to only the $s = 6$ and $7E_R$ data. Equations of motion are generated for the system which are numerically solved in time. The applied force is introduced as a linear potential similar to the magnetic gradient in the experiment. This potential is applied for a set amount of time and the center of mass velocity of the gas is measured.

The comparison of the theoretical predictions for the velocity acquired in the impulse to the experimentally measured motion at $s = 6$ and $7E_R$ is shown in Figure 6.10. No free parameters are used to generate the theory curves, and excellent agreement is found over the range in which comparison is possible. This effort finds that majority of motion in the system is carried by Hubbard-band quasiparticles, and that our observation is consistent with Anderson localization of these Hubbard-band quasiparticles. Aspects of the observed reduction in conductivity with increasing disorder can be related to disorder-induced changes in density, but these do not lead to an insulating state. Scattering from the disorder is found to completely arrest motion for $\Delta > 0.5E_R$. This work emphasizes that a rigorous connection between the localized Hubbard-band quasiparticles and many-body localization has not been made, and that future work examining entanglement is required.

Additionally, Reference [179] raises an important point about adiabatic heating caused by the disordered potential. In inferring the temperature in the disordered lattice within the isentropic assumption, the temperature of the gas will rise as the applied disorder potential increases. This effect can also be seen

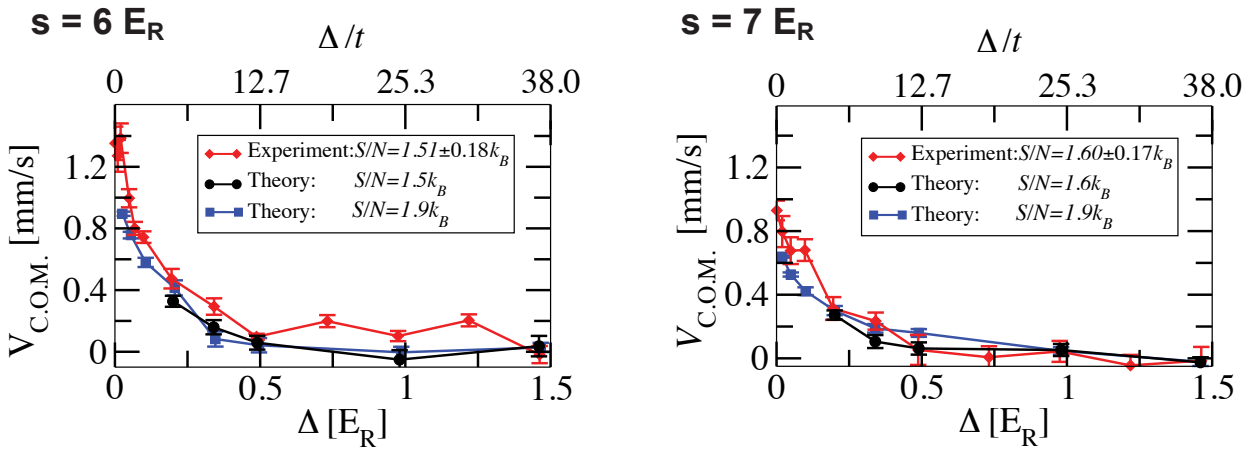

Figure 6.10: Comparison of numerical predictions by Vito Scarola for motion in a disordered lattice to data from Fig. 6.4. Theory curves (black points) are generated for a limited range of data for $s = 6$ and $7E_R$ based on the convergence of the high-temperature series used to infer thermodynamic quantities in the lattice. The theory curves are generated using the published entropy, number, trap, and lattice properties of the experiment, and excellent agreement is found with the measured quantities (red points) with zero free parameters. Predicted motion is also included for higher entropies (blue points) where the high-temperature series expansion allows for comparison at lower Δ. Figures are modified from Reference [179].

by increasing the harmonic confinement or any other method that restricts the number of available states. For the data at $s = 6$ and $7E_R$ and $\Delta <= 1.5E_R$, adiabatic heating from the disorder is found to increase the temperature by at most a factor of two. This heating is a crucial element of the analysis by Scarola and DeMarco as the disorder-induced shift in temperature enables the data at $S/N = 1.5k_B$ to be analyzed within the high-temperature series expansion for $\Delta > 0.2E_R$. For Δ smaller than this value, the series is not convergent and this motivates the analysis at $S/N = 1.9k_B$, which compares favorably with our data at low Δ. In the presence of adiabatic heating due to the exclusion of lattice sites with high ϵ_i, the quasimomentum distribution should also be expected to broaden, though this is not observed in the experiment. Data in Figure 6.11 shows vertical slices through the quasimomentum distribution with and without disorder at $s = 4$ and $7E_R$, though no appreciable broadening is visible. The effect of adiabatic heating on the observed quasimomentum distribution is unknown.

6.3 Quasimomentum Relaxation in a 3D Lattice

We study the dynamics of non-equilibrium quasimomentum distributions in strongly correlated metals to explore momentum relaxation rates, resistivity, and the validity of Fermi liquid theory in the Hubbard model. Experiments are performed by generating relative displacement between the Fermi surfaces of a two component gas in an optical lattice. The gases start spin-polarized in the 3D lattice, and a Raman transition

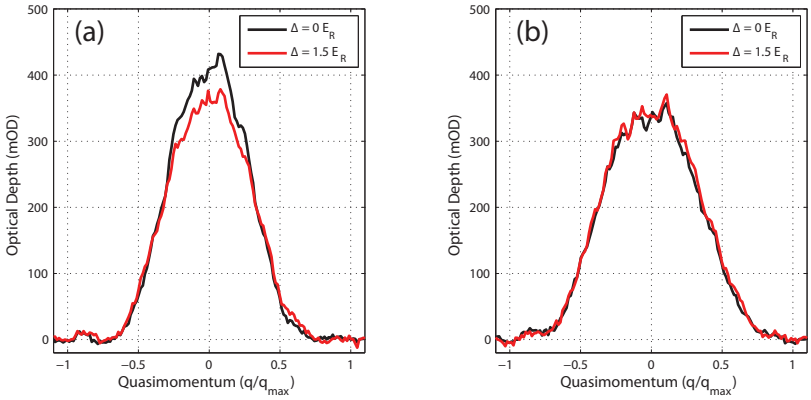

Figure 6.11: Comparison of bandmapped quasimomentum distributions with and without disorder.Vertical slices through $\tilde{n}(q)$ comparing the quasimomentum distributions with and without disorder at lattice depths of $4E_R$ (a) and $7E_R$ (b).

is used to transfer a set fraction of the gas to different spin state with a shift in quasimomentum of $q_B/2$. The displacement between the Fermi surfaces of the two spins relaxes in time, and the relative motion of the two gases is measured as a function of time. This measurement is repeated at different ratios of $U/12t$ and temperatures in the lattice (by varying the lattice depth and the entropy and number at the end of evaporative cooling). The motivation for these measurements and the experimental methods are presented in the following section.

6.3.1 Motivation and Resistivity in Materials

As mentioned in the introduction to this chapter, there are a large number of open questions about the strange metal regime of the high-temperature superconductors. The T-linear scaling of the resistivity is the most prominent "strange" behavior in this regime, and it is so named because the scaling at low temperatures is typically T^2. Other scalings are present at higher temperature due to the relative contributions of electron-electron and electron-phonon scattering [8], but at the lowest temperatures, phonon modes are frozen out, and the resistivity is controlled only by the electron-electron scattering rate. In this scenario, only the electrons within an energy range of width T around the Fermi energy can scatter, as there is unity occupation of all lower lying states, and the scattering rate scales as T^2. In the cuprates, T-linear resistivity has been measured from temperatures as low as 1 Kelvin to as high as 1000 Kelvin. The low-temperature value is measured in the normally superconducting regime by suppressing superconductivity with a 35 Tesla external magnetic field [35].

Recent analysis of materials with T-linear resistivity (including high-temperature superconductors, heavy fermion materials, quantum critical metals, and normal metals) has motivated a speculative phenomenolog-

ical limit on relaxation [74] and the energy diffusion rates [24] in strongly-correlated materials independent of the nature and number of the underlying relaxation mechanisms. This is related to the Mott-Ioffe Regel criterion which states that coherent quasiparticle conductivity disappears when the mean-free-path reaches the inter-atomic spacing [78]. In Reference [24], the authors consider a large number of materials that exhibit T-linear resistivity, and a simple Drude model calculation shows that these materials have very similar scattering rates per Kelvin. In the Drude model, the resistivity $\frac{1}{\rho} = ne^2\tau/m$, where n is the carrier density, e is the charge, τ is the mean time between scattering events, and m is the mass of the charge carrier. This can be rearranged to express the mean time between scattering events as $\tau = m/(\rho n e^2)$. The proposed phenomenological bound set on the scattering time is $\tau = h/(k_B T)$. This timescale can be rewritten to incorporate the Fermi energy as $\tau = v_F/(k_F k_B T)$ where v_F is the Fermi velocity and k_F is the Fermi wavevector. The Drude model prediction for the mean time for scattering can be related to the phenomenological bound to find the following dimensionless variable:

$$\frac{ne^2 v_F}{k_B k_F}\frac{d\rho}{dT} \approx 1. \tag{6.3}$$

Reference [24] shows that this condition is satisfied across a large range of materials with varying dimensionality and scattering processes.

6.3.2 Quasimomentum Relaxation in Optical Lattices

We probe transport and relaxation dynamics in the metallic regime of the Hubbard model for $U < 12t$ and for characteristic densities less than required to generate a band insulator. Atoms are loaded into 3D optical lattice with $s = 4$ to $7E_R$, and thermodynamic quantities in the lattice are inferred using methods described in Section 5.3. A non-equilibrium quasimomentum distribution is created by first loading a spin-polarized gas into the optical lattice and then applying a Raman transition to transfer a fraction of the gas to a different spin state with non-zero momentum relative to the initial state. The relative motion between the two states is allowed to evolve, and the relative velocity of the two components is measured in time.

A sketch of the experimental apparatus is shown in Figure 6.12. Two single frequency laser beams drive Raman transitions as described in Section 2.5, where each beam is detuned by $\Delta \approx 20GHz$ from the ^{40}K D1 line. The beams labeled Raman_1 and Raman_2 have wavevectors k_1 and k_2 and frequencies ω_1 and ω_2. Both beams are derived from the same laser; frequency shifts between the two beams are provided by AOMs. These beams drive transitions with energy $\delta\omega = \omega_1 - \omega_2$ between the initial state in the lattice $|F = 9/2, m_F = 9/2\rangle$ and $|9/2, 7/2\rangle$, with imparted momentum set by $\boldsymbol{\delta k} = \boldsymbol{k}_1 - \boldsymbol{k}_2$ along the y-direction in the experiment. The magnitude of the shift in momentum is set by the 30° angle between the beams and

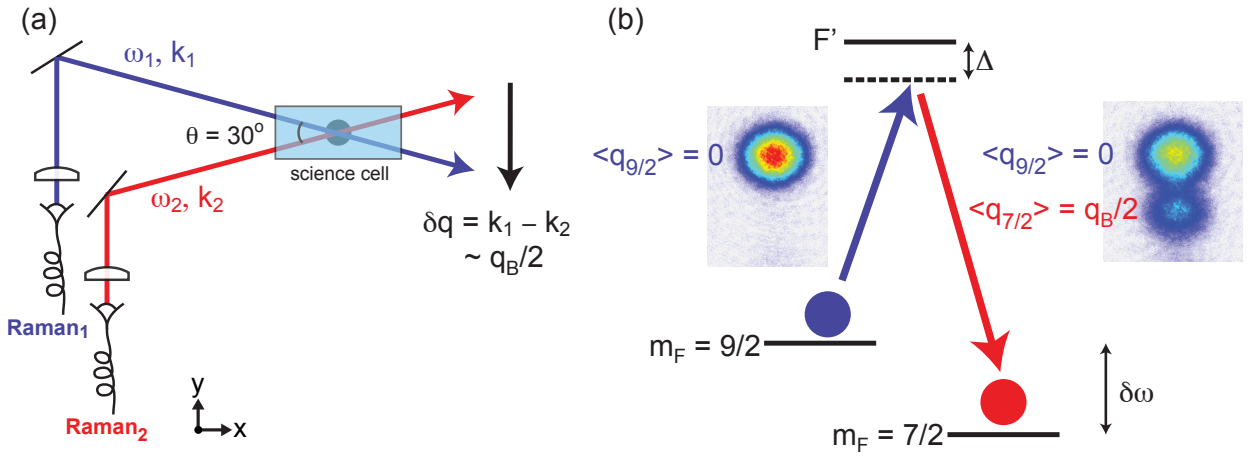

Figure 6.12: Raman transitions are used to generate relative motion between spin states in an optical lattice. (a) Two single frequency Raman beams with frequencies ω_1 and ω_2 are focused on the position of the lattice gas. The beams cross at an angle of 30° that sets the momentum imparted to the atoms of $\boldsymbol{\delta q} = \boldsymbol{k_1} - \boldsymbol{k_2}$ with magnitude $q_B/2$. (b) The experiment begins with a single spin component in the lattice in the $|9/2, 9/2\rangle$ state. The Raman transition is tuned to the energy difference between the $m_F = 9/2$ and 7/2 states ($\delta\omega = \omega_1 - \omega_2$), and a set fraction of the atoms are driven to the $|9/2, 7/2\rangle$ state with a shifted average quasimomentum of $q_B/2$.

corresponds to $\approx q_B/2$ in the $\lambda = 782.2$ nm lattice. The fraction of atoms transferred is set by the pulse time and the Rabi rate, which scales with the electric field in each Raman beam. Transitions are performed at low magnetic fields, typically 3.2 Gauss; and within the bandwidth of the Raman pulses, transitions between all Zeeman levels in the F = 9/2 manifold are degenerate. Starting with a polarized gas in $|9/2, 9/2\rangle$, typical transitions transfer $\approx 30\%$ of the gas to $|9/2, 7/2\rangle$ as a trade-off between significant transfer into the $m_F = 7/2$ state without appreciable population in $|9/2, 5/2\rangle$. Variation in the transferred fraction is at the single percent level due to active stabilization of the beam intensity.

Generating relative motion with Raman transitions has several benefits over generating an impulse with magnetic field gradients, as was done in the disordered lattice transport measurements described at the beginning of this chapter. The most significant benefit is that the transition can be carried out rapidly while still providing a large shift in momentum space. Typical relaxation times measured in the non-disordered lattice are on the millisecond timescale or shorter, as shown in Figure 6.13(b). The magnetic field gradient pulses used to generate motion in Section 6.2.2 were 2 ms long to generate an impulse equivalent to $\approx q_B/4$, and dynamics during this time would complicate the interpretation of a relaxation rate. Here, the Raman light is pulsed on resonance for 20 μs, which is instantaneous compared to the trap frequency and observed relaxation timescales. The short pulse time affords a transition bandwidth of $\approx 50kHz$ and allows for quasimomentum insensitivity in the transfer. The bandwidth of the ground band in the lattice

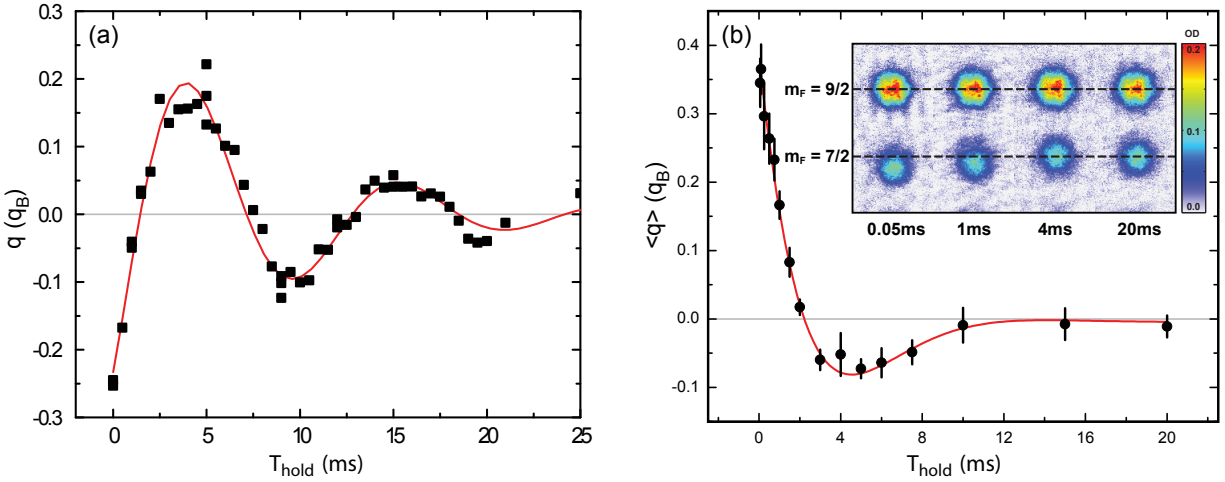

Figure 6.13: Spin relaxation measurement in the lattice. (a) A dipole oscillation is generated for a spin-polarized gas in an $s = 4E_R$ lattice to measure the quasimomentum dephasing rate without interaction. Initial motion is generated by applying a linear potential produced by magnetic field gradient for $2ms$; the damped oscillation has a decay time of $\tau = 8.0 \pm 0.6ms$. (b) Measurements of interaction-induced relation are made by loading a spin polarized gas into the lattice, transitioning a portion of the gas to a second spin state with mean quasimomentum displaced from zero (as in Figure 6.12), and observing the relative velocity of the two components as a function of interaction time. Data show relative velocity between two spin components with an initial relative momentum of $\delta q = q_B/2$, and the damped oscillation has a decay constant of 3.0 ± 0.2 ms. The inset shows bandmapped and spin-separated images of the two spin components, $m_F = 9/2$ and $m_F = 7/2$; zero net quasimomentum for each state is marked by a dotted line. The Raman induced displacement of the $m_F = 7/2$ atoms from zero net quasimomentum at short time is clearly visible, and both spin states settle to net zero momentum at long time.

is approximately $8kHz$ at $s = 4E_R$ and smaller at higher lattice depths, and the broad frequency spread of the Raman transition makes the quasimomentum distribution of the transferred atoms an exact copy of the original gas shifted by $\boldsymbol{\delta k} \approx q_B/2$. This spin insensitivity is useful as the shifted distribution has the same profile as the original quasimomentum distribution in the lattice. Additionally, since $\boldsymbol{\delta k}$ is fixed by the geometry of the Raman beams, the imparted momentum does not depend on the lattice depth used to set the ratio of U/t, though the net shift in quasimomentum will depend on the initial width of n_q. Generating large relative motion between the $m_F = 9/2$ and $7/2$ states with magnetic field gradients would be experimentally challenging due to the small difference in magnetic moment between the two states, except at prohibitively large magnetic fields.

Data comparing interaction-induced relaxation to quasimomentum dephasing in a $s = 4E_R$ lattice is shown in Figure 6.13. In measuring relaxation due to interactions, it is important that we distinguish our signal from other sources of dephasing in the experiment. The lattice dispersion produces anharmonic motion with energy dependent periods as described in Section 6.3.3, and a gas with initially coherent motion

and a finite spread in quasimomentum will dephase without the presence of interactions. We measure this dephasing rate directly by loading a spin polarized gas in the lattice and applying an impulse using a magnetic field gradient as shown in Figure 6.13(a). This process is similar to the disorder-induced localization measurement discussed in Section 6.2.2 except with a non-interacting, single-component gas. Damped sinusoidal oscillations are observed in the center-of-mass quasimometum with a decay time of $\tau = 8.0 \pm 0.6ms$. Data showing relaxation, after generating relative between two spin states using the Raman transition, is shown in Figure 6.13(b). The measured quasimomentum relaxation rate is $\tau = 3.0 \pm 0.2ms$ with interactions, and this timescale is significantly shorter than the relaxation rate due to anharmonicity. The clear separation of timescales between the two processes allows for the accurate determination of the interaction-induced relaxation timescale. The inset of Figure 6.13(b) shows spin separated images at various hold times after the relative motion is initiated. The zero position in these figures is marked for each spin component and is carefully measured to account for any residual dipole force from the Raman beams by imaging spin mixed gas with the Raman pulse applied off resonance.

A related transport measurement was performed by the Esslinger group examining dipole oscillations in a 3D lattice with interactions tuned via a Feshbach resonance [198]. In this work, dipole oscillations were created by displacing the trap center and observing the gas position in time. Several dipole oscillation periods are observed in the weakly interacting limit. Increasing the interaction energy causes rapid damping of the oscillatory motion, and the gas slowly relaxes to the new spatial equilibrium position in the trap plus lattice system. The relaxation rate is found to decrease with increasing interaction energy as the dynamics at large U/t are dominated by molecule formation induced by the Feshbach resonance. The presence of molecules limits the relevance to comparisons with predictions for relaxation rates in the Hubbard model.

6.3.3 Oscillations with Lattice Dispersion

In probing transport properties of lattice gases we create a variety of non-equilibrium quasimomentum distributions. The time evolution of these distributions can be calculated semi-classically using the lattice dispersion and the harmonic trap to generate a series of differential equations in q and x. These equations can be integrated numerically and thermally averaged using statistical weighting to determine the behavior of the ensemble:

$$\dot{x} = \frac{d\epsilon}{dq} = \frac{2\pi t}{q_B}\sin\left(\pi\frac{q}{q_B}\right) \tag{6.4}$$

$$\dot{q} = -\nabla U = -m\omega^2 x. \tag{6.5}$$

Solutions to this series of equations provide harmonic motion in the low quasimomentum, effective-mass limit. Behavior outside of this limit is periodic and anharmonic with amplitude-dependent periods of oscillation as evident in Fig. 6.14. Ensemble averaging over a distribution of quasimomentum states will lead to dephasing of the initial motion as states oscillate with different periods. The rate of this dephasing will increase with the initial width of the quasimomentum distribution and the offset from zero quasimomentum. A 1D example thermal distribution of quasimomenta displaced by $q_B/2$ is shown in Figure 6.14(b). Note that the thermally averaged profile does not show $q_B/2$ motion at zero time due to states wrapping around to negative values of q. This dephasing has been observed by displacing a spin-polarized Fermi gas in a three-dimensional optical lattice, as shown in Fig 6.13a. Direct comparison to these data can be made by solving Equations 6.5 and 6.4 in 3D with the measured quasimomentum distributions.

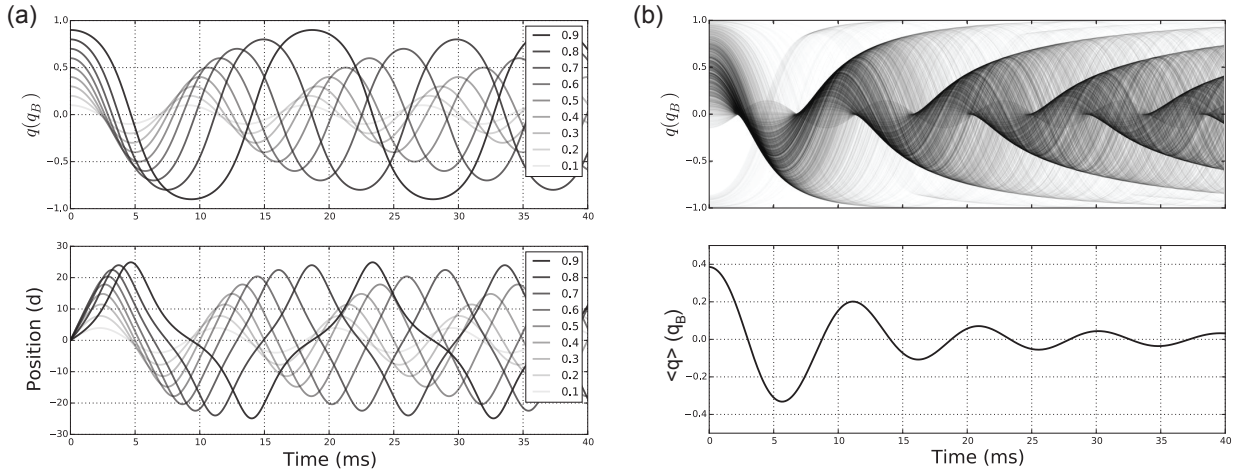

Figure 6.14: Classical trajectories in a lattice with harmonic confinement. (a) Equations 6.4 and 6.5 are integrated numerically to show trajectories in the lattice with harmonic confinement for various values of q from 0.1 to 0.9 q_B in both quasimomentum and position space. Parameters used are $s = 4E_R$, $\omega = 2\pi 170Hz$, $q_B = h/782.2$ nm, and the mass is that of ^{40}K. Note that trajectories are periodic, but that the period is strongly amplitude dependent. (b) Classical trajectories are calculated for a thermal ensemble of particles with a mean quasimomentum of $0.5q_B$ using the lattice parameters in (a). The lower image is the weighted average of the thermal distribution in the upper frame and shows that initially coherent motion in the lattice rapidly damps, similar to the measurement shown in Figure 6.13(a).

6.4 Conclusions

Through transport measurements in a disordered optical lattice, we have observed a strongly-interacting insulating state, measured an interaction induced insulator-to-metal transition, and probed this insulating state across a doubling in temperature in the lattice. Recent theoretical work duplicates the observed transport for $s = 6$ and $7E_R$ and shows that our observation is consistent with Anderson localization of Hubbard-band quasiparticles. We probe the analog of the many-body localization scenario by performing a transport experiment on a gas localized in the disordered lattice over a doubling in the gas temperature. No increase in conductivity is measured over this range of temperature, and the observed localized state is consistent with predictions from many-body localization. Future theoretical studies of the critical temperature in trapped systems as well as experimental measures of entanglement in lattice gases are needed before strong claims about the nature of the localized state are made. Additionally, we have developed a method for exploring quasimomentum relaxation in strongly correlated metals using Raman induced relative motion between two spin states in a lattice. This probe will be used to explore the analog of resistivity and non-Fermi liquid behavior in lattice gases.

Appendix A

Magnetic Field Simulation

A.1 Field from QUIZ Trap

```
%all distance are in microns, currents in amps, fields in gauss
rr = -40000:230:40000;
zz = -40000:230:40000;
[R,Z] = meshgrid(rr,zz);
cart_current = 152.5;
cart_pos = -53210;
quic_current = 710;
ioffe_current = -1*quic_current;
ioffe_pos = -1440;

[cart_radial,cart_axial] = cart_field(R,Z,cart_current,cart_pos);
[ioffe_radial, ioffe_axial] = ioffe_field(R,Z,ioffe_current,ioffe_pos);
[sciquad_radial, sciquad_axial] = sciquad_field(R,Z,quic_current,0);

axial = sciquad_axial + ioffe_axial + cart_axial;
radial = sciquad_radial + ioffe_radial + cart_radial;
field = sqrt(axial.^2 + radial.^2);

close all
nf = figure;
imagesc(rr/1000,zz/1000,field)
colormap(abs(cbjet))
xlabel('Distance (mm)','FontSize',20)
ylabel('Distance (mm)','FontSize',20)

axis image
colorbar
caxis([0,3500])
set(nf,'Color','w')
```

A.2 Field from a Current Loop

```
function [axial, radial]=current_loop(R,Z,current,radius,zcenter)
%all distance are in microns, currents in amps, fields in gauss
%written by WRM on 10/30/2012

prefactor = 20*100*current;
arg1 = 4*radius*abs(R)./((abs(R)+radius).^2+(Z-zcenter).^2);
arg2 = 1./sqrt((abs(R)+radius).^2+(Z-zcenter).^2);
arg3 = (radius^2-R.^2-(Z-zcenter).^2)./((radius-abs(R)).^2+(Z-zcenter).^2);
arg4 = (radius^2+R.^2+(Z-zcenter).^2)./((radius-abs(R)).^2+(Z-zcenter).^2);
[K,E] = ellipke(arg1);

axial = prefactor*arg2.*(K+E.*arg3);
radial = prefactor*((Z-zcenter)./R).*arg2.*(-1*K+E.*arg4);
end
```

A.3 Field from Coils

```
function [radial, axial]=sciquad_field(R,Z,current,position)
%all distance should be in microns, currents in amps, field in gauss
%written by WRM on 10/30/2012
axial = zeros(size(R));
radial = zeros(size(R));
radius_sci = 12850; %in microns
zcenter_sci = 20850; %vertical displacement

sci_quad_pos = [0,0;0,1;0,2;0,3;1,1;1,2;1,3;2,2;2,3;3,3];
for i = 1:10,
    for polarity = [1,-1],
        zcenter = (zcenter_sci+4250*sci_quad_pos(i,2));
```

```
        radius = radius_sci+4250*sci_quad_pos(i,1);
        [temp_axial,temp_radial] = current_loop(R-position,Z,polarity*current,radius,polarity*zcenter);
        axial = axial + temp_axial;
        radial = radial + temp_radial;
    end
end
end

function [radial, axial]=ioffe_field(R,Z,current,position)
%all distance should be in microns, currents in amps, field in gauss
%written by WRM on 10/30/2012
axial = zeros(size(R));
radial = zeros(size(R));
radius_ioffe = 10000; %in microns
zcenter_ioffe = 19000; %vertical displacement
ioffe_pos = [0,0;0,1;1,1;1,2;1,3;2,2;2,3];

for i = 1:7,
    zcenter = -1*(zcenter_ioffe+4250*ioffe_pos(i,2));
    radius = radius_ioffe+4250*ioffe_pos(i,1);
    [temp_radial,temp_axial] = current_loop(Z,-1*(R-position),-1*current,radius,zcenter);
    axial = axial + -1*temp_axial;
    radial = radial + temp_radial;
end
end

function [radial_cart,axial_cart]=cart_field(R,Z,current,position)
%all distance should be in microns, currents in amps, field in gauss
%written by WRM on 10/30/2012
axial_cart = zeros(size(R));
radial_cart = zeros(size(R));
radius_cart = 28000; %in microns
zcenter_cart = 47000;

for zcenter = zcenter_cart+(0:3)*4250,
    for radius = radius_cart+(0:11)*4250,
        for polarity = [1,-1];
            [temp_axial,temp_radial] = current_loop(R-position,Z,polarity*current,radius,polarity*zcenter);
            axial_cart = axial_cart + temp_axial;
            radial_cart = radial_cart + temp_radial;
        end
    end
end
end
```

A.4 Breit-Rabi Equation for ^{40}K

```
function [energy_GHz,energy_mK,moment]=breit_rabi_40K(F,mF,B)
%calculate the energy splitting of the various zeeman levels in the
%hyperfine ground states of 40K
%written by WRM on 10/31/2012. Happy Halloween mofo.
%returns the potential in milliKelvin with no offset.
mK_prefactor = 50;
atomicmass = 40; %atomic mass of Potassium
SS = 1/2;  %electron spin
LL = 0; %orbital angular momentum
JJ = 1/2; %coupled l and s
II = 4; %nuclear spin
% FF = 2; %coupled i and j
gI = 2.002; %nuclear g factor
A52S12 = -0.2857; %hyperfine A constant
Ehfs = (A52S12/2)*(2*II + 1); %Energy of the hypefine splitting in GHz

u0 = 1.4/1000; %Bohr magneton in GHz
u0un = 1/(atomicmass*1836); %ratio of Bohr to nucelar magnetic moment
un = u0un*u0;
gJ = 1 + (JJ*(JJ+1)-LL*(LL+1)+SS*(SS+1))/(2*JJ*(JJ+1)); % approximation for gJ
XX = u0*(gJ + gI*u0un)/Ehfs; %parameter fed into Breit-Rabi formula divided by magnetic field

if (mF > 4.2),
    energy_GHz = (B<=(-1/XX)).*(-1*Ehfs/(2*(II+1))-gI*un*mF*B+((-1)^(9/2-F))*(Ehfs/2)*...
    sqrt(1+((4*mF*XX*B)/(2*II+1))+(XX*B).^2))+...
    (B>(-1/XX)).*(-1*Ehfs/(2*(II+1))-gI*un*mF*B-((-1)^(9/2-F))*(Ehfs/2)*...
    sqrt(1+((4*mF*XX*B)/(2*II+1))+(XX*B).^2));
else
    energy_GHz = -1*Ehfs/(2*(II+1))-gI*un*mF*B+((-1)^(9/2-F))*(Ehfs/2)*...
    sqrt(1+((4*mF*XX*B)/(2*II+1))+(XX*B).^2);
end

%fix odd problem with 9/2, 9/2 state above -1/XX, stupid hack
if (mF > 4.2),
    energy_mK = (B>(-1/XX)).*(mK_prefactor*(-1*gI*un*mF*B-((-1)^(9/2-F))*(Ehfs/2)*...
      sqrt(1+((4*mF*XX*B)/(2*II+1))+(XX*B).^2)-((-1)^(9/2-F))*(Ehfs/2)))+...
      (B<=(-1/XX)).*(mK_prefactor*(-1*gI*un*mF*B+((-1)^(9/2-F))*(Ehfs/2)*...
      sqrt(1+((4*mF*XX*B)/(2*II+1))+(XX*B).^2)-((-1)^(9/2-F))*(Ehfs/2)));
else
   energy_mK = mK_prefactor*(-1*gI*un*mF*B+((-1)^(9/2-F))*(Ehfs/2)*...
    sqrt(1+((4*mF*XX*B)/(2*II+1))+(XX*B).^2)-((-1)^(9/2-F))*(Ehfs/2));
end
%returns field in milliKelvin

if (mF > 4.2),
    moment = 1000*(gI*un*mF+(-1)^(9/2-F)*(Ehfs/2)*XX);
else
    moment = 1000*(gI*un*mF+(-1)^(9/2-F)*(Ehfs/4)*...
        (4*mF*XX/(2*II+1)+2*XX^2*B)./(sqrt(1+(4*mF*XX*B/(2*II+1))+(XX*B).^2)));
end

end
```

Appendix B

Scattering in Speckle Potentials

B.1 Ratio of Boltzmann and Scattering Mean Free Path in Speckle.

```
ps = @(kx,ky,kz)  (1./sqrt(kx.^2+ky.^2)).*...
    exp(-0.25*(kx.^2+ky.^2)-0.25*(5.8^2)*((kz.^2)./(kx.^2+ky.^2)));

angleList = 0:180;
rrList = 10^-2;
lb_ls_correction = [];
for angle = angleList,
    nn = 5e6;
    rr = 1; %sets the radius of the sphere is k-space
    theta0 = pi*angle/180.0; %sets the angle from the positive z axis

    TH = 2*pi*rand(1,nn);
    PH = asin(-1+2*rand(1,nn));
    [X,Y,Z] = sph2cart(TH,PH,1);

    %scale the rotated coordinates such that
    x = rr*X; y = rr*Y; z = rr*Z;

    %evaluate weight of power spectrum on displaced surface
    val = ps(x-rr*sin(theta0),y,z-rr*cos(theta0));
    delta_k = [sin(theta0);0;cos(theta0)]*ones(1,nn)-[X;Y;Z];
    costheta = 1 - sum(delta_k.^2,1)/2;
    lb_ls_correction = cat(1,lb_ls_correction,1/(1-sum(val.*costheta)/sum(val)));
end

% plot above

close all
plot(angleList,lb_ls_correction,'-k','LineWidth',2)
set(gcf,'Color','w')
grid on
xlabel('Polar Angle','FontSize',16)
ylabel('L_B/L_s','FontSize',16)

% find the energy dependence of the scattering correction

ps = @(kx,ky,kz)  (1./sqrt(kx.^2+ky.^2)).*...
    exp(-0.25*(kx.^2+ky.^2)-0.25*(5.8^2)*((kz.^2)./(kx.^2+ky.^2)));

angleList = [0,30,60,90];
rrList = logspace(-2,2,40);
lb_ls_correction = [];
for angle = angleList,
    temp = [];
    for rr = rrList,
        nn = 1e7;
%         rr = 1; %sets the radius of the sphere is k-space
        theta0 = pi*angle/180.0; %sets the angle from the positive z axis

        TH = 2*pi*rand(1,nn);
        PH = asin(-1+2*rand(1,nn));
        [X,Y,Z] = sph2cart(TH,PH,1);

        %scale the rotated coordinates such that
        x = rr*X; y = rr*Y; z = rr*Z;

        %evaluate weight of power spectrum on displaced surface
        val = ps(x-rr*sin(theta0),y,z-rr*cos(theta0));
        delta_k = [sin(theta0);0;cos(theta0)]*ones(1,nn)-[X;Y;Z];
        costheta = 1 - sum(delta_k.^2,1)/2;
        temp = cat(1,temp,1/(1-sum(val.*costheta)/sum(val)));
    end
    lb_ls_correction = cat(2,lb_ls_correction,temp);
end

% plot above
cList = [0.64 0 0.15; 0.88 0.51 0.08; 0 0.41 0.21; 0.19 0.21 0.58];
nf = figure;
for i = 1:numel(angleList),
    loglog(rrList.^2,lb_ls_correction(:,i),'-','LineWidth',2,'Color',cList(i,:))
```

```
    hold on
end
set(gcf,'Color','w')
grid on
xlabel('E/E_s','FontSize',16)
ylabel('L_B/L_s','FontSize',16)
legend('0','30','60','90','Location','NorthWest')
ylim([0.5,10^3])
```

B.2 On-Shell Scattering Probability in Speckle

```
% integrate over on-shell scattering weight
E_Esigma = 100; %particle energy
k = sqrt(E_Esigma); %magnitude of k-vector
anisotropy = 5.8; %ratio of sigma_parallel to sigma_perp
theta_shift = 0*pi/180; %direction of

ps = @(kx,ky,kz) pi^(1.5)*(1./sqrt(kx.^2+ky.^2)).*...
    exp(-0.25*(kx.^2+ky.^2)-0.25*(anisotropy^2)*((kz.^2)./(kx.^2+ky.^2)));
ps_shift = @(r,t,p,p0) sin(p).*ps(r.*(cos(t).*sin(p)-sin(p0)),...
    r.*sin(t).*sin(p),r.*(cos(p)-cos(p0)));
on_shell_weight = @(theta,phi) rr*anisotropy/(4*pi^2)*...
    ps_shift(k,theta,phi,theta_shift);
tauDelta_hbarEsigma = 1/(integral2(on_shell_weight,0,2*pi,0,pi));
```

Appendix C

Thermodynamics in Lattice + Trap System

C.1 Hartree-Fock Thermodynamics in Optical Lattice

```
% generate distribution of cos(q) for doing fast 2D evaluation
npoints = 5000000;
cosq = 3-sum(cos(pi*(1-2*rand(npoints,3))),2);
nq = 100;
cosq_vals = linspace(0,6,nq);
cosq_prob = hist(cosq(),cosq_vals);
cosq_prob = cosq_prob/npoints;

rmax = 60;
nr = 60+1;
xlist = linspace(0,rmax,nr);
[qval, xval] = meshgrid(cosq_vals,xlist);
[qprob,xprob] = meshgrid(cosq_prob,4*pi*(rmax/nr)*linspace(0,rmax,nr).^2);

%convert all to columns
qval = qval(:);
xval = xval(:);
qprob = qprob(:);
xprob = xprob(:);

% sum(qprob.*xprob.*exp(-1*(xval/10).^2-qval))
%this should equal 562.614, it does! checked with mathematica.

% OK now actually do the hartree fock calculation

% s = [4 4.5 5 5.5 6 6.5 7];
% t = [0.0862,...
%      0.0754,...
%      0.0661,...
%      0.0579,...
%      0.0509,...
%      0.0448,...
%      0.0395];
%
% U = [0.19953,...
%      0.22612,...
%      0.25275,...
%      0.27928,...
%      0.30561,...
%      0.33168,...
%      0.35745];

%number_constraint represent the number in a single spin state (N_tot/2)
 t = 0.0862; Umax = 0.19953; number_constraint = 49*1000/2; %in units of ER
% t = 0.0661; Umax = 0.25275; number_constraint = 32.8*1000/2; %in units of ER
% t = 0.0509; Umax = 0.30561; number_constraint = 22.2*1000/2; %in units of ER
% t = 0.0395; Umax = 0.357; number_constraint = 15.2*1000/2; %in units of ER
% gamma = 0.25*0.00170*(100/107)^2; % in units of ER per wavelenth^2
% gamma = 0.25*0.00170*(100/107)^2; % in units of ER per wavelenth^2
gamma = 0.000425*(100/107)^2; % in units of ER per lattice site^2
entropy_constraint = 1.7;

%thermodynamics are done for a single spin state. Divide the interaction energy
%equally between the two states so that energy is not double counted!
Umax = Umax/2;

gridpoints = 50;
[TT,mumu] = meshgrid(linspace(0,0.3,gridpoints),linspace(0.01,1,gridpoints));
TT_col = TT(:);
mumu_col = mumu(:);
temp_density = zeros(size(xval));
density = zeros(size(xlist));

gdensity = [];
qdist = [];
checkNumber = [];
thermodynamics = [];

adj_max = 0.5;
adj = 0.5;
if Umax==0,
    Ulist = zeros(1,6);
else
    Ulist = [zeros(1,6),linspace(0,Umax,15),Umax*ones(1,6)];
end
```

```
76
77  for ii = 1:numel(Ulist),
78      U = Ulist(ii)
79      entropy_mc = zeros(size(TT_col));
80      number_mc = zeros(size(TT_col));
81      for i = 1:numel(TT),
82          T = TT_col(i);
83          mu = mumu_col(i);
84          number_mc(i) = sum(qprob.*xprob.*1./(...
85              exp((2*t*qval+gamma*xval.^2+U*temp_density-mu)./T)+1));
86          entropy_mc(i) = sum(qprob.*xprob.*(log(1+exp((mu-2*t*qval-gamma*xval.^2-U*temp_density)./T))...
87              -((mu-2*t*qval-gamma*xval.^2-U*temp_density)./T).*...
88              (1./(exp(-1*(mu-2*t*qval-gamma*xval.^2-U*temp_density)./T)+1))));
89      end
90      entropy_mc = reshape(entropy_mc,size(TT));
91      number_mc = reshape(number_mc,size(TT));
92
93      fracerror = abs(number_mc-number_constraint)/number_constraint+...
94          abs(((entropy_mc./number_mc)-entropy_constraint)/entropy_constraint);
95      fracerror = fracerror(:);
96
97      %find best T and mu from error functional
98      [x,indx] = min(fracerror);
99      T = TT_col(indx);
100     mu = mumu_col(indx);
101
102     % density as a function of radius
103     density1 = zeros(size(density));
104     for i = 1:numel(xlist),
105         x = xlist(i);
106         density1(i) = sum(cosq_prob.*1./(...
107             exp((2*t*cosq_vals+gamma*x.^2+U*density(i)-mu)./T)+1));
108     end
109     density = density1;
110     gdensity = cat(1,gdensity,density);
111
112     %calculate quasimomentum distributin from (000) to (100)
113     qdist_temp = [];
114     for i = linspace(0,pi,20),
115         temp = sum(xlist.^2.*1./(...
116             exp((2*t*(1-cos(i))+gamma*xlist.^2+U*density-mu)./T)+1));
117         qdist_temp = cat(2,qdist_temp,temp);
118     end
119     qdist = cat(1,qdist,qdist_temp);
120
121     %generate density list to be used in next iteration
122     [foo, temp_density] = meshgrid(ones(nq,1),density);
123     temp_density = temp_density(:);
124
125     %generate new grid point based on last value found
126     gridpoints = 25;
127
128     [TT,mumu] = meshgrid(linspace(T*(1-adj),T*(1+adj),gridpoints),...
129         linspace(mu*(1-adj),mu*(1+adj),gridpoints));
130     TT_col = TT(:);
131     mumu_col = mumu(:);
132
133     if (ii<7) adj = adj*0.5; end
134     if (ii==7) adj = adj_max; end
135     if (U == Umax) adj = adj*0.5; end
136
137     checkNumber = cat(1,checkNumber,sum(qprob.*xprob.*1./(...
138         exp((2*t*qval+gamma*xval.^2+U*temp_density-mu)./T)+1)));
139
140     thermodynamics = cat(1,thermodynamics,[t,U,T,mu,density(1),...
141         qdist_temp(end)/qdist_temp(1)]);
142 end
143 close all
144 plot(gdensity')
145 %this prints the thermodynamic variabls as a function of iteartion
146 %number. check this for convergence and adjust accordingly!
147 thermodynamics
148
149 % plot quasimomentum dist, compare NI and HF
150 close all
151 qxlist = linspace(0,pi,20);
152 norm = max([qdist(6,:) qdist(end,:)]);
153 plot(qxlist/pi,qdist(6,:)/norm,'k','LineWidth',2)
154 hold on
155 plot(qxlist/pi,qdist(end,:)/norm,'r','LineWidth',2)
156 set(gcf,'Color','w')
157 xlabel('Quasimomentum (q / q_B)','FontSize',12)
158 ylabel('Occupation (arb)','FontSize',12)
159 h = legend('Non-Interacting','Hartree-Fock');
160 set(h,'FontSize',12)
161 grid on
162 ylim([0,1])
163 set(gcf,'Position',[700 670 560 420])
164
165 nf = figure;
166 plot(xlist,gdensity(6,:),'k','LineWidth',2)
167 hold on
168 plot(xlist,gdensity(end,:),'r','LineWidth',2)
169 set(gcf,'Color','w')
170 xlabel('Radial Distance (d)','FontSize',12)
171 ylabel('Occ. per Spin State (#)','FontSize',12)
172 hh = legend('Non-Interacting','Hartree-Fock');
173 set(hh,'FontSize',12)
174 xlim([0,45])
175 grid on
176 set(gcf,'Position',[100 670 560 420])
```

C.2 Calculating Bandmapped Optical Depth Images

```
%calculate OD image by summing n(q) along a line parallel with imaging
%axis for each pixel in the imaging system. don't expect fast evaluation.
t = 0.0862;
T = t/2;
mu = 5*t;
gamma = 0.000425*(100/107)^2;

ximg = linspace(-2,2,160);
%this gives same magnification as imaging at 10ms
[xx,yy] = meshgrid(ximg,ximg);
xxc = reshape(xx,numel(xx),1);
yyc = reshape(yy,numel(yy),1);
npoints = 500.0;
tt = linspace(-2.0,2,npoints);
OD = zeros(size(xxc));
for i = 1:numel(xxc),
    xprime = xxc(i);
    yprime = yyc(i);
    x0 = [xprime/sqrt(2.0)+yprime/sqrt(3.0),...
        -1*xprime/sqrt(2.0)+yprime/sqrt(3.0),yprime/sqrt(3.0)];
    imagingDir = (1/sqrt(6.0))*[1,1,-2];
    x = x0(1)+imagingDir(1)*tt;
    y = x0(2)+imagingDir(2)*tt;
    z = x0(3)+imagingDir(3)*tt;

    tempProb = 0;
    for j = 1:numel(x),
        if logical((abs(x(j))<1).*(abs(y(j))<1).*(abs(z(j))<1)),
            prob = sum(xlist.^2.*1./(...
                exp((2*t*(3-cos(pi*x(j))-cos(pi*y(j))-cos(pi*z(j)))...
                +gamma*xlist.^2+U*density-mu)./T)+1));
            tempProb = tempProb + prob;
        end
    end
    OD(i) = tempProb/npoints;
end
number = 20000;
OD = number*3*766.7^2/((3.19)^2*2*pi*1000)*reshape(OD/sum(OD(:)),size(xx));
```

References

[1] Abrahams, E. *Fifty Years of Anderson Localization*. World Scientific Publishing Company, 2010. 55

[2] Abrahams, E., Anderson, P. W., Licciardello, D. C., and Ramakrishnan, T. V. Scaling Theory of Localization: Absence of Quantum Diffusion in Two Dimensions. *Phys. Rev. Lett. 42* (Mar 1979), 673–676. 55

[3] Aidelsburger, M., Atala, M., Lohse, M., Barreiro, J. T., Paredes, B., and Bloch, I. Realization of the Hofstadter Hamiltonian with Ultracold Atoms in Optical Lattices. *Physical Review Letters 111*, 18 (Oct 2013). 86

[4] Aidelsburger, M., Atala, M., Nascimbne, S., Trotzky, S., Chen, Y.-A., and Bloch, I. Experimental Realization of Strong Effective Magnetic Fields in an Optical Lattice. *Physical Review Letters 107*, 25 (Dec 2011). 86

[5] Aikawa, K., Frisch, A., Mark, M., Baier, S., Grimm, R., and Ferlaino, F. Reaching Fermi Degeneracy via Universal Dipolar Scattering. *Phys. Rev. Lett. 112* (Jan 2014), 010404. 8

[6] Anderson, P. W. Absence of Diffusion in Certain Random Lattices. *Phys. Rev. 109* (Mar 1958), 1492–1505. 55, 56

[7] Anderson, P. W. More Is Different. *Science 177*, 4047 (1972), pp. 393–396. 2

[8] Ashcroft, N., and Mermin, D. *Solid State Physics*. Harcourt College Publishers, 1976. 87, 110, 133

[9] Bakr, W. S., Gillen, J. I., Peng, A., Folling, S., and Greiner, M. A quantum gas microscope for detecting single atoms in a Hubbard-regime optical lattice. *Nature 462*, 7269 (Nov 2009), 74–77. 18, 85, 86

[10] Bakr, W. S., Peng, A., Tai, M. E., Ma, R., Simon, J., Gillen, J. I., Flling, S., Pollet, L., and Greiner, M. Probing the Superfluid-to-Mott Insulator Transition at the Single-Atom Level. *Science 329*, 5991 (2010), 547–550. 95, 108

[11] Basko, D., Aleiner, I., and Altshuler, B. Metal-insulator transition in a weakly interacting many-electron system with localized single-particle states. *Annals of Physics 321*, 5 (May 2006), 1126–1205. 120, 126

[12] Basko, D. M., Aleiner, I. L., and Altshuler, B. L. On the Problem of Many-Body Localization. In *Problems of Condensed Matter Physics*, International Series of Monographs on Physics. Oxford University Press, 2007. 120, 126

[13] Basko, D. M., Aleiner, I. L., and Altshuler, B. L. Possible experimental manifestations of the many-body localization. *Phys. Rev. B 76* (Aug 2007), 052203. 126

[14] Bergeman, T., Erez, G., and Metcalf, H. J. Magnetostatic trapping fields for neutral atoms. *Phys. Rev. A 35* (Feb 1987), 1535–1546. 13

[15] Bergmann, G. Physical interpretation of weak localization: A time-of-flight experiment with conduction electrons. *Phys. Rev. B 28* (Sep 1983), 2914–2920. 54

[16] Berry, M. V., and Dennis, M. R. Knotted and linked phase singularities in monochromatic waves. *Proceedings of the Royal Society of London A: Mathematical, Physical and Engineering Sciences 457*, 2013 (2001), 2251–2263. 39

[17] Best, T. *Interacting Bose-Fermi mixtures in optical lattices.* PhD thesis, Johannes Gutenberg-Universitat in Mainz, 2010. 11

[18] Billy, J., Josse, V., Zuo, Z., Bernard, A., Hambrecht, B., Lugan, P., Clement, D., Sanchez-Palencia, L., Bouyer, P., and Aspect, A. Direct observation of Anderson localization of matter waves in a controlled disorder. *Nature 453*, 7197 (Jun 2008), 891–894. 37, 55, 71

[19] Bloch, I., Dalibard, J., and Zwerger, W. Many-body physics with ultracold gases. *Rev. Mod. Phys. 80* (Jul 2008), 885–964. 85

[20] Born, M., and Wolf, E. *Principles of Optics: Electromagnetic theory of propagation, interference and diffraction of light, 7th Edition.* Cambridge University Press, 1999. 40, 41

[21] Bourdel, T., Khaykovich, L., Cubizolles, J., Zhang, J., Chevy, F., Teichmann, M., Tarruell, L., Kokkelmans, S. J. J. M. F., and Salomon, C. Experimental Study of the BEC-BCS Crossover Region in Lithium-6. *Phys. Rev. Lett. 93* (Jul 2004), 050401. 116

[22] Bradley, C. C., McClelland, J. J., Anderson, W. R., and Celotta, R. J. Magneto-optical trapping of chromium atoms. *Phys. Rev. A 61* (Apr 2000), 053407. 8

[23] Brinkmann, M. Optimierung der Detektion und Auswertung von 87Rb-Spinor-Kondensaten. Master's thesis, Universitat Hamburg, 2005. 34

[24] Bruin, J. A. N., Sakai, H., Perry, R. S., and Mackenzie, A. P. Similarity of Scattering Rates in Metals Showing T-Linear Resistivity. *Science 339*, 6121 (Feb 2013), 804807. 115, 116, 134

[25] Chabé, J., Lemarié, G., Grémaud, B., Delande, D., Szriftgiser, P., and Garreau, J. C. Experimental Observation of the Anderson Metal-Insulator Transition with Atomic Matter Waves. *Phys. Rev. Lett. 101* (Dec 2008), 255702. 37, 55

[26] Chen, D., Meldgin, C., Russ, P., Mueller, E., and DeMarco, B. Quasimomentum Cooling and Relaxation in a Strongly Correlated Optical Lattice. *arxiv:1503.07606* (2015). 23

[27] Cherroret, N., Karpiuk, T., Müller, C. A., Grémaud, B., and Miniatura, C. Coherent backscattering of ultracold matter waves: Momentum space signatures. *Phys. Rev. A 85* (Jan 2012), 011604. 82

[28] Chien, C.-C., Peotta, S., and Ventra, M. D. Quantum transport in ultracold atoms. *arXiv:1504.02907* (2015). 86

[29] Chin, C., Bartenstein, M., Altmeyer, A., Riedl, S., Jochim, S., Denschlag, J. H., and Grimm, R. Observation of the Pairing Gap in a Strongly Interacting Fermi Gas. *Science 305*, 5687 (2004), 1128–1130. 116

[30] Conti, C., and Fratalocchi, A. Dynamic light diffusion, three-dimensional Anderson localization and lasing in inverted opals. *Nat Phys 4*, 10 (Oct 2008), 794–798. 55

[31] Dagotto, E. Correlated electrons in high-temperature superconductors. *Rev. Mod. Phys. 66* (Jul 1994), 763–840. 116

[32] Dagotto, E. Complexity in Strongly Correlated Electronic Systems. *Science 309*, 5732 (Jul 2005), 257262. 116

[33] Dagotto, E. Open questions in CMR manganites, relevance of clustered states and analogies with other compounds including the cuprates. *New Journal of Physics 7*, 1 (2005), 67. 116

[34] Damascelli, A., Hussain, Z., and Shen, Z.-X. Angle-resolved photoemission studies of the cuprate superconductors. *Rev. Mod. Phys. 75* (Apr 2003), 473–541. 116

[35] Daou, R., Doiron-Leyraud, N., LeBoeuf, D., Li, S. Y., Laliberte, F., Cyr-Choiniere, O., Jo, Y. J., Balicas, L., Yan, J.-Q., Zhou, J.-S., Goodenough, J. B., and Taillefer, L. Linear temperature dependence of resistivity and change in the Fermi surface at the pseudogap critical point of a high-Tc superconductor. *Nat Phys 5*, 1 (Jan 2009), 31–34. 85, 116, 133

[36] Davidovich, L., Orszag, M., and Zagury, N. Quantum nondemolition measurements of vibrational populations in ionic traps. *Phys. Rev. A 54* (Dec 1996), 5118–5125. 25

[37] Davis, K., Mewes, M.-O., and Ketterle, W. An analytical model for evaporative cooling of atoms. *Applied Physics B 60*, 2-3 (1995), 155–159. 8

[38] De Leo, L., Bernier, J.-S., Kollath, C., Georges, A., and Scarola, V. W. Thermodynamics of the three-dimensional Hubbard model: Implications for cooling cold atomic gases in optical lattices. *Phys. Rev. A 83* (Feb 2011), 023606. 110

[39] de Melo, C. A. R. S. When fermions become bosons: Pairing in ultracold gases. *Phys. Today 61*, 10 (Oct 2008), 45–51. 116

[40] Delande, D., and Orso, G. Mobility Edge for Cold Atoms in Laser Speckle Potentials. *Phys. Rev. Lett. 113* (Aug 2014), 060601. 68, 81

[41] Delande, D., Sacha, K., Plodzien, M., Avazbaev, S. K., and Zakrzewski, J. Many-body Anderson localization in one-dimensional systems. *New Journal of Physics 15*, 4 (2013), 045021. 72

[42] DeMarco, B., Bohn, J. L., Burke, J. P., Holland, M., and Jin, D. S. Measurement of p-Wave Threshold Law Using Evaporatively Cooled Fermionic Atoms. *Phys. Rev. Lett. 82*, 21 (May 1999), 4208–. 8, 57

[43] DeMarco, B., and Jin, D. S. Onset of Fermi Degeneracy in a Trapped Atomic Gas. *Science 285*, 5434 (1999), 1703–1706. 6, 8

[44] DeMarco, B. L. *Quantum Behavior of an Atomic Fermi Gas.* PhD thesis, University of Colorado, 2001. 6, 96

[45] DeSalvo, B. J., Yan, M., Mickelson, P. G., Martinez de Escobar, Y. N., and Killian, T. C. Degenerate Fermi Gas of ^{87}Sr. *Phys. Rev. Lett. 105* (Jul 2010), 030402. 8

[46] Deutsch, J. M. Quantum statistical mechanics in a closed system. *Phys. Rev. A 43* (Feb 1991), 2046–2049. 128

[47] Doiron-Leyraud, N., Auban-Senzier, P., René de Cotret, S., Bourbonnais, C., Jérome, D., Bechgaard, K., and Taillefer, L. Correlation between linear resistivity and T_c in the Bechgaard salts and the pnictide superconductor $Ba(Fe_{1-x}Co_x)_2As_2$. *Phys. Rev. B 80* (Dec 2009), 214531. 85

[48] Duarte, P. M., Hart, R. A., Hitchcock, J. M., Corcovilos, T. A., Yang, T.-L., Reed, A., and Hulet, R. G. All-optical production of a lithium quantum gas using narrow-line laser cooling. *Phys. Rev. A 84* (Dec 2011), 061406. 7

[49] Ernst, P. T., Gotze, S., Krauser, J. S., Pyka, K., Luhmann, D.-S., Pfannkuche, D., and Sengstock, K. Probing superfluids in optical lattices by momentum-resolved Bragg spectroscopy. *Nat Phys 6*, 1 (Jan 2010), 56–61. 23

[50] Esslinger, T., Bloch, I., and Hänsch, T. W. Bose-Einstein condensation in a quadrupole-Ioffe-configuration trap. *Phys. Rev. A 58* (Oct 1998), R2664–R2667. 11

[51] Fernandes, D. R., Sievers, F., Kretzschmar, N., Wu, S., Salomon, C., and Chevy, F. Sub-Doppler laser cooling of fermionic 40 K atoms in three-dimensional gray optical molasses. *EPL (Europhysics Letters) 100*, 6 (2012), 63001. 7

[52] Fernandez-Marin, A. A., Mendez-Bermudez, J. A., Carbonell, J., Cervera, F., Sanchez-Dehesa, J., and Gopar, V. A. Beyond Anderson Localization in 1D: Anomalous Localization of Microwaves in Random Waveguides. *Phys. Rev. Lett. 113* (Dec 2014), 233901. 55

[53] Fert, A. Nobel Lecture: Origin, development, and future of spintronics. *Rev. Mod. Phys. 80*, 4 (Dec 2008), 1517–1530. 115

[54] Fukuhara, T., Kantian, A., Endres, M., Cheneau, M., Schausz, P., Hild, S., Bellem, D., Schollwock, U., Giamarchi, T., Gross, C., Bloch, I., and Kuhr, S. Quantum dynamics of a mobile spin impurity. *Nat Phys 9*, 4 (Apr 2013), 235–241. 86

[55] Fukuhara, T., Takasu, Y., Kumakura, M., and Takahashi, Y. Degenerate Fermi Gases of Ytterbium. *Phys. Rev. Lett. 98* (Jan 2007), 030401. 8

[56] Gadway, B., Pertot, D., Reeves, J., Vogt, M., and Schneble, D. Glassy Behavior in a Binary Atomic Mixture. *Phys. Rev. Lett. 107* (Sep 2011), 145306. 37

[57] Gadway, B., Pertot, D., Reimann, R., Cohen, M. G., and Schneble, D. Analysis of Kapitza-Dirac diffraction patterns beyond the Raman-Nath regime. *Opt. Express 17*, 21 (Oct 2009), 19173–19180. 91

[58] Gadway, B., Reeves, J., Krinner, L., and Schneble, D. Evidence for a Quantum-to-Classical Transition in a Pair of Coupled Quantum Rotors. *Phys. Rev. Lett. 110* (May 2013), 190401. 37, 55

[59] Gaebler, J. P., Stewart, J. T., Drake, T. E., Jin, D. S., Perali, A., Pieri, P., and Strinati, G. C. Observation of pseudogap behaviour in a strongly interacting Fermi gas. *Nat Phys 6*, 8 (Aug 2010), 569–573. 23

[60] Garg, A., Randeria, M., and Trivedi, N. Strong correlations make high-temperature superconductors robust against disorder. *Nat Phys 4*, 10 (Oct 2008), 762–765. 116

[61] Gatti, A., Magatti, D., and Ferri, F. Three-dimensional coherence of light speckles: Theory. *Phys. Rev. A 78* (Dec 2008), 063806. 40

[62] Gaunt, A. L., Schmidutz, T. F., Gotlibovych, I., Smith, R. P., and Hadzibabic, Z. Bose-Einstein Condensation of Atoms in a Uniform Potential. *Physical Review Letters 110*, 20 (May 2013). 18, 86

[63] Gemelke, N., Zhang, X., Hung, C.-L., and Chin, C. In situ observation of incompressible Mott-insulating domains in ultracold atomic gases. *Nature 460*, 7258 (Aug 2009), 995–998. 119

[64] Goodman, J. W. *Speckle Phenomena in Optics: Theory and Applications.* Roberts and Company Publishers, 2007. 38, 40, 41

[65] Greiner, M., Bloch, I., Mandel, O., Hänsch, T. W., and Esslinger, T. Exploring Phase Coherence in a 2D Lattice of Bose-Einstein Condensates. *Phys. Rev. Lett. 87* (Oct 2001), 160405. 93

[66] Greiner, M., Bloch, I., Mandel, O., Hnsch, T., and Esslinger, T. Bose-Einstein condensates in 1D- and 2D optical lattices. *Applied Physics B 73*, 8 (2001), 769–772. 93

[67] Greiner, M., and Folling, S. Condensed-matter physics: Optical lattices. *Nature 453*, 7196 (Jun 2008), 736–738. 86

[68] Greiner, M., Mandel, O., Esslinger, T., Hansch, T. W., and Bloch, I. Quantum phase transition from a superfluid to a Mott insulator in a gas of ultracold atoms. *Nature 415*, 6867 (Jan 2002), 39–44. 85, 86

[69] Grimm, R., Weidemüller, M., and Ovchinnikov, Y. B. Optical Dipole Traps for Neutral Atoms. *Advances In Atomic, Molecular, and Optical Physics Volume 42* (2000), 95–170. 18

[70] Gurarie, V., Pollet, L., Prokofiev, N. V., Svistunov, B. V., and Troyer, M. Phase diagram of the disordered Bose-Hubbard model. *Phys. Rev. B 80*, 21 (Dec 2009), 214519. 122, 123

[71] Gutzwiller, M. C. Effect of Correlation on the Ferromagnetism of Transition Metals. *Phys. Rev. Lett. 10* (1963), 159–162. 85

[72] Hadzibabic, Z., Gupta, S., Stan, C., Schunck, C., Zwierlein, M., Dieckmann, K., and Ketterle, W. Fiftyfold Improvement in the Number of Quantum Degenerate Fermionic Atoms. *Physical Review Letters 91*, 16 (Oct 2003). 9, 98

[73] Hart, R. A., Duarte, P. M., Yang, T.-L., Liu, X., Paiva, T., Khatami, E., Scalettar, R. T., Trivedi, N., Huse, D. A., and Hulet, R. G. Observation of antiferromagnetic correlations in the Hubbard model with ultracold atoms. *Nature 519*, 7542 (Mar 2015), 211–214. 9, 86, 98, 108, 117

[74] Hartnoll, S. A. Theory of universal incoherent metallic transport. *arXiv:1405.3651v3* (2014). 98, 134

[75] Heinzen, D. J., and Wineland, D. J. Quantum-limited cooling and detection of radio-frequency oscillations by laser-cooled ions. *Phys. Rev. A 42* (Sep 1990), 2977–2994. 25

[76] Hu, H., Strybulevych, A., Page, J. H., Skipetrov, S. E., and van Tiggelen, B. A. Localization of ultrasound in a three-dimensional elastic network. *Nat Phys 4*, 12 (Dec 2008), 945–948. 55

[77] Hubbard, J. Electron Correlations in Narrow Energy Bands. *Proc. R. Soc. A 276* (1963), 237–257. 85

[78] Hussey, N. E., Takenaka, K., and Takagi, H. Universality of the Mott-Ioffe-Regel limit in metals. *Philosophical Magazine 84*, 27 (Sep 2004), 28472864. 134

[79] Imada, M., Fujimori, A., and Tokura, Y. Metal-insulator transitions. *Rev. Mod. Phys. 70*, 4 (oct 1998), 1039–1263. 116

[80] Jaksch, D., Briegel, H.-J., Cirac, J. I., Gardiner, C. W., and Zoller, P. Entanglement of Atoms via Cold Controlled Collisions. *Phys. Rev. Lett. 82* (Mar 1999), 1975–1978. 19

[81] Jaksch, D., Bruder, C., Cirac, J. I., Gardiner, C. W., and Zoller, P. Cold Bosonic Atoms in Optical Lattices. *Phys. Rev. Lett. 81* (Oct 1998), 3108–3111. 86

[82] Jendrzejewski, F. *Quantum transport of ultracold atoms in disordered potentials: Anderson Localization in three dimensions, Coherent Backscattering.* PhD thesis, Universite Paris Sud, 2012. 55, 82

[83] Jendrzejewski, F., Bernard, A., Muller, K., Cheinet, P., Josse, V., Piraud, M., Pezze, L., Sanchez-Palencia, L., Aspect, A., and Bouyer, P. Three-dimensional localization of ultracold atoms in an optical disordered potential. *Nat Phys 8*, 5 (May 2012), 398–403. 55, 82, 83

[84] Jendrzejewski, F., Mller, K., Richard, J., Date, A., Plisson, T., Bouyer, P., Aspect, A., and Josse, V. Coherent Backscattering of Ultracold Atoms. *Phys. Rev. Lett. 109*, 19 (Nov 2012), 195302–. 37, 55, 82

[85] Jordens, R. *Metallic and Mott-insulating phases in fermionic quantum gases.* PhD thesis, ETH Zurich, 2010. 110

[86] Jordens, R., Strohmaier, N., Gunter, K., Moritz, H., and Esslinger, T. A Mott insulator of fermionic atoms in an optical lattice. *Nature 455*, 7210 (sep 2008), 204–207. 85, 86

[87] Jordens, R., Tarruell, L., Greif, D., Uehlinger, T., Strohmaier, N., Moritz, H., Esslinger, T., De Leo, L., Kollath, C., Georges, A., and et al. Quantitative Determination of Temperature in the Approach to Magnetic Order of Ultracold Fermions in an Optical Lattice. *Physical Review Letters 104*, 18 (May 2010). 110, 119

[88] Kanamori, J. Electron Correlation and Ferromagnetism of Transition Metals. *Prog. Theor. Phys. 30* (1963), 275–289. 85

[89] Karbasi, S., Frazier, R. J., Koch, K. W., Hawkins, T., Ballato, J., and Mafi, A. Image transport through a disordered optical fibre mediated by transverse Anderson localization. *Nat Commun 5*, 3362 (Feb 2014). 55

[90] Kasevich, M. A. *Atom Interferometry in a Atomic Fountain.* PhD thesis, Stanford University, 1992. 31

[91] Kastberg, A., Phillips, W. D., Rolston, S. L., Spreeuw, R. J. C., and Jessen, P. S. Adiabatic Cooling of Cesium to 700 nK in an Optical Lattice. *Phys. Rev. Lett. 74* (Feb 1995), 1542–1545. 93

[92] Ketterle, W., Davis, K. B., Joffe, M. A., Martin, A., and Pritchard, D. E. High densities of cold atoms in a *dark* spontaneous-force optical trap. *Phys. Rev. Lett. 70* (Apr 1993), 2253–2256. 6

[93] Ketterle, W., and Druten, N. V. Evaporative Cooling of Trapped Atoms. In *Advances In Atomic, Molecular, and Optical Physics*, B. Bederson and H. Walther, Eds., vol. 37. Academic Press, 1996, pp. 181 – 236. 8

[94] Kim, H., Ikeda, T. N., and Huse, D. A. Testing whether all eigenstates obey the eigenstate thermalization hypothesis. *Phys. Rev. E 90*, 5 (Nov 2014). 128

[95] Kinoshita, T., Wenger, T., and Weiss, D. S. A quantum Newton's cradle. *Nature 440*, 7086 (Apr. 2006), 900–903. 86, 128

[96] Kobayashi, J., Izumi, Y., Kumakura, M., and Takahashi, Y. Stable all-optical formation of BoseEinstein condensate using pointing-stabilized optical trapping beams. *Applied Physics B 83*, 1 (2006), 21–25. 21

[97] Köhl, M., Moritz, H., Staferle, T., Schori, C., and Esslinger, T. Superfluid to Mott insulator transition in one, two, and three dimensions. *Journal of Low Temperature Physics 138*, 3-4 (2005), 635–644. 91

[98] Köhl, M., Moritz, H., Stöferle, T., Günter, K., and Esslinger, T. Fermionic Atoms in a Three Dimensional Optical Lattice: Observing Fermi Surfaces, Dynamics, and Interactions. *Phys. Rev. Lett. 94* (Mar 2005), 080403. 93

[99] Kollath, C., Iucci, A., Giamarchi, T., Hofstetter, W., and Schollwöck, U. Spectroscopy of Ultracold Atoms by Periodic Lattice Modulations. *Phys. Rev. Lett. 97* (Jul 2006), 050402. 91

[100] Kondov, S. S. *Ultracold Fermionic Atoms in Disordered Potentials.* PhD thesis, University of Illinois at Urbana-Champaign, 2013. 6, 11, 13, 23, 44, 47, 53, 55, 91, 119

[101] Kondov, S. S., McGehee, W. R., Xu, W., and DeMarco, B. Disorder-Induced Localization in a Strongly Correlated Atomic Hubbard Gas. *Phys. Rev. Lett. 114* (Feb 2015), 083002. 117, 129

[102] Kondov, S. S., McGehee, W. R., Zirbel, J. J., and DeMarco, B. Three-Dimensional Anderson Localization of Ultracold Matter. *Science 334*, 6052 (2011), 66–68. 53

[103] Kramer, B., and MacKinnon, A. Localization: theory and experiment. *Reports on Progress in Physics 56*, 12 (1993), 1469–. 55, 120

[104] Krinner, S., Stadler, D., Husmann, D., Brantut, J.-P., and Esslinger, T. Observation of quantized conductance in neutral matter. *Nature 517*, 7532 (Jan. 2015), 64–67. 37

[105] Kronjager, J. *Coherent Dynamics of Spinor Bose-Einstein Condensates*. PhD thesis, Universitat Hamburg, 2007. 34, 36

[106] Kuhn, R. C., Sigwarth, O., Miniatura, C., Delande, D., and Mller, C. A. Coherent matter wave transport in speckle potentials. *New Journal of Physics 9*, 6 (2007), 161–. 60, 71, 72, 79

[107] Lagendijk, A., van Tiggelen, B., and Wiersma, D. S. Fifty years of Anderson localization. *Phys. Today 62*, 8 (Aug. 2009), 24–29. 55

[108] Lahini, Y., Avidan, A., Pozzi, F., Sorel, M., Morandotti, R., Christodoulides, D. N., and Silberberg, Y. Anderson Localization and Nonlinearity in One-Dimensional Disordered Photonic Lattices. *Phys. Rev. Lett. 100*, 1 (Jan. 2008), 013906–. 55

[109] Landini, M., Roy, S., Carcagní, L., Trypogeorgos, D., Fattori, M., Inguscio, M., and Modugno, G. Sub-Doppler laser cooling of potassium atoms. *Phys. Rev. A 84* (Oct 2011), 043432. 7

[110] Langer, J. S., and Neal, T. Breakdown of the Concentration Expansion for the Impurity Resistivity of Metals. *Phys. Rev. Lett. 16* (May 1966), 984–986. 55

[111] Leach, J., Dennis, M. R., Courtial, J., and Padgett, M. J. Laser beams: Knotted threads of darkness. *Nature 432*, 7014 (Nov 2004), 165–165. 39

[112] LeBlanc, L. J. *Exploring many-body physics with ultracold atoms*. PhD thesis, University of Toronto, 2011. 33, 98

[113] Lee, P. A., and Ramakrishnan, T. V. Disordered electronic systems. *Rev. Mod. Phys. 57*, 2 (Apr. 1985), 287–. 55

[114] Lee, P. A., and Wen, X.-G. Doping a Mott insulator: Physics of high-temperature superconductivity. *Rev. Mod. Phys. 78*, 1 (Jan 2006), 1785. 115, 116

[115] Lee, P. J., Anderlini, M., Brown, B. L., Sebby-Strabley, J., Phillips, W. D., and Porto, J. V. Sublattice Addressing and Spin-Dependent Motion of Atoms in a Double-Well Lattice. *Phys. Rev. Lett. 99* (Jul 2007), 020402. 19

[116] Lee, P. J., Blinov, B. B., Brickman, K., Deslauriers, L., Madsen, M. J., Miller, R., Moehring, D. L., Stick, D., and Monroe, C. Atomic qubit manipulations with an electro-optic modulator. *Opt. Lett. 28*, 17 (Sep 2003), 1582–1584. 31

[117] Lin, G.-D. *Quantum Simulation with Ultracold Atoms and Trapped Ions*. PhD thesis, University of Michigan, 2010. 104

[118] Lin, G.-D., Zhang, W., and Duan, L.-M. Characteristics of Bose-Einstein condensation in an optical lattice. *Phys. Rev. A 77* (Apr 2008), 043626. 104

[119] Lin, Y.-J., Compton, R. L., Perry, A. R., Phillips, W. D., Porto, J. V., and Spielman, I. B. Bose-Einstein Condensate in a Uniform Light-Induced Vector Potential. *Phys. Rev. Lett. 102* (Mar 2009), 130401. 19

[120] Lin, Y.-J., Jimenez-Garcia, K., and Spielman, I. B. Spin-orbit-coupled Bose-Einstein condensates. *Nature 471*, 7336 (Mar. 2011), 83–86. 23

[121] Lu, M., Burdick, N. Q., and Lev, B. L. Quantum Degenerate Dipolar Fermi Gas. *Phys. Rev. Lett. 108* (May 2012), 215301. 8

[122] Lü, Q.-Q., Patton, K. R., and Sheehy, D. E. Self-consistent Hartree-Fock approach for interacting bosons in optical lattices. *Phys. Rev. A 90* (Dec 2014), 063625. 104

[123] Mackenzie, A. P., Haselwimmer, R. K. W., Tyler, A. W., Lonzarich, G. G., Mori, Y., Nishizaki, S., and Maeno, Y. Extremely Strong Dependence of Superconductivity on Disorder in Sr_2RuO_4. *Phys. Rev. Lett. 80* (Jan 1998), 161–164. 117

[124] Mackenzie, A. P., and Maeno, Y. The superconductivity of Sr_2RuO_4 and the physics of spin-triplet pairing. vol. 75, American Physical Society, pp. 657–712. 85, 117

[125] MacKinnon, A., and Kramer, B. The scaling theory of electrons in disordered solids: Additional numerical results. *Zeitschrift fr Physik B Condensed Matter 53*, 1 (1983), 1–13. 81

[126] Magatti, D., Gatti, A., and Ferri, F. Three-dimensional coherence of light speckles: Experiment. *Phys. Rev. A 79* (May 2009), 053831. 40

[127] Maret, G., Sperling, T., Buhrer, W., Lubatsch, A., Frank, R., and Aegerter, C. M. Inelastic scattering puts in question recent claims of Anderson localization of light. *Nature Photonics 7*, 12 (Dec 2013), 934–935. 62

[128] Mathy, C. J. M., and Huse, D. A. Accessing the Néel phase of ultracold fermionic atoms in a simple-cubic optical lattice. *Phys. Rev. A 79* (Jun 2009), 063412. 119, 120

[129] McClelland, J. J., and Hanssen, J. L. Laser Cooling without Repumping: A Magneto-Optical Trap for Erbium Atoms. *Phys. Rev. Lett. 96* (Apr 2006), 143005. 8

[130] McGehee, W. R. Three-dimensional Anderson localization. *Physics Today 61*, 11 (2011), 92. 3

[131] McGehee, W. R., Kondov, S. S., Xu, W., Zirbel, J. J., and DeMarco, B. Three-Dimensional Anderson Localization in Variable Scale Disorder. *Phys. Rev. Lett. 111* (Oct 2013), 145303. 53

[132] McGehee, W. R., Kondov, S. S., Xu, W., Zirbel, J. J., and DeMarco, B. McGehee *et al.* Reply. *Phys. Rev. Lett. 113* (Aug 2014), 099602. 53, 70

[133] McKay, D., and DeMarco, B. Thermometry with spin-dependent lattices. *New Journal of Physics 12*, 5 (2010), 055013. 19

[134] McKay, D., White, M., and DeMarco, B. Lattice thermodynamics for ultracold atoms. *Phys. Rev. A 79* (Jun 2009), 063605. 93, 122, 125

[135] McKay, D. C. *Quantum Simulation in Strongly Correlated Optical Lattices*. PhD thesis, University of Illinois at Urbana-Champaign, 2012. 6, 9, 90, 95, 110, 117

[136] McKay, D. C., and DeMarco, B. Cooling in strongly correlated optical lattices: prospects and challenges. *Reports on Progress in Physics 74*, 5 (2011), 054401. 95, 120, 121, 125

[137] McKay, D. C., Jervis, D., Fine, D. J., Simpson-Porco, J. W., Edge, G. J. A., and Thywissen, J. H. Low-temperature high-density magneto-optical trapping of potassium using the open 4S→5P transition at 405 nm. *Phys. Rev. A 84* (Dec 2011), 063420. 7

[138] Meldgin, C., Ray, U., Russ, P., Ceperley, D., and DeMarco, B. Probing the Bose-Glass–Superfluid Transition using Quantum Quenches of Disorder. *arXiv:1502.02333* (2015). 122

[139] Miranda, E., and Dobrosavljevic, V. Disorder-driven non-Fermi liquid behaviour of correlated electrons. *Reports on Progress in Physics 68*, 10 (2005), 2337. 116

[140] Mirzaei, S. I., Stricker, D., Hancock, J. N., Berthod, C., Georges, A., van Heumen, E., Chan, M. K., Zhao, X., Li, Y., Greven, M., and et al. Spectroscopic evidence for Fermi liquid-like energy and temperature dependence of the relaxation rate in the pseudogap phase of the cuprates. *Proceedings of the National Academy of Sciences 110*, 15 (Mar 2013), 57745778. 116

[141] Miyake, H., Siviloglou, G. A., Kennedy, C. J., Burton, W. C., and Ketterle, W. Realizing the Harper Hamiltonian with Laser-Assisted Tunneling in Optical Lattices. *Physical Review Letters 111*, 18 (Oct 2013). 86

[142] Modugno, G., Ferlaino, F., Heidemann, R., Roati, G., and Inguscio, M. Production of a Fermi gas of atoms in an optical lattice. *Phys. Rev. A 68* (Jul 2003), 011601. 111

[143] Moore, F. L., Robinson, J. C., Bharucha, C. F., Sundaram, B., and Raizen, M. G. Atom Optics Realization of the Quantum δ-Kicked Rotor. *Phys. Rev. Lett. 75* (Dec 1995), 4598–4601. 37

[144] Mott, N. Conduction in glasses containing transition metal ions. *Journal of Non-Crystalline Solids 1*, 1 (1968), 1 – 17. 55, 127

[145] Mott, N. F. Conduction in non-crystalline materials. *Philosophical Magazine 19*, 160 (1969), 835–852. 127

[146] Müller, C. A., and Delande, D. Disorder and interference: localization phenomena. *Chapter 9 in: Les Houches 2009 - Session XCI: Ultracold Gases and Quantum Information* (2011). 55

[147] Müller, C. A., and Shapiro, B. Comment on "Three-Dimensional Anderson Localization in Variable Scale Disorder". *Phys. Rev. Lett. 113* (Aug 2014), 099601. 69

[148] Naether, U., Kartashov, Y. V., Vysloukh, V. A., Nolte, S., Tünnermann, A., Torner, L., and Szameit, A. Observation of the gradual transition from one-dimensional to two-dimensional Anderson localization. *Opt. Lett. 37*, 4 (Feb 2012), 593–595. 55

[149] O'Holleran, K., Dennis, M. R., Flossmann, F., and Padgett, M. J. Fractality of Light's Darkness. *Phys. Rev. Lett. 100*, 5 (Feb. 2008), 053902–. 39

[150] Oitmaa, J., Hamer, C., and Zheng, W. *Series Expansion Methods for Strongly Interacting Lattice Models*. Cambridge University Press, 2006. 109

[151] Ott, H., de Mirandes, E., Ferlaino, F., Roati, G., Türck, V., Modugno, G., and Inguscio, M. Radio Frequency Selective Addressing of Localized Atoms in a Periodic Potential. *Phys. Rev. Lett. 93* (Sep 2004), 120407. 111

[152] Ovchinnikov, Y. B., Müller, J. H., Doery, M. R., Vredenbregt, E. J. D., Helmerson, K., Rolston, S. L., and Phillips, W. D. Diffraction of a Released Bose-Einstein Condensate by a Pulsed Standing Light Wave. *Phys. Rev. Lett. 83* (Jul 1999), 284–287. 91

[153] Pal, A., and Huse, D. A. Many-body localization phase transition. *Phys. Rev. B 82* (Nov 2010), 174411. 127

[154] Palzer, S., Zipkes, C., Sias, C., and Köhl, M. Quantum Transport through a Tonks-Girardeau Gas. *Phys. Rev. Lett. 103* (Oct 2009), 150601. 86

[155] Partridge, G. B., Strecker, K. E., Kamar, R. I., Jack, M. W., and Hulet, R. G. Molecular Probe of Pairing in the BEC-BCS Crossover. *Phys. Rev. Lett. 95* (Jul 2005), 020404. 116

[156] Pasienski, M. *Transport Properties of Ultracold Atoms in a Disordered Optical Lattice*. PhD thesis, University of Illinois at Urbana-Champaign, 2011. 6, 117

[157] Pasienski, M., and DeMarco, B. A high-accuracy algorithm for designing arbitrary holographic atom traps. *Opt. Express 16*, 3 (Feb 2008), 2176–2190. 18, 37

[158] Pasienski, M., McKay, D., White, M., and DeMarco, B. A disordered insulator in an optical lattice. *Nature Physics* (July 2010), 677–680. 37, 122

[159] Paulisch, V., Rui, H., Ng, H., and Englert, B.-G. Beyond adiabatic elimination: A hierarchy of approximations for multi-photon processes. *The European Physical Journal Plus 129*, 1 (2014). 25

[160] Petrovic, C., Pagliuso, P. G., Hundley, M. F., Movshovich, R., Sarrao, J. L., Thompson, J. D., Fisk, Z., and Monthoux, P. Heavy-fermion superconductivity in CeCoIn 5 at 2.3 K. vol. 13, p. L337. 115

[161] Pezzè, L., Pitaevskii, L., Smerzi, A., Stringari, S., Modugno, G., de Mirandes, E., Ferlaino, F., Ott, H., Roati, G., and Inguscio, M. Insulating Behavior of a Trapped Ideal Fermi Gas. *Phys. Rev. Lett. 93* (Sep 2004), 120401. 111

[162] Piggot, A. Angular Drift of CrystalTech $3080-197$ AOMs due to Thermal Transients. *Thywissen Lab Report, Unviersity of Toronto* (2010). 21

[163] Pilati, S., Giorgini, S., Modugno, M., and Prokof'ev, N. Dilute Bose gas with correlated disorder: a path integral Monte Carlo study. *New Journal of Physics 12*, 7 (2010), 073003. 39

[164] Piraud, M. *Anderson localization of matter waves in correlated disorder: from 1D to 3D*. PhD thesis, University of Paris South, 2012. 42, 60, 70, 74, 78, 81

[165] Piraud, M., Aspect, A., and Sanchez-Palencia, L. Anderson localization of matter waves in tailored disordered potentials. *Phys. Rev. A 85*, 6 (Jun 2012), 063611. 74

[166] Piraud, M., Pezze, L., and Sanchez-Palencia, L. Matter wave transport and Anderson localization in anisotropic three-dimensional disorder. *EPL (Europhysics Letters) 99*, 5 (2012), 50003. 74, 77, 78

[167] Piraud, M., Pezze, L., and Sanchez-Palencia, L. Quantum transport of atomic matter waves in anisotropic two-dimensional and three-dimensional disorder. *New Journal of Physics 15*, 7 (2013), 075007. 74

[168] Piraud, M., Sanchez-Palencia, L., and van Tiggelen, B. Anderson localization of matter waves in three-dimensional anisotropic disordered potentials. *Phys. Rev. A 90* (Dec 2014), 063639. 74

[169] Polkovnikov, A., Sengupta, K., and Silva, A. Colloquium: Nonequilibrium dynamics of closed interacting quantum systems. *Rev. Mod. Phys. 83*, 3 (Aug 2011), 863–883. 128

[170] Pozar, D. M. *Microwave Engineering*. John Wiley and Sons, Inc., 1998. 16

[171] Ramasesh, V. V. *Construction of a Quantum Gas Microscope for Fermionic Atoms*. PhD thesis, Massachusetts Institute of Technology, 2013. 11, 18

[172] Regal, C. A., Greiner, M., and Jin, D. S. Observation of Resonance Condensation of Fermionic Atom Pairs. *Phys. Rev. Lett. 92* (Jan 2004), 040403. 116

[173] Rey, A., Pupillo, G., Clark, C., and Williams, C. Ultracold atoms confined in an optical lattice plus parabolic potential: A closed-form approach. *Phys. Rev. A 72*, 3 (Sep 2005). 110

[174] Rey, A. M., Hu, B. L., Calzetta, E., Roura, A., and Clark, C. W. Nonequilibrium dynamics of optical-lattice-loaded Bose-Einstein-condensate atoms: Beyond the Hartree-Fock-Bogoliubov approximation. *Phys. Rev. A 69* (Mar 2004), 033610. 104

[175] Rigol, M., and Muramatsu, A. Confinement control by optical lattices. *Phys. Rev. A 70*, 4 (Oct 2004). 111, 119

[176] Rigol, M., and Muramatsu, A. Quantum Monte Carlo study of confined fermions in one-dimensional optical lattices. *Phys. Rev. A 69* (May 2004), 053612. 119

[177] Roati, G., D/'Errico, C., Fallani, L., Fattori, M., Fort, C., Zaccanti, M., Modugno, G., Modugno, M., and Inguscio, M. Anderson localization of a non-interacting Bose-Einstein condensate. *Nature 453*, 7197 (June 2008), 895–898. 37, 55

[178] Salomon, G., Fouch, L., Wang, P., Aspect, A., Bouyer, P., and Bourdel, T. Gray-molasses cooling of 39 K to a high phase-space density. *EPL (Europhysics Letters) 104*, 6 (2013), 63002. 7

[179] Scarola, V. W., and DeMarco, B. Transport of Hubbard-Band Quasiparticles in Disordered Optical Lattices. *arXiv:1503.07195* (2015). 117, 131, 132

[180] Schneider, U., Hackermuller, L., Ronzheimer, J. P., Will, S., Braun, S., Best, T., Bloch, I., Demler, E., Mandt, S., Rasch, D., and Rosch, A. Fermionic transport and out-of-equilibrium dynamics in a homogeneous Hubbard model with ultracold atoms. *Nat Phys 8*, 3 (Mar. 2012), 213–218. 85, 86

[181] Schneider, U., Hackermller, L., Will, S., Best, T., Bloch, I., Costi, T. A., Helmes, R. W., Rasch, D., and Rosch, A. Metallic and Insulating Phases of Repulsively Interacting Fermions in a 3D Optical Lattice. *Science 322*, 5907 (2008), 1520–1525. 119

[182] Schreiber, M., Hodgman, S. S., Bordia, P., Luschen, H. P., Fischer, M. H., Vosk, R., Altman, E., Schneider, U., and Bloch, I. Observation of many-body localization of interacting fermions in a quasi-random optical lattice. *arXiv:1501.05661* (2015). 130

[183] Schwartz, T., Bartal, G., Fishman, S., and Segev, M. Transport and Anderson localization in disordered two-dimensional photonic lattices. *Nature 446*, 7131 (Mar. 2007), 52–55. 55

[184] Semeghini, G., Landini, M., Castilho1, P., Roy, S. andSpagnolli, G., Trenkwalder, A., Fattori, M., and Inguscio, M. & Modugno, G. Measurement of the mobility edge for 3D Anderson localization. *arxiv:1404.3528v1*. 55, 83

[185] Shapiro, B. Cold atoms in the presence of disorder. *Journal of Physics A: Mathematical and Theoretical 45*, 14 (2012), 143001. 39

[186] Sherson, J. F., Weitenberg, C., Endres, M., Cheneau, M., Bloch, I., and Kuhr, S. Single-atom-resolved fluorescence imaging of an atomic Mott insulator. *Nature 467*, 7311 (Sept. 2010), 68–72. 86

[187] Shklovskii, B., and Efros, A. L. *Electronic Properties of Doped Semiconductors*. Springer-Verlag, Berlin, 1984. 127

[188] Smith, L., and Lobb, C. Percolation in two-dimensional conductor-insulator networks with controllable anisotropy. *Phys. Rev. B 20* (Nov 1979), 3653–3658. 39

[189] Soltan-Panahi, P., Struck, J., Hauke, P., Bick, A., Plenkers, W., Meineke, G., Becker, C., Windpassinger, P., Lewenstein, M., and Sengstock, K. Multi-component quantum gases in spin-dependent hexagonal lattices. *Nat Phys 7*, 5 (May 2011), 434–440. 19

[190] Sommer, A. T. *Strongly Interacting Fermi Gases: Non-Equilibrium Dynamics and Dimensional Crossover*. PhD thesis, Massachusetts Institute of Technology, 2013. 11

[191] Sperling, T., Buhrer, W., Aegerter, C. M., and Maret, G. Direct determination of the transition to localization of light in three dimensions. *Nat Photon 7*, 1 (Jan 2013), 48–52. 62

[192] Srednicki, M. Chaos and quantum thermalization. *Phys. Rev. E 50* (Aug 1994), 888–901. 128

[193] Steck, D. A. Rubidium 87 D Line Data. http://steck.us/alkalidata/, 2003. 25

[194] Steglich, F., Aarts, J., Bredl, C. D., Lieke, W., Meschede, D., Franz, W., and Schäfer, H. Superconductivity in the Presence of Strong Pauli Paramagnetism: $CeCu_2Si_2$. *Phys. Rev. Lett. 43* (Dec 1979), 1892–1896. 85, 115

[195] Steinbach, J., Twamley, J., and Knight, P. L. Engineering two-mode interactions in ion traps. *Phys. Rev. A 56* (Dec 1997), 4815–4825. 25

[196] Stellmer, S., Grimm, R., and Schreck, F. Production of quantum-degenerate strontium gases. *Phys. Rev. A 87* (Jan 2013), 013611. 8

[197] Stöferle, T., Moritz, H., Schori, C., Köhl, M., and Esslinger, T. Transition from a Strongly Interacting 1D Superfluid to a Mott Insulator. *Phys. Rev. Lett. 92* (Mar 2004), 130403. 91

[198] Strohmaier, N., Takasu, Y., Günter, K., Jördens, R., Köhl, M., Moritz, H., and Esslinger, T. Interaction-Controlled Transport of an Ultracold Fermi Gas. *Physical Review Letters 99*, 22 (Nov 2007), 220601. 85, 111, 137

[199] Struck, J., Weinberg, M., Olschlager, C., Windpassinger, P., Simonet, J., Sengstock, K., Happner, R., Hauke, P., Eckardt, A., Lewenstein, M., and Mathey, L. Engineering Ising-XY spin-models in a triangular lattice using tunable artificial gauge fields. *Nat Phys 9*, 11 (Sep 2013), 738–743. 86

[200] Stützer, S., Kartashov, Y. V., Vysloukh, V. A., Konotop, V. V., Nolte, S., Torner, L., and Szameit, A. Hybrid Bloch-Anderson localization of light. *Opt. Lett. 38*, 9 (May 2013), 1488–1490. 55

[201] Thouless, D. Electrons in disordered systems and the theory of localization. *Physics Reports 13*, 3 (Oct 1974), 93–142. 55

[202] van Oosten, D., van der Straten, P., and Stoof, H. T. C. Quantum phases in an optical lattice. *Phys. Rev. A 63* (Apr 2001), 053601. 104

[203] van Tiggelen, B. A. Anderson Localization of Waves - Course at Les Houches. In *http://www.andersonlocalization.com/canonal50.php* (1998). 55

[204] Varma, C. High-temperature superconductivity: Mind the pseudogap. *Nature 468*, 7321 (Nov. 2010), 184–185. 85, 116

[205] Vollhardt, D., and Wolfle, P. Anderson Localization in $d <= 2$ Dimensions: A Self-Consistent Diagrammatic Theory. *Phys. Rev. Lett. 45* (Sep 1980), 842–846. 79

[206] Vollhardt, D., and Wolfle, P. Diagrammatic, self-consistent treatment of the Anderson localization problem in $d <= 2$ dimensions. *Phys. Rev. B 22* (Nov 1980), 4666–4679. 79

[207] Vuletić, V., Chin, C., Kerman, A. J., and Chu, S. Degenerate Raman Sideband Cooling of Trapped Cesium Atoms at Very High Atomic Densities. *Phys. Rev. Lett. 81* (Dec 1998), 5768–5771. 8

[208] Weinrib, A. Percolation threshold of a two-dimensional continuum system. *Phys. Rev. B 26* (Aug 1982), 1352–1361. 39

[209] Weitenberg, C., Endres, M., Sherson, J. F., Cheneau, M., Schausz, P., Fukuhara, T., Bloch, I., and Kuhr, S. Single-spin addressing in an atomic Mott insulator. *Nature 471*, 7338 (Mar. 2011), 319–324. 86

[210] Weld, D. M., Medley, P., Miyake, H., Hucul, D., Pritchard, D. E., and Ketterle, W. Spin Gradient Thermometry for Ultracold Atoms in Optical Lattices. *Phys. Rev. Lett. 103* (Dec 2009), 245301. 95

[211] White, M. *Ultracold Atoms in a Disordered Optical Lattice*. PhD thesis, University of Illinois at Urbana-Champaign, 2009. 6, 117

[212] White, M., Pasienski, M., McKay, D., Zhou, S. Q., Ceperley, D., and DeMarco, B. Strongly Interacting Bosons in a Disordered Optical Lattice. *Phys. Rev. Lett. 102* (Feb 2009), 055301. 118

[213] Wiersma, D. S., Bartolini, P., Lagendijk, A., and Righini, R. Localization of light in a disordered medium. *Nature 390*, 6661 (Dec. 1997), 671–673. 55, 62

[214] Williamson, R. S. I. *Magneto-optical trapping of potassium isotopes.* PhD thesis, University of Wisconsin - Madison, 1997. 6

[215] Wineland, D. J., Monroe, C., Itano, W. M., Leibfried, D., King, B. E., and Meekhof, D. M. Experimental Issues in Coherent Quantum-State Manipulation of Trapped Atomic Ions. *Journal of Research of the National Institute of Standards and Technology 103*, 3 (1998), 259–328. 25

[216] Yedjour, A., and Van Tiggelen, B. A. Diffusion and localization of cold atoms in 3D optical speckle. *Eur. Phys. J. D 59*, 2 (Aug. 2010), 249–255. 60

[217] Youn, S. H., Lu, M., Ray, U., and Lev, B. L. Dysprosium magneto-optical traps. *Phys. Rev. A 82* (Oct 2010), 043425. 8

[218] Yu, D., Wang, C., Wehrenberg, B. L., and Guyot-Sionnest, P. Variable Range Hopping Conduction in Semiconductor Nanocrystal Solids. *Phys. Rev. Lett. 92* (May 2004), 216802. 127

[219] Yukalov, V. I. Equilibration and thermalization in finite quantum systems. *Laser Physics Letters 8*, 7 (2011), 485. 128

[220] Zupancic, P. P. J. Dynamic Holography and Beamshaping using Digital Micromirror Devices. Master's thesis, Ludwig-Maximilians-Universitat Munchen, 2013. 19

[221] Zwierlein, M. W., Abo-Shaeer, J. R., Schirotzek, A., Schunck, C. H., and Ketterle, W. Vortices and superfluidity in a strongly interacting Fermi gas. *Nature 435*, 7045 (Jun 2005), 10471051. 116

[222] Zwierlein, M. W., Stan, C. A., Schunck, C. H., Raupach, S. M. F., Kerman, A. J., and Ketterle, W. Condensation of Pairs of Fermionic Atoms near a Feshbach Resonance. *Phys. Rev. Lett. 92* (Mar 2004), 120403. 116